

# Satellite Observations of Atmospheric Gravity Waves

Thesis submitted for the degree of  
Doctor of Philosophy  
at the University of Leicester

**Xiuping Yan**  
Department of Physics & Astronomy  
University of Leicester

November 2009

© Xiuping Yan, November 2009

This thesis is copyright material and no quotation from it may be published without proper acknowledgement.

# Declaration

I hereby declare that no part of this thesis has been previously submitted to this or any other University as part of the requirement for a higher degree. The work within this document has been conducted by the undersigned except for contributions where acknowledged in this text.

Xiuping Yan

November 2009

## Abstract

### Satellite Observations of Atmospheric Gravity Waves

Xiuping Yan

A new methodology of gravity wave observations has been developed for the High Resolution Dynamics Limb Sounder (HIRDLS). Individual vertical profiles of gravity-wave temperature perturbations that were determined by subtraction of a dynamic 31-day background field and a 1000 km along-track temperature filter were Fourier transformed to estimate the gravity-wave temperature amplitudes and vertical wavelengths ( $\sim 2 - 16$  km) in the stratosphere.

Gravity wave activity is highly variable with season and can be highly orographically dependent, especially in the winter extratropics. Investigations of episodes of enhanced gravity waves over the southern Andes, the Cascade Range and the Rockies in the winter months of 2006 indicate that orographic gravity waves propagate downwind from the mountains. By way of contrast, observations of gravity waves around the Himalayas show a strong relationship with the cyclones in that region.

HIRDLS observations over the southern Andes during July-September 2006 were compared to the orographic gravity-wave parameterization scheme in the UK Met Office Unified Model®. The results indicate that the observed waves are likely to be orographically excited. The observed wave activity extends large distances (a few thousand kilometres) downwind of the mountains and over the ocean. This downstream wave activity is not represented by the parameterization scheme similar to many schemes, which assume that the waves propagate vertically above the mountains only.

Gravity waves over the tropics and tropical South America were compared with the AVHRR Outgoing Longwave Radiation (OLR), TRMM convective rainfall and ECMWF winds for convective sources. The comparisons show that the peak gravity wave temperature amplitudes correspond closely to the  $OLR \leq 200 \text{ W/m}^2$ , in good agreement with the mesoscale cyclones and are above the updrifts, which indicate deep convective generation of the gravity waves. These waves show vertical propagation with higher-frequency and  $\sim 7.5$  km vertical wavelengths in the lower stratosphere.

## Acknowledgement

I am grateful to the EPSRC (Engineering and Physical Sciences Research Council) for their financial support of my doctoral research through the DHPA (Dorothy Hodgkin Postgraduate Awards) scheme.

I am heartily thankful to my supervisor, Neil Arnold, for his time, enthusiasm and support, and for sharing his ideas with me, from the initial to the final level. He inspired me to persist with this difficult project in spite of the fact that there was no pre-existing expertise in satellite gravity wave observations in Leicester. I would like to thank my co-supervisor, John Remedios, for his support and his help in HIRDLS simulation, and for the interesting discussions we had during my PhD. Mike Goad deserves special thanks as my thesis committee member.

I am especially grateful to my collaborators, Simon Vosper and Helen Wells from the UK Met Office, for helpful discussions, lots of good ideas, and giving wise advice. I learned a lot from them about orographic gravity-wave parameterizations in the Met Office Unified Model. They were supportive of my work in general during our collaboration and we all enjoyed working together. This collaboration will be of great benefit to both parties and was totally independent from the work done in my PhD. Jian-Guo Li in the UK Met Office played a crucial role in initiating the collaboration started for which I am grateful.

I would like to thank John Gille and John Barnett, for allowing me to attend the HIRDLS science team meeting, for providing me with an opportunity to present my work at one of the meetings, and for happily and seriously treating my feedback on HIRDLS temperature data. I am grateful for the helpful discussions with them as well as other HIRDLS science team members.

A big thank you must go to David Moore, for allowing me to adapt his MIPAS gas retrieval algorithm for HIRDLS temperature retrieval and teaching me about his code. Regrettably, the simulation work that includes the temperature retrieval is excluded from this thesis due to both time and word count limitations.

## Acknowledgement

---

I am grateful to Prof. Stanley Cowley, for giving me advice on the JGR paper review process. I wish to thank Prof. of Applied Mathematics, Alexander Gorban, for his willingness to provide helps in mathematics and for his kindness. Thanks also go to Prof. Terry Robinson, for helpful discussions about wave theories.

I would like to thank all my colleagues, for their kind assistance with computers and programming, and for helping with various applications. All my office buddies made the office a convivial place to work.

Finally, I would like to thank my family and my friends, for helping me get through the difficult times, for all of their emotional support, and for the care that they provided. My deepest gratitude goes to my parents, Zihua Ming and Chenglin Yan. They bore me, raised me, unflaggingly supported me, taught me and loved me. To them I dedicate this thesis.

# Contents

## Chapter 1

<b>Introduction .....</b>	<b>1</b>
1.1 Purpose .....	1
1.2 Why Gravity Waves are Important .....	1
1.3 Layout of the Thesis .....	3

## Chapter 2

<b>Background Theory .....</b>	<b>6</b>
2.1 Basic Atmospheric Structures .....	6
2.2 Composition of the Atmosphere .....	11
2.3 Global-Scale Circulation of the Atmosphere .....	12
2.4 Gravity Waves .....	16
2.4.1 Characteristics of Gravity Waves .....	18
2.4.1.1 Wave Scales .....	18
2.4.1.2 Phase Velocity and Group Velocity .....	19
2.4.2 Gravity Wave Sources .....	20
2.4.2.1 Topographic Source .....	21
2.4.2.2 Convective Source .....	22
2.4.3 Gravity Wave Dispersion .....	23
2.4.4 Gravity Wave Propagation .....	24
2.4.5 Gravity Wave Observations .....	25
2.4.6 Climatologies of Gravity Wave Activity .....	30
2.5 Other Relevant Atmospheric Waves .....	33
2.5.1 Planetary Waves .....	33
2.5.2 Equatorial Waves .....	36
2.5.3 Atmospheric Thermal Tides .....	37
2.6 Summary .....	38

## Chapter 3

<b>HIRDLS and HIRDLS Temperature .....</b>	<b>40</b>
3.1 Overview of HIRDLS Instrument .....	40

3.2	The Platform of the HIRDLS Instrument: Aura .....	42
3.3	Design of the HIRDLS Instrument .....	43
3.3.1	Heritage .....	43
3.3.2	HIRDLS Subsystem.....	44
3.3.3	Optical System .....	45
3.3.4	Spectral Band-Pass Filters .....	47
3.3.5	Spectral Channels Characteristics .....	47
3.3.6	FOV and IFOV Characteristics .....	47
3.4	Present Status of HIRDLS.....	50
3.5	Revised Operational Scan Patterns .....	53
3.6	Limb Viewing .....	54
3.7	HIRDLS Data Products .....	56
3.7.1	L0-1 Process (L1PP, L1X, L1C) .....	56
3.7.2	L2 Pre-Processor (L2PP) .....	56
3.7.3	L2 Cloud Detection (L2CLD) .....	57
3.7.4	L1-2 Processor (L2).....	57
3.8	HIRDLS Temperature.....	57
3.8.1	Temperature Retrieval.....	57
3.8.2	Random Error .....	60
3.8.3	Systematic Bias .....	61
3.8.4	Effects from Clouds .....	61
3.9	Summary .....	61

## Chapter 4

<b>Gravity Wave Observations: Methodology and Results .....</b>	<b>64</b>
4.1 Extraction of Gravity Waves: Temperature Perturbations .....	65
4.1.1 Background Field.....	66
4.1.2 The Along-Track Temperature Filter .....	71
4.2 Data Analysis .....	73
4.3 Results and Discussion.....	76
4.3.1 Gravity Wave Temperature Amplitude and Vertical Wavelength .....	76
4.3.2 Case Studies: Wave Events over the Southern Andes, the Cascade Range and the Rockies and the Himalayas .....	91
4.4 Summary .....	96

**Chapter 5**

**Gravity Waves over the Southern Andes: a Comparison with Predictions from an Orographic Gravity-Wave Parameterization Scheme ..... 98**

- 5.1 Orographic Gravity-Wave Parameterization in the Met Office Unified Model 100
- 5.2 The HIRDLS Observations ..... 102
- 5.3 HIRDLS observations vs. MetUM parameterizations ..... 107
- 5.4 Discussion and Summary ..... 115

**Chapter 6**

**Convective Gravity Waves ..... 118**

- 6.1 Introduction ..... 118
- 6.2 Indicators of Convection ..... 119
- 6.3 Gravity Waves over the Tropics ..... 120
- 6.4 Gravity Waves over the Tropical South America ..... 130
- 6.5 Summary ..... 137

**Chapter 7**

**Conclusions and Outlook ..... 139**

**Appendix A**

**A General Gravity-Wave Solution to Equations of Motion ..... 146**

**Appendix B**

**The Operational Scheme of OGW Parameterization in the MetUM ..... 151**

**References ..... 155**

# Chapter 1

## Introduction

### 1.1 Purpose

Small-scale gravity waves are often not resolved in global forecast, climate and general circulation models. These models take account of the sub-grid gravity waves via parameterization. The gravity wave parameterizations without being constrained by observations could result in unrealistic model predictions. Therefore, observations of gravity waves are necessary for placing constraints on the parameterization of gravity waves in global forecast, climate and general circulation models. The project aims to observe global atmospheric gravity waves using satellite data to provide datasets for gravity wave parameterization in these models and more fully understand the contribution that these waves make to atmospheric transport and chemical processes.

### 1.2 Why Gravity Waves are Important

Atmospheric gravity waves modify the atmospheric circulation and influence the atmospheric thermal structure by transferring momentum from their sources, which are dominant in the troposphere and lower stratosphere, to anywhere between the troposphere and thermosphere, where they break or dissipate. In 1960, *Hines* [1960] first postulated the role of internal gravity waves in the atmosphere. By developing a parameterization of gravity waves, *Lindzen* [1981] and *Holton* [1982, 1983] demonstrated the contribution of gravity wave driving forces in determining the reversed meridional temperature gradient and thus the average 70° – 80°K colder summer mesopause than the winter mesopause. The influence of gravity wave breaking in the mesosphere on the mean meridional circulation and temperature distribution in the stratosphere was explored by *Haynes et al.* [1991], *Garcia and Boville* [1994], *Rosenlof* [1996] and *Alexander and Rosenlof* [1996] using the “downward control”

principle. Figure 1.1 schematically illustrates mean-flow forcing effects of gravity waves in the middle atmosphere.

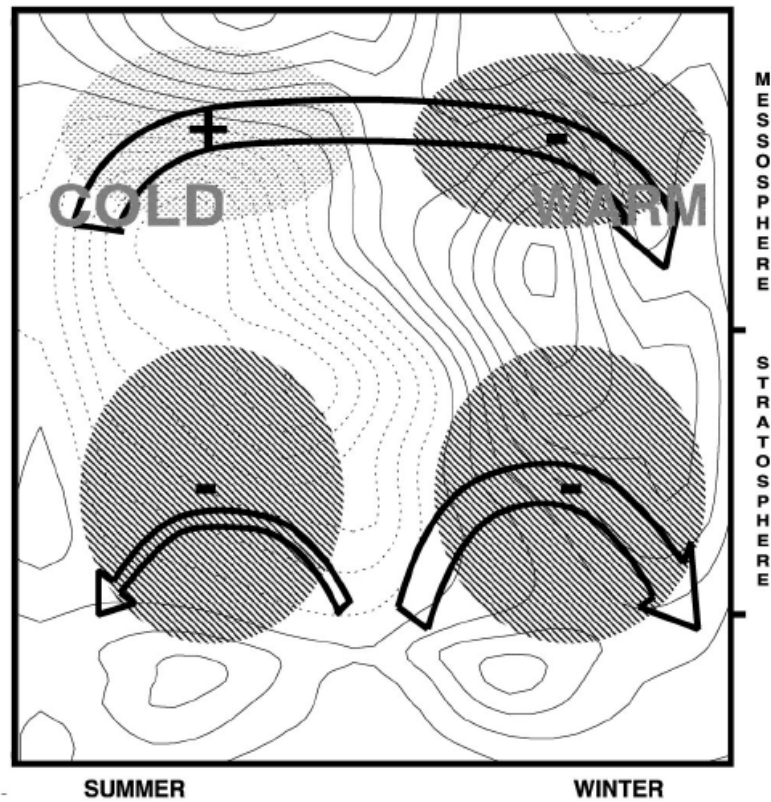


Figure 1.1 Driving forces of gravity waves on the middle atmosphere transport circulation and effects on wind and temperature structures. The thin contours denote zonal mean wind at intervals of 10 m/s (dotted contours are for westward winds). The transport circulation is illustrated with thick arrows and the gravity wave driving is illustrated with hatched areas with minus signs denoting westward forcing and a plus sign denoting eastward forcing [Fritts and Alexander, 2003].

Studies using numerical models, for example, *Lindzen and Holton* [1968], *Sassi and Garcia* [1994], *Alexander and Holton* [1997], *Mayr et al.* [1997], and *Ray et al.* [1998], found that gravity wave dissipation produces a driving force on the tropical quasi-biennial oscillation (QBO) in the stratosphere and semi-annual oscillation (SAO) both in the stratosphere and mesosphere. Studies by *Walterscheid* [1981], *Holton* [1984], *Miyahara* [1985], *Miyahara et al.* [1986], *Forbes et al.* [1991], *Lu and Fritts* [1993], *Mayr et al.* [1998], and *Meyer* [1999] indicate that gravity waves also interact with larger scale wave motions such as tidal and planetary wave motions.

Gravity waves not only influence the atmospheric thermal structure, but also play an important role in the atmospheric compositional structure. Gravity wave-induced turbulence and thus turbulent mixing and heat transport could affect the local composition of chemical species. This effect has been studied by *Fritts and Dunkerton* [1985], *Garcia and Solomon* [1985], *Strobel et al.* [1987], *Fuller-Rowell* [1994], *Liu et al.* [2000] and *Hays et al.* [2003]. In the northern hemisphere, orographically generated gravity waves can locally cool the stratosphere and provide favourable conditions for the formation of polar stratospheric clouds (PSCs). The implications for ozone destruction in the Arctic have been investigated by *Dornbrack et al.* [1999], *Carslaw et al.* [1999], *Dornbrack et al.* [2001] and *Dörnbrack and Leutbecher* [2001]. *Fritts and Alexander* [2003] summarized and reviewed the role of gravity waves in the middle atmosphere.

The majority of investigations into the atmospheric circulation are carried out numerically without resolving all gravity waves in the atmosphere in the numerical models. The unresolved gravity waves are relatively small in scale compared with the resolvable gravity waves and must be included via parameterization. Those numerical models employing gravity wave parameterizations not constrained by observations tend to produce unrealistic predictions and weather forecasts [e.g. *Sawyer*, 1959; *Pielke*, 1984; *Grasso*, 2000].

### 1.3 Layout of the Thesis

In this thesis, observations of atmospheric gravity waves are discussed for the satellite HIRDLS (HIGH Resolution Dynamics Limb Sounder) instrument. HIRDLS is an infrared limb-viewing instrument with the highest vertical resolution ( $\sim 1$  km) compared with previous infrared limb sounders. This high vertical resolution is suitable for observing short vertical wavelength gravity waves. *Alexander et al.* [2008a] have demonstrated the ability of HIRDLS to observe gravity waves by analyzing one month of data (May 2006). They extracted gravity waves by removing the zonal mean temperatures and planetary-scale zonal waves 0 – 3 from the HIRDLS temperatures. The planetary-scale zonal waves were estimated using S transform analysis and the gravity wave characteristics were determined using the S transform on adjacent temperature perturbation profile pairs. The thesis describes a new methodology that is

developed to extract and analyze global gravity wave temperature amplitudes and vertical wavelength using HIRDLS temperature data. Maps of gravity waves are extended to cover a year-long record for seasonal variation and global distribution of wave activity.

Chapter 2 gives the necessary background theory on atmospheric structure and composition and global-scale circulations of the atmosphere. A large portion of the chapter is devoted to gravity waves including wave characteristics, gravity wave sources, dispersion and propagation, gravity wave observations and climatologies of gravity waves. Topographic and convective sources are described in more detail for a better understanding of these sources excited gravity waves observed by HIRDLS. Other relevant large-scale waves in the atmosphere are also introduced in order to understand the basic ideas of the gravity wave extraction procedure. The knowledge given in this chapter is fundamental for understanding the connections between gravity waves and mean-flow circulations as well as other relevant planetary-scale waves.

Chapter 3 introduces the satellite remote sensing HIRDLS instrument, which is the data source for observing gravity waves and its level 2 temperature data. Since gravity wave observations are instrumentally dependent, a detailed introduction of the instrument and its platform is necessary for understanding the observed gravity waves. In addition, after launch, an unexpected blockage of  $\sim 80\%$  of the front aperture was discovered by the HIRDLS scientists. Due to this unexpected problem, the operational mode has been readjusted and extra algorithms have been developed for the removal of the blockage effects from the spectral signal of the atmosphere. These made the introduction of the instrument and its temperature data more important.

Chapter 4 focuses on the description of a new methodology of gravity wave observations from HIRDLS. The development of the methodology is physically and mathematically explained in detail. Small-scale perturbations that are assumed to be caused by gravity waves, called gravity wave temperature perturbations, are isolated by subtracting a background field and an along-track temperature filter from HIRDLS temperature profiles. The gravity wave temperature perturbations are Fourier transformed to estimate vertical wavelength and temperature amplitude. In this chapter, the results for the whole year 2006 are presented and compared with observations from other satellite instruments such as MLS, CRISTA and from the same instrument but

using a different technique. Seasonal variations and global distribution are investigated based on maps of gravity waves from HIRDLS. Three cases are discussed for orographic gravity waves over the southern Andes and the North America Cordillera and non-orographic gravity waves around the Himalayas as primary wave-source studies.

Following the case studies in chapter 4, an investigation is carried out for orographic gravity waves over the southern Andes in chapter 5. The observed HIRDLS gravity waves are compared with the orographic gravity wave parameterization scheme in the Met Office forecast model. Three configurations of the operational orographic gravity wave parameterization scheme are discussed in the comparison. The observed gravity waves are also compared with the ECMWF (European Centre for Medium-Range Weather Forecasts) operational analysis. The comparisons provide evidence of orographically excited gravity waves over the southern Andes and also demonstrate the application of observations in constraining gravity wave parameterizations in models.

Chapter 6 focuses on convectively generated gravity waves in the tropical stratosphere, particularly over tropical South America. The observed gravity waves are compared with convective indicators such as outgoing long-wave radiation (OLR) from AVHRR and convective rainfall from the TRMM satellite. The ECMWF operational analysis is also used to support the convection source.

The studies in chapters 4 to 6 suggest that the observed gravity waves from HIRDLS are consistent with the climatology of gravity waves developed by other satellite instruments. Conclusions and future work are given in chapter 7.

# Chapter 2

## Background Theory

### 2.1 Basic Atmospheric Structures

The atmosphere is an envelope of gases and suspended particles surrounding the Earth. The absorption of solar radiation and infrared emission by the gases in different height regions results in several atmospheric layers characterized by variations in temperature. The vertical distribution of certain atmospheric properties of the atmosphere, such as the height distribution of temperature, pressure, density and wind, is fundamental to the observation of gravity waves. The temperature layers are, from the Earth's surface to 100 km, the troposphere, stratosphere, mesosphere and thermosphere, with the corresponding upper boundary layers called the tropopause, stratopause and mesopause, respectively. Approximately 90% of the atmospheric mass is in the troposphere, a little under 10% in the stratosphere and only about 0.1% in the mesosphere and above. The vertical temperature profile for the midlatitude and the atmospheric layers are shown in figure 2.1.

The region from the Earth's surface to the tropopause is called the lower atmosphere, where temperature decreases with height. The tropopause, the boundary between the lower and middle atmosphere, has a typical height of 8 km in the polar regions and a height of 18 km over the equator. The region from the tropopause to the mesopause (at approximately 90 km) is referred to as the middle atmosphere. The temperature in the stratosphere increases with altitude and there is a local temperature maximum at the stratopause (~ 50 km). In the mesosphere, the global mean temperature falls with altitude to the coldest region of the atmosphere, the mesopause. The temperature structure of this region is greatly affected by the global-scale meridional circulation, resulting in a colder summer mesopause and a warmer winter mesopause. In the middle atmosphere the atmospheric constituents are well mixed by eddy processes.

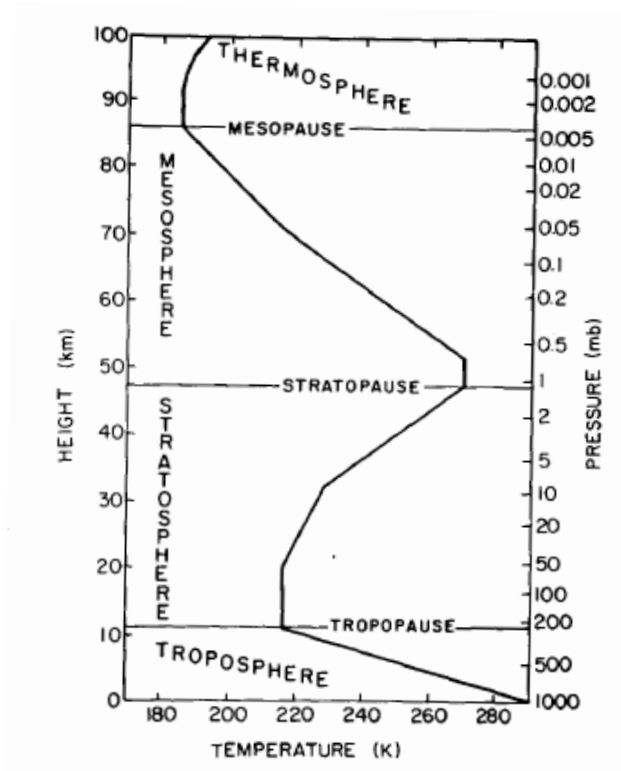


Figure 2.1 Midlatitude temperature profile. Based on the *U.S. Standard Atmosphere* [1976].

The vertical profile of atmospheric pressure can be determined by use of the hydrostatic equation and the ideal gas law. Consider a thin vertical slice of the atmosphere from height  $z$  to height  $z + dz$ . The upward/downward pressure force acting on the lower/upper surface of the slice at  $z / (z + dz)$  is  $p(z)A / p(z + dz)A$ , where  $p$  is the pressure and  $A$  is the area. The net upward force is  $[p(z) - p(z + dz)]A$ . In equilibrium, this upward force must be balanced by the downward force generated by the weight of the slice,  $\rho g A dz$ , where  $\rho$  is density and  $g$  is the magnitude of the gravity acceleration. This equilibrium can be written as

$$[p(z) - p(z + dz)]A = \rho g A dz \quad 2-1$$

and reformatted to

$$\partial p / \partial z = -\rho g. \quad 2-2$$

Equation 2-2 is called the hydrostatic equation. The density of the atmosphere can be derived from the ideal gas law

$$p = \rho RT, \quad 2-3$$

where  $R$  is the gas constant for dry air ( $= 287 \text{ J}/(\text{kg} \cdot \text{K})$ ) that is determined by the Universal Gas Constant  $R_u$  ( $= 8.314 \text{ J}/(\text{mol} \cdot \text{K})$ ) divided by the molecular weight of dry air  $m_{gas}$  ( $\approx 28.98 \text{ g/mol}$ ). Combining equations 2-2 and 2-3 gets

$$\frac{\partial p}{p} = -\frac{g}{RT} \partial z, \quad 2-4$$

which is simplified

$$p = p_s \exp(-z/H), \quad 2-5$$

where  $H$  ( $\equiv RT_s/g_0$ , where  $g_0 = 9.81 \text{ ms}^{-2}$  is the global average of gravity at mean sea level and  $T_s$  is a constant reference temperature) is a mean scale height and  $p_s$  is a standard reference pressure taken as 1000 hPa. The equation (2-5) shows the exponential decrease of pressure with height, which is illustrated by the vertical axis of figure 2.1 on the right.

On substituting for  $p$  and  $p_s$  in 2-3, using 2-5 and rearranging, the density equation is obtained

$$\rho = \rho_s \exp(-z/H), \quad 2-6$$

where  $\rho_s$  is the density at the ground surface. The density in the atmosphere is proportional to the pressure and exponentially decreases with height.

Potential temperature relates the temperature of an air parcel to a reference pressure. Under adiabatic conditions it is a conserved quantity and is therefore much more useful than temperature. The potential temperature is defined by

$$\theta \equiv T(p_s/p)^\kappa, \quad 2-7$$

where  $\kappa \equiv R/c_p \approx 2/7$  and  $c_p$  is the specific heat at constant pressure. Equation 2-5 and 2-7 together give

$$\theta = T \exp(\kappa z / H). \quad 2-8$$

Equation 2-8 implies that the potential temperature increases with height.

The buoyancy frequency (also called Brunt-Väisälä frequency), is the angular frequency of internal waves (a vertical displaced air parcel oscillating within a stable stratified environment). Consider an air parcel of in equilibrium was adiabatically displaced upward from one particular height  $z_e$  to a different level. The parcel at some height  $z$  is subject to two forces, gravity and the buoyant force from the environmental atmosphere. Let  $p_p(z)$  and  $\rho_p(z)$  denote the pressure and density in the parcel and  $p(z)$  and  $\rho(z)$  the pressure and density of the environment. By the second law of motion

$$\rho_p \frac{\partial^2 z}{\partial t^2} = -\rho_p g - \frac{\partial p}{\partial z}. \quad 2-9$$

Substituting for the hydrostatic equation in equation 2-2 gives

$$\frac{\partial^2 z}{\partial t^2} = -\frac{\rho_p - \rho}{\rho_p} g. \quad 2-10$$

Assume that the volumes of the air parcel and the displaced environmental air are equal and that the pressure in the air parcel is always equal to the environmental pressure so that buoyancy is due only to the difference in density of the parcel compared to the environment. By the idea gas law

$$\frac{\rho_p - \rho}{\rho_p} = \frac{T - T_p}{T} = 1 - T_p / T. \quad 2-11$$

Since the pressures are equal

$$\frac{\theta_p}{\theta} = \frac{T_p}{T}. \quad 2-12$$

Thus equation 2-10 becomes

$$\frac{\partial^2 z}{\partial t^2} = -g(1 - \theta_p / \theta). \quad 2-13$$

If the left hand term of equation 2-13 is designated by  $a(z)$ , due to zero acceleration at  $z_e$  a Taylor's series expansion gives

$$a(z) = \left. \frac{\partial a}{\partial z} \right|_{z_e} (z - z_e). \quad 2-14$$

Since the process is adiabatic, the potential temperature of the parcel  $\theta_p$  is constant. Therefore the change in  $a(z)$  with height is due entirely to the variation in  $\theta$  with height so that

$$\frac{\partial a}{\partial z} = \frac{\partial[-g(1 - \theta_p / \theta)]}{\partial \theta} \frac{\partial \theta}{\partial z} = -g \frac{\theta_p}{\theta^2} \frac{\partial \theta}{\partial z}. \quad 2-15$$

Since  $\theta_p = \theta$  at  $z = z_e$ , equation 2-15 is reduced to

$$\frac{\partial a}{\partial z} = -\frac{g}{\theta} \frac{\partial \theta}{\partial z}. \quad 2-16$$

Substituting this equation into equation 2-14 results in

$$\frac{\partial^2 z}{\partial t^2} = -\frac{g}{\theta} \frac{\partial \theta}{\partial z} (z - z_e), \quad 2-17$$

which is the differential equation of harmonic motion about an equilibrium at  $z_e$  and the frequency of oscillation is given by

$$N = \sqrt{\frac{g}{\theta} \frac{\partial \theta}{\partial z}}, \quad 2-18$$

where  $N$  is the buoyancy frequency and is sometimes called Brunt-Väisälä frequency.  $N$  varies with height as well as with latitude, longitude and season. For example, in the stratosphere  $N \approx (5 \times 10^{-4})^{1/2} s^{-1}$ , while in the mesosphere  $N \approx (3 \times 10^{-4})^{1/2} s^{-1}$  [Andrews *et al.*, 1987]. However, the buoyancy frequency is often assumed to be a constant

throughout the middle atmosphere. The square of  $N$  is used to measure the stability of the atmosphere. When  $N^2 > 0$  the atmosphere is statically stable.

Note that the buoyant force described by 2-9 is restricted to vertical displacements of air parcels. However, in the atmosphere gravity waves can propagate at any direction and almost always at an angle to the vertical. If a displacement occurs on a surface at an angle  $\beta$  to the horizontal, the frequency of oscillation is consequently reduced to  $N \sin \beta$ . Therefore, the frequency of gravity waves depends on the propagation angle and the Brunt-Väisälä frequency described by equation 2-18 is the maximum frequency.

## 2.2 Composition of the Atmosphere

The Earth's atmosphere is composed primarily of nitrogen and oxygen, which together account for 98.65% of the total mass of the dry atmosphere. The noble gas argon accounts for another 1.28%. The remainder, less than 0.1% of the total mass, contains many small but important trace gases. Major trace species in the atmosphere including water vapor ( $\text{H}_2\text{O}$ ), carbon dioxide ( $\text{CO}_2$ ) and ozone ( $\text{O}_3$ ) and minor trace species such as nitrous oxide ( $\text{N}_2\text{O}$ ), methane ( $\text{CH}_4$ ) and the chlorofluoromethanes ( $\text{CF}_2\text{Cl}_2$  and  $\text{CFCl}_3$ ) have important effects on the Earth's climate. The troposphere contains approximately 90% of the atmospheric mass and nearly all the water vapor. The stratosphere contains most of the atmospheric ozone which absorbs solar ultraviolet radiation to protect the biosphere from the damaging effects of the radiation. In addition to gases, the atmosphere has a wide variety of tiny particles suspended in the air, known as aerosols.

In the lower and middle atmosphere, the mixing ratios of all the gases of the atmosphere tend to be uniform by fluid motions on all scales. Except for the constituents with significant sources or sinks resulting in spatially and temporally varying mixing ratios, most species have vertical variability that is much greater than horizontal and temporal variability. The primary constituents have nearly constant mass fractions in height in the atmosphere. The major trace gas  $\text{CO}_2$  is well mixed in most of the middle atmosphere, so that it is relatively stable in space and time compared with  $\text{H}_2\text{O}$  and  $\text{O}_3$ .

### 2.3 Global-Scale Circulation of the Atmosphere

The zonal mean temperature and wind distributions in the middle atmosphere are maintained by the competing effects between the net radiative forcing (the solar heating and infrared heating or cooling) and the dynamical heating and cooling. The radiative heating gives a clear seasonal variation, i.e. maximum heating/cooling at the summer/winter pole and for the equinoxes (spring and autumn), the maximum heating is at the equator and cooling at both poles. This differential heating is balanced by the diabatic circulation in the meridional plane, which is primarily driven by eddy forcing [Andrews *et al.*, 1987]. The circulation in summer and winter consists of rising motion near the summer pole and sinking near the winter pole, with a meridional drift from the summer into the winter hemisphere in between. In spring and autumn, rising motion is around the equator with a poleward meridional drift in both hemispheres showing a fairly weak diabatic circulation. The Coriolis torque exerted by the meridional drift tends to generate mean zonal westerlies in the winter hemisphere, weak easterlies in the summer hemisphere and westerlies in both hemispheres in spring and autumn. Figures 2.2 and 2.3 show the zonally averaged solstice mean temperature and wind fields, respectively, based primarily on Northern Hemisphere data. It should be noted that the temperature above 60 km increases from the summer pole to the winter pole, resulting in the reversed temperature gradient and much colder summer mesopause and warmer winter mesopause than the radiative equilibrium. In the lower stratosphere between the cold tropical tropopause and the winter pole the temperature increases.

In the middle atmosphere, the principle acceleration/deceleration force on the general circulation is due to gravity waves. The gravity waves generated by air flow over terrain features carry upward a stress, which will act against the mean flow and is called gravity wave drag. However, gravity waves generated by other sources in the middle atmosphere can decelerate and accelerate the mean flow, respectively. Chun and Baik [1998] calculated the momentum transport by convectively generated gravity waves. Their results show that a maximum acceleration of the zonal wind by the gravity wave momentum flux is about 10 m/s/day at 3.4 km height and a deceleration is about 24 m/s/day at 10 km height. These values suggest that the upward and downward transport of stress by gravity waves is very important to atmospheric dynamics.

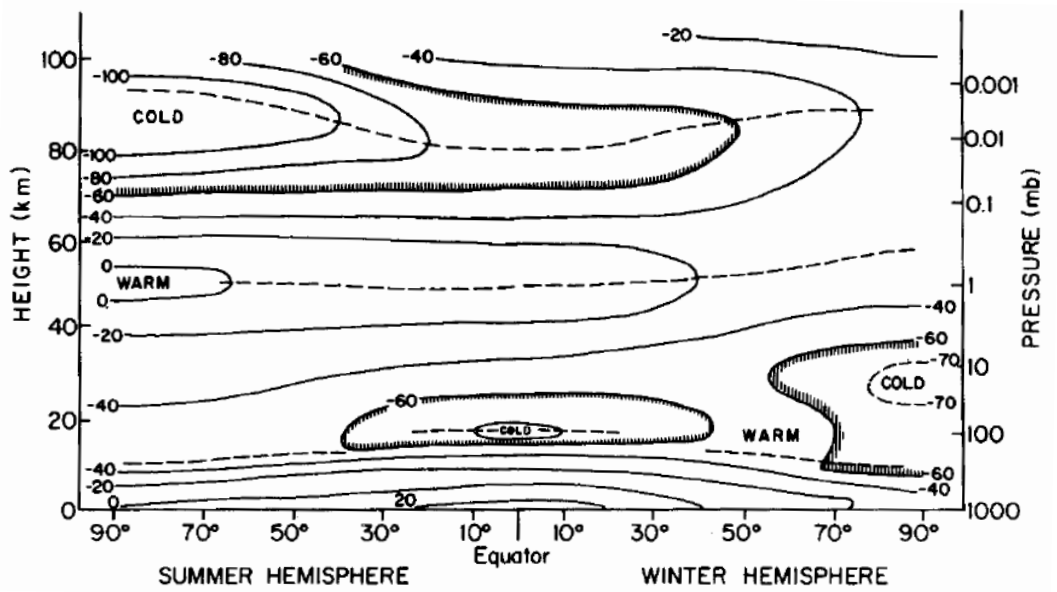


Figure 2.2 Schematic latitude-height section of zonal mean temperatures (°C) for solstice conditions. Dashed lines indicate the tropopause, stratopause, and mesopause levels [Andrews et al., 1987].

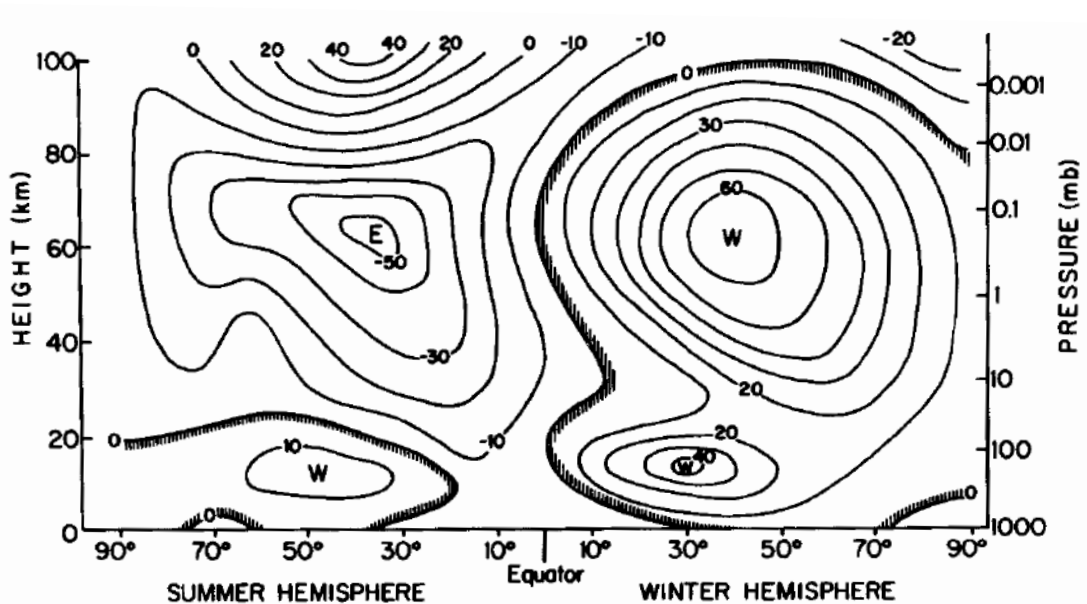


Figure 2.3 Schematic latitude-height section of zonal mean zonal wind (m/s) for solstice conditions; W and E designate centers of westerly (from the west) and easterly (from the east) winds, respectively [Andrews et al., 1987].

The equatorial atmosphere below 35 km is characterized primarily by a quasi-biennial oscillation (QBO), whereas a semiannual oscillation (SAO) dominates above this height. The SAO is at first analogically explained by the thermal forcing since the sun passes over the equator twice a year, resulting in a significant semiannual characteristic of radiative heating. However, the equatorial circulations theory indicates that, in the absence of eddies, thermal forcing alone is far less effective in generating mean zonal temperature and wind oscillations in the equatorial regions than at higher latitudes. Therefore, for the equatorial QBO and SAO, wave driving must be considered the primary forcing.

The QBO has an average period of about 27 months and nearly constant amplitude in height between about 40 and 10 hPa but rapidly decreasing amplitude below the pressure altitude 50 hPa. It is a downward propagating and equatorially symmetrical oscillation with a latitudinal half-width of about  $12^\circ$ . These features are shown in figure 2.4. Planetary waves could not explain the downward propagation of the QBO without loss of amplitude [*Wallace and Holton*, 1968]. Studies by *Lindzen and Holton* [1968], *Holton and Lindzen* [1972], *Plumb* [1977] and *Plumb and McEwan* [1978] suggested that the QBO results from vertically propagating Kelvin and inertia-gravity waves that are radiatively or mechanically damped in the lower stratosphere.

The SAO first observed by *Reed* [1965] has a maximum in the lower stratosphere above 30 km. Later observations by *Hirota* [1978] show that the SAO really consists of two separate oscillations centered at the stratopause and the mesopause, respectively. The SAO has an amplitude minimum near 65 km as shown in figure 2.5. The maximum amplitude of the SAO is near the equator and decays away from the equator with a halfwidth of about  $25^\circ$  latitude. The oscillation propagates downward from the mesosphere into the stratosphere. The observational studies from the LIMS instrument suggest that Kelvin waves do not have sufficient amplitude to completely account for the observed SAO [*Hitchman and Leovy*, 1986]. *Dunkerton* [1982] suggested that the breaking or saturation of vertically propagating gravity waves might explain the SAO in the mesosphere.

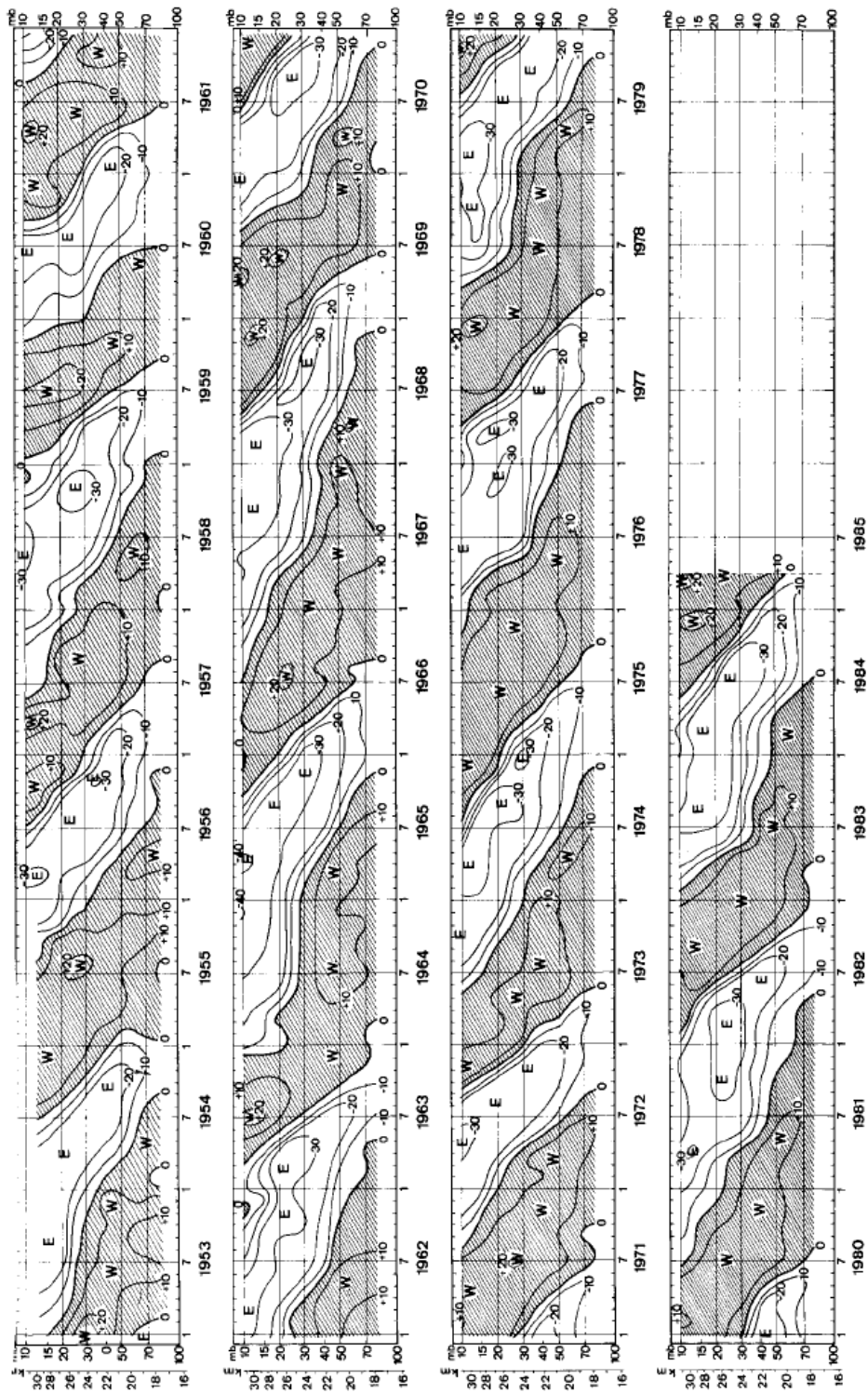


Figure 2.4 Time-height section of monthly mean zonal winds (m/s) at equatorial stations (Jan. 1953-Aug. 1967: Canton Island, 3°S/172°W; Sept. 1967-Dec. 1975: Gan/Maldives Islands, 1°S/73°E; Jan. 1976-Apr. 1985: Singapore, 1°N/104°E). Isoleths are at 10 m/s intervals. Note the alternating downward propagating westerly (W) and easterly (E) regimes [Naujokat, B., 1986].

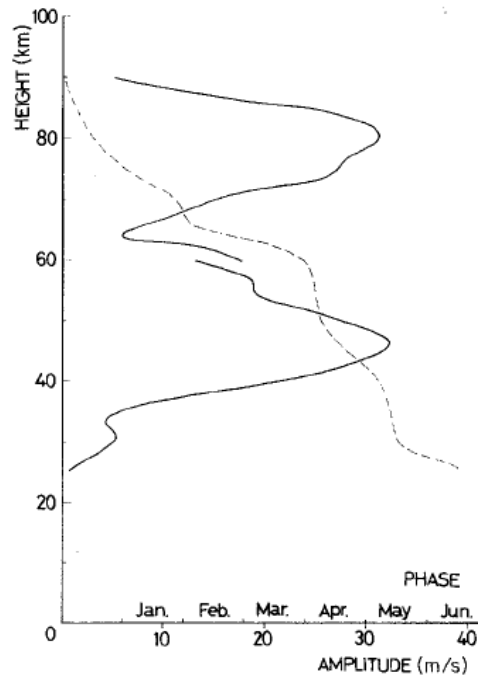


Figure 2.5 The SAO at Ascension Island ( $8^{\circ}\text{S}$ ); amplitude (Solid lines), phase (dashed line). Phase refers to time of first maximum westerly component in the calendar year. Break near 60 km is caused by separately fitting data above and below that level to sinusoidal curves [Hirota, 1978].

## 2.4 Gravity Waves

Much of the momentum, heat and tracer transport in the middle atmosphere is due to coherent wave motions of various classes. These waves also interact with the mean flow. Waves in the atmosphere can be considered to be a perturbation on the quasi-steady, slowly changing background. Atmospheric gravity waves first studied by *Hines* [1960] are one of these types of waves generated in the atmosphere due to the action of gravity on density variations in the stratified atmosphere. In the atmosphere, flow over topographic obstacles such as mountains and hills, deep convection, wind shear and fronts can produce gravity waves. Gravity waves can be generated at different altitudes and move in many directions. An idealized representation of these waves is shown in figure 2.6. Figure 2.7 shows a vertical transverse wave which is a horizontal propagating gravity wave with vertical displacement.

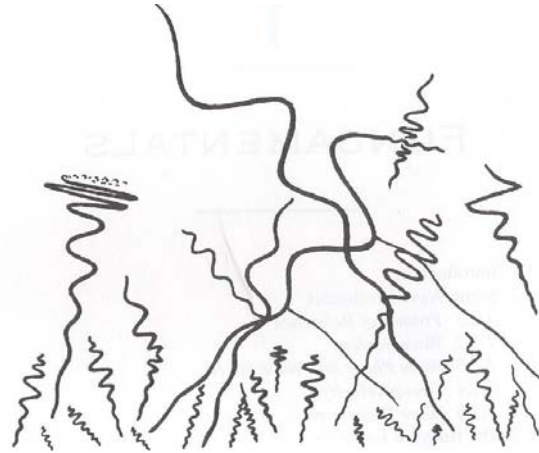


Figure 2.6 An idealized representation of atmospheric gravity waves [Hines, 1974].

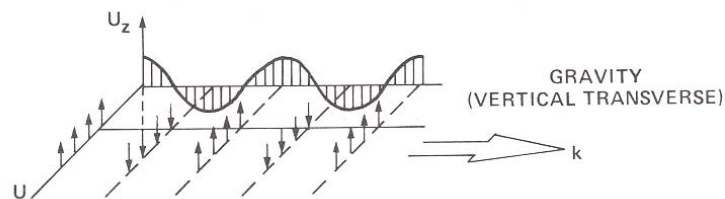


Figure 2.7 A vertical transverse gravity wave [Hilger, 1974].

Gravity waves can be classified in various ways. They can be categorized according to their restoring mechanisms as internal gravity waves, which exist in the stratified atmosphere by buoyancy and inertio-gravity waves which result from a combination of buoyancy and Coriolis forces. The periods of the internal gravity waves are typically a few minutes to a few hours. In the middle atmosphere, their vertical wavelengths typically range from a few kilometres ( $\sim 5$  km) to  $\sim 15$  km, and the horizontal wavelengths range from tens to hundreds of kilometres. The inertio-gravity waves have periods close to the local “inertial period” ( $2\pi/f$  where  $f$  is Coriolis parameter), vertical wavelengths on the order of 10 km and horizontal wavelengths of over a thousand kilometres. Both internal gravity waves and inertio-gravity waves have been observed in the stratosphere and mesosphere by different instruments [e.g. Fritts *et al.*, 1990, 1992; Hamilton, 1991; Mitchell *et al.*, 1994; Sato, 1994; Eckermann *et al.*, 1995; de la Torre *et al.*, 1996; Wu and Waters, 1996a, 1996b; Fritts *et al.*, 1997; Isler *et*

*al.*, 1997; *Sato and Dunkerton*, 1997; *Taylor et al.*, 1997; *Alexander*, 1998; *Eckermann and Preusse*, 1999; *McLandress et al.*, 2000; *Tsuda et al.*, 2000; *Vincent and Alexander*, 2000].

### 2.4.1 Characteristics of Gravity Waves

The present section introduces some basic concepts of characteristics of gravity waves. The key properties of gravity waves in the middle atmosphere are described by the gravity waves solutions to a linearized form of the equations of motion (see appendix A).

#### 2.4.1.1 Wave Scales

Like other waves, gravity waves are periodic in time and space and satisfy a wave equation. Within a Cartesian coordinate system  $(x, y, z)$ , a wave can be described by the generalization of a one-dimensional equation,

$$A = \Re A_0 e^{i\phi} = A_0 \cos(\vec{\kappa} \cdot \vec{r} - \omega t), \quad 2-8$$

where  $A_0$  is the wave amplitude,  $\omega$  is the angular frequency,  $\vec{\kappa}$  is the wave vector,  $\vec{r}$  is the radius vector,  $t$  is time, and  $\phi = \vec{\kappa} \cdot \vec{r} - \omega t$  is the phase of the wave. The wave frequency is given by

$$\omega = \frac{2\pi}{\tau}, \quad 2-9$$

where  $\tau$  is the wave period, representing the time required for the fluid particles to make one oscillation or the time required for successive wave crests to pass a stationary observer. The wave vector defines the direction of wave propagation and the wavenumber,  $\kappa = \sqrt{(k^2 + l^2 + m^2)}$  in the  $\vec{\kappa}$  direction.  $\vec{\kappa}$  is given by

$$\vec{\kappa} = k\hat{x} + l\hat{y} + m\hat{z}, \quad 2-10$$

where the wavenumbers,  $k$ ,  $l$  and  $m$  in the  $x$ ,  $y$  and  $z$  directions, respectively, are defined by

$$k = \frac{2\pi}{\lambda_x}, \quad l = \frac{2\pi}{\lambda_y}, \quad m = \frac{2\pi}{\lambda_z}. \quad 2-11$$

The  $\lambda_x$ ,  $\lambda_y$ , and  $\lambda_z$  are the wavelengths in the x, y and z direction, respectively. The radius vector is defined by

$$\vec{r} = x\hat{x} + y\hat{y} + z\hat{z}. \quad 2-12$$

Now equation 2-8 can be expressed as

$$A(x, y, z, t) = \Re A_0 e^{i\phi} = A_0 \cos(kx + ly + mz - \omega t). \quad 2-13$$

Equation 2-13 expressed in the two-dimensional case is suitable for gravity waves which is given by

$$A(x_h, z, t) = \Re A_0 e^{i\phi} = A_0 \cos(k_h x_h + mz - \omega t), \quad 2-14$$

where  $x_h$  is the horizontal coordinate,  $k_h$  is the horizontal wavenumber.

#### 2.4.1.2 Phase Velocity and Group Velocity

For the two-dimensional equation 2-14, the wave phase is

$$\phi = \vec{\kappa} \cdot \vec{r} - \omega t = k_h x_h + mz - \omega t. \quad 2-15$$

Assuming  $\phi$  a constant, differentiating 2-15 gives

$$\left. \frac{d\phi}{dt} \right|_{\phi} = \vec{\kappa} \cdot \frac{d\vec{r}}{dt} - \omega = 0. \quad 2-16$$

The phase velocity,  $c$  that is the speed of a point of constant phase moving in the direction of wave propagation, is obtained by changing the form of 2-16,

$$\left. \frac{d|\vec{r}|}{dt} \right|_{\phi} = c = \frac{\omega}{\kappa} = \frac{\omega}{\sqrt{k_h^2 + m^2}}, \quad 2-17$$

and by analogy with 2-17,

$$c_{x_h} = \frac{\omega}{k_h}, \quad c_z = \frac{\omega}{m}. \quad 2-18$$

It follows from  $\kappa = \sqrt{(k^2 + l^2 + m^2)}$ , 2-17 and 2-18,

$$\left(\frac{1}{c}\right)^2 = \left(\frac{1}{c_{x_h}}\right)^2 + \left(\frac{1}{c_z}\right)^2. \quad 2-19$$

It should be noted that the phase speed is the speed of a wave moving with respect to a fluid frame. Sometimes it is referred to as the intrinsic phase speed.

It is group velocity rather than phase velocity that transports energy and information. The group velocity is defined as the velocity of the overall shape of wave amplitudes (or a wave packet) propagating through space. It is calculated in the x-direction by

$$v_{gx} = \frac{\partial \omega}{\partial k}, \quad 2-20$$

and in the vertical direction by

$$v_{gz} = \frac{\partial \omega}{\partial m}. \quad 2-21$$

### 2.4.2 Gravity Waves Sources

The dominant sources of gravity waves are topography, convection and wind shear. Other sources may also be significant under certain circumstance but not obvious, for example, wave-wave interaction and adjustment of unbalanced flows in frontal systems and vicinity of jet streams [*Fritts and Alexander, 2003*]. Additionally, it is worth mentioning that gravity wave breaking in the middle atmosphere can also generate secondary gravity waves [*Bacmeister and Schoeberl, 1989; Satomura and Sato, 1999*]. Gravity waves generated by different mechanisms have different spatial and temporal characteristics. Due to the widely distributed gravity wave sources in the troposphere and stratosphere, gravity waves that propagate into the higher layers are common in the stratosphere and mesosphere. Understanding gravity wave sources is important for

understanding 1) the principal excitation mechanisms, 2) the spectral properties of the gravity waves, 3) the spatial (global) and temporal (diurnal, seasonal and inter-annual) variability of sources, and 4) developing statistical as well as physical climatologies to describe the wave sources and distributions [Geller *et al.*, 2006].

### 2.4.2.1 Topographic Source

The topographic features of both terrain obstacles, such as mountains and hills, and terrain depressions, such as canyons and valleys can excite gravity waves when a stably stratified flow is over these features. For satellite observations, large topographic features such as mountains, “orography” are more suitable candidates for study. The orographically generated gravity waves have amplitudes that are proportional to the amplitudes of the orography and have a spectrum as wide as the spectrum of the orographic features. These orographic gravity waves can be stationary relative to the ground surface, called standing waves, for example, mountain waves and travelling downwind from the generating obstacle, such as lee waves. Because its intrinsic phase speed is equal to the background wind speed in the opposite direction, a standing wave appears stationary to the observer on the Earth’s surface, but note that the wave still propagates in the vertical. Small and up to breaking amplitudes of orographic gravity waves have been estimated by observations and simulations and horizontal wavelengths are typically from tens to hundreds of kilometres [Lilly and Kennedy, 1973; Nastrom and Fritts, 1992; Chan *et al.*, 1993; Dörnbrack *et al.*, 1999; Leutbecher and Volkert, 2000].

Orographic gravity waves play an important role in the middle atmosphere. The orographic gravity waves at high latitudes in the northern hemisphere are believed to contribute to polar stratospheric clouds (PSCs) and thus the ozone depletion in the stratosphere [Dörnbrack *et al.*, 1999; Carslaw *et al.*, 1999; Dörnbrack *et al.*, 2001; Dörnbrack and Leutbecher, 2001]. The assessments of orographic gravity waves by the Global Atmospheric Sampling Program (GASP) and other aircraft observations reveal that horizontal velocity and temperature variations over significant orography to be 2-3 times higher than over plains and oceans [Nastrom *et al.*, 1987; Jasperson *et al.*, 1990; Bacmeister *et al.*, 1990a] and ~5 times higher than the regions that have no obvious meteorological sources [Fritts and Nastrom, 1992]. There was an argument that orographic gravity waves likely account for a large fraction of zonally averaged wave-

induced force in the mesosphere [Bacmeister, 1993]. Due to the importance of orographic gravity waves for the mean circulation relative to other significant sources, scientists have attempted to parameterize their effects in large-scale models, for example global numerical weather forecast and climate models [e.g. Palmer *et al.*, 1986; McFarlane, 1987; Iwasaki *et al.*, 1989].

### 2.4.2.2 Convective Source

In recent years, convectively generated gravity waves have been observed numerically and instrumentally. However, due to the inherent intermittency of convection, the wave generation mechanism has still not been fully understood and there is still controversy [Fritts and Alexander, 2003]. Because convection in the atmosphere has the characteristics of random scales and a slow or rapid rate, the convectively generated gravity waves can have different phase speeds, wave frequencies and vertical and horizontal scales throughout the gravity wave spectrum. This is different from orographic gravity waves typically having a single prominent phase speed and frequency. Both high-frequency and low-frequency gravity waves linked to convection as the source have been observed (for high-frequency [Sato, 1992, 1993; Alexander and Pfister, 1995; Sato *et al.*, 1995; Dewan *et al.*, 1998; McLandress *et al.*, 2000; Alexander *et al.*, 2000] and for low-frequency [Pfister *et al.*, 1986; Tsuda *et al.*, 1994a; Karoly *et al.*, 1996; Shimizu and Tsuda, 1997; Wada *et al.*, 1999; Vincent and Alexander, 2000]). The gravity waves observed in the tropics that is a region far from orography and baroclinic instability have been classified as convection excited waves [Pfister *et al.*, 1986; Tsuda *et al.*, 1994a; Karoly *et al.*, 1996; Shimizu and Tsuda, 1997; Wada *et al.*, 1999; Vincent and Alexander, 2000].

In the atmosphere, convection involves the movement of air. In the tropics, as the Earth is heated by the Sun, hot air thermally rises upward from the surface causing convection. Because the Earth is tilted and revolves around the Sun and orbit axis, convection in the atmosphere is a time-varying thermal forcing. Depending on the generation mechanisms, the convection source is described by pure thermal forcing, an “obstacle” effect (or called “transient mountain” effect) and a “mechanical oscillator” effect [Fritts and Alexander, 2003]. Pure thermal convection occurs when heating causes a system to become unstable and therefore begins to mix by the movement of air. Studies of these gravity waves observed by Alexander *et al.* [1995] and Piani *et al.*

[2000] suggested that the vertical wavelength approximately equates to the heating depth. Gravity waves excited by pure thermal forcing have been observed by *McLandress et al.* [2000]. These pure thermally forced gravity waves would be expected to be isotropic, while anisotropies can occur primarily via background wind filtering effects [*Fritts and Alexander, 2003*].

The obstacle effect is the interaction of wind with the latent heating cells, which was described by *Clark et al.* [1986] for short horizontal wavelength waves in the troposphere, but the ideas are also applicable to the larger horizontal wavelength waves in the middle atmosphere generated by deep convection. As analogous to orographic gravity wave generation, the obstacle effect excited convective gravity waves [*Vincent and Alexander, 2000; Alexander and Vincent, 2000*] are anisotropic and propagate opposite to the mean flow with respect to the obstacle. According to the theory of *Clark et al.* [1986], the gravity waves generated by the obstacle effect have much larger amplitudes compared with the waves generated by pure thermal forcing.

The “mechanical oscillator” effect is a description for the gravity waves excited by mechanical forcing owing to oscillatory updrafts, which was discussed by *Fovell et al.* [1992]. *Fovell et al.* [1992] found that the waves generated by this mechanism have periods match the primary periods of the forcing. The studies of *Salby and Garcia* [1987] and *McLandress et al.* [2000] showed that this type of gravity waves has a frequency equal to the oscillation frequency and sometimes is not distinguishable from the thermal source when that source periodically oscillates. The gravity waves generated by this mechanism can be anisotropies with the background wind effects resulting in similar wave fields to the obstacle effect [*Fovell et al., 1992*].

In this thesis, the gravity waves generated by the three excitation mechanisms will be simply sorted into the group of convective gravity waves and in fact in the atmosphere, these three mechanisms are not distinct.

### 2.4.3 Gravity Wave Dispersion

As it is discussed in section 2.4.1, the phase speed is a function of wave frequency and wavenumber or wavelength, i.e.  $c = \omega / k = (\lambda_x \omega) / 2\pi = \lambda_x / \tau$ . The phase speed function indicates that for a given wave period,  $\tau$ , waves with different wavelengths

travel at different phase speeds and the waves with longer wavelengths are faster than those with shorter wavelengths in a fluid. This is called wave dispersion, described in figure 2.8. It is clear that the width of the disturbance at a later time in figure 2.8 is larger than that at an earlier time, but the amplitude decreases in the direction of propagation. This reflects the phase speed as a function of frequency and the total energy of the wave packet stays constant. The phenomenon is expressed by a dispersion relation. The dispersion relation is the single most important formula to characterize a wave in that it allows most of the important properties of a wave to be calculated, such as phase velocity, group velocity and refraction. The dispersion relation for internal gravity waves in the atmosphere derived by *Jones* [2005] is generalized to include all components of baroclinicity, vorticity and rate of strain. Note that wave dispersion doesn't affect the total energy of the wave packet, which means the total energy of the wave packet remains constant during wave dispersion.

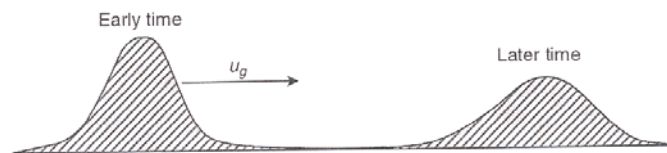


Figure 2.8 A cross-section of a wave packet seen at early and late times [*Nappo*, 2002].

### 2.4.4 Gravity Wave Propagation

Wave propagation can be defined in terms of wavelengths, frequencies, amplitudes and phase velocities, which are introduced in the previous sections. Although imaginary gravity waves can be produced at any level and propagate in many directions (see figure 2.6), in the real atmosphere the gravity waves generated by different sources often show different characteristics of propagation. Orographically generated mountain waves propagate upwind at the speed of the wind with respect to the background, resulting in standing wave properties, while the trapped lee waves extend downwind from the generating obstacle, showing ducted wave features. Convectively generated gravity waves can be isotropic or anisotropic depending on the generation mechanism. Gravity wave-background interactions, instability processes and wave-wave interactions in the atmosphere often cause wave refraction, reflection, absorption, ducting, breaking and

new gravity wave generations. The temporally variable winds alter wave phase speeds. These dynamics make the observation and understanding of gravity wave propagation difficult. Observations by, for example, *Isler et al.* [1997], *Walterscheid et al.* [1999], *Taylor et al.* [1995] and *Mitchell and Howells* [1998] showed that gravity waves with short horizontal wavelengths of 20 km or less have a higher probability of being ducted by the wind and/or thermal structures of the atmosphere. The probability of being ducted decreases as horizontal wavelengths increase [*Swenson et al.*, 2000].

The Earth's atmosphere, like any other fluid, is in fact dissipative, and therefore, the waves in the atmosphere, like all other fluid motions, are subject to this dissipation. Wave dissipation can be caused by atmospheric molecular viscosity and thermal conductivity [*Gossard and Hooke*, 1975]. It can also happen in processes such as wave breaking and instability, wave-wave and wave-mean flow interactions, and radiative damping [*Fritts and Alexander*, 2003]. In the stratosphere and mesosphere, viscosity and conductivity are generally not important dissipation mechanisms. Normally, wave damping by dissipative processes becomes an important factor only at some later stage in the wave propagation where cumulative damping becomes significant in the sense that the wave amplitude is markedly reduced or even that the wave is no longer detectable. So dissipation is not a process that is strongly influencing the wave propagation observation at non-great distances from its source. In many cases, observations with respect to wavelengths and wave amplitudes can be made without reference to the effects of dissipation. Giving wave sources and wave dissipation attention will be important to understand the observed gravity waves and the properties of wave propagation.

In the ideal case, gravity waves exponentially grow with height. However, observations show that the growth of gravity wave-caused fluctuation variance with height is limited by a number of processes in the atmosphere. This constraint in amplitude is called wave saturation. The wave saturation can be responsible for small-scale turbulence and diffusion and mixing [*Fritts*, 1984].

### **2.4.5 Gravity Wave Observations**

Gravity waves in the atmosphere can be observed by in-situ or remote instruments on a stationary or moving platform. Radar, lidar and radiosondes provide observations

made at a single station. The observations from these instruments are generally based on the temporal variations of wave perturbations associated with the time-continuous (e.g. radar and lidar) or time-discrete (e.g. radiosondes) measurements. However, these methods fail when waves that are stationary with respect to the ground are considered. Instrumented aircraft and balloons can resolve the spatial structure of both stationary and travelling waves, such as mountain waves and lee waves. Whilst the observations from aircraft and balloons are geographically flexible, a global climatology of gravity waves is still not possible from these instruments. Recently, satellite remote sensing technique made continuously global coverage utilizable for providing global gravity wave observations.

Radar has been used to observe gravity waves throughout the atmosphere by analysing wind profiles. For example, in the troposphere and lower stratosphere, observations from radar have been made by *Ottersten et al.* [1973], *Gauge and Balsley* [1978], *Tsuda et al.* [1994b], *Murayama et al.* [1994] and *Sato* [1994]; and in the mesosphere and lower thermosphere, gravity waves have been observed by *Vincent and Reid* [1983], *Fritts and Vincent* [1987], *Tsuda et al.* [1990a, 1990b], *Manson* [1990] and *Fritts and Isler* [1994]. Radars normally have high temporal and spatial resolutions. For example, MST (Mesospheric, Stratospheric and Tropospheric) radars have typical spatial resolutions of order 30 m in the vertical and temporal resolutions of order 1 minute along the beam to provide continuous observations in the troposphere and lower stratosphere and above 75 km altitude. Therefore, MST radars can be used to measure wind variances that contain information about gravity wave periods, momentum fluxes and the kinematic energy of gravity waves. The basic concepts of radar observations are given in *Chadwick and Gossard* [1986]. Although radar can provide continuous measurements with high resolution, observations are restricted to fixed stations in a limited number of sites.

Lidar measures properties of backscattered light and is similar in principle to radar [*Schwiesow*, 1986]. Lidar has a vertical resolution of  $\sim 1$  km and a temporal resolution of a few minutes. Gravity waves with vertical wavelengths as short as 1 km at altitudes in the middle atmosphere can be extracted from lidar temperature profiles [e.g. *Collis et al.*, 1968; *Gardner and Shelton*, 1985; *Gardner and Voelz*, 1987; *Blumen and Hart*, 1988; *Know and Gardner*, 1990; *Marsh et al.*, 1991; *Mitchell et al.*, 1991; *Wilson et al.*,

1991; *Whiteway and Carswell, 1995; Ralph et al., 1997; Newsom et al., 2000*]. Similar to radar, lidar provides time-continuous and fine-resolution measurements of small-scale waves, but the observations are limited to single stations and are spatially discontinuous in the horizontal direction. In addition, lidar observations are subject to meteorological conditions (cloud cover) and some lidars can only operate during the night.

In 1957, *Corby [1957]* suggested that observed periodic variations of a few metres per second of the vertical velocities of ascending radiosondes could be related to gravity waves. To the present day, observations from balloon soundings (radiosondes) have been extensively used for gravity wave studies in the troposphere and lower stratosphere. Assuming the perturbations with height are caused by gravity waves, short vertical wavelength gravity waves are generally obtained by subtracting a low-order polynomial fit from the temperature and horizontal wind profiles from the radiosondes. Observations from *Sato et al. [1994]*, *Sato and Dunkerton [1997]*, *Vincent et al. [1997]*, *Vincent and Alexander [2000]*, and *Zink and Vincent [2001]* suggested that gravity waves in radiosondes measurements are dominated by low intrinsic frequency inertia-gravity waves.

Aircraft have been used as moving platforms for remote sensors to measure winds and temperatures. Fluctuations of the measured winds and temperatures have yielded information of horizontal wavelengths of gravity waves and turbulence associated with wave dissipation over small horizontal scales in the stratosphere [e.g. *Nastrom et al., 1987; Bacmeister et al., 1996*]. The majority of observations have been made over mountains [*Gary, 1989; Bacmeister et al., 1990a, 1990b; Nastrom and Fritts, 1992; Leutbecher and Volkert, 2000*]. Other sources, such as convection and frontal system generated gravity waves have also been detected by instrumented aircraft [*Fritts and Nastrom, 1992; Pfister et al., 1993a, 1993b; Alexander and Pfister, 1995; Alexander et al., 2000*]. Although aircraft are moving platforms, the observations are also localized and too limited in their duration to provide much information about global climatology of gravity waves.

Temperature and horizontal winds from rocket soundings have also been used to observe seasonal and latitudinal variations of gravity wave activity in the stratosphere below  $\sim 60$  km at  $\sim 1$  km resolution [*Hirota, 1984; Hirota and Niki, 1985; Hamilton,*

1991; *Eckermann et al.*, 1995; *Eckermann*, 1995; *Holton et al.*, 2001]. The common method used in rocket sounding gravity waves is to subtract a background profile from rocket profiles and assuming the resulted small-scale perturbations are gravity waves. Observations from rocket soundings are also limited by few launches due to cost.

The above observations are either made at a fixed location or over larger but still localized area, while satellites, due to their consistent global coverage have made global climatologies of gravity waves possible. In recent years, the spatial resolution of satellite instruments has been much improved to facilitate small-scale gravity-wave observations. However, each instrument as a specific design is sensitive to only some fraction of the gravity wave spectrum that may present itself in the atmosphere and misses other portions of the spectrum. Limb-viewing instruments, such as the Limb Infrared Monitor of the stratosphere (LIMS) [*Gille and Russell*, 1984a] and the Microwave Limb Sounding (MLS) [*Barath*, 1993], have good vertical but poor horizontal resolutions make them suitable for short vertical wavelengths, while only longer horizontal wavelengths can be observed by these instruments. In contrast, profiles from nadir-view instruments, such as the Advanced Microwave Sounding Unit-A (AMSU-A) [*Lambrigtsen*, 2003] and the Atmospheric InfraRed Sounder (AIRS) [*Aumann and Pagano*, 1994], with finer horizontal but coarser vertical resolutions can be used to extract shorter horizontal but longer vertical wavelength gravity waves.

Typically, temperature and radiance profiles from satellite instruments are used to extract information about gravity waves. The analysis method has varied between different studies, but the most common procedure is to subtract a background state that contains planetary-scale waves 0 – 6 or 0 - 3 from the data and assuming the perturbations are due to gravity waves. *Fetzer and Gille* [1994, 1996] first published their observations from the infrared limb-viewing temperature profiles of LIMS for 15 – 60 km altitude with a vertical resolution of  $\sim 1.5$  km. In the procedure of the LIMS observations, the planetary-scale waves with zonal wave number 0-6 were Kalman-filtered. The observed gravity waves have vertical wavelengths of  $\sim 6 - 50$  km and horizontal wavelengths longer than  $\sim 200$  km. Gravity wave temperature variances have been similarly derived by *Preusse et al.* [2002] for the temperature data from the limb-viewing CRISTA (Cryogenic Infrared Spectrometers and Telescopes for the Atmosphere) instrument. Compared with LIMS, CRISTA has finer horizontal resolution

and slightly better vertical resolution and the measurements can extend from  $\sim 20$  to 80 km. Global maps of gravity waves show similar features to those from LIMS. By applying the same analysis method, *Pressue et al.* [2006, 2009] derived gravity wave maps for the SABER (Sounding of the Atmosphere using Broadband Emission Radiometry) instrument over altitudes between 20 and 100 km.

Gravity waves in the UARS (Upper Atmosphere Research Satellite) MLS radiance have been studied by *Wu and Waters* [1996a, 1996b, 1997], *McLandress et al.* [2000], *Jiang and Wu* [2001], and *Jiang et al.* [2002, 2004a, 2004b, 2005]. Due to the deeper weighting functions associated with microwave profiles compared to infrared profiles, only gravity waves with vertical wavelengths longer than 12 km were observed by the UARS MLS instrument. With improved vertical resolution and sensitivity, Aura MLS is capable of deriving gravity waves with vertical wavelengths larger than 5 km and horizontal along-track wavelengths of  $\sim 100 - 200$  km [*Wu and Eckermann, 2008*]. The Aura MLS gravity wave variances are  $\sim 5 - 8$  times larger than those from UARS MLS. The global maps from both UARS and Aura MLSs show peaks in variance at middle to high latitudes in winter, while at subtropical latitudes in summer [*McLandress et al., 2000; Wu and Eckermann, 2008*].

Using GPS/MET (Global Positioning System/Meteorology) occultation data temperature profiles, *Tsuda et al.* [2000] have derived global maps of gravity waves. The vertical wavelengths are in the range of  $\sim 2$  to 10 km between 15 and 40 km in altitude. The horizontal wavelengths are similar to LIMS and CRISTA.

Gravity waves from nadir-viewing instruments have also been observed. For example, *Eckermann and Wu* [2006] and *Eckermann et al.* [2006] detected stratospheric gravity waves with vertical wavelengths larger than  $\sim 10$  km and horizontal wavelengths of  $\sim 150 - 200$  km for the radiances from AMSU-A (Advanced microwave Sounding Unit-A) on both the NOAA meteorological satellites and NASA's EOS Aqua satellite. *Alexander and Barnett* [2007] and *Limpasuvan et al.* [2007] have used AIRS (Atmospheric Infrared Sounder) to derive maps of gravity waves of long vertical wavelengths ( $> 12$  km).

#### 2.4.6 Climatologies of Gravity Wave Activity

Global climatologies of gravity wave activity are needed by global weather forecast and climate models. Suitable observations of geographical and temporal variations in gravity wave activity and its characteristics (amplitudes, wavelengths, etc.) and better understanding of the global climatology of gravity waves are required to constrain gravity waves in the parameterization schemes in these global models. Understanding gravity wave sources is important to describe the temporal and geographical variations in gravity wave occurrence and the characteristics of specific waves for certain meteorological conditions.

In the past few decades, gravity waves have been observed at single sites for seasonal and interannual variation, cross globe over limited periods of time, and over regions for both temporal and geographical variations. The observations show substantial variations of gravity waves with time, with height, as well as with geography. Because each observation technique tends to be sensitive only to some portion of the whole spectrum of gravity wave characteristics, while being almost totally insensitive to other portions, it is difficult to infer a climatology of gravity waves. Because models do not always agree with observations, a climatology of gravity waves based only on models is also not acceptable.

Based on the existing observations together with gravity wave theories, the global patterns and seasonal variations are summarized as follows. In the middle atmosphere, internal gravity waves typically have vertical wavelengths between 5 and 15 km and horizontal wavelengths of tens to hundreds of kilometres. Unless absorption and reflection occurs, they can move in many directions and can propagate through the middle atmosphere without encountering critical levels at which the mean wind speed equals the wave phase speed. As gravity waves propagate higher into the atmosphere, the amplitudes tend to grow as the density falls. When gravity waves across the critical levels, there is an exponential decrease in wave amplitudes and the wave stress is reduced by a factor of  $\exp(-2\pi\sqrt{R_i - 0.25})$ , where  $R_i$  is the Richardson number at the critical level [Nappo, 2002]. Thus, gravity wave breaking occurs at or near a critical level and waves are dissipated on passing through a critical level. Figure 2.9 presents a terrain-generated gravity wave with a horizontal wavelength of about 16 km and a

vertical wavelength of about 6 km observed at Shanwell, UK. The frequency of internal gravity waves,  $\omega$ , is always smaller than the buoyancy frequency,  $N$ . Indeed, under the hydrostatic approximation,  $\omega \ll N$  [Gill, 1982], and thus the period is much greater than the buoyancy period,  $2\pi N^{-1}$  (approximately 5 min in the middle atmosphere). Inertia-gravity waves are larger space and time scale waves with horizontal wavelengths  $\sim 1000$  km and periods of several hours. These gravity waves will be influenced by the rotation of the Earth, i.e. the Coriolis force should be taken into account in the equations of motion. The frequency of inertia-gravity waves is greater than the Coriolis parameter. Because of larger horizontal scale (i.e. smaller horizontal wavenumber) and smaller frequency compared with the internal gravity waves, the vertical group velocity of inertia-gravity waves is generally smaller than that of pure internal gravity waves. Therefore, inertia-gravity waves tend to propagate more horizontally than do pure internal gravity waves. The vertical wavelengths of inertia-gravity waves are on the order of 10 km.

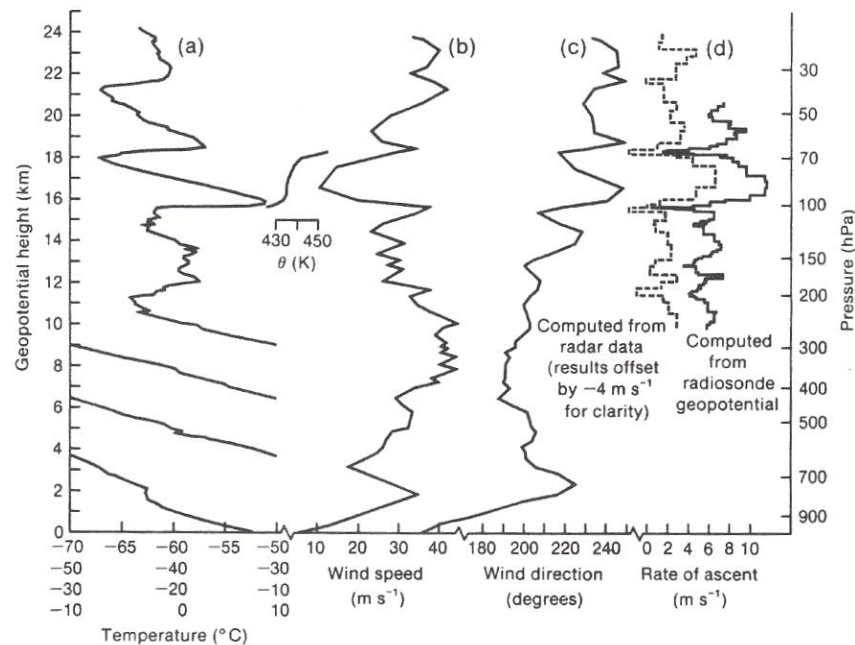


Figure 2.9 Radiosonde ascent profiles at Shanwell, UK, 2318 GMT December 12, 1986: (a) temperature and potential temperature; (b) wind speed; (c) wind direction; (d) ascent rate, computed from the geopotential (solid line) and radar data (dashed line) and offset by -4 m/s [Shutts *et al.*, 1988].

Observations of gravity waves show clearly seasonal and latitudinal variations in the stratosphere with maximum amplitude in winter and minimum amplitude in summer. These seasonal and latitudinal dependences have been observed by using MLS, GPS CRISTA, radiosonde and rocket sounding data [e.g. *Mclandress et al.*, 2000; *Tsuda et al.*, 2000; *Preusse et al.*, 2002; *Wu and Eckermann*, 2008]. *Mclandress et al.* [2000] found that the MLS gravity waves in the winter hemisphere have smaller intrinsic phase speeds ( $\sim 20$  m/s or less), while the subtropical gravity waves in the summer hemisphere have larger intrinsic phase speeds ( $\sim 50$  m/s or less). This is consistent with orographic sources being more important at high latitudes and deep convective sources being more important at low latitudes [*Mclandress et al.*, 2000]. Very low intrinsic frequency gravity waves at latitudes  $> 30^\circ$  are related to the variations in the Coriolis parameter,  $f$ , while those very low intrinsic frequency gravity waves at latitudes  $< 30^\circ$  have intermittent sources in time and should be expected to be generated by convection. In the tropics, long vertical wavelength gravity waves with high intrinsic phase speeds that are linked to deep convection also exist [*Fritts and Alexander*, 2003]. Observations have provided evidence for the seasonal and geographical variations in the important sources of gravity waves such as orography and convection [e.g. *Eckermann and Preusse*, 1999; *Mclandress et al.*, 2000]. Figure 2.10 gives an example of global climatologies of gravity waves from MLS.

Without significant damping, the horizontal amplitude of gravity waves increases with altitude because of the decrease of atmospheric density. Gravity waves are the dominant modes in the middle atmosphere and contribute significant impacts on the global-scale circulation. However, the existing gravity wave climatologies that described monthly mean gravity wave activity are still weak for some significant sources such as shear and wave-wave interaction generations. Satellite instruments are in a more advantageous position over ground-based instruments and aircrafts to provide the kind of geographical and temporal coverage to understand gravity wave variability. However, the full spectrum of gravity waves in the atmosphere will still benefit from the continued in-situ observations from aircraft and high resolution ground-based instruments.

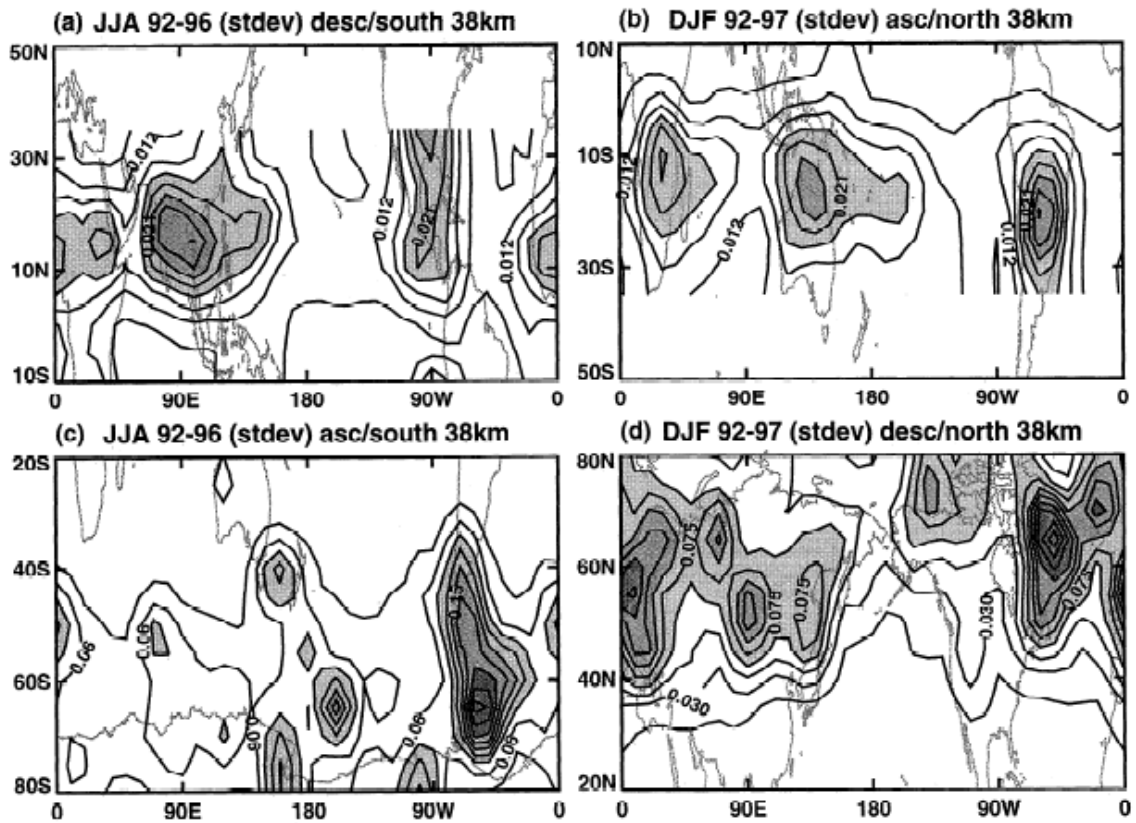


Figure 2.10 Standard deviations of the MLS limb-scanning temperature variances [Mclandress *et al.*, 2000].

## 2.5 Other Relevant Atmospheric Waves

In addition to gravity waves, the atmosphere is also capable of sustaining planetary (or Rossby) waves, equatorial waves and tides which are noise for the purpose of observing gravity waves using satellite data. Planetary waves, equatorial waves and tides show global features of so called planetary-scale waves. It is necessary to understand, identify and filter these planetary-scale waves for gravity wave observations.

### 2.5.1 Planetary Waves

The poleward gradient of the planetary vorticity (Coriolis force) is responsible for Rossby waves, which are often referred to as planetary waves. Planetary waves are horizontally global-scale stationary or travelling waves with respect to the ground with wavelengths thousands of kilometres long. Travelling planetary waves are further

classified as free and forced travelling planetary waves. Planetary waves are a common feature within the extratropical stratosphere in the winter. Most forced planetary waves propagate with vertical phase structure in the stratosphere and mesosphere. The most prominent planetary waves in the middle atmosphere are the westward migrating waves with respect to the mean wind with zonal wave number 1 to 3 and periods around 2, 5 and 16 days. Figure 2.11 shows a planetary wave observed by the Selective Chopper Radiometer on the Nimbus 5. The wavelengths of planetary waves as a function of latitude and mean eastward wind speed are listed in table 2.1. It is notable that planetary waves are extratropical waves travelling slowly with westward phase velocity as usually 4-6 large-scale meanders of the jet stream. Their westward phase velocity is often in the opposite direction to the background wind. Their group velocity can be any direction.

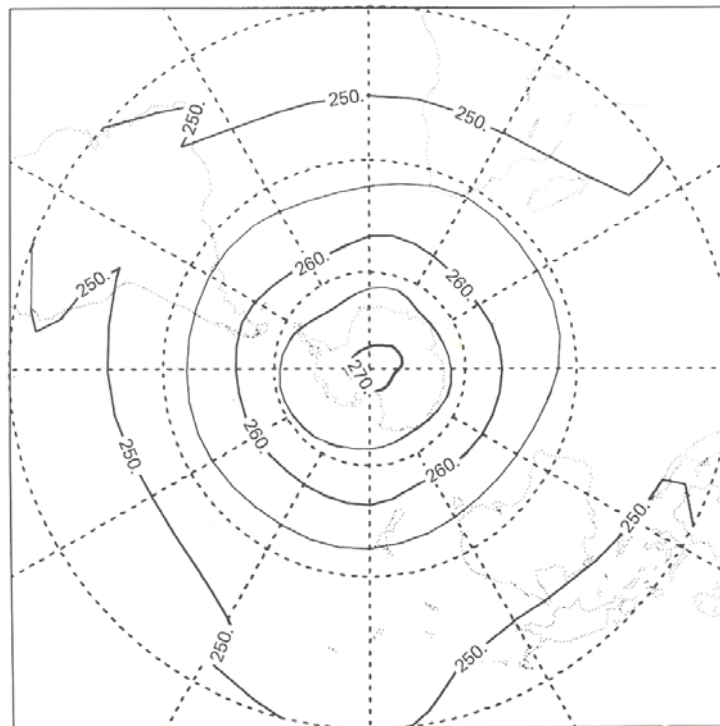


Figure 2.11 A zonal wave number 3 as observed by the Selective Chopper Radiometer on the Nimbus 5 satellite: bright temperature contours at about 42 km altitude on January 16, 1973 [Rogers and Prata, 1981].

A qualitative indication of the variation of horizontal wind amplitude with height for various types of wave motions is given in figure 2.12. As indicated in figure 2.12, synoptic-scale planetary waves dominate the troposphere and decay rapidly with height in the stratosphere. It is believed that the largest-amplitude planetary waves are

stationary with respect to the ground and unable to penetrate beyond the lower stratosphere in the summer hemisphere [Charney and Drazin, 1961]. Planetary wave amplitudes are comparable to the magnitude of the mean zonal wind only in the winter hemisphere where the mean winds are westerly throughout the middle atmosphere and show planetary-scale structures.

Table 2.1 Wavelengths of planetary waves [km] as a function of latitude and mean eastward wind speed [Hilger, 1974. p. 145]

Wind speed (m/s) \ Latitude	4	8	12	16	20
30°	2822	3990	4888	5644	6310
45°	3120	4412	5405	6241	6978
60°	3713	5252	6432	7428	8304

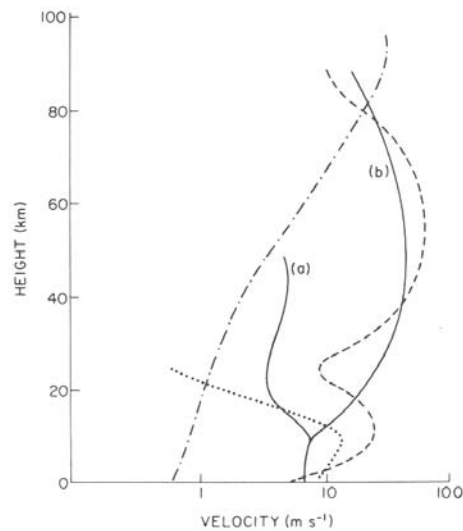


Figure 2.12 Vertical profiles of horizontal wind amplitudes corresponding to various types of atmospheric motions. Solid line: planetary waves in summer (a) and winter (b); dashed line: zonal mean; dotted line: synoptic-scale Rossby waves; dotted-dashed line: gravity waves [Andrews et al., 1987].

### 2.5.2 Equatorial Waves

In addition to extratropical Rossby waves, there are other planetary-scale waves at the equator called equatorial Kelvin waves and Rossby-gravity waves. Equatorial waves play significant roles in forcing the equatorial QBO and SAO. A Kelvin wave is generated in order to balance the Earth's Coriolis force against a topographic boundary such as a coastline. An equatorial Kelvin wave is a special type of Kelvin wave in which the equator acts analogously to a topographic boundary for both the Northern and Southern Hemispheres. Unlike Rossby waves, equatorial Kelvin waves are equatorially trapped within about  $15^\circ$  north and south and always propagate eastward with respect to the basic flow. Figure 2.13 illustrates the wind fluctuations for the Kelvin wave. Observed Kelvin waves generally have zonal wave number 1 and 2 with periods in the range 10-20 days. Kelvin waves are often observed during periods when easterly winds exist at the base of the equatorial stratosphere. The temperature oscillations associated with Kelvin waves are presented in figure 2.14.

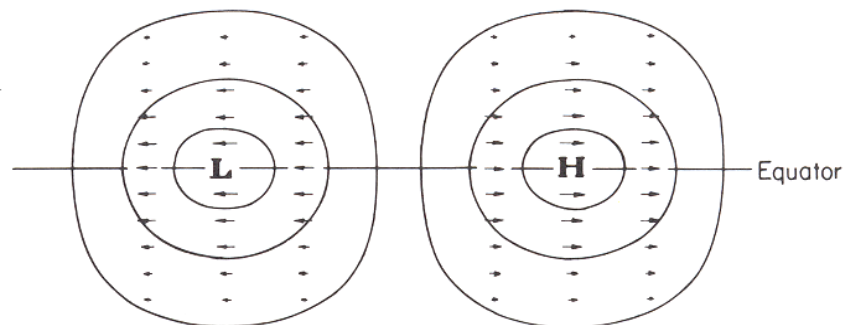


Figure 2.13 A schematic illustration of geopotential and horizontal wind fluctuations for the Kelvin wave [Andrews *et al.*, 1987].

Rossby-gravity waves, sometimes also called equatorial inertio-gravity waves, are the result of the combination of buoyancy and Coriolis force. They are also equatorially trapped within about  $15^\circ$  north and south of the equator. Convection is generally believed to be the source for the Rossby-gravity waves. The wind fluctuations in the  $xy$  plane for Rossby-gravity waves are illustrated in figure 2.15. The observed Rossby-gravity waves propagate westward with respect to the mean flow, are primarily of wave number 4, and with periods of 4-5 days.

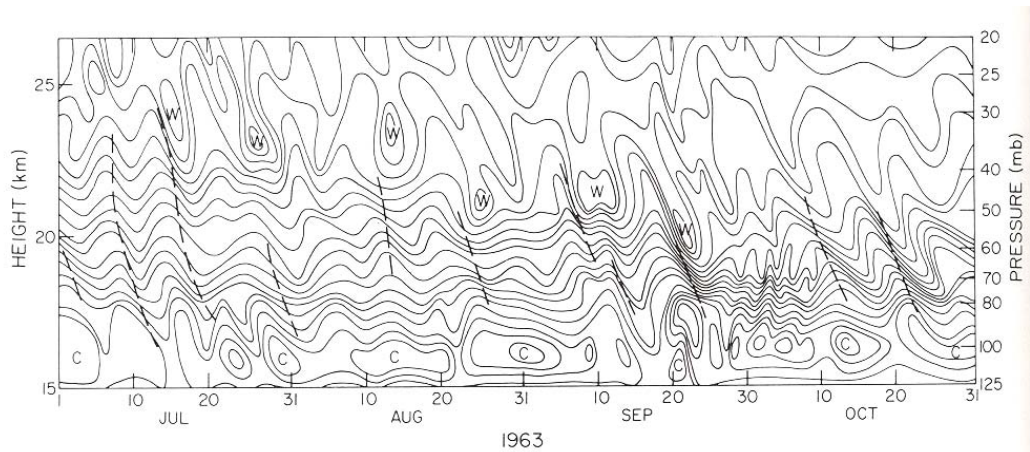


Figure 2.14 Time-height sections for the equatorial lower stratosphere, showing evidence of Kelvin-wave activity in the temperature oscillations at Canton Island (3°S) [Andrews *et al.*, 1987].

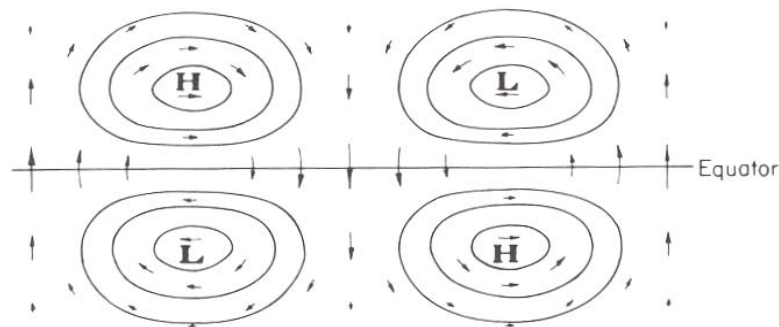


Figure 2.15 Schematic illustration of geopotential and horizontal wind fluctuations for the Rossby-gravity wave of westward phase speed [Andrews *et al.*, 1987].

### 2.5.3 Atmospheric Thermal Tides

Thermal tides are the global-scale atmospheric motions whose periods are submultiples of the solar or lunar day. The atmospheric temperature variability is primarily driven by the heating effects of the Sun, therefore the dominant tides are the solar diurnal tides (thermal tides). Because the kinetic energy given by  $\rho\psi_0^2/2$  is conserved, and the atmospheric density  $\rho$  decreases exponentially with height, both gravity waves and tides have amplitudes,  $\psi_0$ , exponentially growing with altitude. For a

tidal mode the frequency is given by  $2\pi m/24$  hours. The most important tides in the middle atmosphere are the solar semidiurnal tide with  $m = 2$  ( $\omega = 2\Omega$ ) and the solar diurnal tide with  $m = 1$  ( $\omega = \Omega$ ). Theory and observation show that the forced semidiurnal tides have larger vertical wavelengths (larger than 100 km), whilst the diurnal tides at between 30°N and 30°S can vertically propagate with a vertical wavelength of 28 km. The absorption of solar ultraviolet radiation by ozone in the stratosphere is responsible for the semidiurnal tides. Because the ozone absorption is regular, the structure of semidiurnal tides is fairly uniform. At and above the stratopause, the diurnal tide can be comparable with the semidiurnal tide. Figure 2.16 shows amplitude and phase of solar diurnal component of temperature disturbance at various latitudes for equinox.

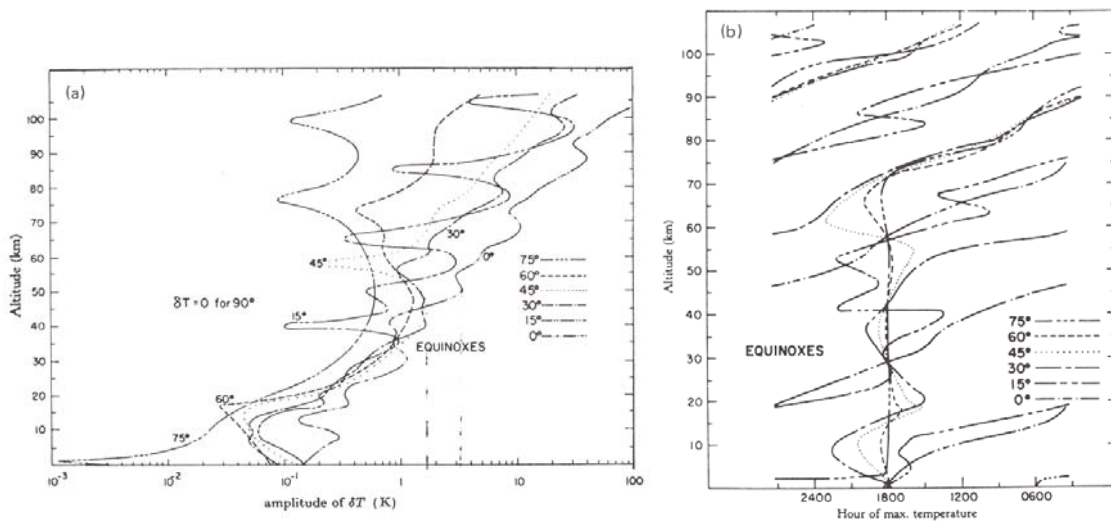


Figure 2.16 (a) Amplitude and (b) phase of solar diurnal component of temperature perturbation at various latitudes for equinox [Lindzen, 1967].

## 2.6 Summary

In the atmosphere, gravity waves coexist and interact with planetary-scale and zonal-mean circulations. Gravity waves and planetary-scale waves such as planetary waves, equatorial waves, and atmospheric thermal tides can be identified according to their horizontal and vertical structures and their sources of excitation. Table 2.2

summarizes the spatial and temporal properties of gravity waves, Rossby waves (or planetary waves), equatorial waves, and thermal tides in the atmosphere.

Table 2.2 Types of atmospheric waves

<b>Wave</b>	<b>Spatial scale</b>	<b>Period</b>
Gravity waves	Small-scale	A few minutes - a few hours
Rossby waves	Extratropical global-scale	>12 hours
Equatorial Kelvin waves	Planetary-scale at equator	10 - 20 days
Rossby-gravity waves	Planetary-scale (15°N to 15°S)	Few days
Thermal tides	Global-scale	24/m hours (m = 1, 2, ...)

## Chapter 3

# HIRDLS and HIRDLS Temperature

### 3.1 Overview of HIRDLS Instrument

The High Resolution Dynamics Limb Sounder (HIRDLS) is a multichannel infrared (IR) limb-scanning radiometer flying on the NASA Earth Observing System (EOS) Aura satellite which was launched on July 15, 2004. HIRDLS is an international joint US-UK development project between the University of Colorado at Boulder and the University of Oxford.

The instrument was designed to sound the upper troposphere, stratosphere and mesosphere to provide measurements of temperature, a number of atmospheric trace gases such as O<sub>3</sub>, H<sub>2</sub>O, CH<sub>4</sub>, N<sub>2</sub>O, NO<sub>2</sub>, HNO<sub>3</sub>, N<sub>2</sub>O<sub>5</sub>, CFC11, CFC12, and ClONO<sub>2</sub>, aerosols, and the locations of polar stratospheric clouds and cloud tops. HIRDLS obtains profiles of radiance at high vertical and horizontal resolution between 8 and 80 km over most of the globe, both day and night, and completes near global coverage in twelve hours. It has 21 infrared special narrow and more-transparent spectral channels with spectral range from 6.12 to 17.76 microns. Each channel is used to make retrievals over the possible altitude range. *Gille et al.* [2003] have described the HIRDLS experiment, with a description of HIRDLS in operation provided by *Gille et al.* [2008].

HIRDLS has the highest vertical resolution (~1 km) compared with previous infrared limb sounders and the spacing of reported levels is only ~ 0.68 km with a large degree of oversampling. This together with a fast scan period of ~ 15.5 seconds compared with the Brunt-Väisälä period (typically 5 minutes in the middle atmosphere) makes the instrument suitable for observing gravity wave properties in the vertical. A piece of plastic closeout material, probably Kapton®, came loose during launch, blocking about 80% of the front aperture and causing a small oscillation in the radiometric signal by vibrating with movement of the scan mirror. The blockage limits longitudinal resolution to the orbital spacing of 24.72° but increases the designed along-

track spacing to  $\sim 100$  km [Gille *et al.*, 2008]. It also restricts coverage from  $65^{\circ}\text{S}$  to  $82^{\circ}\text{N}$ . The HIRDLS team has developed extra algorithms to correct for the effects of the obstruction. Validation of the oscillation correction and of the retrieved temperature profiles shows that HIRDLS can still reproduce the atmospheric horizontal and vertical structure [Gille *et al.*, 2005, 2008]. Therefore, despite the blockage, the HIRDLS data is still very useful for atmospheric sounding and has led to a more favourable and regular IR array for gravity wave research.

The main scientific goals of HIRDLS are of monitoring of upper tropospheric, stratospheric and mesospheric temperature and important atmospheric trace gases. The measurements provided by HIRDLS can improve our knowledge of the lower and middle atmosphere for better understanding of a variety of global environmental issues related to the chemistry and dynamics of the atmosphere. The issues to be investigated by HIRDLS include [Lambert *et al.*, 1999]:

- a. Fluxes of mass and chemical constituents determined down to small scales, including retrieved gases such as  $\text{O}_3$ ,  $\text{H}_2\text{O}$ ,  $\text{NO}_2$ ,  $\text{HNO}_3$ , CFC11, CFC12,  $\text{N}_2\text{O}_5$ ,  $\text{N}_2\text{O}$ ,  $\text{ClONO}_2$  and  $\text{CH}_4$  and aerosols between the troposphere and stratosphere to understand their effects on the dynamics and composition of the atmosphere, particularly the stratosphere-troposphere exchange (STE) of the chemical species.
- b. Chemical processes, transport and small-scale irreversible mixing in the upper troposphere, stratosphere and mesosphere, particularly for the chemical and dynamical processes responsible for the Antarctic/Arctic ozone holes.
- c. Balance of momentum, energy, heat, and potential vorticity in the middle atmosphere, down to smaller horizontal and vertical scales, for understanding large-scale characteristics of the atmospheric chemistry and dynamics.
- d. Seasonal, interannual and long-term climatologies of upper tropospheric, stratospheric and mesospheric quantities, in particular, the profiles of temperature, trace gases, gravity waves and cloud top heights, by combining the measurements from other EOS instruments with pre-EOS and future EOS observations.

- e. Global distributions and interannual variations of aerosols, cirrus clouds and PSCs for understanding the depletion of ozone in the lower stratosphere and impact of cirrus clouds in the upper troposphere on the radiative heating and cooling of the atmosphere.
- f. Studies of tropospheric chemistry through temperature and joint constituent retrievals with other EOS instruments.
- g. Diagnostic studies of atmospheric dynamics, chemistry and transport processes, for model improvement and validation.

### **3.2 The Platform of the HIRDLS Instrument: Aura**

Aura is a sun-synchronous, near polar-orbiting satellite launched on July 15, 2004 at 11:02 AM BST from Vandenberg AFB, California, with six years design life time. It flies at 705 km altitude with the ascending node crossing the equator at approximately 1:45 PM and an orbit period of approximately 100 minutes. Aura repeats its ground track every 16 days to provide atmospheric measurements over the world. The satellite is a part of the NASA EOS, a program dedicated to monitoring the complex interactions that affect the globe through a coordinated series of satellites.

As the platform for four scientific instruments, the Aura spacecraft provides the essential services for operating HIRDLS, MLS (Microwave Limb Sounder), OMI (Ozone Monitoring Instrument), and TES (Tropospheric Emission Spectrometer) with the aim of studying the composition, chemistry and dynamics of the Earth's atmosphere from the ground through to the mesosphere. Particular foci include ozone, climate and air quality.

Aura is a member of a constellation of satellites, the so called the 'A-Train' that currently consists of five satellites flying in close proximity: Aqua, CloudSat, CALIPSO, PARASOL and Aura, as shown in figure 3.1. All five satellites cross the equator behind Aqua within a few minutes of one another near 1:30 pm local time and again in the early morning at about 1:30 am.

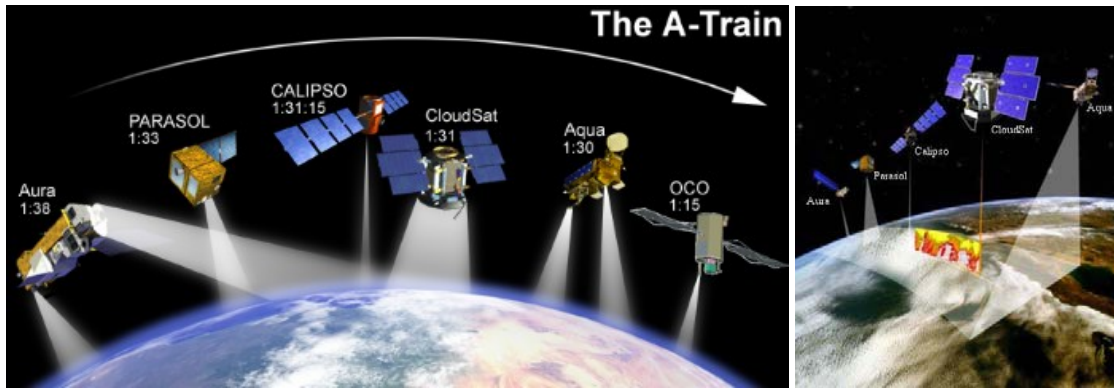


Figure 3.1 Aura in the ‘A-Train’.

### 3.3 Design of the HIRDLS Instrument

#### 3.3.1 Heritage

The Limb Radiance Inversion Radiometer (LRIR) mounted on Nimbus 6 was the first successful flight of an infrared limb viewing radiometer. It was launched in June, 1975 to determine temperature,  $O_3$  and  $H_2O$  in the stratosphere and lower mesosphere. *Gille et al.* [1980a, 1980b] briefly discussed its measurements of temperature and ozone. The Limb Infrared Monitor of the Stratosphere (LIMS) is a similar but expanded instrument flown on Nimbus 7 launched in October, 1978 in order to measure  $O_3$ ,  $H_2O$ ,  $NO_2$  and  $HNO_3$  [*Gille and Russell*, 1984a, 1984b]. The Stratosphere and Mesosphere Sounder (SAMS) was another limb sounder on Nimbus 7 to measure temperature, methane and nitrous oxide [*Drummond et al.*, 1980]. Later on the Upper Atmosphere Research Satellite (UARS) launched in 1991, with two infrared viewers, the Improved Stratosphere and Mesosphere Sounder (ISAMS) [*Taylor et al.*, 1993] and the Cryogenic Limb Array Etalon Spectrometer (CLAES) [*Roche et al.*, 1993] provide measurements of temperature and the distributions of  $O_3$ ,  $H_2O$ ,  $CH_4$ ,  $N_2O$ ,  $HNO_3$ ,  $NO_2$ , CFC11 and CFC12, CO and  $N_2O_5$ , and the distributions and composition of aerosols and PSCs.

Measurements provided by these limb radiometers have greatly improved our knowledge of stratospheric and mesospheric dynamics and chemistry and the experience gained from these precursors was valuable for the design of HIRDLS.

### 3.3.2 HIRDLS Subsystem

HIRDLS consists of nine integrated subsystems that are the telescope subsystem (TSS), the detector subsystem (DSS), the in-flight calibration subsystem (IFC), the sunshield subsystem (SSH), the cooler subsystem (CSS), the instrument processing subsystem (IPS), the structural thermal subsystem (STH), the power subsystem (PSS) and the gyro subsystem (GSS). These subsystems are summarized in table 3.1 and a schematic diagram of the subsystems is shown in figure 3.2. The TSS provides light to optical system which is spectrally filtered before falling on cold detector array. A blackbody and view of cold space provides essential calibration.

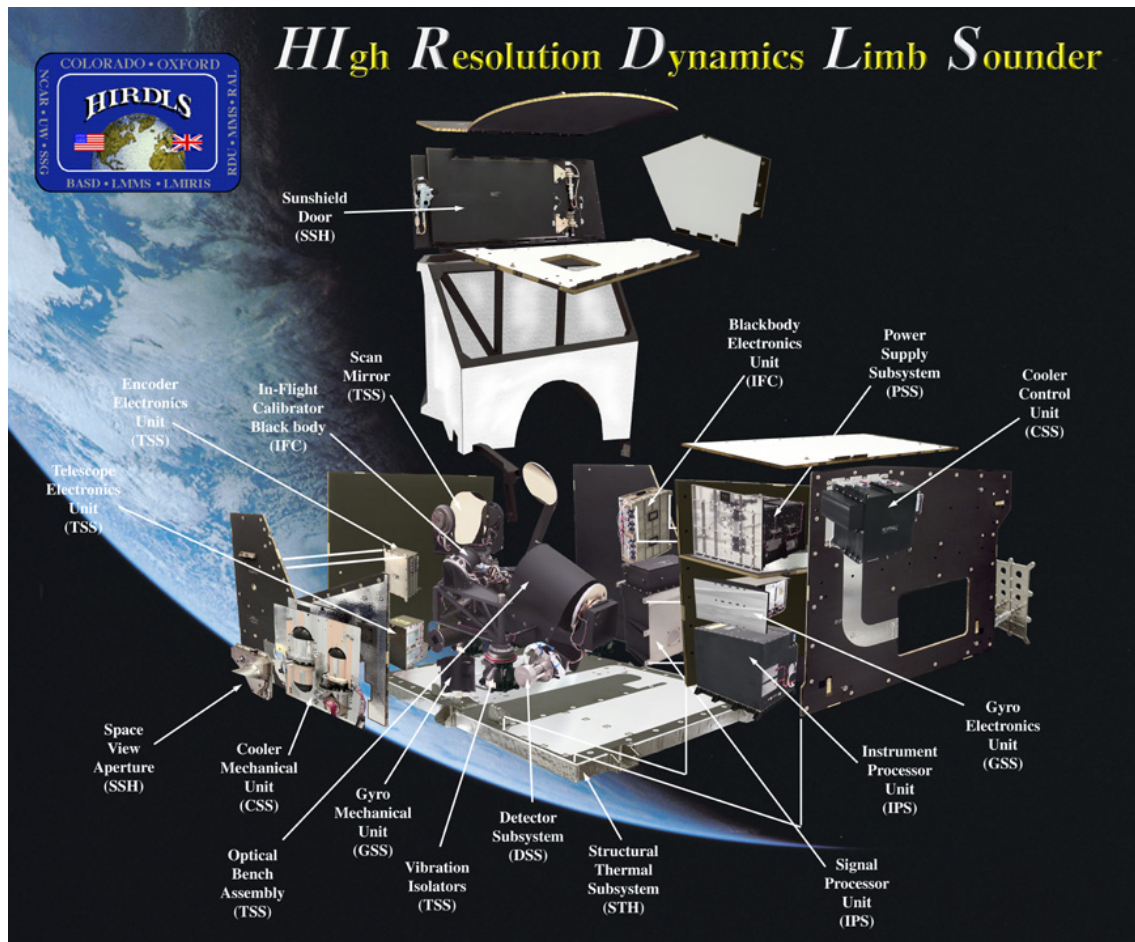


Figure 3.2 Schematic diagram of nine subsystems integrated together in HIRDLS (from <http://www.atm.ox.ac.uk/hirdls/instrument/components.shtml>).

Table 3.1 A summary of HIRDLS subsystems

TSS	Telescope Subsystem	Instrument telescope and related electronic units
DSS	Detector Subsystem	Multi-channel infrared radiometric detector array and dewar assembly
IFC	In-Flight Calibration Subsystem	Optical items and electronics to enable radiometric calibration during flight operations
SSH	Sun-Shield Subsystem	Moveable door excludes solar flux from the interior of the instrument
CSS	Cooler Subsystem	Provides active cryo-cooling for the instrument detector array
IPS	Instrument Processing Subsystem	Signal and data processing to support mission science operations and housekeeping functions
STH	Structural Thermal Subsystem	Primary structural support and environmental enclosure for electronic units and telescope
PSS	Power Subsystem	Provides basic power conversion and switching
GSS	Gyro Subsystem	Provides precision base motion disturbance data

(<http://www.eos.ucar.edu/hirdls/>)

### 3.3.3 Optical System

The optical system shown in figure 3.3 is the main part of the instrument. Limb radiation enters the instrument aperture and then is reflected by the flat scan mirror and collected by the primary mirror. A rotating chopper located at the first focal plane chops the incoming radiation and reflects the light via a relay mirror to the detectors. The image of the atmosphere is produced by the TSS, which consists of a two-axis scan mirror, an off-axis, 3-mirror Gregorian reflecting telescope and two Ge lenses to relay onto the detector focal plane on which 21 detectors are placed. The corresponding field of view of each detector is  $0.19^\circ$  ( $\sim 10$  km) horizontal by  $0.019^\circ$  ( $\sim 1$  km) vertical. The detector focal plane is maintained by coolers at  $\sim 62$  K. In-flight radiance calibration is performed by moving the scan mirror to view cold space and an internal blackbody with an accurately known temperature, although the blackbody was not useable in-flight because of the Kapton problem.

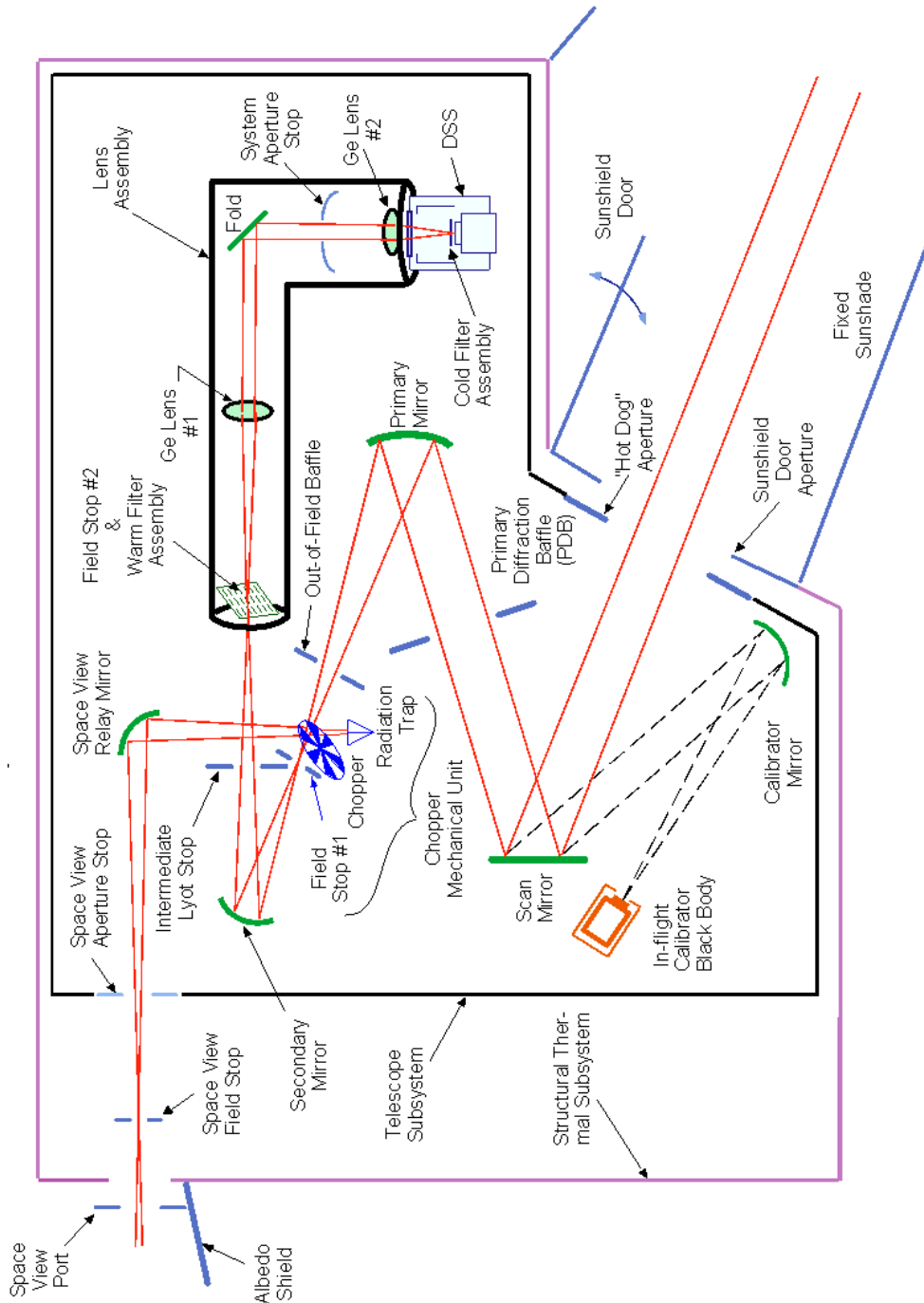


Figure 3.3 HIRDLS optical system [ATBD-HIR-01, 1999].

### 3.3.4 Spectral Band-Pass Filters

HIRDLS uses spectral band-pass filters to select specified wavelengths for its targets [*Hawkins et al.*, 1994; *Hunneman et al.*, 1994; *Lambert et al.*, 1999]. There are 21 individual interference filters placed at an intermediate focal plane corresponding to 21 spectral channels. They operate at ambient temperature and are called warm filters (figure 3.3). Close to the detectors, there are 21 cold filters (figure 3.3) on the cold focal plane with approximately twice the spectral band-pass of the warm filters.

### 3.3.5 Spectral Channels Characteristics

HIRDLS comprises 21 spectral channels ranging from 6.12 to 17.76  $\mu\text{m}$  which separate the spectrum on 21 HgCdTe photoconductive detectors at the detector focal plane (shown in figure 3.4). The physical size of detector elements is 82  $\mu\text{m} \times 820 \mu\text{m}$  determining the instrument angular field of view (FOV) of 0.332 mrad  $\times$  3.32 mrad. The detectors are maintained by a Stirling Cycle cryocooler (CSS) at  $\sim 62$  K. The spectral characteristics and applications of the 21 spectral channels are summarized in table 3.2. The altitude range in the table is limited by the ratio of signal to noise (S/N) and the atmospheric optical saturation of channels at low altitudes. Each channel was targeted at measuring particular species. Major contaminants are given in the table.

### 3.3.6 FOV and IFOV Characteristics

The field of view (FOV) is the angular extent of data acquisition across-track and determines the swath width. The instantaneous field of view (IFOV) is the angle view subtended by a single detector element on the axis of the optical system. The IFOV determines the area of the atmosphere seen from an operating altitude at one particular moment in time and thus the spatial resolution of the sensor, but it is independent of sensor operating altitude. As mentioned in the previous section, the physical size of detector elements determines an angular field of view of 0.332 mrad  $\times$  3.32 mrad resulting in the vertical IFOV of 1 km and the horizontal IFOV of 10 km. The composite FOV of the whole HIRDLS detector array is 55 km  $\times$  55 km as shown in figure 3.4. HIRDLS FOV, IFOV and the FOV-determined swath width are given in table 3.3.

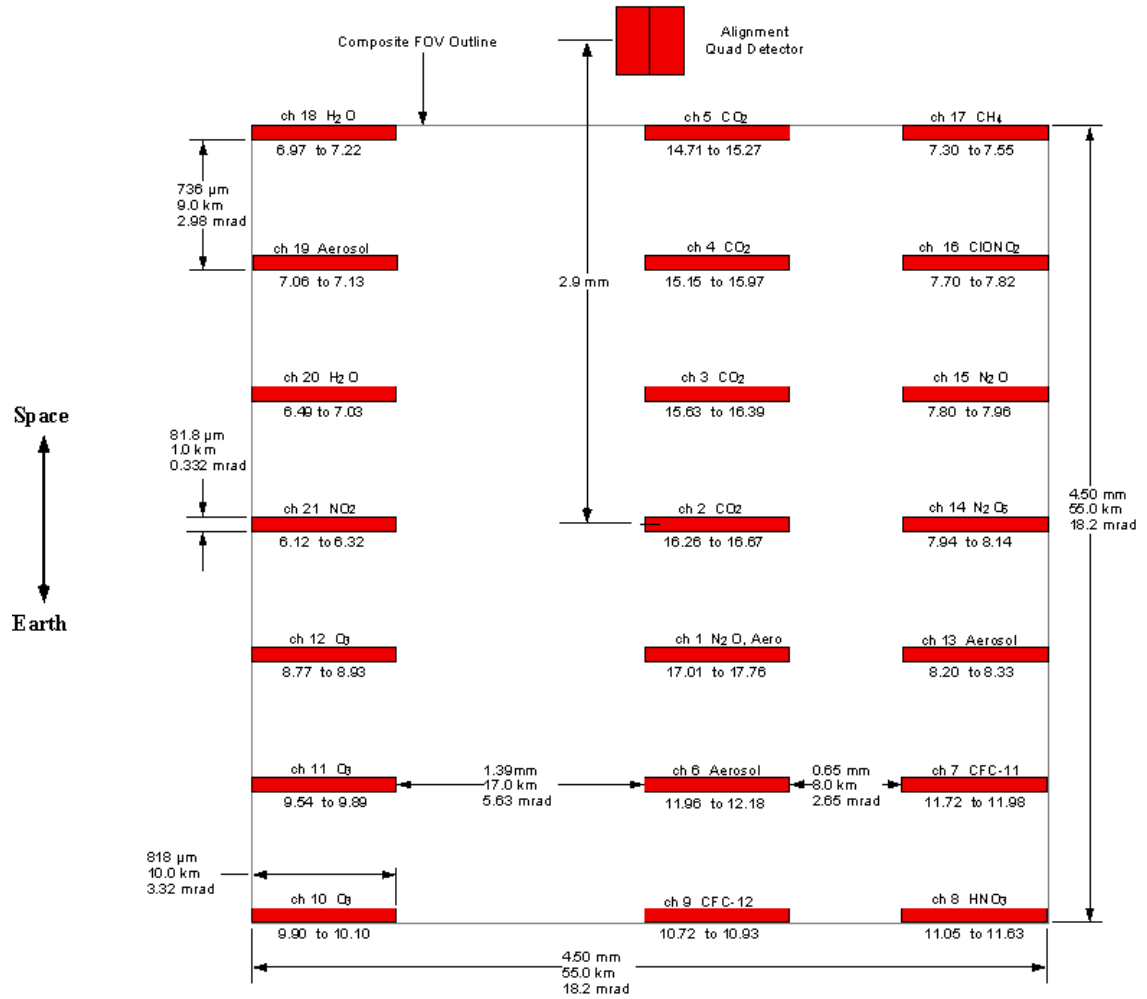


Figure 3.4 HIRDLS detectors at the detector focal plane [ATBD-HIR-01, 1999].

Table 3.2 Characteristics of HIRDLS spectral channels

Channel	Spectral range [ $\mu\text{m}$ ] <sup>(1)</sup>	50% response [ $\text{cm}^{-1}$ ] <sup>(2)</sup>	Species	Contaminants	Sounding Range [km]	Radiometric noise [ $10^{-4}\text{Wm}^{-2}\text{Sr}^{-1}$ ]
1	17.01-17.76	563.50 $\pm$ 2.0 - 587.25 $\pm$ 1.0	N <sub>2</sub> O, aerosol	N <sub>2</sub> O H <sub>2</sub> O CO <sub>2</sub>	8 - 70	12.0
2	16.26-16.67	600.50 $\pm$ 2.0 - 614.75 $\pm$ 1.0	CO <sub>2</sub>	CO <sub>2</sub> O <sub>3</sub> N <sub>2</sub> O Aero	8 - 40	6.3
3	15.63-15.97	610.00 $\pm$ 3.0 - 639.50 $\pm$ 2.0	CO <sub>2</sub>	CO <sub>2</sub> O <sub>3</sub> Aero	8 - 60	5.9
4	15.15-15.97	626.00 $\pm$ 3.0 - 660.00 $\pm$ 3.0	CO <sub>2</sub>	CO <sub>2</sub> O <sub>3</sub> Aero	15 - 60	6.0
5	14.71-15.27	655.00 $\pm$ 3.0 - 680.00 $\pm$ 2.0	CO <sub>2</sub>	CO <sub>2</sub> O <sub>3</sub> Aero	30 -105	4.3
6	11.96-12.18	821.50 $\pm$ 2.3 - 835.00 $\pm$ 2.4	aerosol	CO <sub>2</sub> O <sub>3</sub> H <sub>2</sub> O	8 - 55	1.9
7	11.72-11.98	835.00 $\pm$ 2.4 - 852.00 $\pm$ 2.4	CFCl <sub>3</sub> (CFC11)	HNO <sub>3</sub> CO <sub>2</sub> O <sub>3</sub> Aero	8 - 50	2.0
8	11.05-11.63	861.50 $\pm$ 2.5 - 903.50 $\pm$ 2.5	HNO <sub>3</sub>	CFC <sub>11</sub> CFC <sub>12</sub> H <sub>2</sub> O Aero	8 - 70	4.2
9	10.72-10.93	916.00 $\pm$ 2.6 - 931.50 $\pm$ 2.6	CF <sub>2</sub> Cl <sub>2</sub> (CFC12)	HNO <sub>3</sub> CO <sub>2</sub> H <sub>2</sub> O Aero	8 - 50	2.0
10	9.90-10.10	991.00 $\pm$ 2.8 - 1009.00 $\pm$ 2.8	O <sub>3</sub>	CO <sub>2</sub> Aero	8 - 55	1.5
11	9.54-9.89	1011.00 $\pm$ 2.9 - 1046.50 $\pm$ 2.9	O <sub>3</sub>	CO <sub>2</sub> Aero	30 - 85	2.4
12	8.77-8.93	1120.00 $\pm$ 3.2 - 1138.50 $\pm$ 3.2	O <sub>3</sub>	N <sub>2</sub> O CFC12 H <sub>2</sub> O Aero	8 - 55	0.96
13	8.20-8.33	1202.00 $\pm$ 3.4 - 1259.75 $\pm$ 3.4	aerosol	CH <sub>4</sub> CO <sub>2</sub> N <sub>2</sub> O HNO <sub>3</sub> O <sub>3</sub>	8 - 55	1.1
14	7.94-8.14	1229.50 $\pm$ 2.0 - 1259.75 $\pm$ 1.0	N <sub>2</sub> O <sub>5</sub>	CH <sub>4</sub> N <sub>2</sub> O H <sub>2</sub> O CO <sub>2</sub> Aero	8 - 60	1.1
15	7.80-7.96	1256.25 $\pm$ 1.0 - 1281.75 $\pm$ 1.0	N <sub>2</sub> O	CH <sub>4</sub> HNO <sub>3</sub> ClONO <sub>2</sub> H <sub>2</sub> O CO <sub>2</sub> CF <sub>4</sub> Aero	8 - 70	1.1
16	7.70-7.82	1278.25 $\pm$ 1.0 - 1298.75 $\pm$ 1.0	ClONO <sub>2</sub>	CH <sub>4</sub> N <sub>2</sub> O HNO <sub>3</sub> CF <sub>4</sub> H <sub>2</sub> O Aero	8 - 70	1.1
17	7.30-7.55	1325.50 $\pm$ 3.8 - 1367.50 $\pm$ 3.8	CH <sub>4</sub>	H <sub>2</sub> O HNO <sub>3</sub> N <sub>2</sub> O CO <sub>2</sub> Aero	8 - 80	1.2
18	6.97-7.22	1387.00 $\pm$ 4.0 - 1435.00 $\pm$ 4.0	H <sub>2</sub> O	CH <sub>4</sub> O <sub>3</sub> O <sub>2</sub> CO <sub>2</sub> Aero	8 - 40	1.2
19	7.06-7.13	1402.25 $\pm$ 1.0 - 1415.75 $\pm$ 1.0	aerosol	H <sub>2</sub> O	8 - 55	1.3
20	6.49-7.03	1422.00 $\pm$ 4.1 - 1542.00 $\pm$ 4.3	H <sub>2</sub> O	CH <sub>4</sub> O <sub>3</sub> Aero	15 - 85	1.6
21	6.12-6.32	1585.50 $\pm$ 4.5 - 1630.50 $\pm$ 4.6	NO <sub>2</sub>	H <sub>2</sub> O CH <sub>4</sub> O <sub>2</sub> Aero	8 - 70	1.1

(1): 50% response wavelengths in microns:

[http://www.atm.ox.ac.uk/hirdls/inst/spectral\\_channels.htm](http://www.atm.ox.ac.uk/hirdls/inst/spectral_channels.htm)

(2): [Lambert et al., 1999].

Table 3.3 HIRDLS Parameters as-designed

Item	Parameter
Spectral Range:	21 channels covering from 6 to 18 $\mu\text{m}$
Standard profile spacing:	5° longitude $\times$ 5° latitude and 1 km vertical resolution; programmable to other modes and resolutions
Spatial resolution:	Profile spacing 500 km horizontally (5° lat $\times$ 5° long) $\times$ 1 km vertically; averaging volume for each data sample 1 km vertical $\times$ 10 km across $\times$ 300 km along line-of-sight
Data rate:	65 kbps
Thermal control:	Stirling cycle cooler, heaters, sun baffle, radiator panel
Thermal operating range:	20°-30°C
Scan range:	Elevation, 22.1° to 27.3° below horizontal, Azimuth, -21° (sun side) to +43° (anti-sun side)
Detector IFOV:	1 km vertical $\times$ 10 km horizontal
Swath width	500 - 3000 km (6 positions)
Control & Knowledge:	Such that scan range will allow all channels to observe from 0.25° below the hard horizon to 3.25° above it
Stability:	30 arcsec/sec per axis
Jitter:	84-Hz sample spacing uniform to $\pm 7$ arcsec
Coverage	Global coverage

### 3.4 Present Status of HIRDLS

As mentioned in the introductory section (section 3.1), a piece of plastic film, probably Kapton® that was installed to maintain the cleanliness of the optics, is believed to have come loose during launch, blocking a large part of the front aperture as shown in figure 3.5.

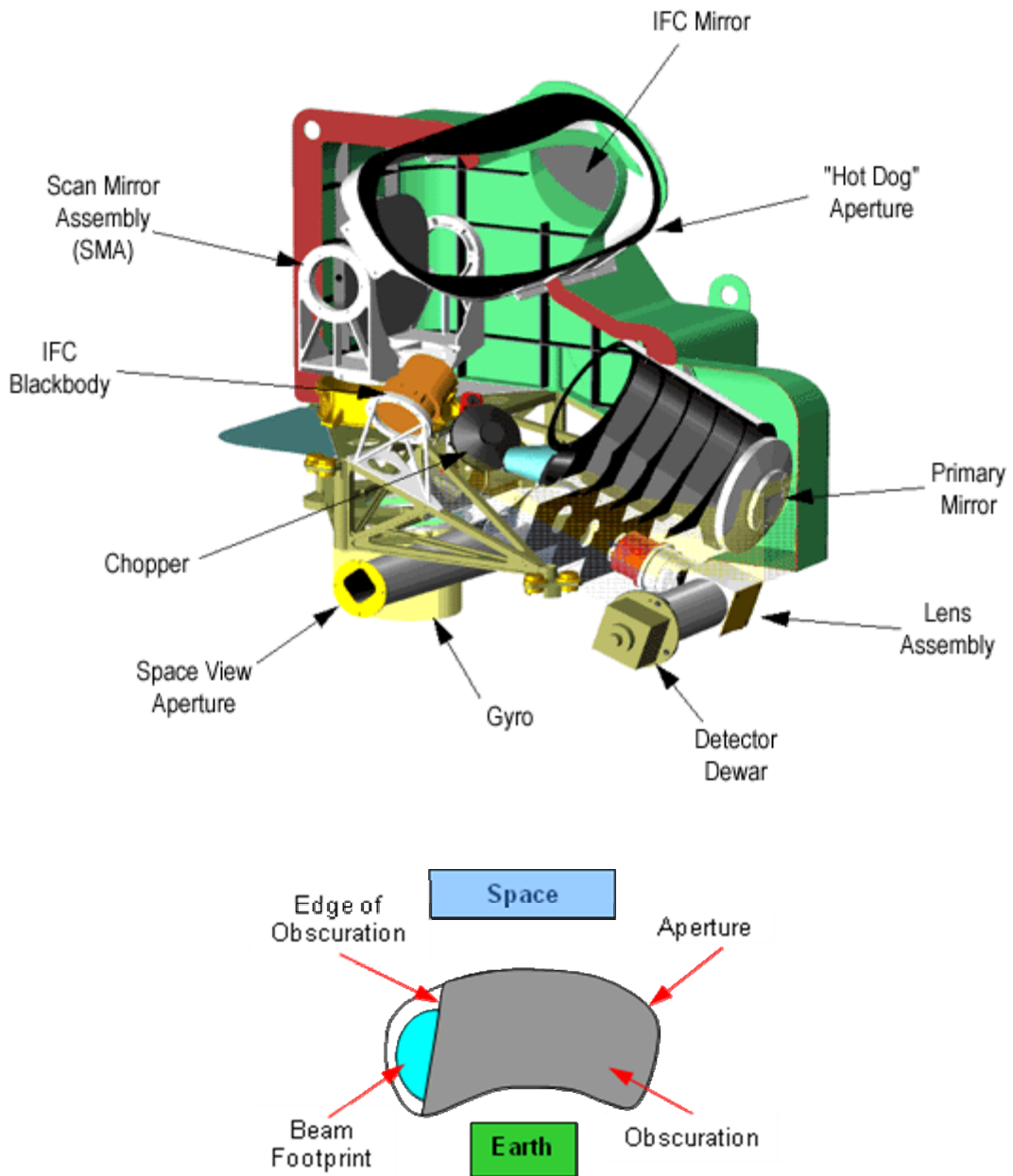


Figure 3.5 Top: HIRDLS internal view [Lambert *et al.*, 1999] and bottom: schematic diagram of the blockage of aperture (reproduced based on figure 2 in Gille *et al.* [2008]).

The blockage was confirmed to be emitting a large, nearly uniform radiance and covering about 80% of the whole aperture, leaving a small visible region at  $47^\circ$  from the orbital plane on the side away from the Sun, looking backward. HIRDLS was originally designed to view the atmosphere at several azimuthal angles, providing orbit-to-orbit coverage with a spacing of about 400-500 km in latitude and longitude as given in table 3.3. Due to the blockage, it is operated only at a single azimuth angle of  $47^\circ$  LOS from

the orbital plane (see figure 3.6). As a result, the longitudinal resolution is limited to the orbital spacing of  $24.72^\circ$  but the designed along-track spacing is increased to  $\sim 100$  km. The improved along-track spacing actually facilitated gravity wave studies. The global coverage is consequently also restricted to a range from  $65^\circ\text{S}$  to  $82^\circ\text{N}$  (see figure 3.7). The HIRDLS team has developed extra algorithms to correct for the effects of the obstruction. The current HIRDLS parameters that changed due to the blockage are summarized in table 3.4. The differences between the current and designed HIRDLS can be found by comparing with the parameters in table 3.3. Validation of the oscillation correction and of the retrieved temperature profiles shows that HIRDLS can still reproduce the atmospheric horizontal and vertical structure [Gille *et al.*, 2008].

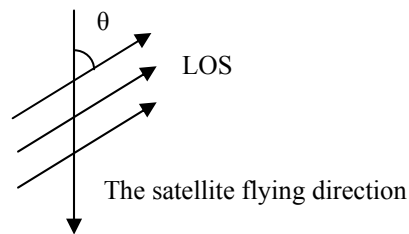


Figure 3.6 The azimuth angle of  $47^\circ$  ( $\theta$ ) line-of-sight.

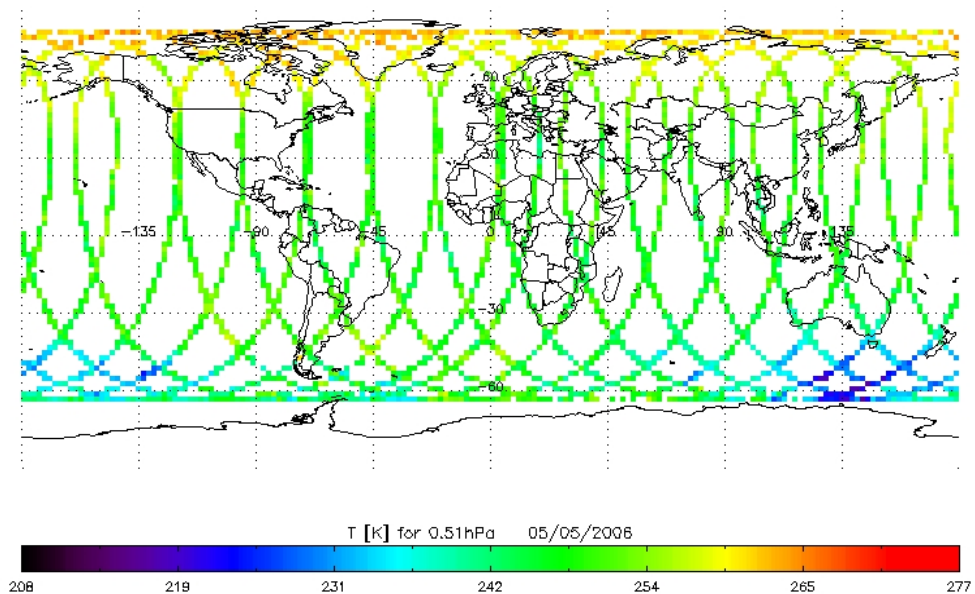


Figure 3.7 HIRDLS orbit coverage.

Table 3.4 Current HIRDLS Parameters (compared with table 3.3)

Item	Parameter
Spatial resolution:	Profile spacing $24.72^\circ$ orbital $\times \sim 100$ km along-track $\times 1$ km vertically; averaging volume for each data sample 1 km vertical $\times 10$ km across $\times \sim 200$ km along LOS
Scan range:	Azimuth $-47^\circ$ (anti-sun side)
Swath width	1 position
Coverage	$65^\circ\text{S} - 82^\circ\text{N}$

The plastic film that is blocking the aperture vibrates with movement of the scan mirror resulting in a small oscillation in the radiometric signal. The oscillation is removed from the radiometric signals in the LIC process (see the HIRDLS processing flow in section 3.7). Details of the removal of the oscillation in the HIRDLS radiometric signal are discussed in *Gille et al.* [2008].

### 3.5 Revised Operational Scan Patterns

The blockage of the aperture required a revision to the designed scan patterns. A few revised science scan modes have been performed in order to obtain the clearest atmospheric view with the obscured aperture [*V004 data quality document*, 2008].

Scan table 30 was used for the period 21 January 2005 – 28 April 2005. This mode made vertical scans at a fast vertical speed with a smaller LOS azimuth angle of  $-44.8^\circ$ . The higher scan speed results in large amplitude spurious oscillation making the data of poorer quality in this period compared with later data obtained from the other scan tables.

Scan table 13 for the period 28 April 2005 - 24 April 2006 made upper and lower limits of scans vary around the orbit, following the Earth's oblateness. This caused different types of oscillations in the signals.

Scan table 22 for the period 25 April 2006 – 3 May 2006 is similar to scan table 23, but with a lower spaceward limit of the scans.

Scan table 23 is the scan mode used since 4 May 2006. This scan makes 27 pairs of vertical up and down scans (each scan takes  $\sim 15.5$  seconds) at a single LOS azimuth angle of  $47^\circ$ . There is a 1-2 second space view before the next 27 scan pairs to complete instrument calibration. The spaceward and earthward limits of the scans are at fixed elevation angles.

### 3.6 Limb Viewing

HIRDLS is an infrared limb view sounder. The geometry of limb viewing is shown in figure 3.8 in which radiation leaving the atmosphere nearly tangentially is observed. Details for limb sounding were described by *Houghton et al.* [1984] and *Rodgers* [2000]. *Lambert et al.* [1999] described the limb view geometry for HIRDLS. Compared with nadir sounding, limb sounding is an improved technique for obtaining high vertical resolution of atmosphere profiles, e.g. HIRDLS provides measurement with a vertical resolution of 1 km. The altitude to be observed depends on the direction of view (also called the line-of-sight) of the instrument. For the infrared limb views, the emission from a gas along the line-of-sight (LOS) is proportional to the emissivity of the gas and to the Planck function at some representative temperature. Note that, each signal depends on non-linear radiance emissions from all altitudes between the tangent height and the instrument. The thermal emission enables HIRDLS to sound the atmosphere both day and night. The upper altitude limit of vertical coverage is determined by the low value of the signal-to-noise, while the lower altitude limit is determined by limb opacity, including the presence of thick aerosol or clouds. The different signal-to-noise level and limb opacity with each channel makes the upper and lower altitude limits different for the 21 HIRDLS spectral channels (see table 3.2 and figure 3.4).

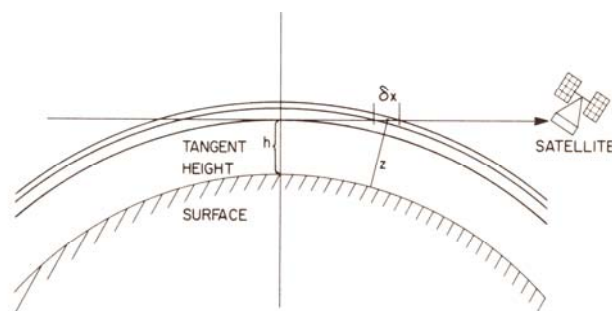


Figure 3.8 Geometry of limb view where  $h$  is the tangent height and  $\delta x$  is the projected thickness of an arbitrary layer at height  $z$  [*Houghton et al.*, 1984].

The geometry of limb view and a 2D vertical cross-section along the LOS are shown in figure 3.9. Note that, as the limb-sounder scans up or down, geometrical tangent points do not lie on one vertical profile through the Earth's centre. A reference tangent ray is used to define the nominal vertical profile location,  $\psi_0$ , along the LOS and its location (latitude and longitude) on the Earth. This reference location is used as the atmospheric profile position in the retrieval.

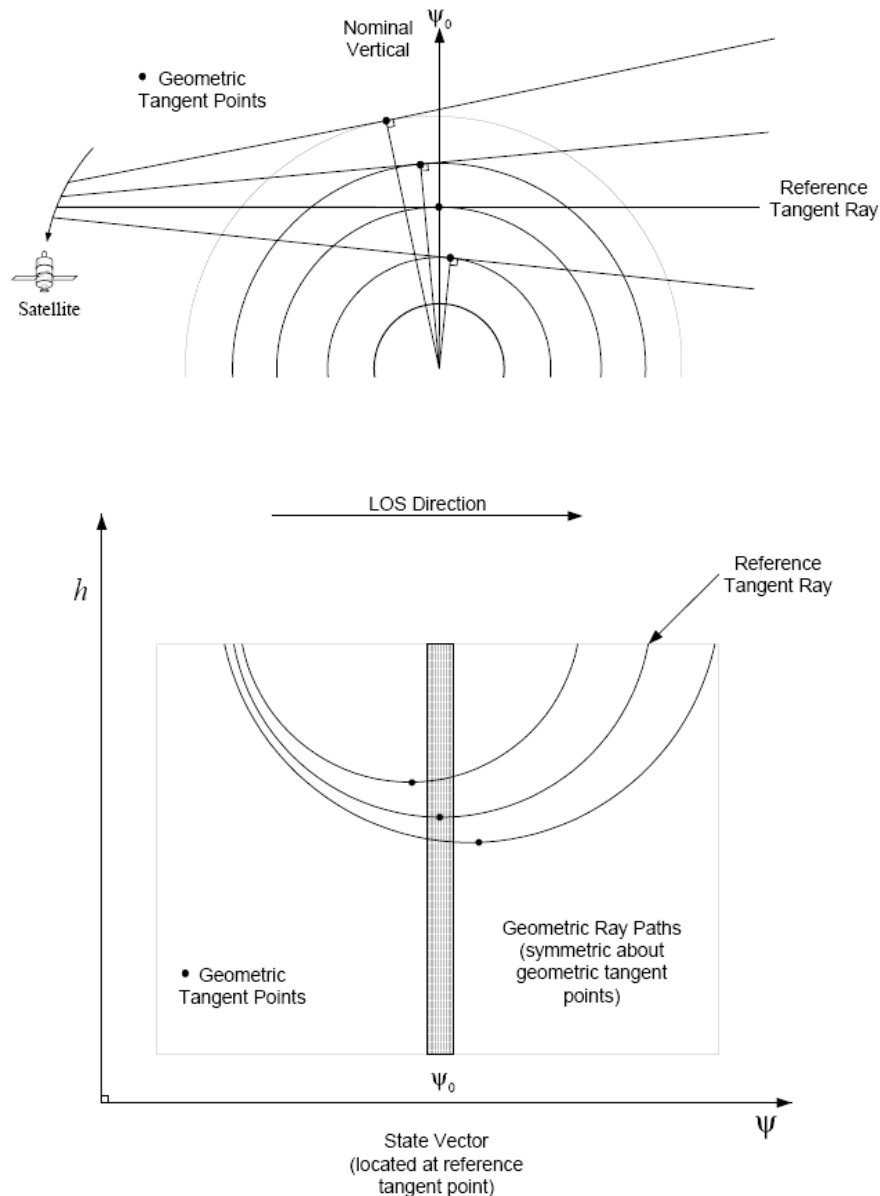


Figure 3.9 Geometry of limb view: vertical cross-section along the LOS [Lambert *et al.*, 1999].

### 3.7 HIRDLS Data Products

HIRDLS data products consist of level 0, level 1 and level 2 products. The flow of data in HIRDLS processing is shown in figure 3.10.

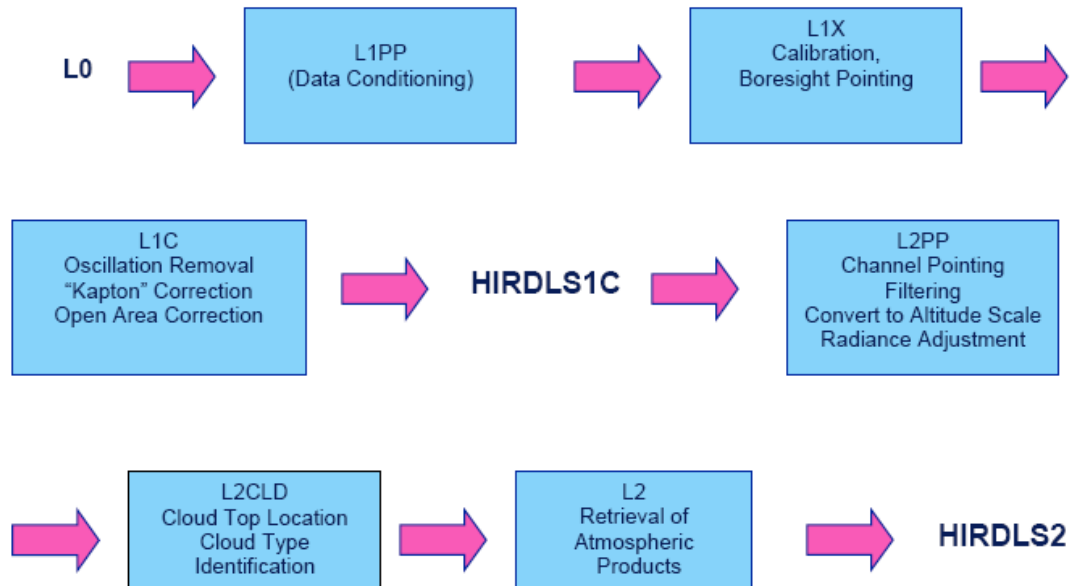


Figure 3.10 HIRDLS processing flow [*V004 Data Quality Document*, 2008].

#### 3.7.1 L0-1 Process (L1PP, L1X, L1C)

L0 data contains the raw data counts of the science measurements as the main input to the L0-1 processor system for calibration and correction states. L1PP processing corrects an occasional problem with the time in L0 data (raw data counts). The modified calibration and geolocation are carried out in L1X. The effect of the blockage is removed by applying three main correction algorithms in L1C [*Gille et al.*, 2008]. L1 provides a time series of calibrated radiances as well as housekeeping data necessary to the further data processing.

#### 3.7.2 L2 Pre-Processor (L2PP)

The L2PP process prepares data for the needs of retrievals in the L2 process. It takes the L1 products as input and separates the products into individual geolocated vertical scans, determines the vertical registration in altitude and performs field-of-view deconvolution and low-pass filtering.

### 3.7.3 L2 Cloud Detection (L2CLD)

The L2CLD process detects clouds by detecting radiance perturbations from the average clear sky case. Cloud tops are located and identified.

### 3.7.4 L1-2 Processor (L2)

The L1-L2 processor takes the conditioned radiance data from the L2CLD for the use in the retrieval algorithms to obtain L2 products. The retrieval is performed through a series of iterations. The L1-2 processor is described in *Lambert et al.* [1999]. From December 4-18<sup>th</sup>, some data products were corrupted because of problems with the data system. As a result, the input data were reconstructed and reprocessed. At this time, data are available from 22<sup>th</sup> January 2005 until 1<sup>st</sup> January 2008. Within the period, spacecraft maneuvers occasionally cause some days to be missing.

## 3.8 HIRDLS Temperature

At this time, the publicly available versions of level 2 temperature data includes HIRDLS V003 and HIRDLS V004, based on the HIRDLS v2.04.09 and v2.04.19 algorithms, respective. The validation of the HIRDLS V003 showed good quality temperature data within the altitude range 10 – 50 km with ~ 0.5 – 0.7 K precision and 1 – 2 K accuracy [*Gille et al.*, 2008]. The V004 data quality document [2008] suggested that the useful temperature measurements are within the pressure range from 400 to 1 hPa. The following description of the HIRDLS temperature data is mainly based on the information provided in *Gille et al.* [2008] which is applicable for both v003 and v004.

### 3.8.1 Temperature Retrieval

HIRDLS temperature in level 2 is retrieved from 4 CO<sub>2</sub> channels (channel 2-5) with spectral range from 15.27 to 16.26  $\mu\text{m}$ . The positions of 4 temperature channels (channels 2-5) along with limb radiances from the principal emitters are shown in figure 3.11. These four channels measure CO<sub>2</sub> emission from lower altitude tangent points (channel 2), mid-altitude tangent points (channel 3 and 4) and high altitude tangent points (channel 5). The main contaminants for the temperature channels are N<sub>2</sub>O and O<sub>3</sub>.

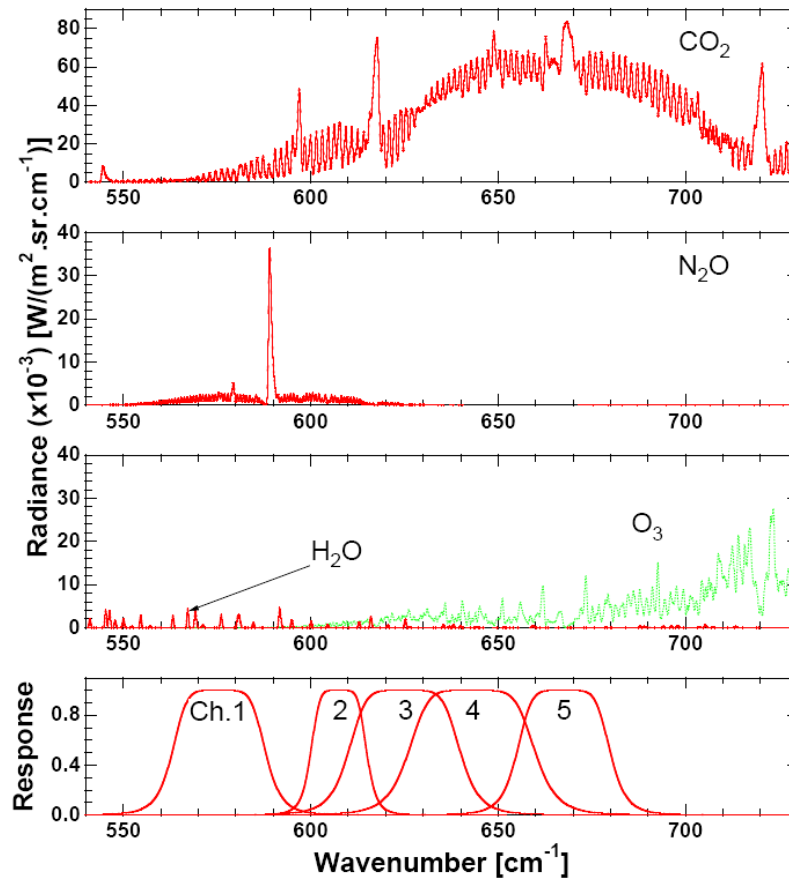


Figure 3.11 Limb radiance spectra for HIRDLS channel 1-5 calculated for a tangent height of 25 km, 21<sup>st</sup> March, 40°N. The spectral resolution is  $0.5 \text{ cm}^{-1}$  [Lambert *et al.*, 1999].

The temperature retrieval algorithm of the HIRDLS instrument has been described by Lambert *et al.* [1999]. The approach is a maximum *a posteriori* retrieval [Rodgers, 2000] of the radiances from channels 2 – 5, following the retrieval theories described by Gille and House [1971]. The aim of the physical retrieval algorithm is to obtain atmospheric temperature profiles for which the radiative transfer model (forward model) predicts synthesized radiances that are consistent with the measured radiances and the *a priori* information. The forward model allows for the temperature variations along the LOS [Francis *et al.*, 2006]. In the model, the transmittance estimates from Curtis-Godson and Emissivity-Growth Approximation with a statistical regression are physically based [Francis *et al.*, 2006]. The radiances calculated from the forward model are compared against a reference model with high accuracy. The comparison gives errors considerably better than 0.5% and often less than 0.2% for the temperature channels 2-5 up to 100 km.

In the retrieval algorithm, an inverse model is used to invert the radiances as measured by the satellite instrument to obtain the temperatures. Using the inverse model, the temperature retrieval starts with an initial guess that is provided by the GEOS-5 assimilated meteorological data. The temperature gradients along the LOS are also from the GEOS-5 assimilated data. The CIRA86 climatology [Fleming *et al.*, 1990] is used for the *a priori* temperature to provide stabilization against the possible gross amplification of noise associated with direct inversion of the measurements. The retrieval quality is controlled by examining the consistency of the retrieval and the measurements and the *a priori* data. For the retrieval of altitude temperature profiles from a satellite remote sensor, an averaging kernel is customarily used to describe the performance limit. The averaging kernel is obtained by multiplying weighting functions by the contribution function matrix. It is desirable to use the contribution function matrix that produces a narrow averaging kernel. The averaging kernels for HIRDLS temperature are shown in figure 3.12 with sharply peaked shape and 1.2 km width. The sum of averaging kernels (dashed line in figure 3.12) is close to 1, which indicates retrieval closely follows radiances and thus the retrieval algorithm is very insensitive to the *a priori*. The useful retrieved temperatures cover the range from 10 to 50 km for the v2.04.09 [Gille *et al.*, 2008] and from 400 to 1 hPa for the v2.04.19 [V004 data quality document, 2008].

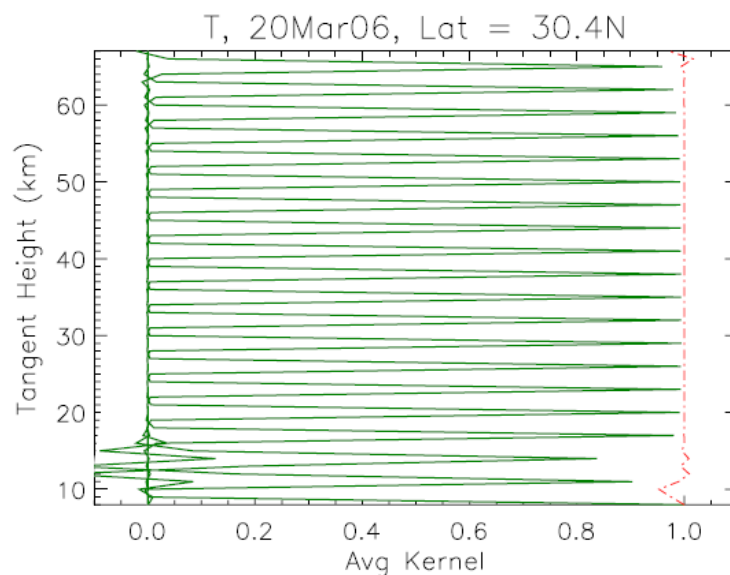


Figure 3.12 Averaging kernels for temperature for midlatitude equinox conditions. Every third averaging kernel is shown. Dashed line is sum of averaging kernels [Gille *et al.*, 2008].

### 3.8.2 Random Error

The random error of HIRDLS temperature was estimated in the course of the retrieval, based on the measurement noise, the uncertainty of the climatological *a priori* information, forward model error and the weighting functions [Rodgers, 2000; Lambert *et al.*, 1999]. Figure 3.13 shows the contributions from these factors to the total random error represented by the solid line. The figure shows the predicted random error is 0.8 K or less over the range from 16 to 50 km. The random error (precision) for v2.04.09 was also estimated by comparing with soundings and GMAO profiles. The random errors estimated by this method range from ~0.5 K at 20 km to ~1.0 K at 60 km close to those predicted [Gille *et al.*, 2008]. For v2.04.09 data, both the predicted and observed precision shows good data quality for most of the stratosphere and progressively less good data quality for the lower stratosphere, lower mesosphere and the troposphere. The observational studies concluded that the noise on the HIRDLS temperatures is much less than the atmospheric variation, and thus the instrument is able to track the meteorological variation and is sensitive to temperature variations with vertical wavelengths as small as 2 km [Gille *et al.*, 2008; V004 data quality document, 2008].

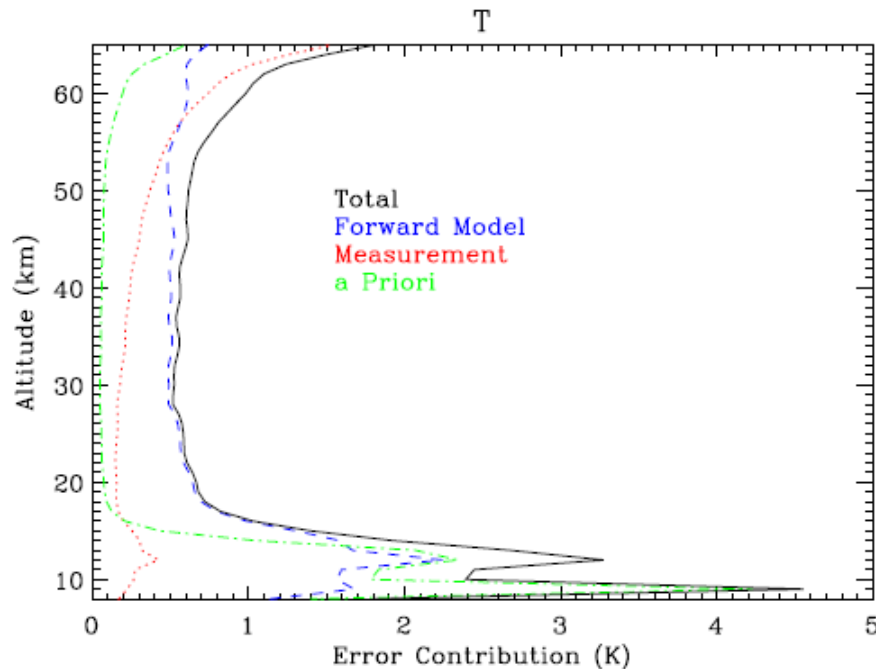


Figure 3.13 Random error contributions for the HIRDLS temperature retrieval. Solid line is the total error. The dotted, dashed, and dot-dashed lines represent the measurement noise, forward model and *a priori* error contributions [Gille *et al.*, 2008].

### 3.8.3 Systematic Bias

The systematic bias is checked through comparisons with temperature profiles from high-resolution radiosondes, lidars, ACE-FTS and the ECMWF analyses. The results indicated that HIRDLS is warmer than other sources by 1.5 – 2 K over the range from 100 to 10 hPa, consistently falling relative to the comparison data above 10 hPa, generally becoming equal to the comparison ~ 5 hPa, 2 K below around 2 hPa, and from 2 to 5 K low at 1 hPa. The systematic biases in the HIRDLS temperature are possibly caused by the effects of the blockage on the radiance, the *a priori* and the forward model. Details about the evaluation and the qualities of the temperature data, as well as the ability to resolve small vertical scales are described by *Gille et al.* [2008]. The systematic bias is removable and thus will not affect the gravity wave observations. Detailed discussion will be given in chapter 4.

### 3.8.4 Effects from Clouds

As discussed in the HIRDLS processing flow diagram, the HIRDLS temperatures are retrieved with the consideration of the located and identified cloud tops. In the data version v2.04.19, the cloud detection algorithm is much improved over that used in the previous version v2.04.09. As a result, the v2.04.19 temperature data are more reliable at lower levels than the v2.04.09 data. However, although it is rare, undetected clouds may still be present in the latest data version. Details of the cloud determination of cloud top pressures and cloud flags are discussed in *Massie et al.* [2007]. The cloud-free percent frequency for 2007 is presented in figure 3.14 in which the latitudinal variation is clearly influenced by the location of the tropopause. The figure shows that the cloud-free frequency is low at higher pressures. However, because HIRDLS provides a large number of profiles (~ 5500 profiles per day), the number of cloud-free profiles is still large at high pressures.

## 3.9 Summary

The HIRDLS instrument is a multichannel infrared (IR) limb-scanning radiometer with 21 specific IR spectral channels covering the spectral range from 6.12 to 17.76 microns. The instrument was designed to sound the upper troposphere, stratosphere and mesosphere to provide measurements of temperature, several atmospheric trace gases,

aerosols, the locations of polar stratospheric clouds and cirrus clouds, and cloud tops at high vertical and horizontal resolution.

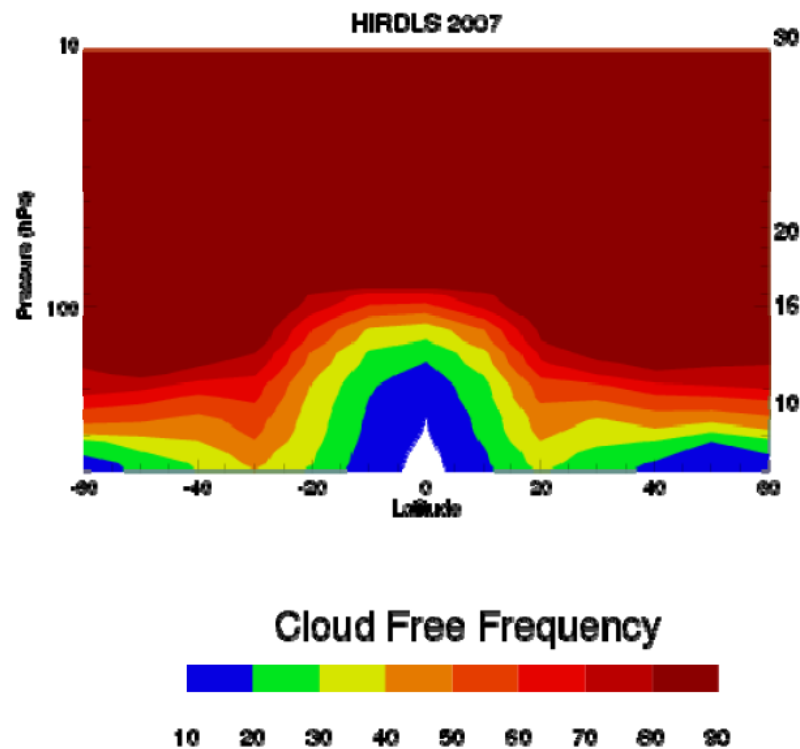


Figure 3.14. Cloud-free percent frequency in 2007. All pressures below the cloud top pressure of a single radiance profile are considered to be influenced by clouds [V004 data quality document, 2008].

A piece of plastic closeout material, probably Kapton®, came loose during launch, blocking about 80% of the front aperture and causing a small oscillation in the radiometric signal by vibrating with movement of the scan mirror. Due to the problem of the blockage, the HIRDLS operational scan patterns have been revised for better data quality. The blockage limits longitudinal resolution to the orbital spacing of  $24.72^\circ$  and restricts coverage from  $65^\circ\text{S}$  to  $82^\circ\text{N}$ . However, the designed along-track spacing is improved to  $\sim 100$  km as a consequence of the blockage. The revised mode makes the limb-sounder scanning the atmosphere at single LOS azimuth angle of  $47^\circ$ . The altitude range is from 8 to 80 km with vertical resolution of  $\sim 1$  km. The effects of the obstruction have been corrected by the HIRDLS team by developing extra algorithms. Validation results indicated that HIRDLS can still reproduce the atmospheric horizontal and vertical structure [Gille *et al.*, 2005, 2008].

HIRDLS has the highest vertical resolution ( $\sim 1$  km) compared with previous infrared limb sounders, and the spacing of reported levels is only  $\sim 0.68$  km with a large degree of oversampling. This together with a fast scan period of  $\sim 15.5$  seconds compared with the Brunt-Väisälä period (typically 5 minutes in the middle atmosphere) makes the instrument suitable for observing gravity wave properties in the vertical.

The data used for gravity wave observations in this thesis are HIRDLS level 2 data (v2.04.09 and v2.04.19) which are retrieved from four CO<sub>2</sub> channels (2, 3, 4, and 5) ranging from 15.27 to 16.26  $\mu\text{m}$ . Extra algorithms have been developed and changes have been made for the temperature retrieval algorithm to correct for the effects of the obstruction of the optical aperture [*Gille et al.*, 2008].

The random error of the temperature has been estimated at between  $\sim 0.5$  K at 20 km and  $\sim 1$  K at 60 km. The total random error indicates good data quality for most of the stratosphere and progressively less good data quality for the lower stratosphere, lower mesosphere and the troposphere. The comparisons with temperature profiles from high-resolution radiosondes, lidars, ACE-FTS and ECMWF analyses show similar systematic biases, i.e. warmer bias at pressure levels between 100 hPa and 5 hPa and colder bias at pressure levels between 5 hPa and 1 hPa. Details about the evaluation and the qualities of the temperature data, as well as the ability to resolve small vertical scales are described by *Gille et al.* (2008). In order to avoid cloud-contamination and to only use the data with high precision, data contaminated with clouds were discarded in the data selection process. The systematic bias is removable and thus will not affect the gravity wave observations.

## Chapter 4

# Gravity Wave Observations: Methodology and Results

Gravity waves can only be observed indirectly by observing their effects on the atmosphere. Waves are perceived through analyzing these observed effects. The analysis is based on the wave behavior. The indirect observations that can be used for gravity wave analysis include wind speed and direction, temperature, density, pressure and trace gas concentrations. These observations are determined by the characteristics of the instrument and its platform. A variety of space-based instruments are able to observe different portions of the gravity-wave spectrum. A limb-viewing instrument can be used to estimate the vertical structure of a wave field, but the horizontal characteristics cannot be determined directly by these instruments. In contrast, a nadir-viewing instrument can be used to observe the horizontal structure of a wave field, but the vertical structure of the wave can be estimated only by indirect means. Nadir instruments such as the AIRS (Atmospheric Infrared Sounder) instrument, for example, provide relatively fine horizontal resolution but can only detect waves with vertical wavelengths longer than 12 km [Alexander and Barnett, 2007; Limpasuvan et al., 2007]. In contrast, limb sounding instruments such as a GPS (Global Positioning System) satellite [e.g. Tsuda et al., 2000], CRISTA (Cryogenic Infrared Spectrometers and Telescopes for the Atmosphere, [e.g. Preusse et al., 2002]) and HIRDLS (High Resolution Dynamics Limb Sounder, [e.g. Alexander et al., 2008a]) have finer vertical resolution but may exclude shorter horizontal wavelengths.

In this thesis, gravity waves are extracted by using HIRDLS level 2 temperature data. Wave fields are inferred by computing temperature perturbations to the mean atmospheric state and the wave characteristics are estimated by analysing the wave behavior in the perturbations.

This chapter describes a new methodology to extract and analyze global gravity wave amplitudes and vertical wavelength using HIRDLS limb temperature data. Monthly mean gravity wave parameters are presented for the year long record, in particular illustrating orographic gravity waves over the southern Andes and the North America Cordillera and non-orographic gravity waves around the Himalayas.

#### 4.1 Extraction of Gravity Waves: Temperature Perturbations

The gravity waves in HIRDLS temperature in this thesis are extracted by calculating the temperature perturbations in the stratosphere that are primarily caused by mesoscale atmospheric gravity waves. The usual approach to the isolation of gravity waves from a given satellite dataset is a subtraction of a background state from the measurements, where the background state contains large-scale zonal waves, to extract gravity wave perturbations [e.g. *Fetzer and Gille, 1994, 1996; Eckermann and Preusse, 1999; Preusse et al., 2000, 2002; Ern et al., 2004, 2006; Alexander et al., 2008a*]. However, it is found in some tests that large-scale fluctuation structures can be retained by this process that are inconsistent with gravity waves and could be caused by not completely removing the background; any improvements in methodology at this stage will result in better results being obtained subsequently for the final analysed gravity wave parameters. The problem has also been mentioned by *Tsuda et al. [2000]* for their extraction of gravity waves from GPS/MET temperature profiles. In order to solve this problem, here gravity waves are extracted by removing a dynamic background field,  $T_{bk}$  (figure 4.1b) and an along-track temperature filter,  $T_f$  (figure 4.1c) from the HIRDLS temperature measurements,  $T$  (figure 4.1a). Details about the background field and the temperature filter are to be provided in subsequent sections. The residual perturbation is the small-scale wave temperature perturbation assumed to be the gravity wave temperature perturbation  $T'$  (see figure 4.1d). Equation 4-1 mathematically summarized the extraction process,

$$T'(lat, lon, p, t) = T(lat, lon, p, t) - T_{bk}(lat, lon, p, t) - T_f(lat, lon, p, t) \quad 4-1$$

where the  $T'$ ,  $T$ ,  $T_{bk}$  and  $T_f$  are a function of location ( $lat, lon$ ), pressure  $p$  and time  $t$ .

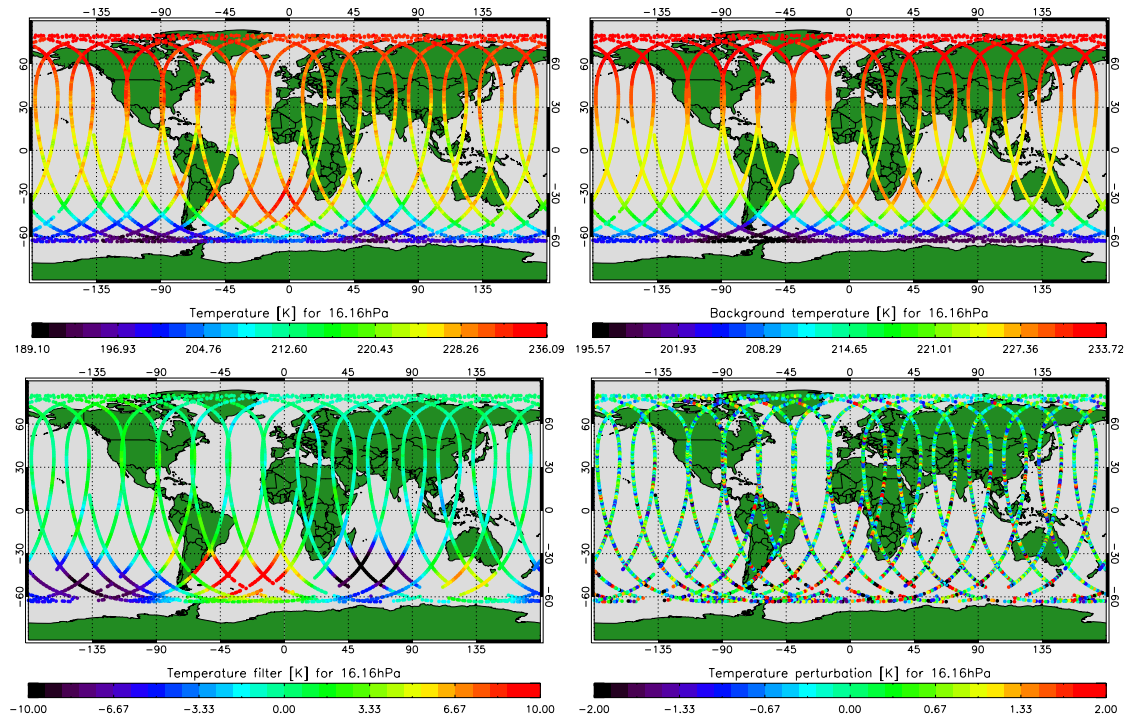


Figure 4.1 The process of extraction of gravity waves from HIRDLS temperature measurements. The maps show daily data at 16.16 hPa with the along-track sampling of  $\sim 100$  km and the orbital spacing of  $24.72^\circ$ . (a): top left, HIRDLS temperatures as the sum of the zonal mean, planetary-scale waves, and gravity waves; (b): top right, background field that is the sum of the zonal mean and low frequency planetary-scale waves; (c): bottom left, the temperature filter including the information of high frequency planetary-scale waves; and (d): bottom right, isolated gravity waves represented by gravity wave temperature perturbations.

#### 4.1.1 Background Field

The background field (figure 4.1b) is derived in order to block low frequency or stationary planetary-scale waves. It is computed dynamically for every day by, firstly, separating temperature measurements into day-time and night-time blocks of  $10^\circ \times 2^\circ$  longitude/latitude over a time period of 31 days ( $\pm 15$  days from the day analyzed); secondly, averaging the temperatures within each block at each pressure level; thirdly, smoothing by weighting the averaged temperatures based on the number of data points within the grid box analyzed and its neighboring grid boxes over the area of  $30^\circ$  in longitude and  $6^\circ$  in latitude; and finally, interpolating and recombining the day and night weighted temperature means, according to the distance from its grid centre to the

data point and to the neighboring grid centre, to build up the background field corresponding to the satellite orbit. The process of deriving the background field is illustrated for 23<sup>rd</sup> April 2006 in figure 4.2 where the averaged and weighted temperatures within each  $10^\circ \times 2^\circ$  grid cells for day-time (left) and night-time (right) are shown on the top and middle panels, respectively. The figure shows that the weighting process smoothes the background field to make it closer to the temporally and spatially continuous variation of atmospheric temperature. The finally interpolated background field that is used for the calculation of temperature perturbations is presented in the bottom panel. The background field is determined in this way for every day using in total 31 days data with 15 days before and after the analysed day including the day itself.

The period of 31-days and the grid of  $10^\circ \times 2^\circ$  longitude/latitude are decided, after several statistical tests, to ensure enough data points and the seasonal and meridional variation of temperature as well as the typical horizontal wavelength of planetary-scale waves. By blocking temperature measurements into  $10^\circ \times 2^\circ$  longitude/latitude grid boxes, the systematic biases in the temperatures are included in the background field and therefore will not contribute to the gravity wave temperature perturbations. Day and night separated blocks enable some tidal information to be included in the background field to reduce the contamination of tides in the isolated gravity wave temperature perturbations. The smoothing and interpolating is the consideration that a background field should be a temporally and spatially continuous function which has been shown in figure 4.2.

The background field that has been dynamically calculated for every day and night using 31 day temperature measurements works as a high-pass filter. This dynamic 31-day filter blocks the majority of planetary-scale waves that have periods longer than 31 days. Additionally, the day and night separated calculation will make this 31-day filter also able to attenuate other planetary-scale waves with shorter periods to a lesser extent. Figure 4.3 shows equatorial waves of zonal wave number 2 captured in the background field between  $30^\circ\text{N}$  and  $30^\circ\text{S}$  latitudes. The plots are day-time followed by night-time wave activity with a time interval of 4 days from 1<sup>st</sup> to 21<sup>st</sup> August 2006. The amplitudes of the waves decay with time and show diurnal variation as a result of day and night-time separation in the calculation of the background. A planetary wave with zonal wavenumber 1 in the background field is shown in figure 4.4 (left). The evolution

of the wave shows that the period of the planetary wave is about 50 days, which is consistent with the filtering function of the background field.

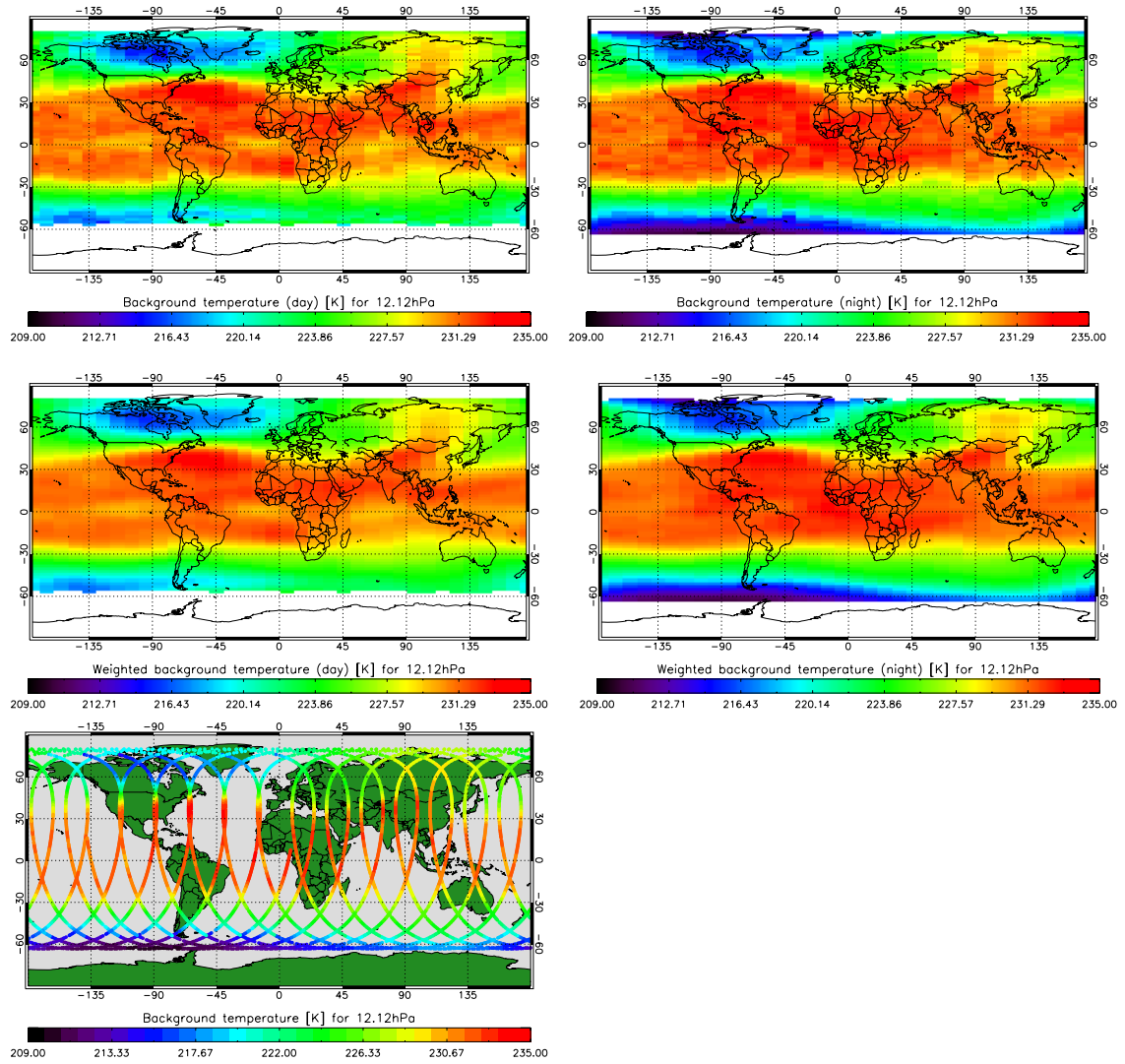


Figure 4.2 The processing of the background field determination for 23<sup>rd</sup> April 2006. Top panels: day-time (left) and night-time (right) averaged temperatures within each  $10^\circ \times 2^\circ$  grid cells; middle panels: day-time (left) and night-time (right) weighted temperatures within each  $10^\circ \times 2^\circ$  grid cells; bottom panel: the background field.

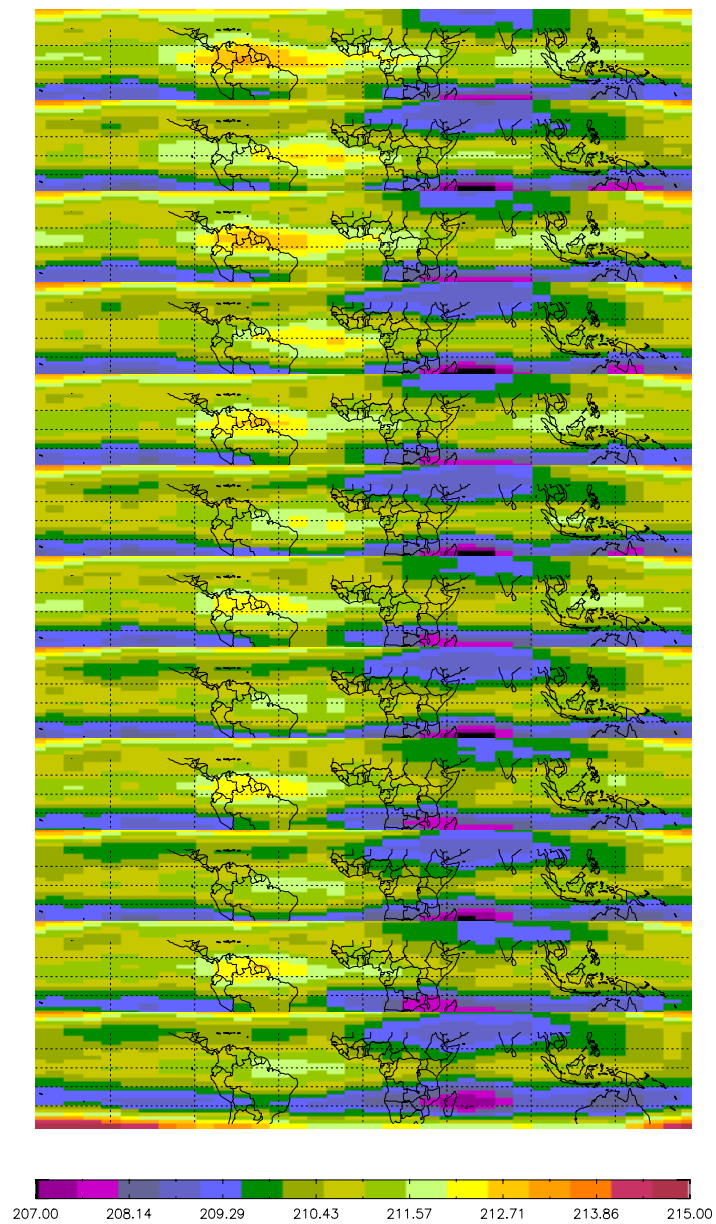


Figure 4.3 Equatorial waves of zonal wave number 2 at 56 hPa captured in the background field over latitudes 30°S to 20°N within the period from 1<sup>st</sup> to 21<sup>st</sup> August 2006 with an interval of 4 days (day-time plots following night-time plots for each day).

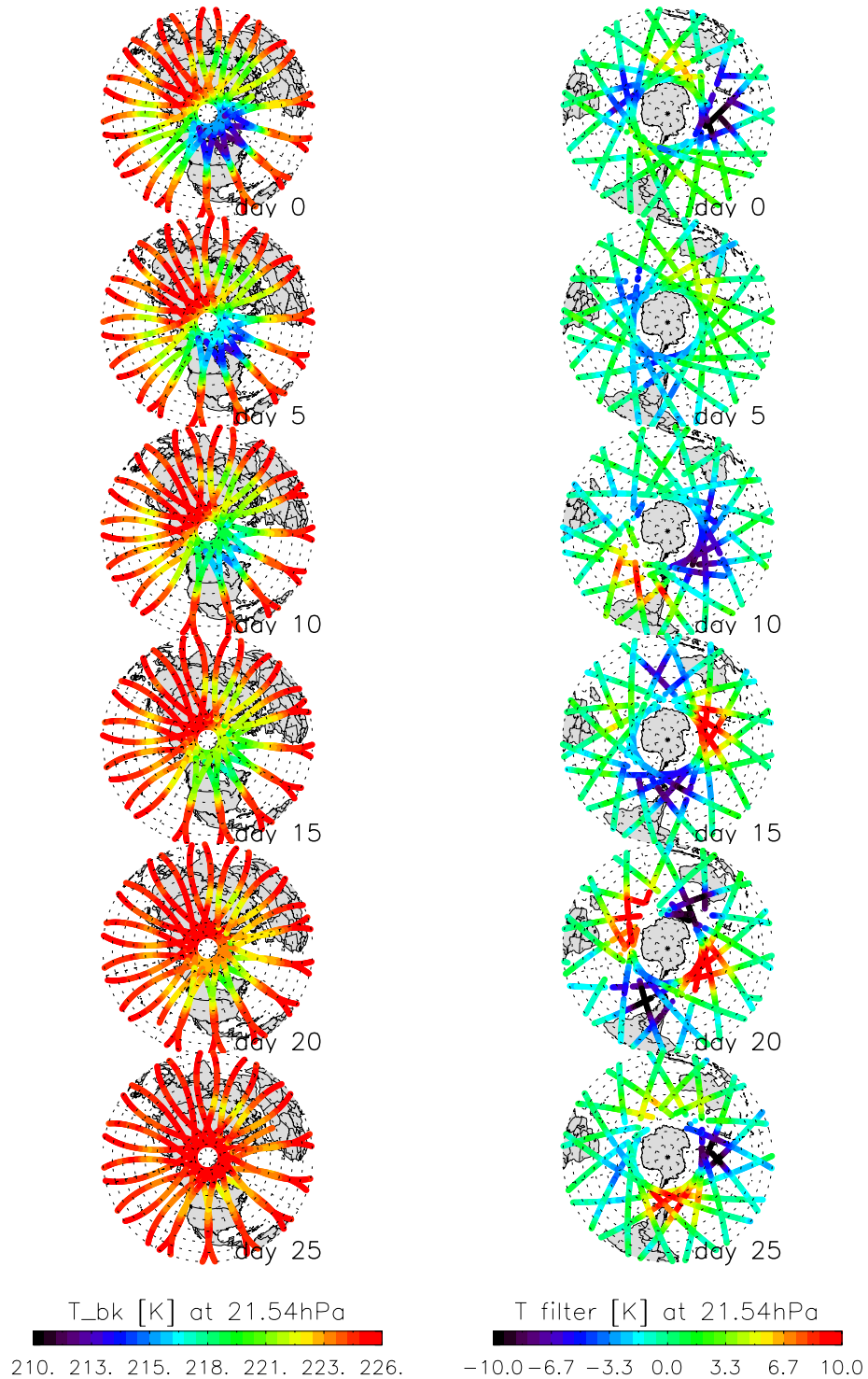


Figure 4.4 Evolution of planetary-scale waves in the  $T_{bk}$  and the  $T_f$ . Left, a low frequency planetary wave in the northern lower stratosphere in the  $T_{bk}$  (day 0 – 25: 20/4/2006 to 15/5/2006 with intervals of 5 days). Right, a high frequency planetary wave in the southern lower stratosphere in the  $T_f$  (day 0 – 25: 1/8/2006 to 26/8/2006 with intervals of 5 days).

### 4.1.2 The Along-Track Temperature Filter

After filtering out low frequency and stationary planetary-scale waves by the background field, an along-track temperature filter is developed to remove higher frequency planetary-scale waves compared to the waves in the background fields. The filter is similar to a boxcar filter and is explained by equation (4-2) where  $T_f$  is the along-track temperature filter as a function of time ( $t$ ), longitude ( $lon$ ), latitude ( $lat$ ) and pressure ( $p$ ).  $i$  is the profile number along the satellite track and  $N$  is the total number of profiles within an along-track window length of  $L$

$$T_f(t_{i-\frac{N}{2}}, lon_{i-\frac{N}{2}}, lat_{i-\frac{N}{2}}, p_{i-\frac{N}{2}}) = \frac{1}{N} \sum (T - T_{bk})(t_i, lon_i, lat_i, p_i). \quad 4-2$$

According to the difference in the meridional scales of gravity waves and planetary-scale waves [Andrews *et al.*, 1987] and considering the along-track sampling of  $\sim 100$  km and scan period of  $\sim 15$  seconds of the instrument, a window length of 1000 km is defined for the filter. Within the along-track filter window that has a length of 1000 km, HIRDLS completes up and down scans in  $\sim 2.75$  minutes ( $\sim 15$  seconds per profile  $\times \sim 11$  profiles).

Typically, gravity waves have horizontal wavelengths up to a thousand kilometres and periods from the Brunt-Väisälä period of about 5 minutes to several hours. Each profile is sampled in 15 s and hence provides close to an instantaneous snapshot of the vertical profile. During 2.75 minutes, the HIRDLS samples at 11 locations separated by 100 km, i.e. at a speed much faster than the phase speed propagation of a gravity wave from one location to another. Furthermore, the duration of the 1000 km window is very short compared with the period of planetary-scale waves which is longer than the inertial period. Therefore a simultaneous view of both the instantaneous gravity wave field in each location and of the more coherent planetary-scale wave fields can be assumed within the 1000 km window. Due to the shorter than 1000 km gravity wave wavelength, the along track average of the 11 profiles within the 1000 km window gives a near zero value for the  $T_f$ , resulting in the passage of gravity waves. However, because of the longer than 1000 km wavelength, the  $T_f$  of a planetary-scale wave within the 1000 km window is close to its real value ( $T - T_{bk}$ ), which means the

planetary-scale wave is captured by the  $T_f$ . Note that the along-track filter will always be blocking planetary-scale waves to some extent.

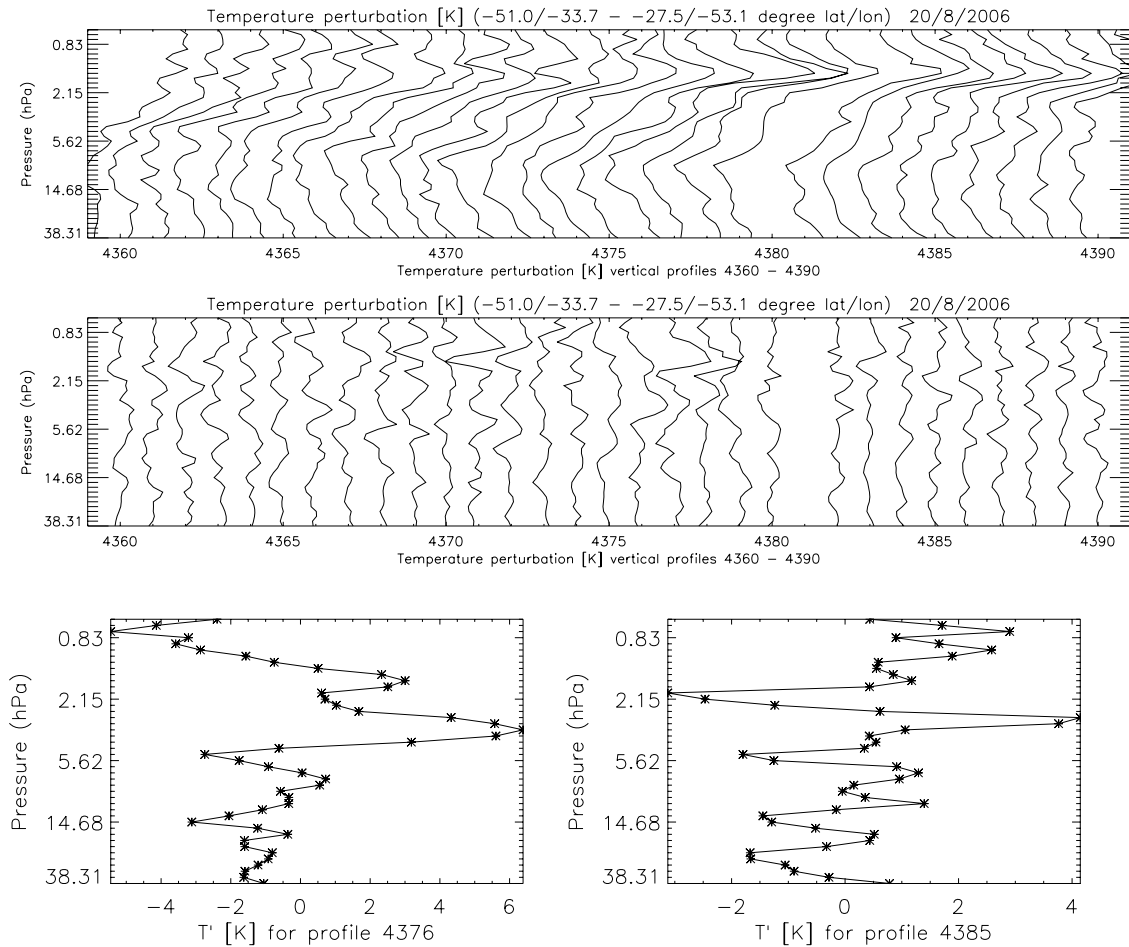


Figure 4.5 Vertical profiles 4360 to 4390 of before-filter temperature perturbations along a HIRDLS orbit on 20/08/2006 (top panel), vertical profiles 4360 to 4390 of after-filter temperature perturbations along the same satellite orbit on the same day (middle panel), and the magnified profiles 4376 and 4385 of the middle panel (bottom panel).

Figure 4.1c shows an example of the along-track temperature filter in which a planetary wave of wavenumber 2 is present in the southern hemisphere. A comparison between the before-filter (BF) profiles and the after-filter (AF) profiles is presented in figure 4.5. The BF temperature perturbations in the top panel show clearly large-scale structures on which small wave structures are superposed. These large-scale structures are coherent along the satellite track for a large along-track distance of a few thousand kilometres, which are consistent with large-scale waves, such as planetary waves, tides and Kelvin waves and need to be removed. By applying the along-track temperature

filter, the embodied large-scale waves by the large-scale structures and the superposed small waves can be separated. The small-scale wave structures isolated from the top panel are shown in the middle panel. These small wave structures are not coherent over a few thousand kilometres and look highly localized. The magnified individual profiles in the bottom panel shows that the amplitudes grow with altitude. Therefore, these small-scale waves, with clear gravity wave features, are assumed to be gravity wave temperature perturbations.

The evolution of a high frequency planetary wave for August 2006 (1/8/2006 to 26/8/2006) as shown in figure 4.4 (right) is compared to the planetary wave in the background field for April/May 2006 (left). The relatively rapid motion around the South pole shows that the wave in the along-track temperature filter is a transient planetary wave of wavenumber 2 with a much shorter period compared with the planetary wave captured in the background field. This demonstrates the different functions the background field and the temperature filter performed for extracting gravity waves from the temperatures.

## 4.2 Data Analysis

Figure 4.6 (top panel) shows an individual vertical profile of gravity wave temperature perturbations with the amplitude increasing with height. Assume a wave-like solution to the profile

$$T'(lat, lon, z, t) = \hat{T}(lat, lon, z, t) \exp^{i(mz - \omega t)}, \quad 4-3$$

where  $m$  denotes wavenumber and horizontal temperature amplitude  $\hat{T}$  is a function of location  $(lat, lon)$ , time  $t$  and height  $z$ . Here  $z = -H \ln(p/p_s)$  is determined by use of the ideal gas law and the hydrostatic equation.  $H = 7km$  is a mean scale height for the middle atmosphere,  $p$  is a pressure, and  $p_s$  is a standard reference pressure taken as 1000 hPa. Since the scan period of HIRDLS is much shorter than the buoyancy period, it is assumed that the instrument is observing an approximately instantaneous view of a given gravity wave in an individual profile. Using the Fast Fourier Transform (FFT) technique, each individual vertical profile is analyzed for amplitudes and vertical wavelengths,  $\lambda_z = 2\pi / m$ ,

$$\hat{T}(z, m) = \frac{1}{\sqrt{2\pi}} \int T' \exp^{-imz} dz . \quad 4-4$$

Windowing a vertical profile is required prior to the FFT analysis. A rectangular window is applied to the profile to limit the observation of the signal to a finite interval. A window with a shorter window length will lose the ability to transform longer waves and a window with a longer window length will lose the ability to analyze accurately the data for amplitudes and wavelengths. It is desirable to balance these two aspects of a window function for gravity waves. The sample interval of the vertical profile is about 0.68 km. In theory, the shortest wavelength that can be transformed is 1.36 km. In the middle atmosphere, internal gravity waves have vertical wavelengths typically from a few kilometres to  $\sim 15$  kilometres and the vertical wavelengths of observed inertia-gravity waves can go up to a few tens of kilometres [Andrews *et al.*, 1987]. If a window length of 16 km is chosen as a transformation cutoff, it will be able to provide the desired results for internal gravity waves and shorter wavelength inertia-gravity waves. For this reason, a window length of 24 measurements is used to transform the windowed data. This allows the transformation of a selected portion of the wave form with wavelength ranging from 1.36 km to 16.32 km. The wave forms outside the area that is selected will not be considered. Because the background field and the along-track filter, as discussed in section 4.1, will always be blocking undesirable planetary-scale wave modes to some extent, planetary-scale waves may still be able to remain in the perturbation profiles and will be represented as long wavelengths. These long wavelengths will be outside the FFT windowing area and thus be blocked. Therefore, the windowing function is another form of high-pass filtering.

The window with a length of 24 samples, extending upward from 121.15 hPa is slid up along the profile with a step of 1 sample until it extends down from 0.215 hPa. The results of the FFT yield the wavenumber spectrum of the windowed samples. The wavenumber spectrum can be analyzed for amplitudes and at the same time vertical wavelengths. However, both amplitudes and wavelengths cannot be estimated by simply picking up the peaks in the wavenumber spectrum because of the leakage problem that arises when applying a window to a data set, which is similar to the filtering function of the background field and the along-track filter. Leakage is related to not including an integer multiple of the period by a window function. The net effect

of leakage is a distortion of the spectrum. There is a spreading, or leakage, of the spectral components away from the correct wavenumber, resulting in an undesirable modification of the total spectrum.

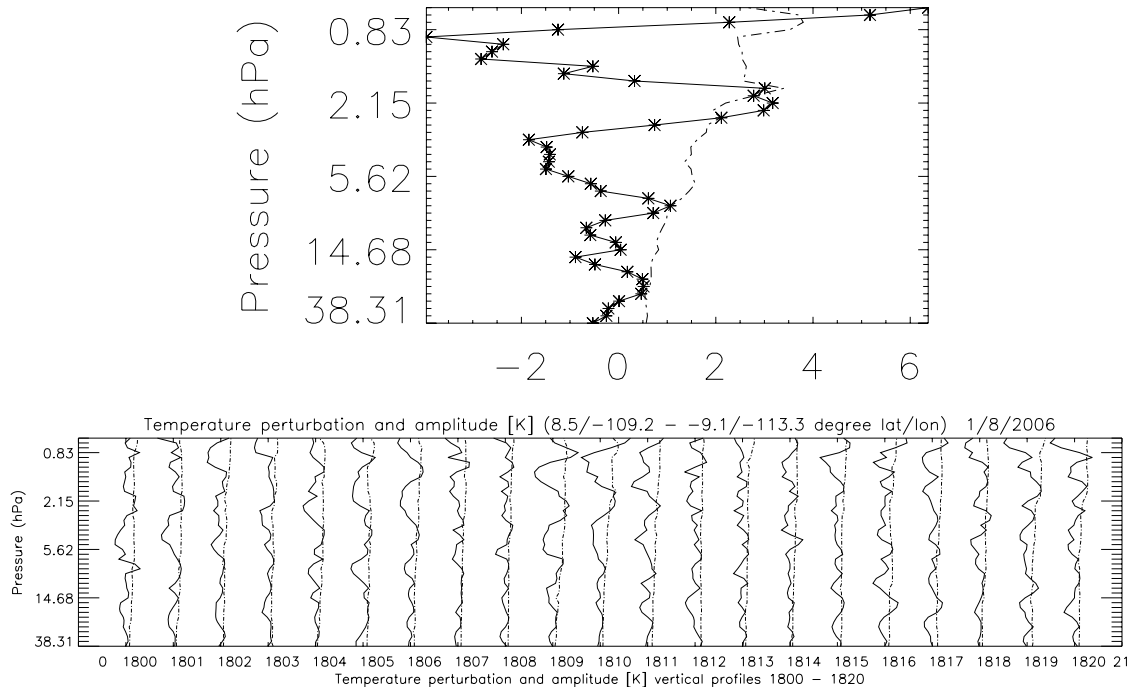


Figure 4.6 Top panel: a single vertical profile of gravity wave temperature perturbations (K) and the amplitude (K, defined in the text) of the gravity wave for the pressure levels between 38.31 hPa (~22 km) and 0.62 hPa (~52 km). Stars denote samples of gravity wave temperature perturbations, the solid line is an interpolation of the samples and the dot-dashed line is the amplitude of the profile. Bottom panel: in total, 21 along-track vertical profiles (solid lines, profile 1800 – 1820 on Aug 1<sup>st</sup> 2006) of gravity wave temperature perturbations and the amplitudes (dot-dashed lines) of the gravity waves for the same pressure range 38.31 to 0.62 hPa (~22 to 52 km).

Leakage is most severe when a simple rectangular window function is used. For a vertical temperature perturbation profile, for example, the profile shown in figure 4.6 (top panel), the chosen window length of 24 samples will not always include an integer multiple of the period in a data set and sidelobes could be found as a result of the windowing function. The approach here to reducing the leakage effect is sorting the local peaks of the wavenumber spectrum in descending order. The FFT of a windowed data set produced a series of local peaks in the wavenumber spectrum. If one treats a

wavenumber as  $x$  and a peak as  $y$ , it will be a series of discrete points  $(x_1, y_1), (x_2, y_2), \dots$ . The peaks  $(y_1, y_2, \dots)$  are sorted in descending order. The corresponding wavenumber spectral lines  $(x_1, x_2, \dots)$  are sorted simultaneously following the sorting of peaks  $(y_1, y_2, \dots)$ . The modified wavenumber spectrum is then analyzed for the amplitude of the wave form in the window by adding together the first three components. The corresponding vertical wavelength is estimated by selecting the first component which is the peak of the spectrum. The FFT of a windowed section of the profile yields amplitude and vertical wavelength as a function of height. The top panel of figure 4.6 gives a clear and detailed illustration of the amplitudes (dot-dashed line) of the single profile. The bottom panel of figure 4.6 shows the amplitudes (dot-dashed lines) of 21 along-track vertical profiles (profile 1800 to 1820 on August 1<sup>st</sup> 2006). The detailed single profile together with the 21 along-track profiles provides convincing evidence that the leakage effect is reduced and the selected window is able to produce the desired results.

In addition to leakage, aliasing and “picket-fence” effects could occur when applying a window to a data set. Since each vertical profile is a discrete data set, the computation of the spectrum is limited to integer multiples of the fundamental wavenumber, resulting in the inability of the FFT to observe the spectrum as a continuous function. This effect is termed the picket-fence effect. However, the instrument can observe the exact behavior only at discrete points, the major peak of a particular component could lie between two of the discrete transform lines, and the peak of this component might not be detected. Any combination of leakage, aliasing and the picket-fence effect can be present in the FFT of a windowed sample and result in subtle differences between amplitudes and wavelengths in terms of location.

### **4.3 Results and Discussion**

#### **4.3.1 Gravity Wave Temperature Amplitude and Vertical Wavelength**

Using the aforementioned data analysis method, the gravity wave temperature perturbations isolated from the HIRDLS temperature measurements (v2.04.09) were analyzed for the whole year of 2006, over pressure levels from 121.15 hPa ( $\sim 15$  km) to 0.215 hPa ( $\sim 60$  km). The mean of the amplitude and vertical wavelength were then calculated for each month in the year 2006. The monthly mean of the amplitude and

vertical wavelength for pressure levels 38.31 to 9.09 hPa ( $\sim 22 - 32$  km) are shown in figure 4.7 and figure 4.8 on a grid resolution of  $5^\circ \times 5^\circ$  latitude/longitude.

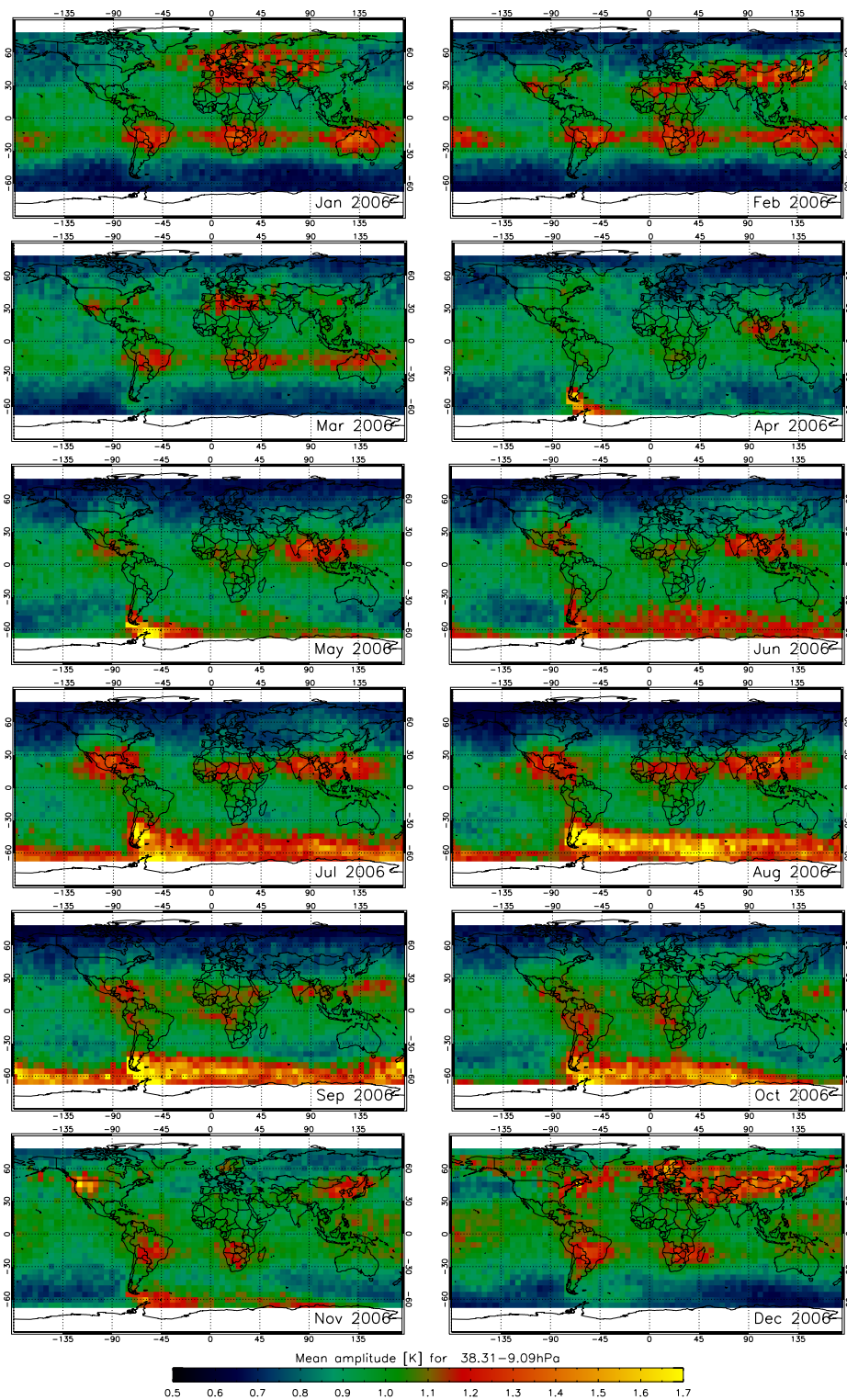


Figure 4.7 Monthly mean amplitudes for 2006 over pressure levels from 38.31 hPa to 9.09 hPa ( $\sim 22$  km to 32 km).

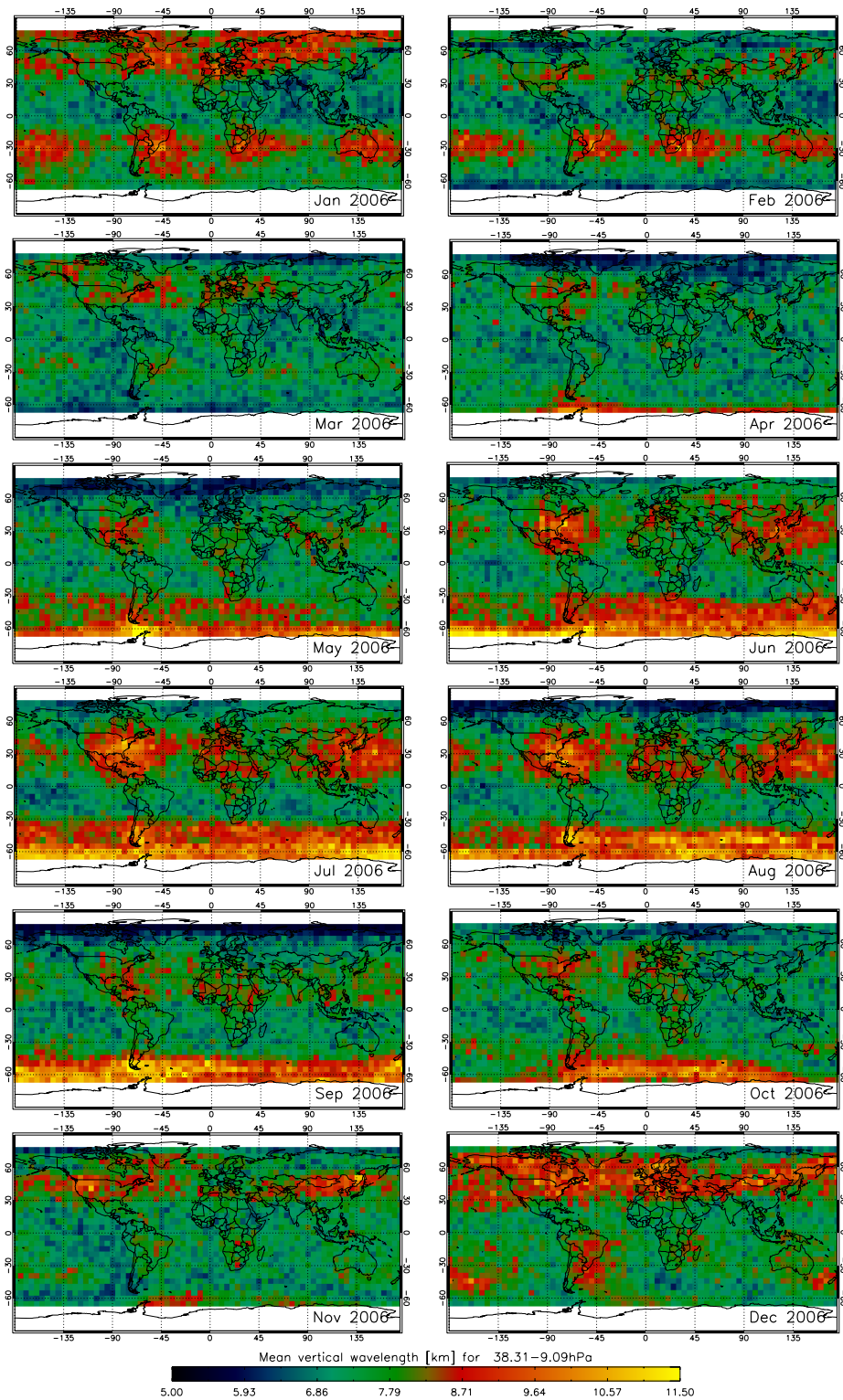


Figure 4.8 Monthly mean vertical wavelengths for 2006 over pressure levels from 38.31 hPa to 9.09 hPa (~ 22 km to 32 km).

The gravity wave activity patterns change with season and are asymmetric about the Equator. The amplitude patterns reasonably closely match the vertical wavelength patterns. The mean amplitudes in the altitude range are mainly within the range of 0.50 to 1.80 K. The mean vertical wavelengths are found mainly from 5 to 12 km. The observations show that gravity wave activity is strong in the winter extratropics and high latitudes and the summer tropics. Generally, the observed gravity waves in the extratropics and high latitudes in the south are much stronger compared with those in the north. In contrast to the extratropics and high latitudes, gravity waves in the summer tropics in both the north and south have comparable magnitude. Globally, the largest amplitudes are found over and around the southern Andes. The enhanced gravity wave activity observed in different seasons in the tropics and the extratropics and high latitudes indicates that the waves in the tropics and the extratropical and high-latitude zone are probably generated by different sources. Because there are a number of north-south mountain ranges and other types of orographic features in the extratropics and high latitudes (see orography of the Earth in figure 4.9) and winds in winter season are strong and often westerly, the gravity waves in the winter extratropics and high latitudes are understood to be generated mainly by flow over orography [Eckermann and Preusse, 1999; Jiang et al., 2002, 2004a; Eckermann et al., 2006; Alexander and Teitelbaum, 2007].

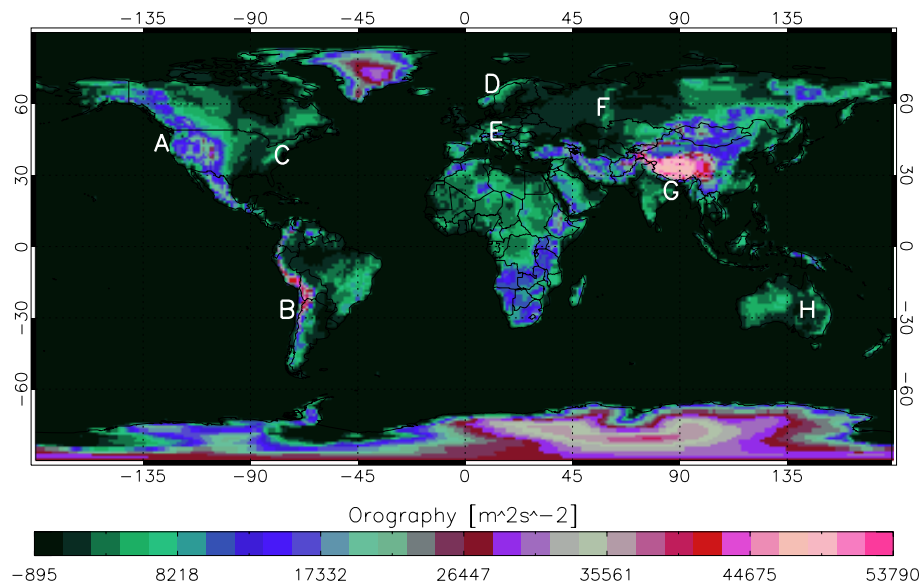


Figure 4.9 The orography of the Earth. Some of the major mountain ranges are labelled with letters on the orography map, which are the North American Cordillera (A), Andes (B), Appalachians (C), Caledonian Belt (D), Alps (E), Urals (F), Himalaya (G), and Tasman Belt (H).

The amplitudes of orographically generated gravity waves are proportional to the amplitudes of the wave-generating orographic obstacles [Nappo, 2002]. The orography map in figure 4.9 shows that in the southern hemisphere, the highest Andes mountain range outside Asia runs from north to south along the western coast of South America acting as a long mountain barrier. This is favorable for orographic gravity wave generation when winter winds are strong and westerly. In the northern hemisphere, the Himalayas, the highest mountains in the world, together with other high mountains standing on the north and north-east of the Himalayas forming a large massif, the Tibet (Qinghai-Xizang) plateau in the central Asia (see figure 4.10). However, the majority of the mountain groups are nearly east-west-orientated, which is not favorable for exciting orographic gravity waves with respect to the westerly winter winds. This implies that the massif of the Tibet plateau is a minor but the Andes are a major wave-generating orographic obstacle, which is probably the reason for the larger gravity wave temperature amplitudes in the southern extratropics and high latitudes than those in the northern extratropics and high latitudes.

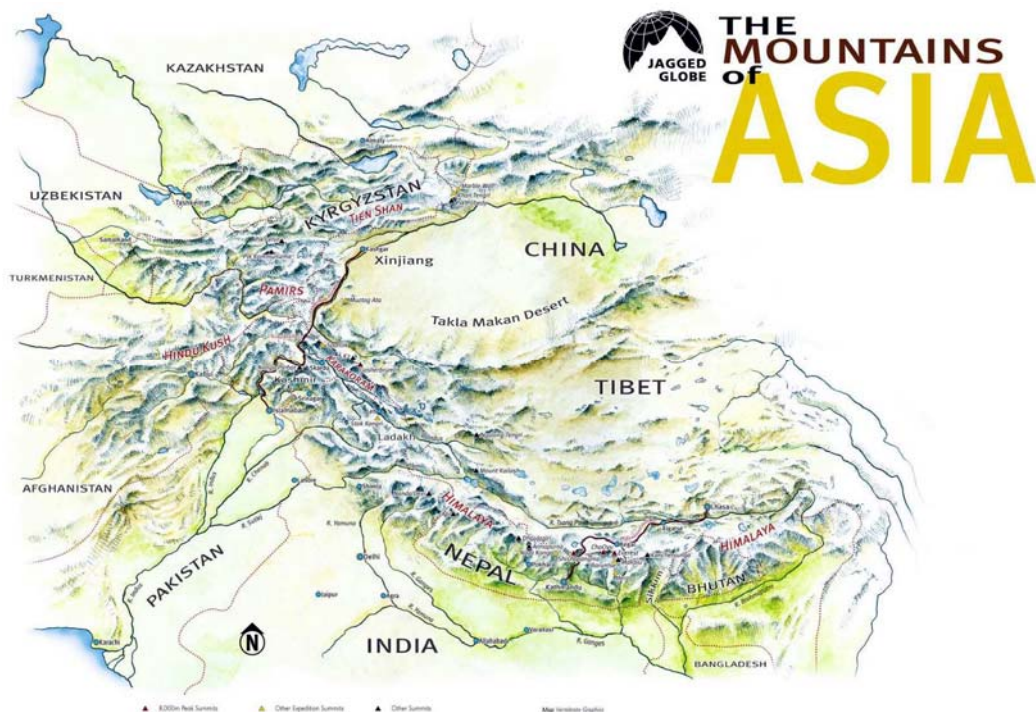


Figure 4.10 Mountains of central Asia.

As mentioned in chapter 3, the plastic film blocking the aperture vibrates with movement of the scan mirror resulting in a small oscillation in the radiometric signal. The oscillation could be a potential problem for gravity wave observations. The HIRDLS science team has developed algorithms to remove the oscillation from the radiometric signals and the temperature data has been extensively validated [Gille *et al.*, 2008]. The oscillation is systematically excited in a repeatable way around the orbit resulting in the regularity of the oscillation in the radiometric signal and thus in the temperature. By searching systematically repeatable signals it will be possible to examine if there is blockage caused oscillation still in the temperature. The wave patterns in figure 4.7 and figure 4.8 show clearly seasonal and topographical dependence. In other words, the waves are not systematically and uniformly distributed over the whole globe. The observed mean wavelengths 5 to 12 km are mainly in the wavelength domain of gravity waves (typically a few kilometres to  $\sim 15$  kilometres for internal gravity waves and up to a few tens of kilometres for inertia-gravity waves [Andrews *et al.* 1987]). This is strong evidence that the observed patterns are due to gravity wave activities and not the plastic film oscillations.

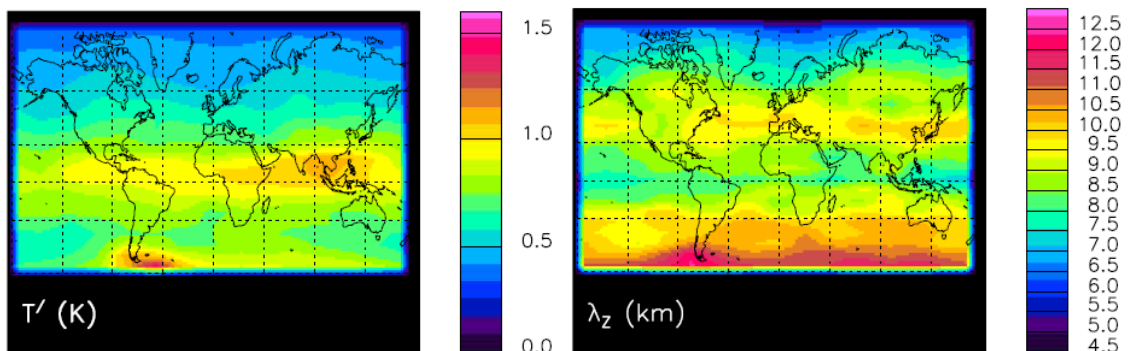


Figure 4.11 Maps of gravity wave temperature amplitude (left) and vertical wavelength (right) derived by Alexander *et al.* [2008a] from HIRDLS averaged over 30 days in May 2006 and over the height range 20 – 30 km [a copy from Alexander *et al.*, 2008a].

The mean amplitudes for May 2006 in figure 4.7 were compared with the study of Alexander *et al.* [2008a] for the same month and year (left panel in figure 4.11). Comparisons show similar patterns but generally approximately 0.3 K larger amplitudes in figure 4.7. This is probably the result of a slight increase of the amplitudes shown in figure 4.7 over the altitude range 22 to 32 km compared with Alexander *et al.*'s mean amplitudes over the altitude range 20 to 30 km. The mean vertical wavelengths for May

in figure 4.8 were also compared with Alexander et al.'s observations (right panel in figure 4.11). The vertical wavelength patterns are generally similar but their observations show about 1 km longer wavelengths over northern tropics and most southern extratropics and very likely extending over high latitudes in the south. This could be due to the different techniques used in the data analysis.

Monthly mean amplitudes of January and July 2006 in figure 4.7 were compared with gravity wave radiance variances of January and July 2005 from the Microwave Limb Sounder (MLS) on Aura [*Wu and Eckermann, 2008*]. Note, the comparison can only be carried out qualitatively and specifically in terms of geographical location. This is because what Wu and Eckermann observed is the gravity wave induced radiance perturbations which are unlike the gravity wave temperature perturbations that are discussed in this thesis. Wu and Eckermann plotted monthly mean gravity wave radiance variances at 21.7, 23.0, 25.6, 31.9, 37.0 and 44.1 km, respectively. The plots in figure 4.7 show the monthly mean temperature amplitudes that were calculated over the pressure altitude range ~22 km to 32 km, so that HIRDLS observations will only be compared with the MLS gravity wave radiance variances at altitudes between 21.7 km and 31.9 km.

The comparison for January (see figure 4.12) found that enhanced gravity wave variances from MLS cover almost the whole tropics both in the south and north at 21.7 km and 23 km. While the HIRDLS gravity waves in the tropics in figure 4.7 are mainly limited to the summer tropics. The enhanced gravity waves over the tropics in MLS were investigated by Wu and Eckermann for convective gravity waves using MLS ice water content (IWC) as an indicator of deep convection [*Wu et al., 2006*]. However, their gravity wave variances cover too large an area of the tropics to show a strong correlation between the gravity wave variances and the IWC. The mainly summer-tropics limited HIRDLS gravity waves in January 2006 are more consistent with their IWC. In the northern extratropics and high latitudes, the enhanced gravity waves from HIRDLS and MLS are obviously different in terms of geographical location. It is known that gravity waves in the winter extratropics and high latitudes are mostly generated by flow over orographic features such as mountains [*Eckermann and Preusse, 1999; Jiang et al., 2002, 2004a; Eckermann et al., 2006; Alexander and Teitelbaum, 2007*]. Any change with wind strength or direction will change the generation of gravity

waves. Therefore, the obvious difference in the winter extratropics and high latitudes could be due to different wind conditions in different years. Comparison with MLS over the same period for 2005 could be future work for investigating the inter-annual differences.

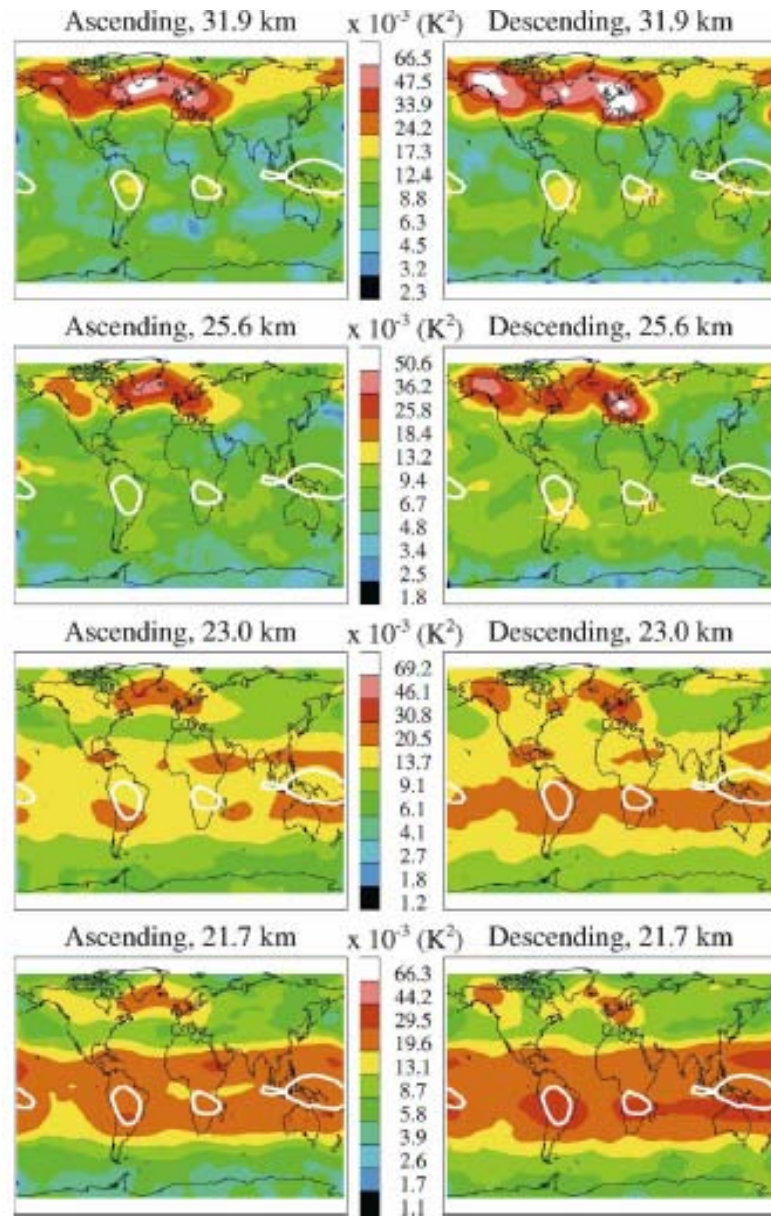


Figure 4.12 MLS gravity wave variance maps for January 2005 by Wu and Eckermann, showing ascending (left) and descending (right). The white contours are 5  $\text{mg/m}^3$  of MLS IWC as an indicator of deep convective forcing [a copy from *Wu and Eckermann, 2008*].

Similar to the comparison for the tropical gravity waves in January, comparison between HIRDLS observations in July 2006 and MLS observations in July 2005 (see figure 4.13) found that MLS gravity waves in the summer tropics greatly extended to the opposite winter tropics, but they become comparable to the observed gravity waves from HIRDLS at higher altitudes 25.6 km and 31.9 km. In the extratropics and high latitudes, gravity waves from both HIRDLS and MLS are similarly distributed with the largest values over the southern Andes.

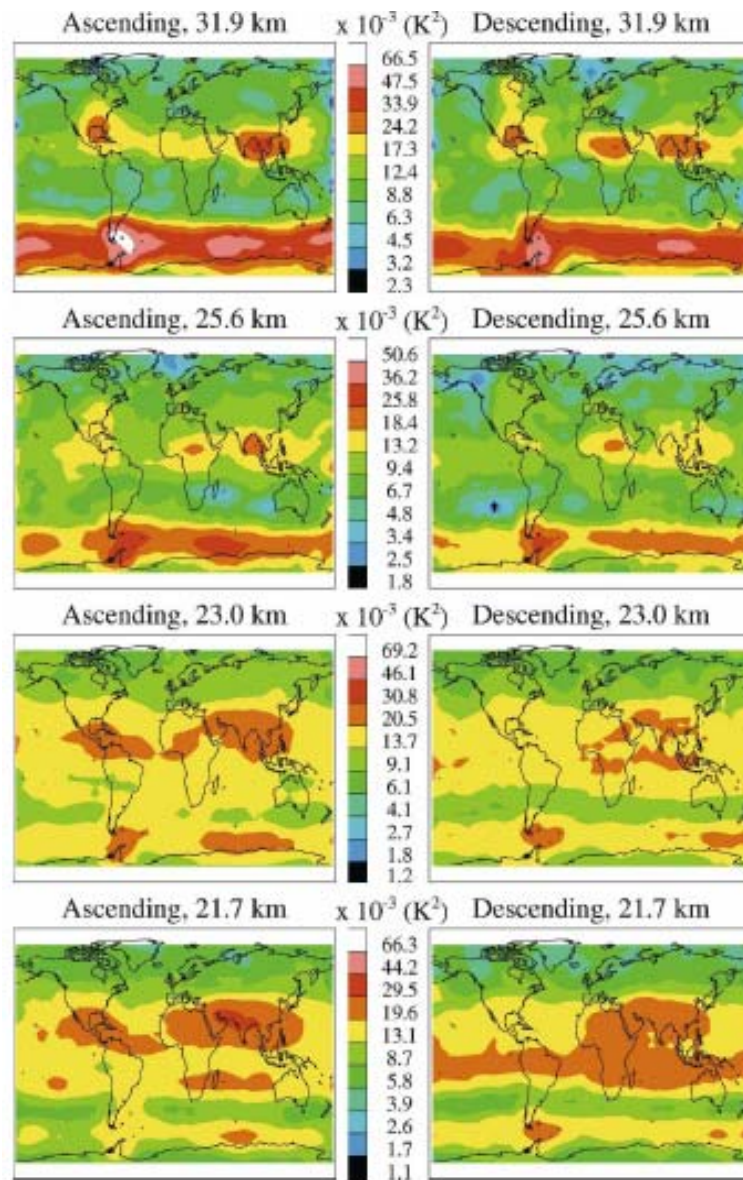


Figure 4.13 As in figure 4.12 but for July 2005 [a copy from *Wu and Eckermann, 2008*].

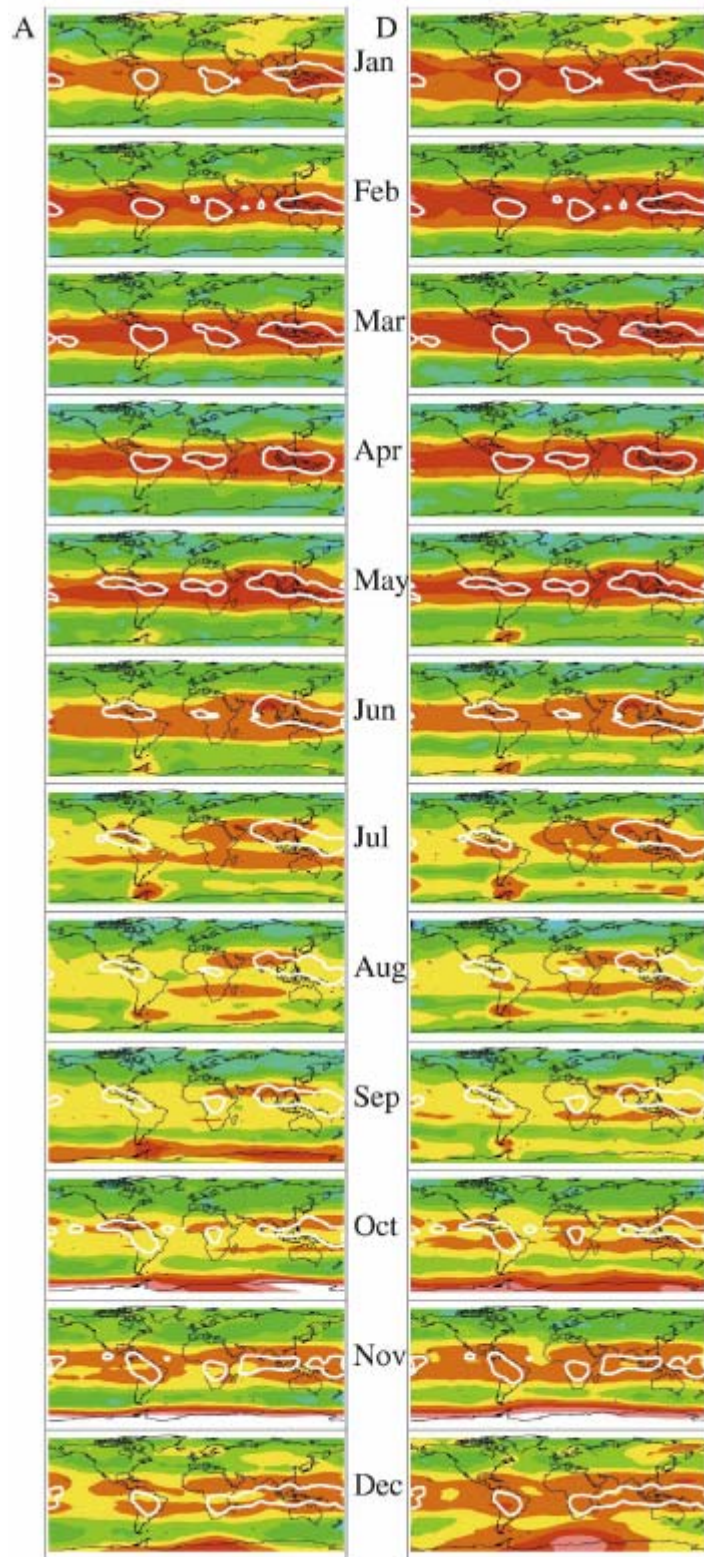


Figure 4.14 Monthly maps of ascending (A) and descending (D) gravity wave variances at  $\sim 21.7$  km pressure altitude for 2006 by Wu and Eckermann. The color scales, ranges and contours have their same values and meaning as the 21.7 km altitude panels in figures 4.12-13 [a copy from *Wu and Eckermann, 2008*].

The comparison with MLS gravity wave observations is extended into 2006 for seasonal variations. The monthly mean temperature amplitudes over pressure altitudes ~22 to 32 km in figure 4.7 were compared with the monthly mean gravity wave radiance variances at 21.7 km from MLS (figure 4.14). Considering that gravity wave amplitudes grow with altitude, the amplitudes in figure 4.7 (over pressure altitude range 22 – 32 km) are expected to have larger scales than the MLS variances at 21.7 km. However, comparison shows the converse. The enhanced gravity wave variances from MLS are found over almost the whole tropical belt in the first half year of 2006. It seems that these MLS-derived gravity waves do not follow the movement of the convective activity represented by the IWC and do not show any seasonal variation in these six months. In the second half of 2006, the MLS gravity wave variances are found over both the southern and northern tropics and split into two latitudinal bands. Similar to the first half of the year, the waves in these two latitudinal bands in the second half of the year do not really follow the movement of the IWC and do not show apparent seasonal variation. By contrast, the observed gravity waves in the tropics in figure 4.7 show clearly seasonal variation, moving from the southern tropics to the northern tropics and then back to the southern tropics at the end of the year with the summer season moving from the south to the north and then back again. In contrast with the MLS gravity waves, the movement of the observed gravity waves from HIRDLS (figure 4.7) perfectly matches the movement of the convective activity represented by IWC. The time series of monthly zonal mean of MLS gravity wave variances shows clearly decreasing amplitudes from 21.7 to 27.3 km and large-scale annual variation rather than seasonal variation in the altitude range. This indicates that these MLS waves may contain significant contributions from other classes of waves. For the extratropics and high altitudes, sometimes gravity waves shown in figure 4.7 in the winter hemisphere are missing in the MLS monthly mean variance plots, such as the enhanced gravity wave amplitudes over northern America in February, March, November and December 2006 in figure 4.7. However, sometimes significant large-scale waves at summer high latitudes that were not observed from HIRDLS are present in the MLS monthly mean plots, for example the large-scale waves at southern high latitudes in December. Observations from both HIRDLS and MLS show similar wave activity over the southern Andes in May, July and August, but HIRDLS observations show the biggest temperature amplitudes over the southern Andes.

Monthly zonal means of gravity wave temperature amplitudes and vertical wavelengths for pressure range 38.31 hPa (~ 22 km) to 0.62 hPa (~ 52 km) are shown in figures 4.15 and 4.16. An important property of gravity waves is that amplitudes exponentially increase with altitude before they saturate or approach the critical level. In the atmosphere, gravity waves are often observed increasing but rarely exponentially increasing with altitude due to complex interactions with the background winds and large-scale oscillations. It is apparent that the zonal mean temperature amplitudes in figure 4.15 increase with altitude in the stratosphere. The amplitude increases in the summer tropics and winter extratropics are significantly different. Except for January and February, the amplitude increases in the winter extratropics are clearly larger than those in the summer tropics. Large amplitudes in the winter extratropics extend poleward. From January to December, the large amplitudes in the tropics move from the south to the north and then back to the south, following the change of summer season. The opposite is observed for the gravity waves in the winter extratropics and high latitudes.

The zonal mean amplitudes for May 2006 were compared with the study of *Alexander et al.* [2008a] for the same month (see left panel in figure 4.17). Comparisons show similar patterns, especially in the winter extratropics and the summer tropics and minimum values very close to each other in the lower stratosphere. However, the observations in May in figure 4.15 found that gravity waves grow more rapidly into the upper stratosphere than their observations. The differences in growth with height are possibly related to different techniques used in the method discussed in this thesis and that of *Alexander et al.* [2008a]. Similar patterns are found qualitatively comparing the zonal mean amplitudes with gravity wave temperature variances from Aura MLS for July 2005 [*Wu and Eckermann, 2008*] in the upper stratosphere, and observations from CRISTA and SABER (Sounding of the Atmosphere using Broadband Emission Radiometry) for August 1997 and 2003 [*Preusse et al., 2006*], except for the differences between MLS observations in January 2005 and HIRDLS observations in January 2006 as noted early in this section.

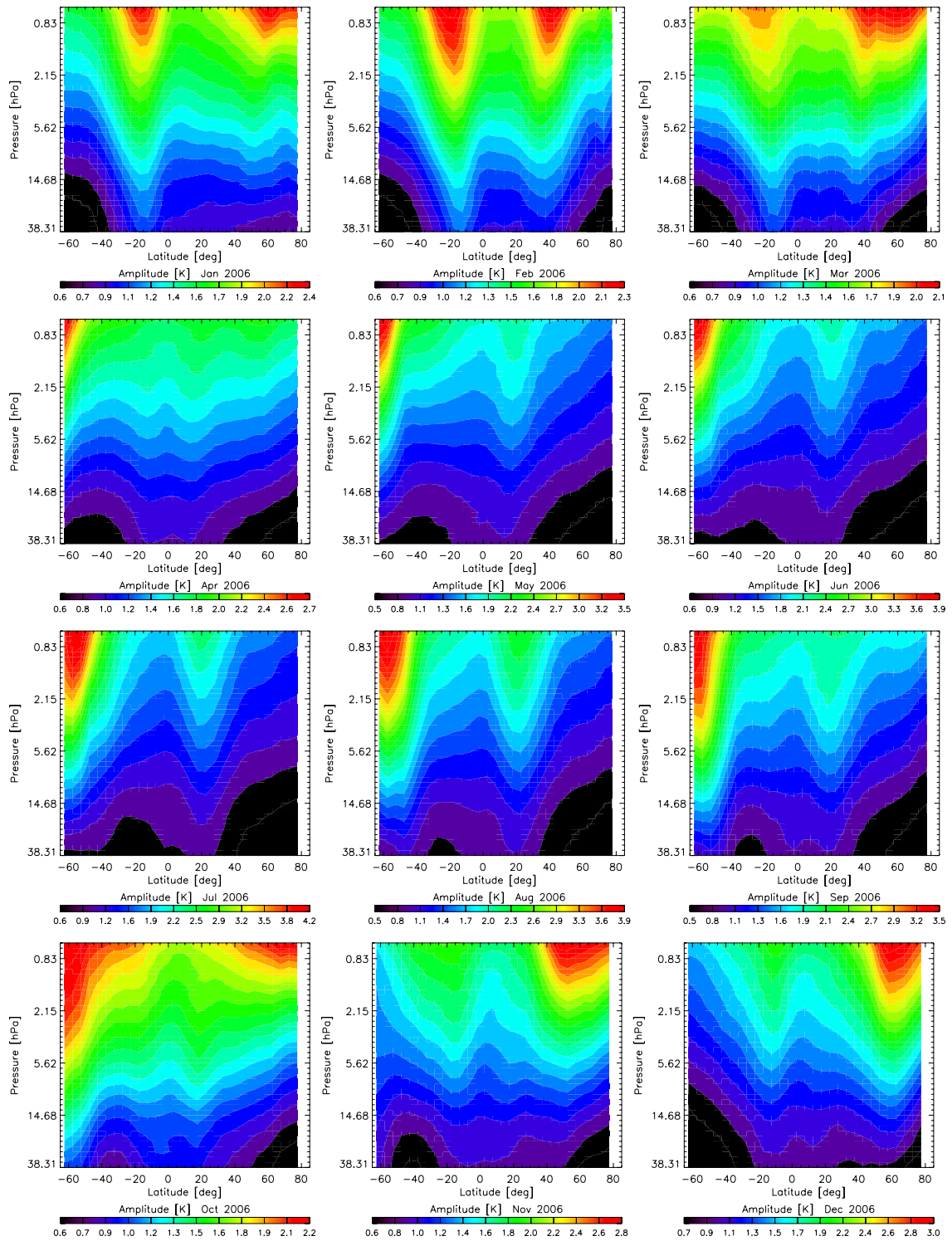


Figure 4.15 Monthly zonal means of temperature amplitudes as a function of latitude and pressure for 2006.

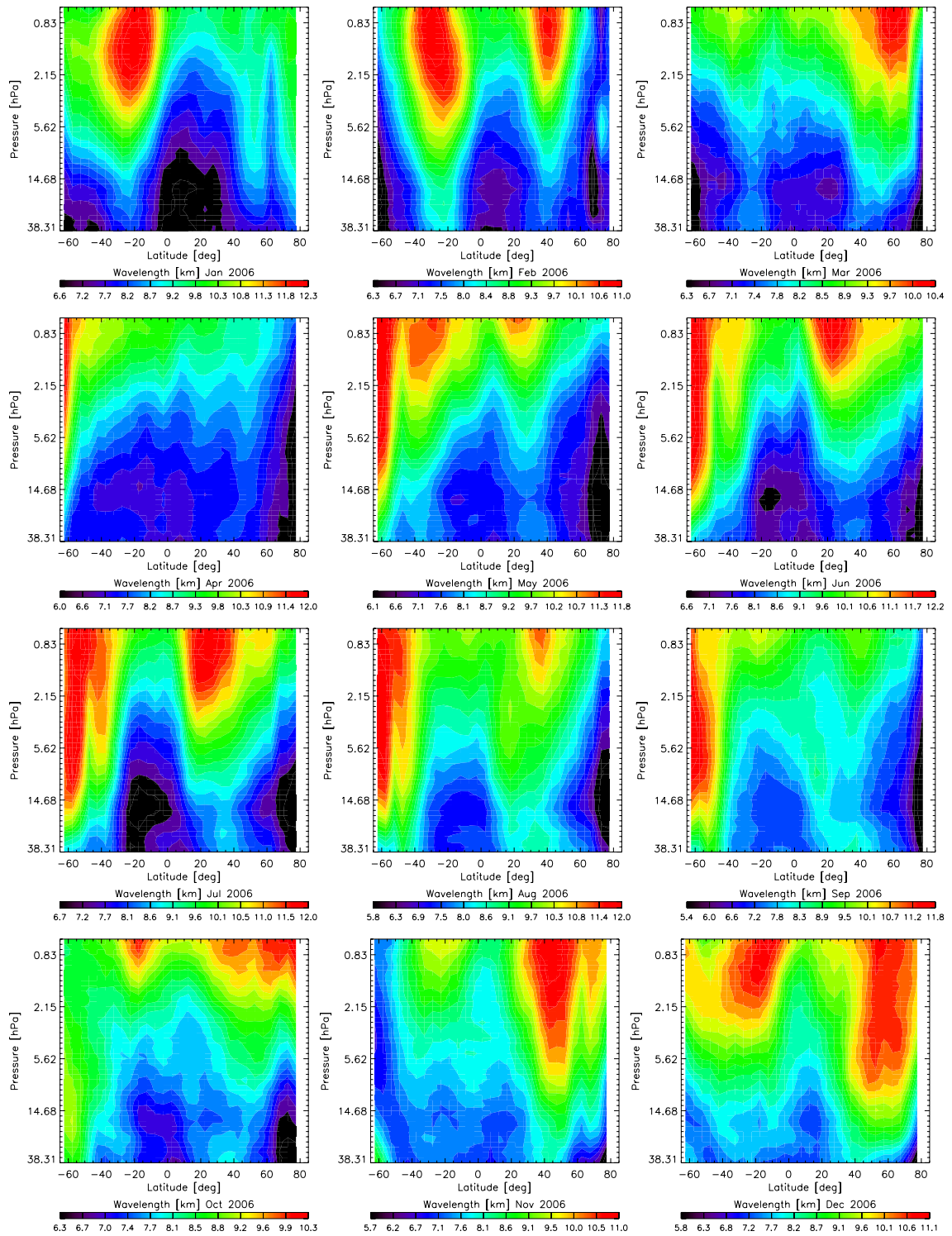


Figure 4.16 Monthly zonal means of vertical wavelengths as a function of latitude and pressure for 2006.

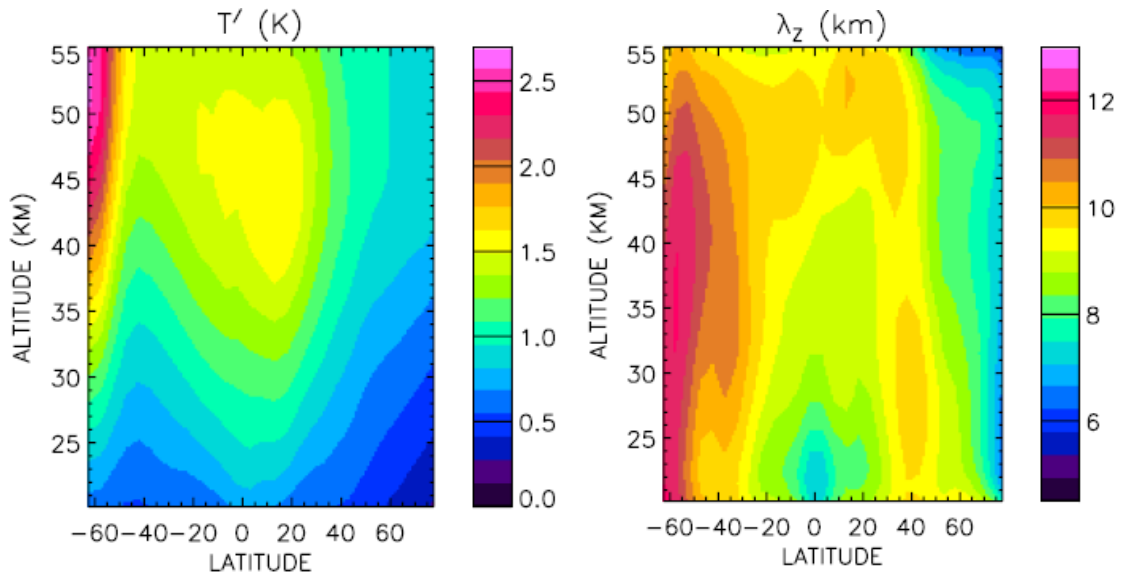


Figure 4.17 Zonal means of gravity wave temperature amplitude (left panel) and vertical wavelength (right panel) as a function of latitude and altitude averaged over the month May 2006 by Alexander et al. [a copy from *Alexander et al.*, 2008a]

The zonal mean vertical wavelengths in figure 4.16 vary from latitude zone to latitude zone and month to month. The peak wavelengths correspond closely to the zonal mean peak amplitudes. The plots show rapidly growing vertical wavelengths corresponding to strong gravity wave activity in the winter extratropics and high latitudes in all months except October. The vertical wavelengths in the summer tropics and subtropics slowly steadily grow with altitude in the stratosphere. The vertical wavelengths that are in the latitude zone  $\sim 62^{\circ}\text{S} - 50^{\circ}\text{S}$  in October and often in the winter extratropical and high-latitude middle and upper stratosphere in other months are nearly constant. Both the amplitudes (figure 4.15) and wavelengths (figure 4.16) in the summer tropics often show clear increases from higher altitude than those in the winter extratropics and high latitudes. This suggests that the source regions in the tropics are higher than those in the extratropics and high latitudes. The comparisons with MLS IWC for the summer tropical gravity waves support higher convective source regions in the tropics. This is also consistent with the investigations on convective gravity waves in the tropics by *McLandress et al.* [2000], *Jiang et al.* [2004b; 2005], *Ratnam et al.* [2004], *Alexander et al.* [2004] and *Tsuda et al.* [2004]. The suggestion of lower source regions in the extratropics and high latitudes is consistent with the studies of orographic gravity waves in these latitude zones by *Eckermann and Preusse* [1999], *Jiang et al.* [2002; 2004a], *Eckermann et al.* [2006] and *Alexander and Teitelbaum* [2007].

Comparisons with the study of *Alexander et al.* [2008a] for May 2006 (see right panel in figure 4.17) show that the vertical wavelengths in figure 4.16 are generally shorter than their vertical wavelengths by  $\sim 1$  km between 22 and 45 km. It is likely due to different techniques used in the data analysis procedures.

#### **4.3.2 Case Studies: Wave Events over the Southern Andes, the Cascade Range and the Rockies and the Himalayas**

In order to improve the understanding of mainly orographic gravity waves observed in the winter extratropics, the orography of the Earth, shown in figure 4.9, was generated using the European Centre for Medium-Range Weather Forecasts (ECMWF) orography data set (version of 1999). The major mountain ranges are labelled with letters and the orography is represented by the surface geopotential ( $\text{m}^2/\text{s}^2$ ). The map is used here to examine the link between orography and gravity waves. It is found that most gravity wave activity in the winter extratropics in figure 4.7 is strongly related to the major north-south or nearly north-south mountain ranges presented in the orography map in figure 4.9. For example, strong orographic gravity waves are found in July, August and September 2006 over the southern Andes and enhanced gravity wave activities are observed in February and November 2006 over the North American Cordillera.

When a day contains mean gravity wave temperature amplitudes over the pressure range 38.31 to 10.00 hPa greater than 1.5 K, the day is termed a strong-wave day. Orographic gravity waves over the southern Andes were investigated for strong-wave days 6 – 8 July, 22 – 24 July and 7 – 9 August 2006 using the ECMWF operational high resolution wind data. Gravity waves of the strong-wave days represented by the mean amplitudes over pressure levels 38.31 to 10.00 hPa ( $\sim 22 - 32$  km) and mean ECMWF horizontal wind vectors of the strong-wave days for pressure levels at 670, 443 and 256 hPa ( $\sim 3, 6$  and 10 km) are presented in figure 4.18. The mean horizontal winds change gradually with altitude in the troposphere and stratosphere. Therefore, winds at only three pressure levels are selected according to the average height of the mountains. Winds at 670 hPa are used to study the generation of the observed gravity waves. Winds at 443 and 256 hPa are used to investigate the relationship between the winds and the propagation of the observed gravity waves. The winds in the stratosphere were found to be not significantly relevant and therefore are not presented in figure 4.18.

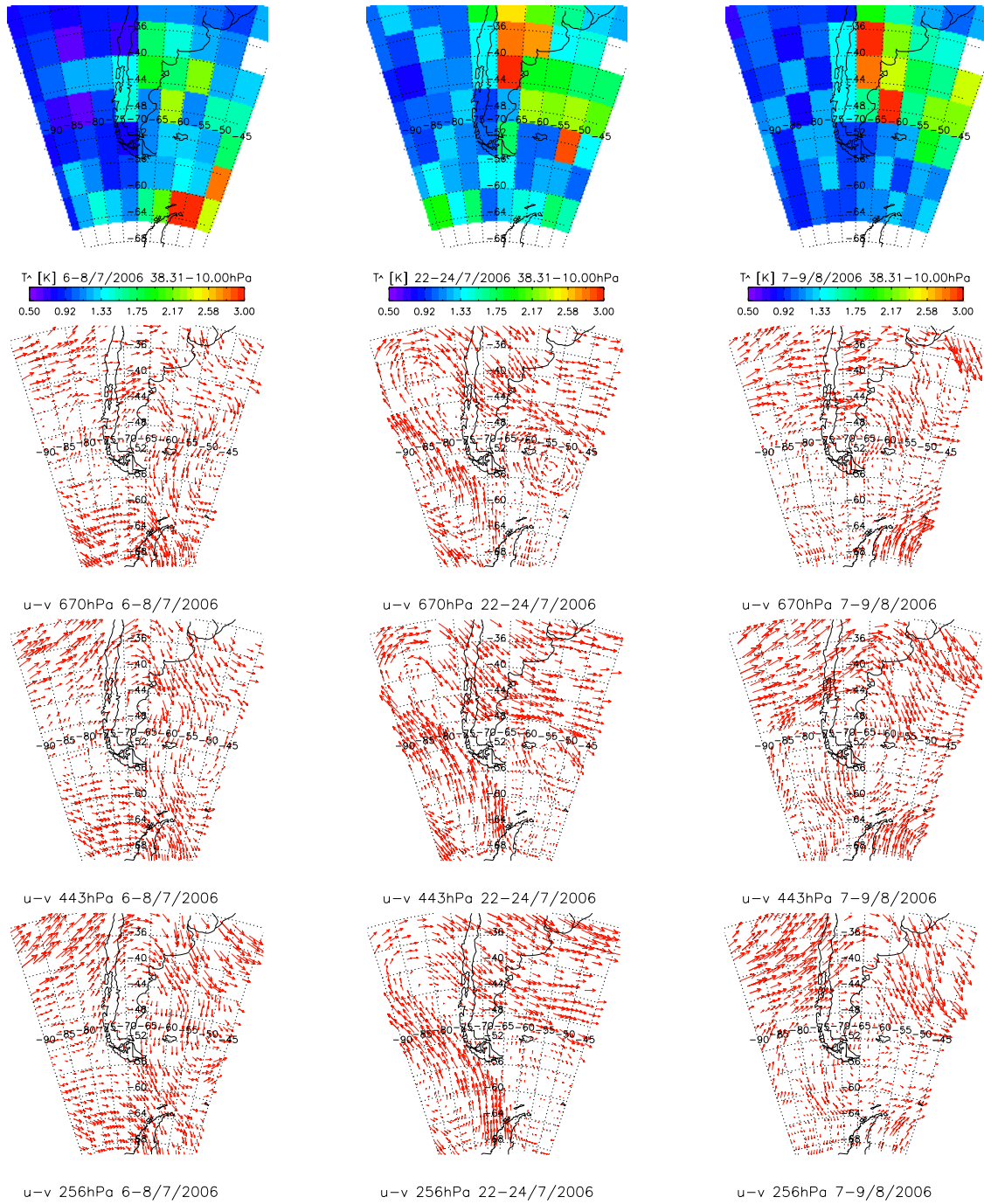


Figure 4.18 Orographic gravity waves and ECMWF horizontal wind vectors over the southern Andes within time periods of 6 to 8 July, 22 to 24 July and 7 to 9 August 2006. The gravity waves are represented by the mean amplitudes over the pressure range 38.31 – 10.00 hPa. The wind vectors are averaged over the three-day period for every pressure level.

The wind direction and strength at 670 hPa indicate that gravity waves are observed, when and where strong winds flow perpendicularly (6 -8 July and 7 – 9 August) or near perpendicularly (22 – 24 July) with respect to the southern Andes. There are no orographic gravity waves generated by the winds parallel to the Andes in a northerly direction. However, amplitude plots show that the observed orographic gravity waves were not propagating vertically exactly over the mountains. Refracted peak amplitudes to the east and a wave tail to the south-east with eastward/south-eastward winds were observed in the strong-wave days in these two months. In the strong-wave period of 6 - 8 July 2006, in addition to the orographic gravity waves over the Andes, strong gravity waves were also observed over the Antarctic Peninsula. The wind maps show strengthened perpendicular flow to the Antarctic Peninsula by winds flowing from the Andes to the Antarctic Peninsula. This indicates that the gravity waves over the Antarctic Peninsula are very likely the combination of the gravity waves generated due to the flow over the Peninsula and the gravity waves generated over the Andes and propagated with winds to the Antarctic Peninsula. The situation for the Antarctic Peninsula is different in the period of 7 – 9 August 2006 when the north-eastward winds were parallel to the Peninsula and the winds from the Andes did not flow over the Antarctic Peninsula. In the strong-wave period of 22 – 24 July 2006, enhanced amplitudes were observed where a cyclone was developed in the wind maps. It is likely that these waves were generated by the storm directly and also enhanced by the interaction of the south-eastward propagating gravity waves with the winds and the cyclone. *Preusse et al.* [2006] observed gravity waves over a large area in the winter hemisphere in August 1997 and 2003 using CRISTA and SABER (see figure 4.19). These waves were explained by Preusse et al. as a result of stratospheric jets associated with the winter polar vortex, that are very different from the clearly orography-generated eastward gravity waves over the southern Andes in August 2006 in figure 4.18.

Similarly to the case of the southern Andes, orographic gravity waves over the south-north running mountains, the Cascade Range and the Rockies in the strong-wave days 13 – 17 November 2006 were observed when the winter winds over northern America were strong and eastward or slightly north-eastward (figure 4.20). These orographic gravity waves were also refracted towards the east from the Cascade Range and the Rockies following the wind direction.

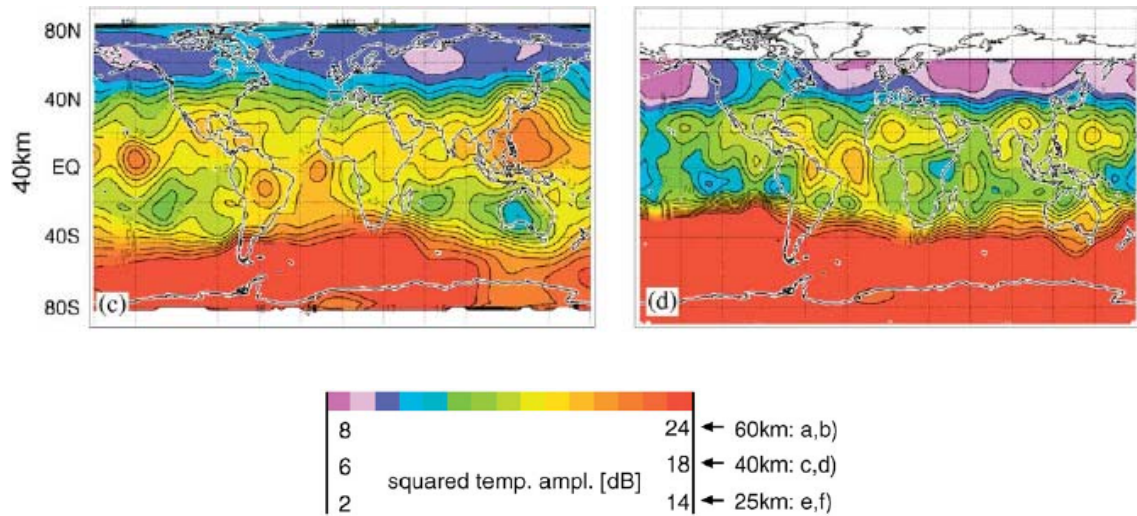


Figure 4.19 Maps of gravity wave-squared temperature amplitude in dB derived from CRISTA (c: 8 – 15 Aug 1997) and SABER (d: 7 – 10 Aug 2003) at 40 km by Preusse et al. [a copy from *Preusse et al.*, 2006].

Additionally, cyclone-associated gravity waves were studied over and near the Himalayas within the strong-wave days 1 – 4 and 17 – 20 August 2006 (figure 4.20). The plots of ECMWF winds at 670 hPa for both strong-wave periods show that the winds are weak and parallel to the mountain ridge. The winds of 1 - 4 August at higher pressure levels became perpendicular to the mountains, but these high-altitude winds compared with the mountain height are not able to generate orographic gravity waves. The observed gravity waves are not exactly over the Himalayas but slightly to the south and east. These waves are weaker than the orographic gravity waves observed over the southern Andes, the Cascade and the Rockies. They are clearly associated with the cyclones on the ECMWF wind maps in this region and slightly refracted following the wind paths. This suggests that the observed enhanced gravity waves in the summer months in the region of the Himalayas are probably excited by convection activities. Further investigation is necessary for better understanding of these non-orographic waves.

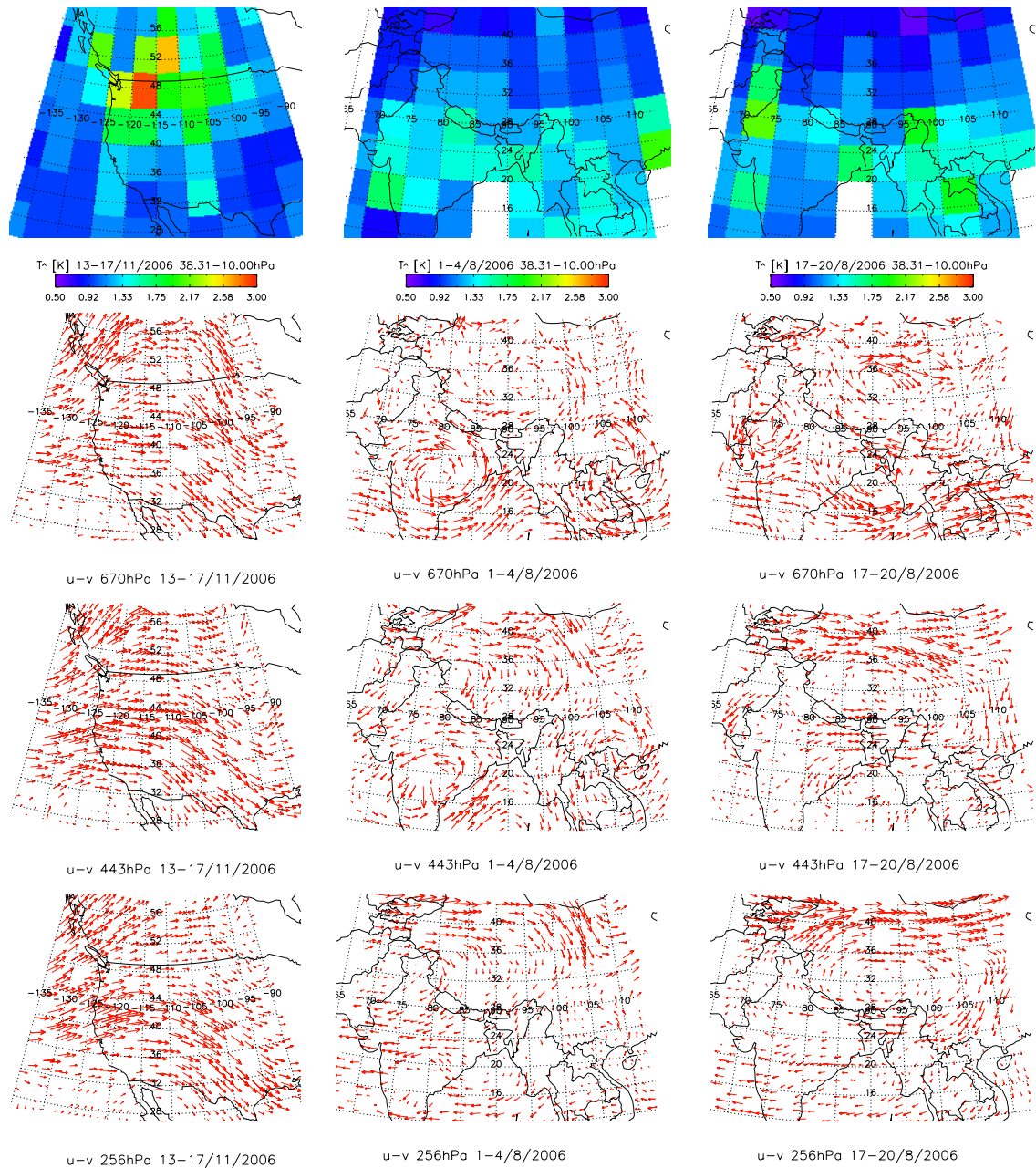


Figure 4.20 Orographic gravity waves and ECMWF horizontal wind vectors over the North American Cordillera (the Cascade Range and the Rockies) within the time period of 13 to 17 November 2006, and gravity waves and ECMWF horizontal wind vectors over the Himalayas within the time periods of 1 to 4 August, and 17 to 20 August 2006. The gravity waves are represented by the mean amplitudes over the pressure range 38.31 – 10.00 hPa. The wind vectors are averaged over the time period for every pressure level.

## 4.4 Summary

Atmospheric gravity waves were extracted from HIRDLS temperature measurements (version 2.04.09) using a new approach. Gravity wave properties such as horizontal amplitude and vertical wavelength were estimated by performing an FFT on each individual gravity wave temperature perturbation profile for pressures from 121.15 hPa (~ 15 km) to 0.215 hPa (~ 60 km). The monthly mean amplitudes and vertical wavelengths were studied for global distribution, seasonal variations and sources of gravity waves. The studies show that the observed wave activity is highly variable spatially with a pronounced seasonal dependence. Both global maps of mean amplitude and zonal mean plots show strong gravity wave activity in the winter extratropical and high-latitude stratosphere and the summer tropical stratosphere. Some extratropical gravity wave activity is highly related to the major north-south or near north-south mountain ranges of the Earth. The investigation into gravity wave activity in the winter extratropics indicates that orography is an important source of the gravity waves observed in the extratropical stratosphere.

The monthly zonal mean plots show that the peak wavelengths correspond closely with the peak amplitudes. In most months, the increased growth rates of amplitude with altitude in the winter extratropical stratosphere are significantly larger than those in the tropical stratosphere. Correspondingly, the wavelengths in the winter extratropical stratosphere grow faster than the wavelengths in the tropical stratosphere. Lower altitude sources in the extratropics and high latitudes and higher altitude sources in the tropics are reflected in both the zonal mean amplitudes and vertical wavelengths. Maps and zonal mean plots of temperature amplitudes and vertical wavelengths show gravity wave characteristics that are in good agreement with gravity wave theories.

Except for good agreement for the southern Andes and some areas in winter extratropics and high latitudes, the comparisons with the observations from MLS [*Wu and Eckermann, 2008*] show noticeable differences in the tropics. The differences were investigated by comparison with the convective activity represented by the MLS IWC used by *Wu and Eckermann* [2008] for their MLS gravity wave studies. The comparison shows that the tropical gravity waves in figure 4.7 are better matching the seasonal variation of convective activity than those of MLS. In general, the observed HIRDLS

gravity waves are in good agreement with the observations by *Alexander et al.* [2008a] and from the satellite instruments CRISTA and SABER [*Preusse et al.*, 2006]. The differences in detail with those from the same HIRDLS instrument, but different techniques [*Alexander et al.*, 2008a] and from other satellite instruments, for example MLS [*Wu and Eckermann*, 2008] and CRISTA and SABER [*Preusse et al.*, 2006] indicate that gravity wave observations depend on the method adopted. The meaningful annual cycle of gravity waves in the monthly means has demonstrated the strength of the methodology described in this thesis. The systematic and regular oscillation in the HIRDLS radiometric signal that is caused by the motion of the blockage has been removed by the HIRDLS team by developing extra algorithms. The retrieved temperature has been extensively validated by the HIRDLS science team. The observed gravity waves in HIRDLS temperature do not show any obvious signals of the oscillation.

Investigations of strong-wave days on orographic gravity waves over the southern Andes for July and August 2006 found that orographic gravity waves generated due to the intense wintertime winds flowing perpendicularly to the mountain ridge are refracted and propagate following the direction of the winds. Many gravity wave parameterization schemes assume vertical propagation [*Palmer et al.*, 1986; *McFarlane*, 1987; *Iwasaki et al.*, 1989] but the observations indicate significant refraction of the wave path following the winds. Observations of the gravity waves over the Cascade Range and the Rockies found similar responses of the intense perpendicular wintertime winds to the north-south mountain ranges. This indicates that the observed gravity waves over the southern Andes, the Cascade Range and the Rockies are all excited by the wintertime flow influenced by orography. The gravity waves over the Himalayas are summertime cyclone associated waves. This suggests that the observed gravity waves in this region are convectively generated gravity waves. In order to deeply understand these sources, further investigation was carried out and will be discussed in the following two chapters for orographic gravity waves over the southern Andes and convective gravity waves in the stratospheric tropics, particularly in tropical South America.

## Chapter 5

# Gravity Waves over the Southern Andes: a Comparison with Predictions from an Orographic Gravity-Wave Parameterization Scheme

Gravity waves are widely recognised as an important driver of atmospheric circulations and affect atmospheric thermal structures [Lindzen, 1981; Holton, 1982; Fritts and Alexander, 2003]. It is believed that orographic gravity waves likely account for a large fraction of zonally averaged wave-induced force in the mesosphere [Bacmeister, 1993]. At high latitudes in the northern hemisphere, orographic gravity waves affect the PSCs and thus the ozone depletion in the stratosphere [Dörnbrack *et al.*, 1999; Carslaw *et al.*, 1999; Dörnbrack *et al.*, 2001; Dörnbrack and Leutbecher, 2001]. The temperature variation and horizontal velocity produced from orographic gravity waves are 2-3 times higher than over plains and oceans [Nastrom *et al.*, 1987; Jasperson *et al.*, 1990; Bacmeister *et al.*, 1990a] and ~5 times higher than the regions that have no obvious meteorological sources [Fritts and Nastrom, 1992]. Thus orographic gravity waves are more important to atmospheric circulation, thermal structures and composition and distribution of chemical species relative to other significant sources.

These orographic gravity waves together with other classes of gravity waves, such as convective gravity waves, need to be accounted for momentum balance in numerical weather prediction (NWP) and climate models, in order to reduce systematic biases in the model circulation [e.g. Palmer *et al.*, 1986; McFarlane, 1987; Iwasaki *et al.*, 1989]. However, due to the limited resolution of such models, these waves are currently not well resolved and must therefore be parameterized. The global observations of gravity

waves by using satellite remote-sensing technology can provide useful constraints for the gravity-wave parameterization schemes used in global NWP and climate models.

In numerical models, gravity waves are typically parameterized by calculating wave momentum fluxes. Gravity-wave momentum fluxes calculated from satellite observations have been used to constrain non-orographic gravity-wave parameterization schemes [Ern *et al.*, 2004, 2006; Preusse *et al.*, 2009]. The calculation of the momentum fluxes requires knowledge of both the horizontal and vertical wavelengths of the gravity waves, as well as the temperature fluctuations. However, as discussed in chapter 4, gravity wave observations are determined by the characteristics of the instrument. A limb-viewing instrument is suitable for an estimate of the vertical structure of a wave field, while a nadir-viewing instrument can be used to observe the horizontal wave parameters. Therefore, obtaining reliable momentum flux estimates using a single measuring technique (limb or nadir technique) is difficult.

In recent years, satellite instruments have been used to observe orographic gravity waves (OGWs) over Greenland [Limpasuvan *et al.*, 2007], Antarctica [Wu and Jiang, 2002; Alexander and Teitelbaum, 2007] and South Georgia [Alexander *et al.*, 2009]. Several satellite studies have focused on waves generated by the Andes mountain range [Eckermann and Preusse, 1999; Preusse *et al.*, 2002; Jiang *et al.*, 2002; Alexander and Barnet, 2007]. The southern Andes are a strong source of OGW since in the winter months the winds in the troposphere and stratosphere are dominated by strong westerlies with little turning with height. Such conditions are ideal for both the generation of OGWs and their propagation into the stratosphere, where they can be observed by satellites. Using Microwave Limb Sounder (MLS) measurements of radiance Jiang *et al.* [2002] revealed strong annual and inter-annual variability in monthly mean gravity wave amplitudes over the Andes, which they successfully reproduced with the Naval Research Laboratory Mountain Wave Forecast Model (MWFM). They showed that OGW activity peaked in the winter months with almost no activity during November-April.

The HIRDLS instrument that has been introduced in chapter 3 is a limb sounder. It has a vertical resolution of  $\sim 1$  km and an along-track spacing of  $\sim 100$  km. The along-track spacing is comparable to the grid spacing of current climate models and a little coarser than current global forecast models. The instrument characteristics make it

suitable for observing gravity wave parameters in the vertical as discussed in chapter 4 (also see *Alexander et al.* [2008a]). In this chapter, the HIRDLS gravity wave temperature amplitudes introduced in chapter 4 were compared with orographic gravity-wave model parameterizations in the UK Met Office Unified Model® (MetUM). The parameterization scheme in the model was modified by Dr. S. Vosper and Dr. H. Wells to output gravity-wave temperature fluctuations, in order to compare directly with the HIRDLS observations. The comparison is focused on the southern Andes (shown in figure 5.1) in July, August and September (JAS) 2006, a time period where the wave activity over the Andes is likely to be dominated by OGWs. The aim of the comparison is validating the HIRDLS observations and in turn, using the HIRDLS observations to constrain the parameterized OGWs in the MetUM.

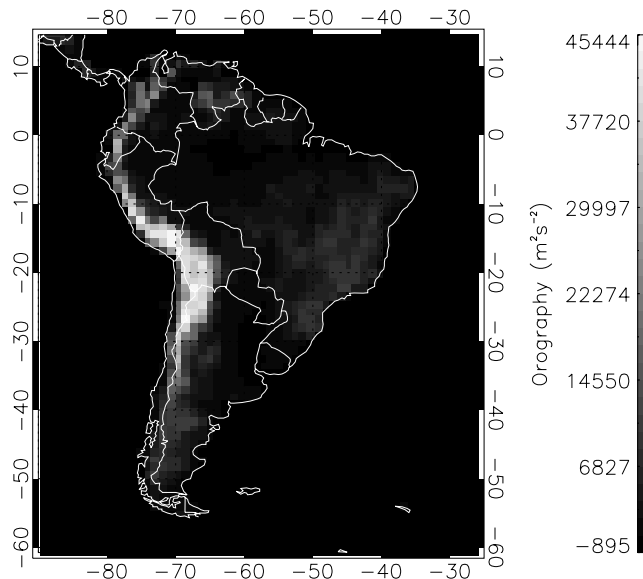


Figure 5.1 Orography of South America represented by the surface geopotential ( $\text{m}^2/\text{s}^2$ ).

## 5.1 Orographic Gravity-Wave Parameterization in the Met Office Unified Model

The MetUM is the numerical modelling system developed and used by the UK Met Office for NWP and climate prediction. The main details of the model are described by *Davies et al.* [2005]. The orographic gravity-wave parameterization scheme in the MetUM is based on the ideas of *McFarlane* (1987) and described in detail by *Gregory et al.* [1998] and *Webster et al.* [2003].

In order to avoid re-running the model and additional calculations, an offline technique was employed in which tunable parameters,  $F_{crit}$ ,  $F_{sat}$  and  $n_\sigma$  (see appendix B) are adjusted for better results. The off-line scheme was applied to archived profiles of wind, Brunt-Väisälä frequency and density at all model grid points over land. The archived profiles are from the operational MetUM with the operational orographic gravity-wave parameterization switched on. The description of the operational scheme is given in the appendix B.

The HIRDLS observations were compared with three versions of the orographic gravity-wave parameterization scheme, which are named version 1 (V1), 2 (V2) and 3 (V3), respectively. Three configurations of the parameterization scheme are summarized in table 5.1. V1 is the operational scheme with the assumption of wave breaking (i.e. saturation) at launched level (see appendix B). The tuning parameters  $F_{crit}$  and  $n_\sigma$  for the operational scheme were chosen originally to optimize overall NWP performance. The saturation assumption is dropped in versions V2 and V3. The values of  $F_{crit}$  and  $n_\sigma$  in V2 are the same as those in V1 and  $F_{sat}$  is set to 1. In V3,  $F_{crit}$  is reduced from 4 to 1, a value more consistent with the dynamics of flow splitting in stratified flows around mountains. The values of  $F_{sat}$  and  $n_\sigma$  have then been adjusted to optimize the performance of the scheme relative to the HIRDLS observations.

Table 5.1 The three versions of the off-line parameterization scheme.

Version	Waves saturated at launch ?	$F_{crit}$	$F_{sat}$	$n_\sigma$
V1	Yes	4	-	2.5
V2	No	4	1	2.5
V3	No	1	2	2

By assuming  $\hat{T}/T = \hat{\theta}/\theta$ , the temperature amplitude from the parameterized gravity waves,  $\hat{T}$ , was calculated as

$$\hat{T} = \eta \frac{T}{\theta} \frac{d\theta}{dz}, \quad 5-1$$

where  $\eta$  is wave vertical displacement amplitude (defined in appendix B),  $T(z)$  and  $\theta(z)$  are the model temperature and potential temperature profiles, respectively, and  $\hat{\theta}$  is the amplitude of the wave-induced fluctuations in potential temperature. The calculation was performed at 6-hour intervals for every day during the JAS 2006 period using data from the global forecast which was initialised at 00 UTC. Thus, for each day the off-line scheme was applied at 00, 06, 12 and 18 UTC.

It should be noted that, since the operational forecasts were themselves computed with the parameterization switched on, the off-line approach suffers from the fact that the flow fields used to diagnose the wave motion have already been affected by the parameterized gravity-wave stress divergence (see appendix B). Whilst this is clearly undesirable, the alternative of re-running the global forecasts for long periods of time would require substantial computing resources. Indeed, the impact of the waves predicted by the operational version of the scheme, particularly in the stratosphere, is relatively small.

Like most orographic gravity-wave parameterization schemes [e.g. *Palmer et al.*, 1986; *Iwasaki et al.*, 1989], the *McFarlane* (1987) scheme assumes vertical only propagation within each grid column of the MetUM. Whether or not the assumption is realistic will be tested by the comparisons with HIRDLS observations.

## 5.2 The HIRDLS Observations

The v02.04.19 temperature measurements from HIRDLS were used to analyze gravity wave temperature amplitudes for the comparison with the MetUM parameterization. The v02.04.19 data has better quality at lower altitudes than that of the v02.04.09. This makes it possible to observe OGWs in v02.04.19 low to the lower stratosphere and closer to the wave generation source in the troposphere.

Figure 5.2 shows monthly mean gravity-wave amplitudes diagnosed from the HIRDLS measurements over the southern Andes for JAS 2006 and 2007. Also shown are monthly mean horizontal wind vectors at 700 hPa, obtained from ECMWF global analyses (operational  $2.5^\circ \times 2.5^\circ$  gridded wind data). For all months shown, temperature perturbations were observed above the Andes, indicative of OGW activity. Peak monthly mean amplitudes are approximately 2 K and the largest values occur above the

mountains. The wave motion clearly extends significant distances downwind and wave amplitudes of order 1.3 K are also observed across the ocean. Generally, the winds are westerly and perpendicular to the north-south oriented Andes range, thus providing conditions which are conducive to the generation of OGWs. In fact, it was the winds larger than  $\sim 10$  m/s in these months, except for September 2007, that are mainly responsible for the enhancement in the temperature amplitudes. In Sep 2007, the winds larger than 10 m/s are almost parallel to the tip of South America resulting in no apparent enhancement, and the relatively weaker enhancement is related to the relatively weaker winds. The comparison between 2006 and 2007 shows a clear, but small, amount of inter-annual variation.

Figure 5.3 shows the vertical and latitudinal variation of zonally averaged gravity-wave amplitudes for JAS 2006 and 2007, where the averaging was performed over the areas shown in figure 5.2. Due to the sparse coverage of the HIRDLS data in the horizontal, a large area is used for averaging so that sufficient data are included for the analysis to be representative of the region. The largest wave amplitudes are observed at the highest latitudes. The wave amplitude decreases rapidly northwards. The wave amplitudes generally increase with height, consistent with a decrease in air density. Note, however, that the rate of increase with altitude is not uniform with latitude, suggesting that other local environmental factors, such as the stratification and the details of the wind profile are important. Interestingly, figure 5.3 hints at the possibility of a local minimum in wave amplitude just below 38 hPa.

A time series of the measured wave amplitude and its variation with altitude during JAS 2006 is shown in figure 5.4(d). The wave amplitudes shown are average measurements made over South America between 30°S and 60°S. For the purposes of comparison with results from the OGW parameterization scheme (see section 5.3) only measurements obtained above land are included in the averaging. Figure 5.4(d) reveals that periods of wave activity generally last for between 2 and 14 days and, consistent with the zonal mean amplitudes of figure 5.3, the amplitude generally increases with height. Comparison with figure 5.3 indicates that the averaging increased the lowest amplitudes approximately 0.5 K and decreased the highest amplitudes approximately 2 K. In figure 5.4(d), enhanced values typical of the lower stratosphere are around 2 K, increasing to around 5 K in the upper stratosphere. The largest temperature amplitudes

are typically observed above 10 hPa (around 30 km above sea level), although the strongest event (which occurred during days 78 to 79) has large-amplitude wave motion present as low as 25 hPa (~24 km).

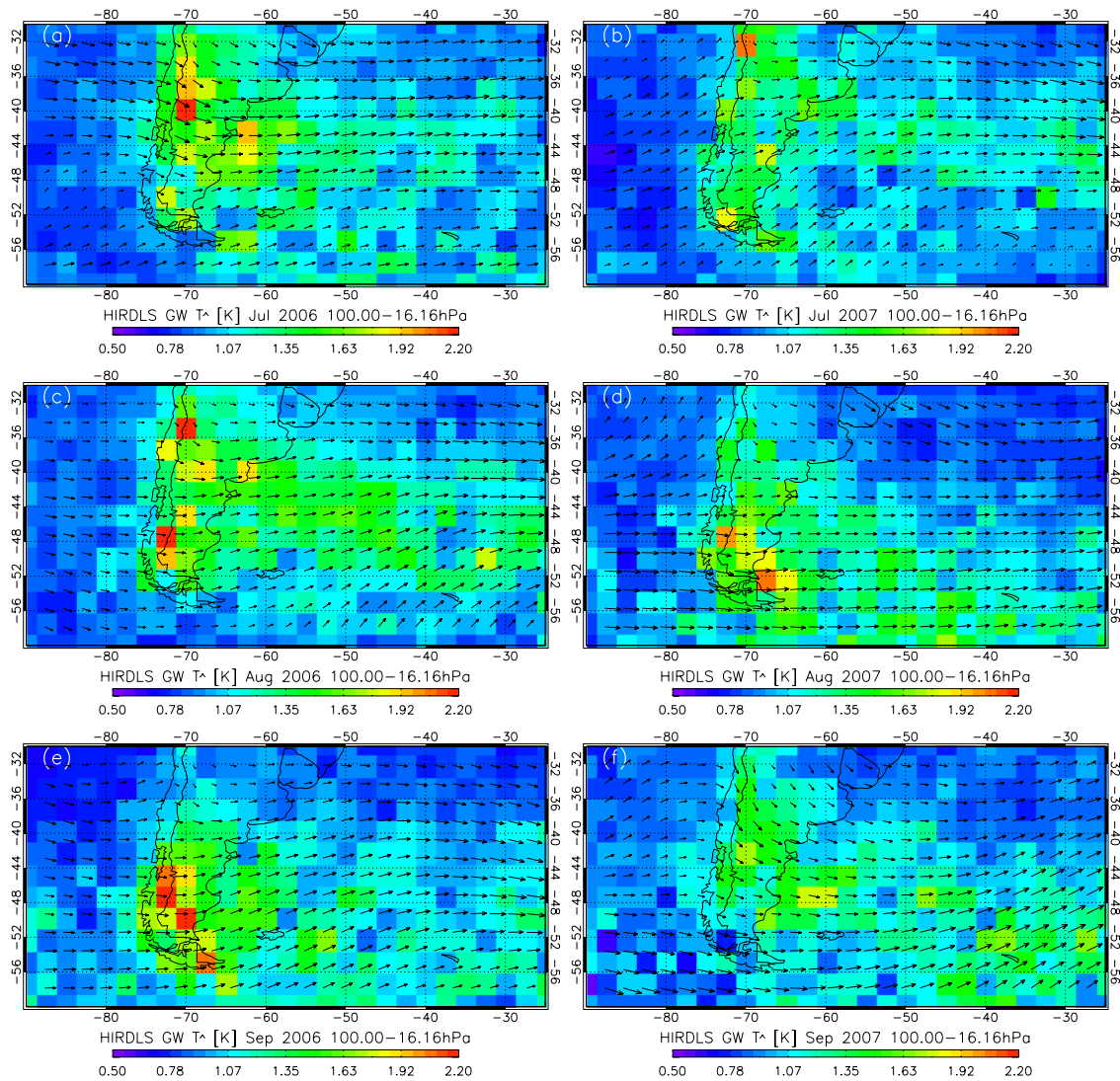


Figure 5.2 HIRDLS monthly mean gravity-wave temperature amplitudes (K) averaged between pressure levels 100 to 16 hPa (approximately 16 to 27 km above sea level) over the southern Andes during (a) July 2006, (c) August 2006, (e) September 2006 and (b) July 2007, (d) August 2007, (f) September 2007. The monthly mean ECMWF analysis wind vectors at 700 hPa are also shown.

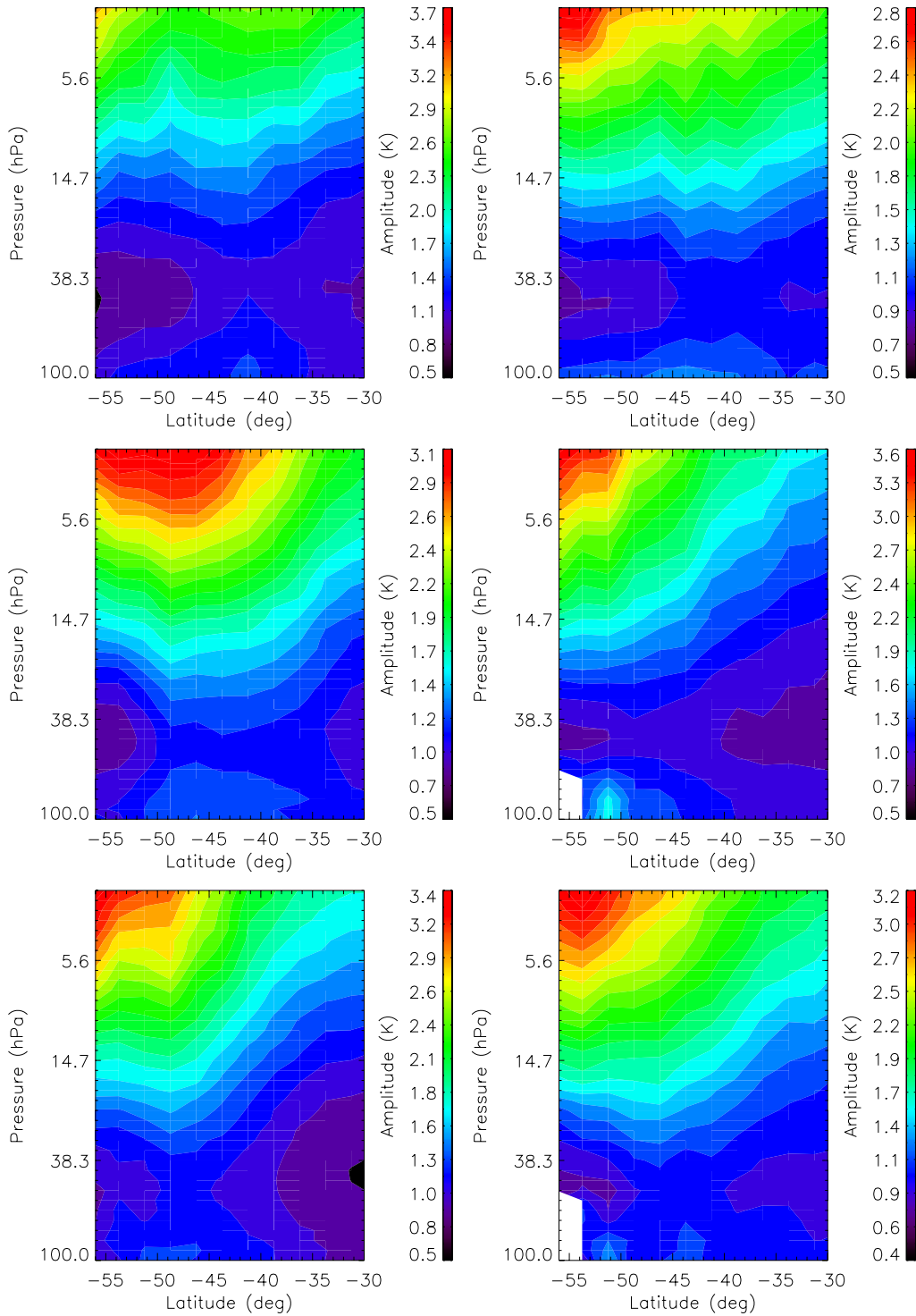


Figure 5.3 HIRDLS zonal mean gravity-wave temperature amplitudes (K) during JAS 2006 (left column) and JAS 2007 (right column), averaged over the area presented in figure 5.2.

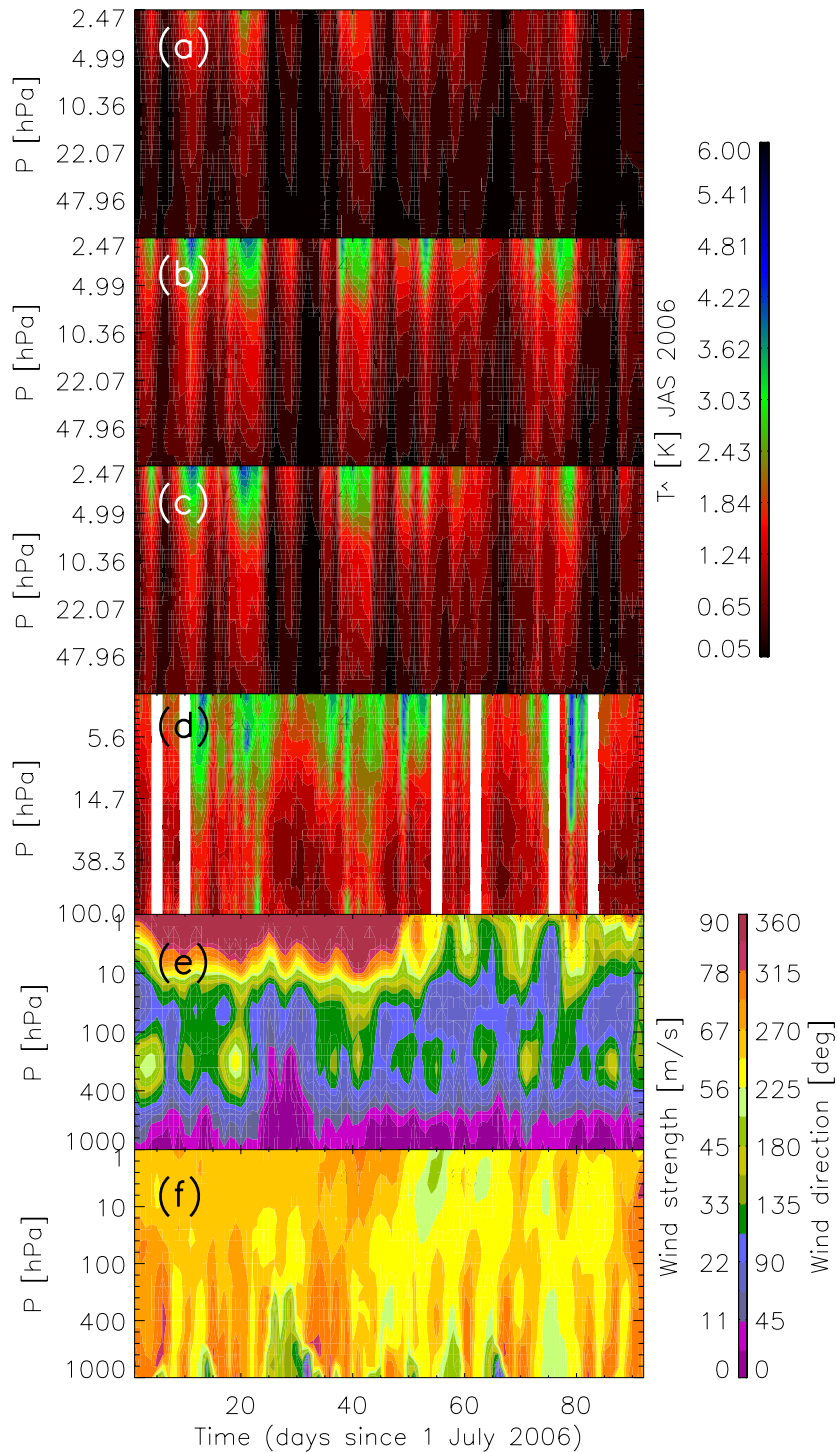


Figure 5.4 Time-series of gravity waves averaged over South America between 30°S and 60°S and upstream ECMWF winds for JAS 2006. Quantities shown are the parameterized orographic gravity-wave temperature amplitudes (K) predicted by the off-line (a) V1, (b) V2 and (c) V3 schemes, (d) the HIRDLS observed temperature amplitudes and (e) ECMWF wind speeds and (f) direction.

Time series of the upstream wind speed and direction obtained from ECWMF analyses are shown in figures 5.4(e) and (f), respectively, where in order to represent upstream conditions, the wind vectors were averaged over a rectangular area in latitude-longitude space whose south-west and north-east corners had coordinates (78°W, 50°S) and (73°W, 35°S), respectively. The wind direction is measured clockwise. From figures 5.4(d) to (f) it is clear that periods of strong gravity-wave activity are generally associated with periods of relatively strong westerly low-level flow. Weaker wave activity is observed when the westerly component of the low-level flow is small. For example, a period of relatively strong wave activity is observed from around day 16 to day 24 which has strong low-level winds that are westerly over the period. In contrast, during a period of weak wave activity from day 25 to day 35 the winds are much weaker throughout the troposphere and are initially southerly before turning north-easterly.

Whilst it is generally true that strong low-level winds directed perpendicular to the mountain range will result in the generation of OGWs, the propagation of the waves through the troposphere and stratosphere will depend on the properties of the vertical profile of wind and atmospheric stability. For example, turning of the wind with height may result in the absorption of wave motion at critical layers (e.g. *Shutts* [1998]), thus restricting the vertical propagation of wave energy. The dependence of the vertical propagation on the details of the background profile means that relating the stratospheric wave amplitude to the flow properties is not straightforward. In order to demonstrate clearly that the observed waves behave in a way consistent with stationary OGWs a more complete analysis is required. One approach is to compare the observations with the predictions of an OGW parameterization scheme.

### **5.3 HIRDLS Observations vs. MetUM Parameterizations**

The temperature amplitude predictions for the V1, V2 and V3 OGW parameterization scheme during JAS 2006 are shown in figures 5.4(a), (b) and (c), respectively. As for the HIRDLS observations (figure 5.4(d)) the amplitudes shown are the average values across the southern Andes between 30°S and 60°S. Comparison of figure 5.4(a) with 5.4(d) shows that the wave amplitudes predicted by the operational version (V1) of the scheme are significantly smaller than those observed. For example,

the average parameterized amplitude between 10 and 1 hPa during JAS 2006 is 0.77 K, whereas the observed average value is approximately 2.4 K. Note that, due to the horizontal resolution of the HIRDLS observations, the observations provide a minimum estimate for the wave activity. It is therefore likely that the under-prediction of gravity waves by the operational scheme is even more severe than that suggested by figure 5.4. Whilst the impact on NWP performance of changes to the scheme clearly needs to be assessed, this under-prediction provides compelling evidence that improvements to the scheme are required.

The effect of removing the assumption that the waves are saturated at launch is evident in the results for the V2 scheme (figure 5.4(b)). This results in greatly increased wave amplitudes in the stratosphere. Comparison of figure 5.4(b) with 5.4(d) reveals that, for individual wave events, the parameterized amplitudes are now in much closer agreement with the HIRDLS observations. The average amplitude for the V2 scheme in the range 10 to 1 hPa during JAS 2006 is 1.48 K, which although still smaller than the observed value (2.4 K), is a significant improvement on that obtained with the operational (V1) scheme. Whilst there are clearly differences in the detailed evolution and structure, the parameterized temperature fluctuations are now more comparable to those diagnosed from the satellite retrievals. It would seem that low-level wave breaking in the operational scheme excessively reduces the stratospheric wave motion compared to observations.

Whilst the performance of the V2 scheme represents a marked improvement over V1, as shown in table 5.1, the V2 scheme retains the same values of the tuning parameters. As noted in appendix B, the choice of  $F_{crit}=4$  is rather unphysical compared with typical values suggested by numerical and theoretical studies. However, reducing  $F_{crit}$  to the more physically acceptable value of unity, whilst keeping the values of the other tuning constants  $F_{sat}$  and  $n_{\sigma}$  unchanged, results in excessively large wave amplitudes in the stratosphere compared to those observed in the HIRDLS data. However, acceptable results with  $F_{crit}=1$  have been achieved by increasing the value of  $F_{sat}$  to 2, which tightens the criterion for wave saturation by allowing smaller amplitude waves to break. The main impact of increasing  $F_{sat}$  to 2 is to increase the wave breaking in the troposphere and lower stratosphere. Figure 5.4(c) shows the results for the V3 scheme in which  $F_{crit}=1$ ,  $F_{sat}=2$  and  $n_{\sigma}$  is reduced slightly from its operational value of

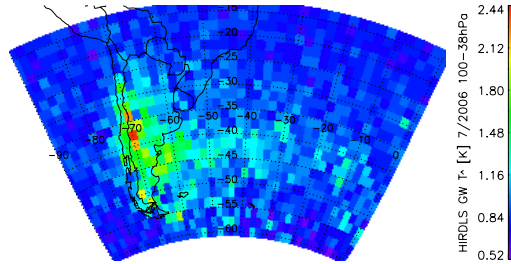
2.5 to 2. The impact of the change in  $n_\alpha$  from 2.5 to 2 is relatively small but this change brings the value in to line with the values recommended by other studies [e.g. *Wallace et al.*, 1983]. The level of agreement between the parameterized amplitudes and those observed by the satellite is broadly similar to that obtained with the V2 scheme and on the basis of these comparisons alone there would be little to choose between the two tunings. The more physically acceptable value of  $F_{crit}$  perhaps makes the V3 scheme marginally more attractive. In order to better discriminate between these choices further work would clearly be required. For example, greater insight might come from examination of the behavior over other mountain ranges or during different seasons.

Comparison of figures 5.4(b), (c) and (d) shows that, although the changes to the operational parameterization scheme improve the agreement with the observations, the schemes still suffer from some marked deficiencies. Firstly, the wave amplitude is under-predicted over the lower portion of the height range sampled by the satellite and appears to generally grow too rapidly with height. Secondly, there is some evidence to suggest a local minimum in the HIRDLS wave amplitude near 38 hPa. This is most apparent in the zonally averaged data (see figure 5.3) but also appears intermittently in the time series shown in figure 5.4(d). No such minimum occurs in the parameterization results. Neither the mechanism for the minimum nor its significance is clear but it is perhaps worthy of further study. Finally, whilst the timing of individual wave events is generally well represented by the V2 and V3 parameterization schemes, their duration tends to be somewhat shorter than observed and episodes of parameterized wave activity are rather intermittent. This is partly responsible for the under-prediction of the three-month mean amplitudes and is perhaps a consequence of the steady-state assumption used in the scheme, which means that the wave motion will adjust instantaneously to changes in the vertical profiles of wind and stability.

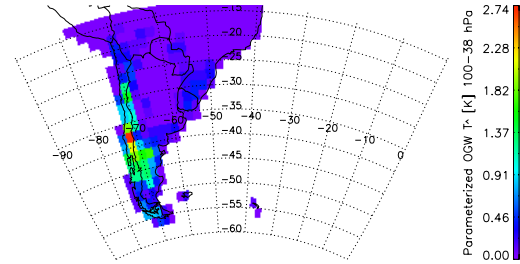
Despite the above discrepancies, the fact that the predictions of the OGW parameterization scheme are broadly similar to the observations indicates that observed temperature fluctuations are likely to be a result of OGW motion rather than some other non-orographic source (e.g. from waves generated by convection). Additionally, the poor agreement of the HIRDLS observations with the operational version of the scheme compared to the closer agreement with the V2 and V3 versions illustrates how the

HIRDLS observations can be used to improve and tune OGW parameterization schemes in general.

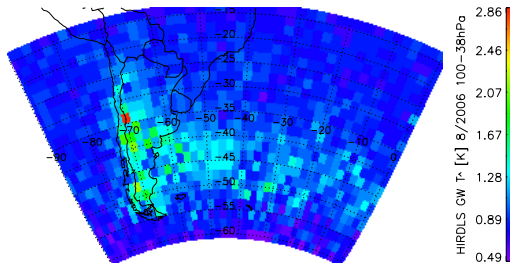
(a) July 2006: HIRDLS



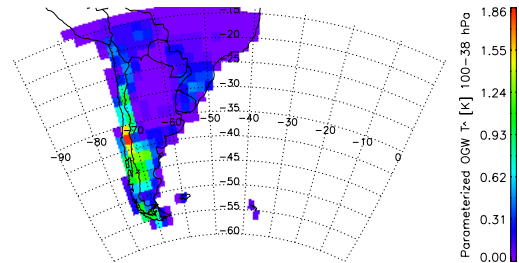
(b) July 2006: Parameterization



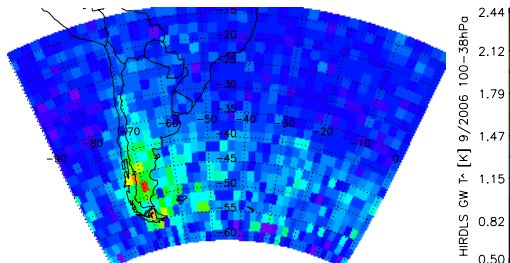
(c) August 2006: HIRDLS



(d) August 2006: Parameterization



(e) September 2006: HIRDLS



(f) September 2006: Parameterization

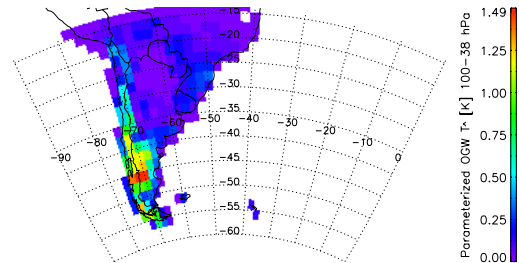
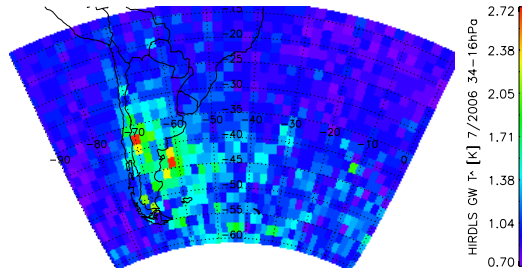
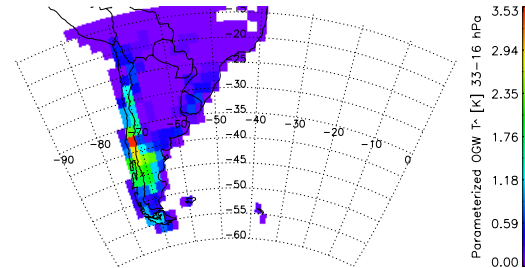


Figure 5.5(i) Monthly means of the HIRDLS observed gravity-wave temperature amplitudes and the V3 parameterized mountain-wave temperature amplitudes (K) averaged over the pressure range 100 to 38 hPa (approximately 16 to 21 km above sea level). Panels (a), (c) and (e) show the HIRDLS measurements for July, August and September 2006, respectively. Figures (b), (d) and (f) show the equivalent results for the parameterization scheme.

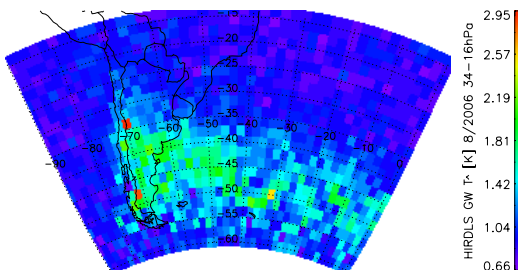
(a) July 2006: HIRDLS



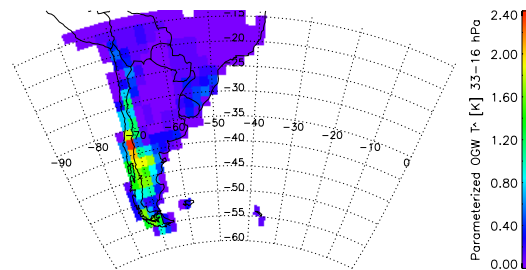
(b) July 2006: Parameterization



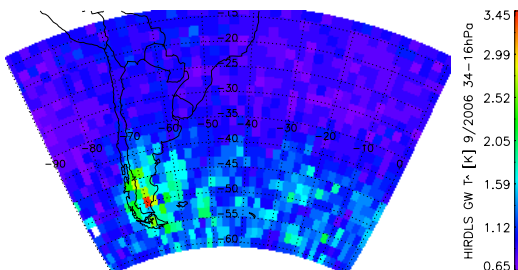
(c) August 2006: HIRDLS



(d) August 2006: Parameterization



(e) September 2006: HIRDLS



(f) September 2006: Parameterization

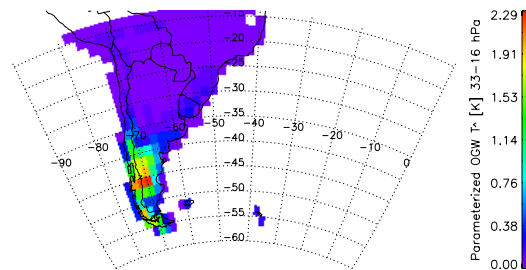
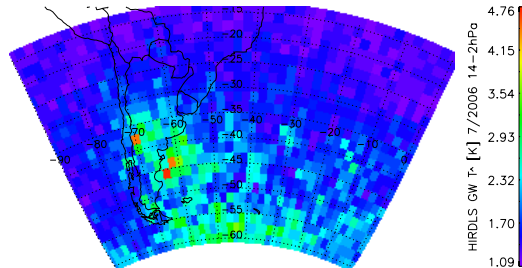
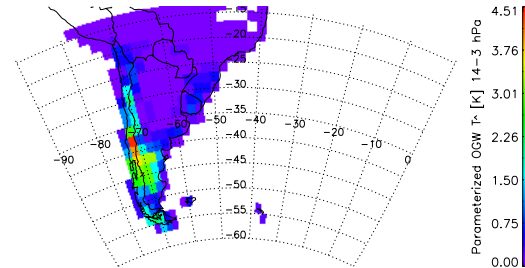


Figure 5.5(ii) Monthly means of the HIRDLS observed gravity-wave temperature amplitudes and the V3 parameterized mountain-wave temperature amplitudes (K) averaged over the pressure range 34 to 16 hPa (approximately 22 to 28 km above sea level). Panels (a), (c) and (e) show the HIRDLS measurements for July, August and September 2006, respectively. Figures (b), (d) and (f) show the equivalent results for the parameterization scheme.

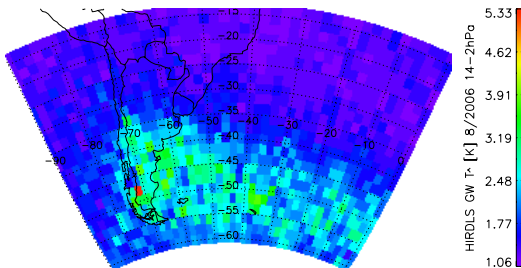
(a) July 2006: HIRDLS



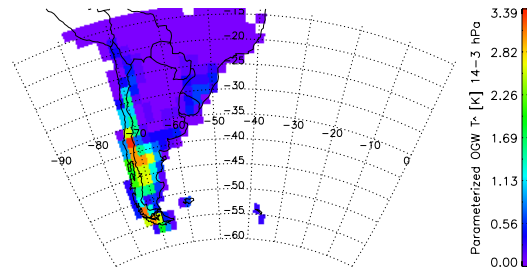
(b) July 2006: Parameterization



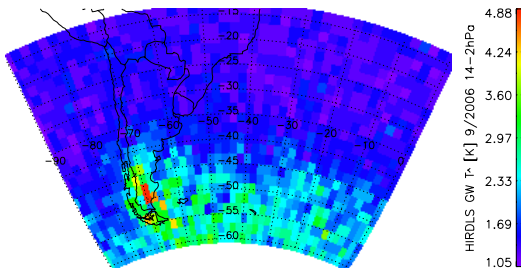
(c) August 2006: HIRDLS



(d) August 2006: Parameterization



(e) September 2006: HIRDLS



(f) September 2006: Parameterization

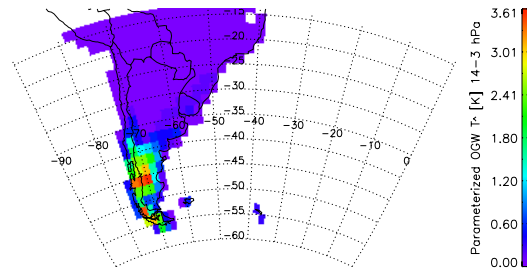
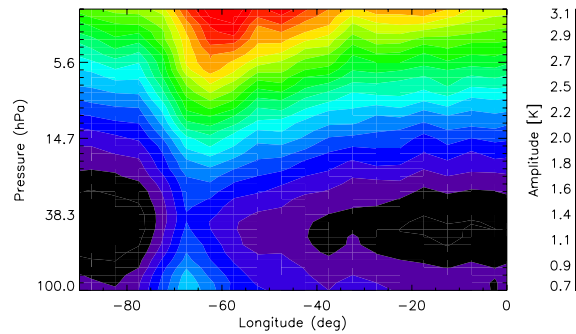
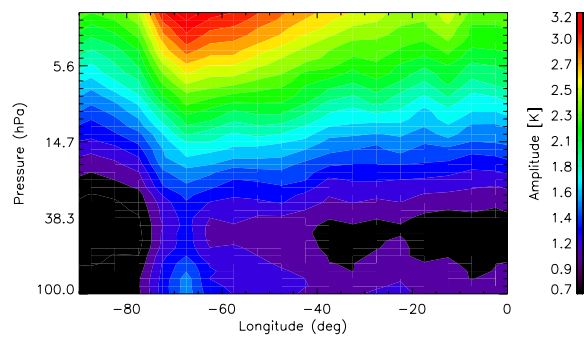


Figure 5.5(iii) Monthly means of the HIRDLS observed gravity-wave temperature amplitudes and the V3 parameterized mountain-wave temperature amplitudes (K) averaged over the pressure range 14 to 2 hPa (approximately 29 to 40 km above sea level). Panels (a), (c) and (e) show the HIRDLS measurements for July, August and September 2006, respectively. Figures (b), (d) and (f) show the equivalent results for the parameterization scheme.

(a)



(b)



(c)

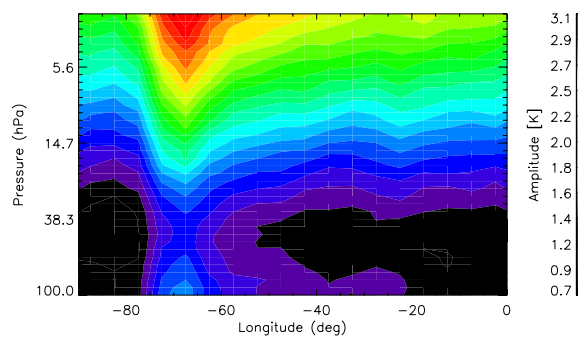


Figure 5.6 The longitudinal and height variation of the meridionally averaged HIRDLS monthly mean temperature amplitude (K) during (a) July, (b) August and (c) September 2006. The meridional average was performed between 30°S and 56°S.

The geographical extent of the observed and parameterized wave motion can be compared in figure 5.5(i) to 5.5(iii) which shows monthly mean amplitudes for JAS 2006 over the pressure ranges 100 to 38 hPa, 34 to 16 hPa and 14 to 2 hPa, respectively. A large area and three pressure ranges were chosen to track horizontal propagation and vertical development of wave activity. The pressure-based HIRDLS and height-based MetUM vertical coordinates result in a small difference in altitude. For the purposes of the comparison the HIRDLS measurements have been averaged onto a  $2^\circ \times 2^\circ$  grid, whereas the parameterization results (those shown are for the V3 scheme) are presented on the global MetUM grid.

Across the continent the locations of the parameterized peak amplitudes are broadly similar to those observed, with the largest wave activity occurring above the southern Andes. Both the observations and parameterization show increased amplitudes with altitude. The peak values in the HIRDLS observations are generally larger than those in the V3 parameterization for all the three pressure ranges reflecting the under-prediction in the parameterization. The under-prediction is consistent with figure 5.4. The obvious difference between the HIRDLS observations and the v3 parameterization is that the wave activity downwind of the Andes and across the ocean in HIRDLS observations is completely absent in the parameterization. Clearly it is the assumption of vertical only propagation in the parameterization resulting in a severe limitation of the spatial distribution compared to that observed by the satellite. However, the vertical only propagation over the orographic obstacles is not only the assumption used in the gravity-wave parameterization scheme of *McFarlane* [1987], it is widely made in numerical models, for example by *Palmer et al.* [1986] and *Iwasaki et al.* [1989].

The extent of the observed downwind propagation is emphasized further in figure 5.6, which shows the meridionally averaged (between 30°S and 56°S) mean monthly temperature amplitude across the southern Andes and ocean. Peak values are observed between approximately 70°W and 65°W (slightly to the east of the Andes) for all three months. The peak amplitudes slightly decreased with altitude from 100 hPa up to about 38 hPa and then increased with height to higher levels resulting in minima in amplitude just below 38 hPa. The minima have already been presented in the time-series plot of amplitude in figure 5.4(d), but it became clearer in figure 5.6. The minima are likely related to the profiles of winds and background instability, but an exact explanation is

not possible at this stage. Over all the three months, the wave amplitude decays gradually downstream, with waves still evident for several hundreds of kilometres across the ocean.

Previous studies of OGWs over the Andes have indicated that the waves have preferential horizontal wavelengths of ~110-130 km and 400 km [Eckermann and Preusse, 1999; Jiang *et al.*, 2002]. Preusse *et al.* [2002] used the GROGAT (Gravity wave Regional Or Global Ray Tracer) model to investigate the downstream propagation of OGWs from the Andes. The study indicates that this downwind wave activity is likely to be associated with long horizontal wavelengths (~400km). Preusse *et al.* [2002] showed that packets of long-wavelength waves propagated significant distances laterally from the source region, with waves with south-westerly oriented wave vectors (a direction favored by the curved shape of the southernmost part of the Andes) propagating furthest downstream to the south-east of the Andes. These waves are able to propagate downstream because their intrinsic frequencies are small and close to the Coriolis frequency, implying that their vertical group velocity is small. The slow vertical propagation of the wave energy means that the wave packets can be blown significant distances downwind. Lateral refraction of the waves may also lead to some southward drift of the waves due to the development of meridional wave components.

### 5.4 Discussion and Summary

In order to understand wave sources and propagation as well as the application of observations in constraining gravity-wave parameterizations in models, HIRDLS gravity wave observations were compared with the OGW parameterization scheme in the MetUM. The comparison was made by directly comparing the observed gravity wave temperature amplitudes with a modified OGW parameterization scheme that output temperature fluctuations rather than momentum fluxes. The observations used v02.04.19 temperature data and the methodology described in chapter 4. Three different off-line versions of the MetUM OGW scheme were run and the predicted fluctuations were compared to the HIRDLS gravity waves for a three-month period (JAS 2006). The operational version of the parameterization scheme significantly under-predicts the observed wave motion in the stratosphere above the southern Andes. After dropping the assumption of wave saturation at launch in the V1 but incurring no changes to other

parameters, the V2 parameterization shows a much improved agreement with the HIRDLS observations. A similarly improved agreement was obtained in the comparison with the V3 that has been further improved by physically tuning  $F_{crit}$ , adjusting  $F_{sat}$  and  $n_{\sigma}$  and removing the assumption of saturation at launch. The fact that the predictions of the OGW parameterization are qualitatively similar to the observations suggests that the observed temperature fluctuations are indeed a result of OGWs. This study demonstrates the utility of satellite measurements in constraining the tuning of OGW drag parameterization schemes.

Whilst reasonable agreement between the parameterized OGW activity and the measurements above the southern Andes has been achieved, differences clearly exist between the observations and parameterization. A striking difference between the HIRDLS observations and the OGW parameterizations is that the minima just below 38 hPa in the observed temperature amplitudes were not present in the parameterization. Comparisons with the ECMWF winds suggest that the minima in the observation are possibly related to the vertical profile of winds and background stability. In the comparisons, the parameterized gravity waves are generally smaller than those observed by HIRDLS reflecting under-predictions of the OGW parameterization scheme in the MetUM. A marked difference is that in the parameterization, the enhanced gravity waves appeared only over the orographic obstacles, while the observation shows downward propagation which persist for several hundreds of kilometres downwind of the mountains and across the Southern Ocean to the east of South America. This difference can be explained by the restriction to the orographic obstacles themselves and the assumption of vertical only propagation in the parameterization scheme that follows the approach of *McFarlane* [1987].

The above comparisons suggest that a significant re-tuning of the operational OGW drag scheme in the MetUM would be required in order to improve the representation of stratospheric OGWs in the global forecasts. However, as noted in previous section, the stress from gravity waves in the parameterization scheme is also controlled by a further tuning parameter, a horizontal scale that represents the gravity-wave horizontal wavelength [*Webster et al.*, 2003]. Thus, although the satellite data have proved useful for the purposes of constraining the parameters which determine both the launch amplitude and the vertical structure of the wave amplitude, an additional degree of

freedom exists which can be used to optimize the scheme for NWP or climate model performance. Once satisfactory parameterized wave amplitudes have been obtained, the momentum fluxes associated with the waves can then be adjusted independently to optimize the forecast performance or model climate.

Previous studies suggest that the downwind wave activity is likely to be associated with long horizontal wavelengths, whose vertical group velocity is sufficiently small that wave packets can be blown significant distances in the horizontal as they propagate vertically. The complete absence of these downwind waves in the OGW parameterization scheme highlights a deficiency in column based schemes, which is also a problem for other global circulation models which used other column based parameterization schemes such as *Palmer et al.* [1986] and *Iwasaki et al.* [1989]. Further investigation will be required in order to determine the importance of this downwind propagation for NWP and climate modelling.

# Chapter 6

## Convective Gravity Waves

### 6.1 Introduction

Chapter 2 has introduced gravity wave sources in which convection is one of the most readily identified sources, particularly in the tropics (see *Fritts and Alexander* [2003] for a comprehensive review). Convection is also mentioned as a wave source in the primary studies of gravity waves in chapter 4. Convectively generated gravity waves play an important role in forcing the equatorial QBO and the SAO in the stratosphere and mesosphere [*Alexander and Holton*, 1997; *Sassi and Garcia*, 1994], and thus are one crucial aspect of momentum transport processes in the large-scale circulation of the middle atmosphere. Convective gravity waves are not fully resolved in modern general circulation models (GCMs) and so the effects of those unresolved waves have to be parameterized [e.g. *Hines*, 1997; *Kiehl et al.*, 1996; *Alexander and Dunkerton*, 1999; *Warner and McIntyre*, 2001; *Kim et al.*, 2003]. Reliable observations can provide constraints on convective gravity-wave parameterizations in GCMs.

Characterizing convective sources is difficult because of the inherent intermittency of convective activity. Due to the characteristics of convective sources, convectively generated gravity waves can be found throughout the full range of the wave spectrum. Previous observations by *Sato* [1992, 1993], *Alexander and Pfister* [1995], *Sato et al.* [1995], *Dewan et al.* [1998], *McLandress et al.* [2000] and *Alexander et al.* [2000] showed that high-frequency waves in the stratosphere closely correspond to deep convective clouds, while the low-frequency waves that may be observed in the middle atmosphere can be a long distance away from the convective source, making it difficult to correlate with clouds or other indicators of convection [*Fritts and Alexander*, 2003].

Convectively generated gravity waves using satellite data have been discussed by *McLandress et al.* [2000] and *Jiang et al.* [2004b, 2005] for the UARS MLS and by *Wu and Eckermann* [2008] for the Aura MLS. The tropics and subtropics are dominated by

organized convective systems. The tropical convection is on a hierarchy of scales including mesoscale deep convection and tropical cyclones. Gravity waves are generated from rapid adjustment processes to disperse the imbalance caused by the mesoscale deep convection or tropical cyclones. Tropical deep convection and the convectively generated gravity waves have been discussed in *Pfister et al.* [1993a], *Tsuda et al.* [1994a], *Karoly et al.* [1996], *Alexander et al.* [2000], *Vincent and Alexander* [2000], *McLandress et al.* [2000] and *Jiang et al.* [2004b]. *Pfister et al.* [1993b], *Sato* [1993] and *Chane-Ming et al.* [2002] have observed gravity waves excited by tropical cyclones.

The Andes in South America (see figure 5.1) run from north to south along the western coast and act as a climatic wall with dry conditions to the west and moist conditions to the east (see for example *Garreaud et al.* [2008]). Whilst the southern Andes, as discussed in chapter 5, is a region dominated by OGWs during the southern winter season, the hot and moist conditions in the north-east of South America (0°S and 30°S) are favourable for deep, moist convection during the summer and thus the production of convective gravity waves.

In this chapter, convectively generated gravity waves from HIRDLS temperature measurements (v02.04.19) are studied over the tropics between 30°N and 30°S in latitude for the summer and winter of 2006/7 and especially over the tropical South America for December, January and February (DJF) 2006/7 by comparing with outgoing longwave radiation (OLR), convective rainfall and vertical winds.

## 6.2 Indicators of Convection

The indicators of convection used in this study include OLR, convective rainfall and vertical winds. The OLR is taken from the NCEP (National Center for Atmospheric Research) archived, twice-daily (0600 UT and 1800 UT), uninterpolated, soundings of the AVHRR on the National Oceanic and Atmospheric Administration (NOAA) satellite. OLR is inversely related to convection and has been widely used as an indicator of deep convection in previous studies [e.g. *Gruber and Krueger*, 1984; *Karoly et al.*, 1996; *Wheeler and Kiladis*, 1999; *Alexander et al.*, 2008b; *Dutta et al.*, 2008]. In this study, the AVHRR OLR data are averaged monthly at  $2.5 \times 2.5$  grid resolution and the values below  $200 \text{ W/m}^2$  (200-OLR) are considered to be determined

by deep convection activity [*Chane-Ming et al.*, 2002]. The convective rainfall is from the TRMM (Tropical Rainfall Measuring Mission) convective monthly  $5^\circ \times 5^\circ$  mean rainfall product 3A25. The TRMM satellite was launched in late 1997 for observing precipitation over the tropical and subtropical regions [*Kummerow et al.*, 2000]. The 3A25 data product is from the precipitation radar on the TRMM satellite and has been validated using surface data from for example oceanic buoys [*Bowman et al.*, 2003] and surface rain radars and rain gauges [*Wolff et al.*, 2005]. The wind data are the ECMWF operational analysis. The data are regular  $2.5^\circ \times 2.5^\circ$  gridded products from 1000 to 1 hPa at 21 pressure levels. The observed gravity waves for convective source were analysed for pressure altitude range 100 to 2.87 hPa over the tropics and the tropical South America.

### 6.3 Gravity Waves over the Tropics

Figures 6.1 to 6.8 show the AVHRR OLR and the averaged HIRDLS gravity waves over pressure levels 100 to 16 hPa for the tropics ( $30^\circ\text{N} - 30^\circ\text{S}$ ) for June - September (JJAS) and November - February (NDJF) 2006/7. The minima OLR indicate strong deep convection activity over the tropics in the summer hemisphere. The seasonal variation of convective activity is observed by the movement of the minima OLR from the southern tropics in JJAS to the northern tropics in NDJF. However, the deep convection indicated by the minima OLR shows different characteristics over the summer northern and southern tropics. In the northern hemisphere, the convective region over southern Asia is particularly large in the summer northern hemisphere and often crosses the equator extending to the southern tropics. In the southern hemisphere, convective regions are approximately equal in magnitude and the covered areas include both land and ocean.

The HIRDLS observations over all the three pressure altitude ranges 100-38 hPa, 34-16 hPa and 14-2 hPa were compared with the convective indicator OLR for the summer northern and southern tropics. Enhanced gravity wave activity was found above the convective regions indicated by the small OLR values. The gravity wave panels in each figure shows that the gravity wave temperature amplitudes grew from top troposphere/lower stratosphere to upper stratosphere which is consistent with the decrease of atmospheric density with height. The enhanced wave temperature

amplitudes over a large area of southern Asia correspond to the large convective region in the summer northern hemisphere.

The comparison with the OLR shows a marked poleward shift of the enhanced gravity wave temperature amplitudes in both hemispheres. The poleward shift varies from a small distance to approximate 10 degrees in latitude. There is no apparent shift in temperature amplitude in the zonal direction. It is known that the gravity waves generated by convection are not characterised by a single frequency and the low-frequency waves particularly observed in the middle atmosphere may be at large distances from the convective sources, making correlations with indicators of convection more difficult [Fritts and Alexander, 2003]. The convective gravity waves observed by Jiang *et al.* [2004b, 2005] also showed a poleward shift of  $\sim 10^\circ$  in latitude, which was explained by the authors as the result of the background wind filtering of the gravity wave propagating into the stratosphere and also the MLS gravity wave visibility function.

The propagation-angle from the horizontal plane of an upward-propagating gravity wave is approximately proportional to the ratio of its vertical to its horizontal wavelength [Hines, 1967]. Therefore, higher-frequency gravity waves propagate closer to vertical and lower-frequency gravity waves propagate closer to horizontal. Additionally, the vertical velocity of a wave (see chapter 2) is proportional to its frequency times its vertical wavelength. For a fixed frequency, the larger the vertical wavelength, the faster the wave can propagate into the middle atmosphere, assuming it avoids critical levels and evanescence. The characteristics of the HIRDLS instrument and the techniques of gravity wave extraction determine the observable gravity waves are with a frequency of a few 10s minutes to several hours and vertical wavelengths from  $\sim 2$  km to 16 km. The HIRDLS measurements are able to detect all horizontal wavelengths greater than 200 km for waves propagating along the line of sight (LOS) and much shorter wavelengths propagating perpendicular to the LOS [Alexander *et al.*, 2008a]. This wide observational range makes the gravity waves with different propagation-angles visible to the instrument. These waves with different propagating angles can present as poleward waves depending on wind directions.

Tropical South America was investigated in detail in the following section for the study of convective source and the propagation of the convective gravity waves by

comparing with the AVHRR OLR and the TRMM convective rainfall, as well as the ECMWF operational analysis.

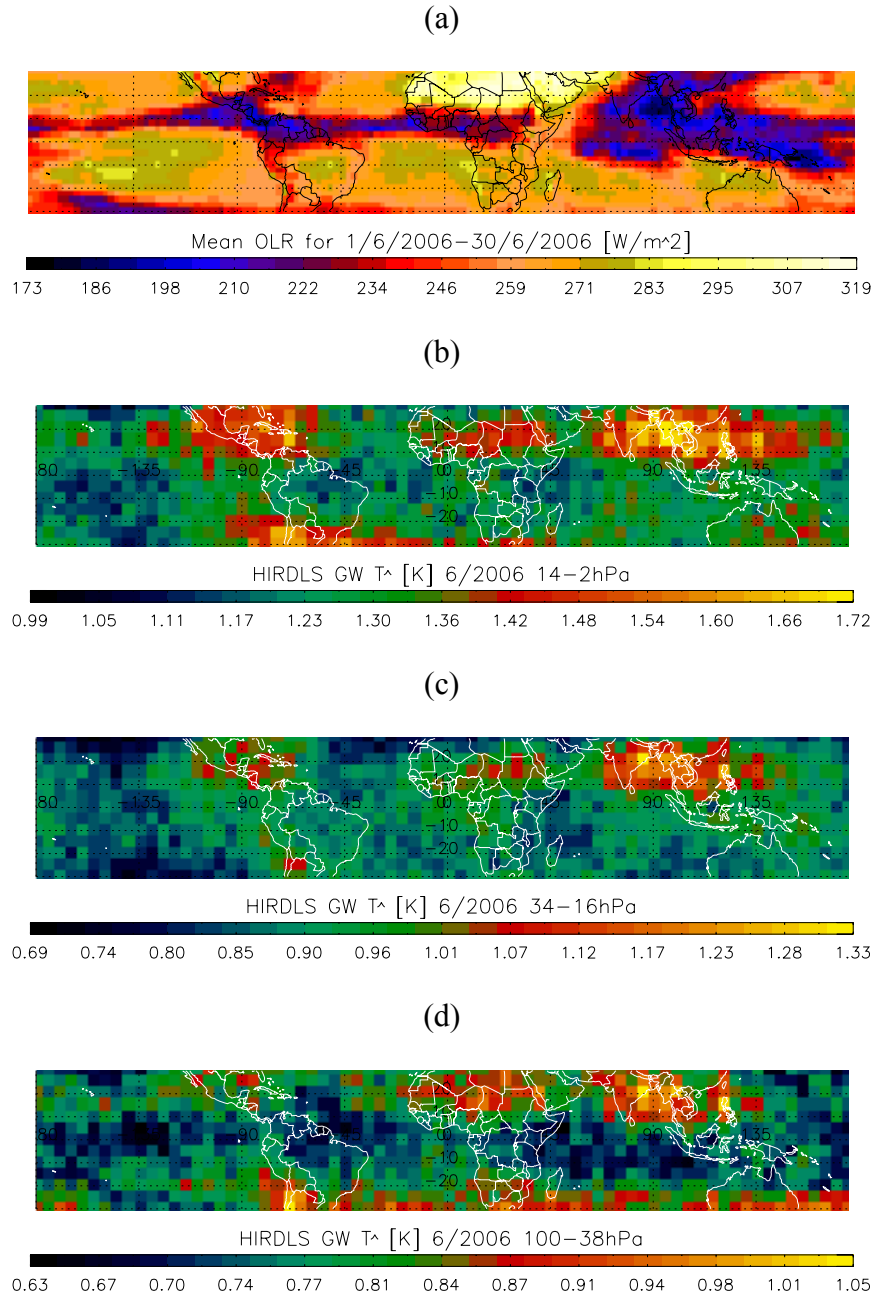


Figure 6.1 OLR from AVHRR and HIRDLS gravity wave temperature amplitudes for June 2006 over pressure ranges 14 – 2 hPa, 34 – 16 hPa and 100 – 38 hPa, respectively.

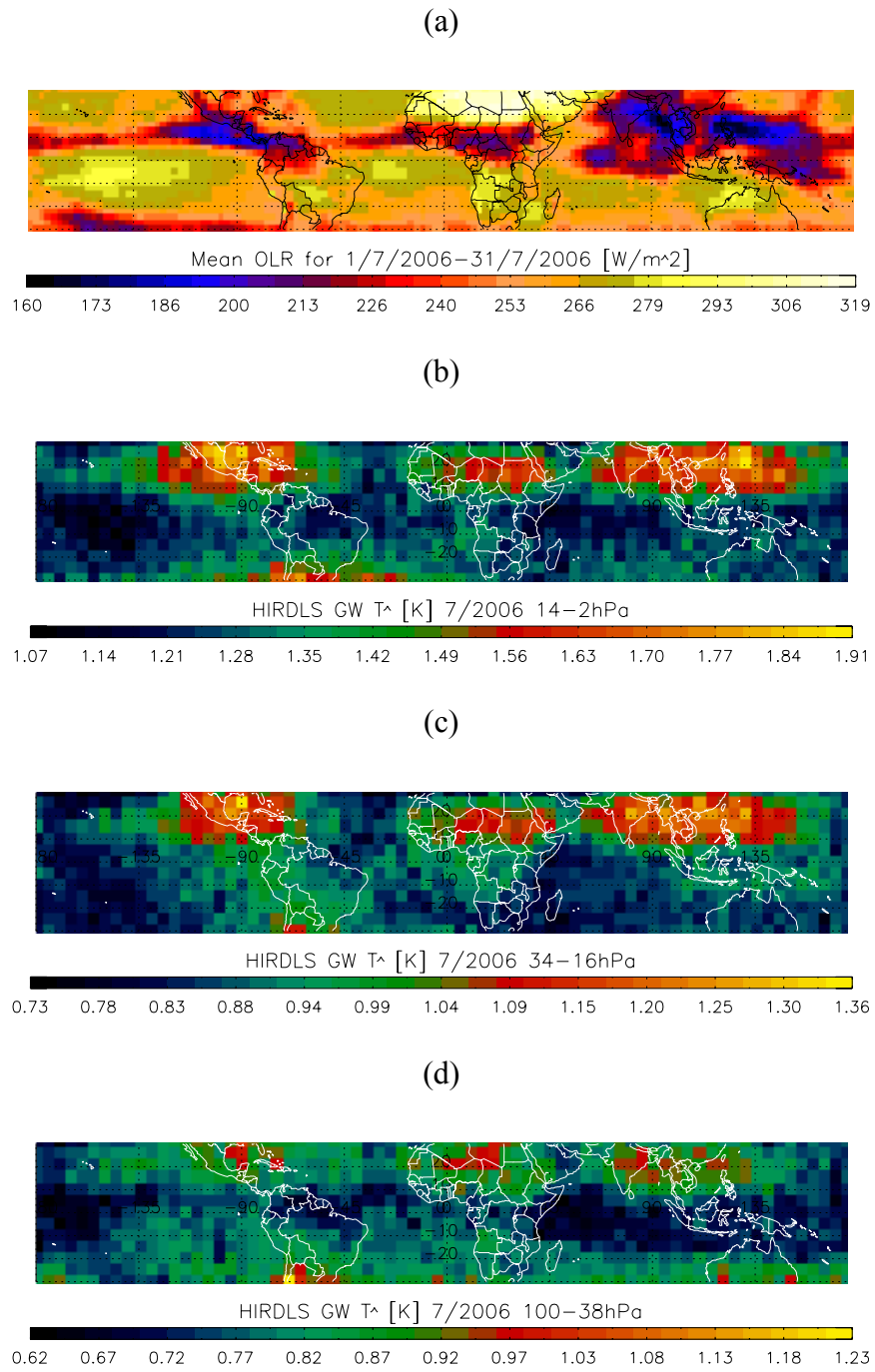


Figure 6.2 OLR from AVHRR and HIRDLS gravity wave temperature amplitudes for July 2006 over pressure ranges 14 – 2 hPa, 34 – 16 hPa and 100 – 38 hPa, respectively.

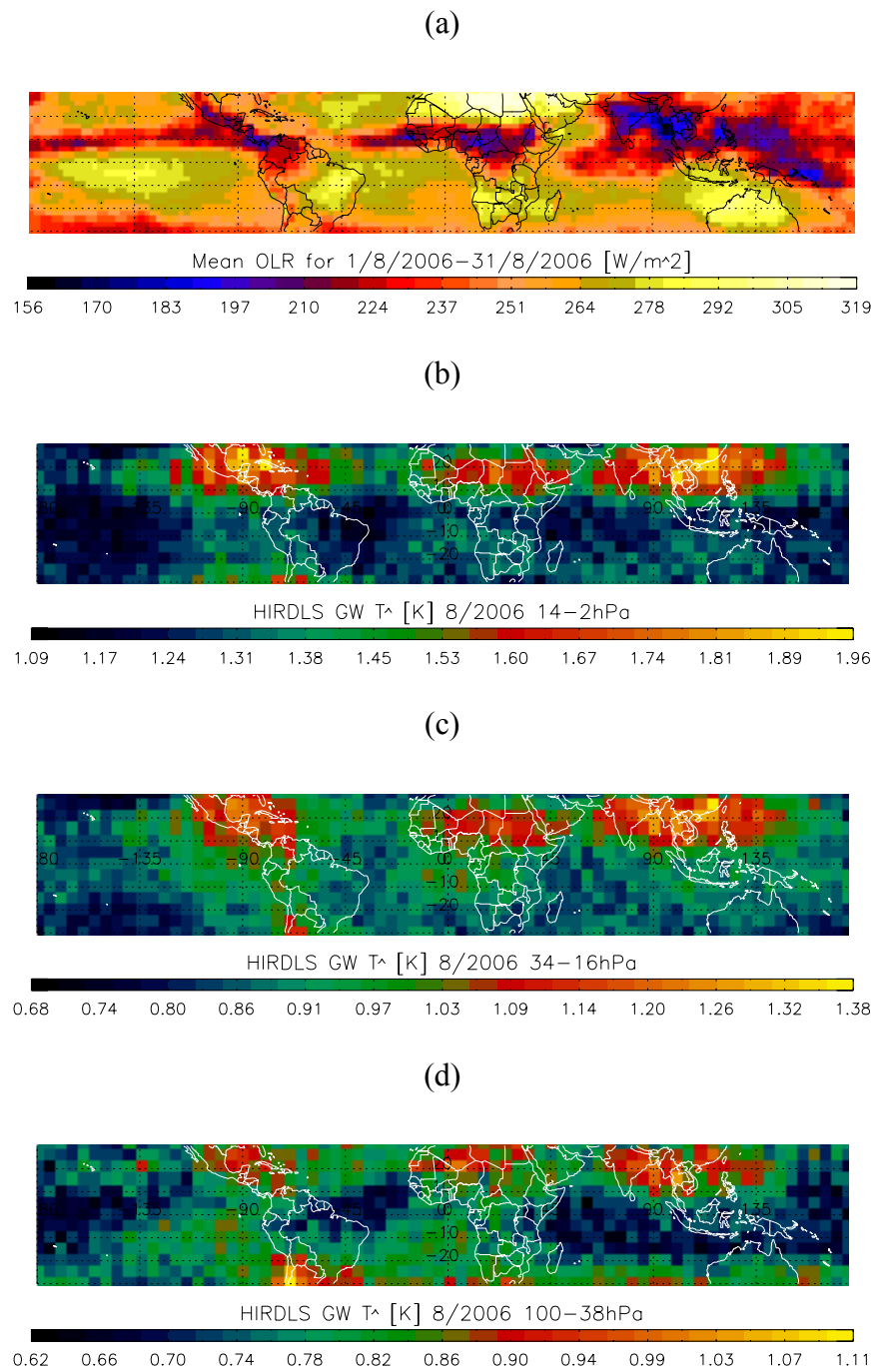


Figure 6.3 OLR from AVHRR and HIRDLS gravity wave temperature amplitudes for August 2006 over pressure ranges 14 – 2 hPa, 34 – 16 hPa and 100 – 38 hPa, respectively.

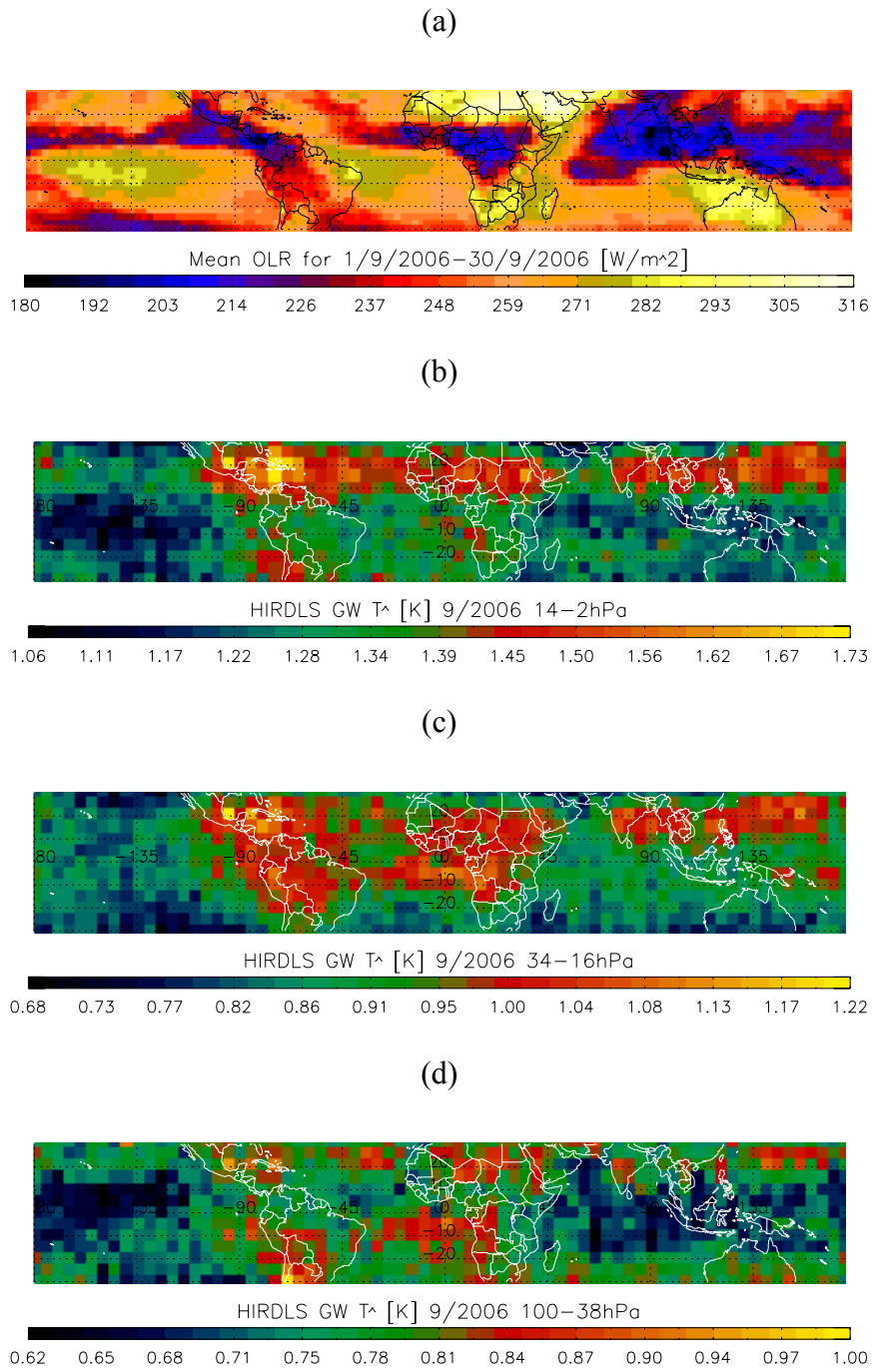


Figure 6.4 OLR from AVHRR and HIRDLS gravity wave temperature amplitudes for September 2006 over pressure ranges 14 – 2 hPa, 34 – 16 hPa and 100 – 38 hPa, respectively.

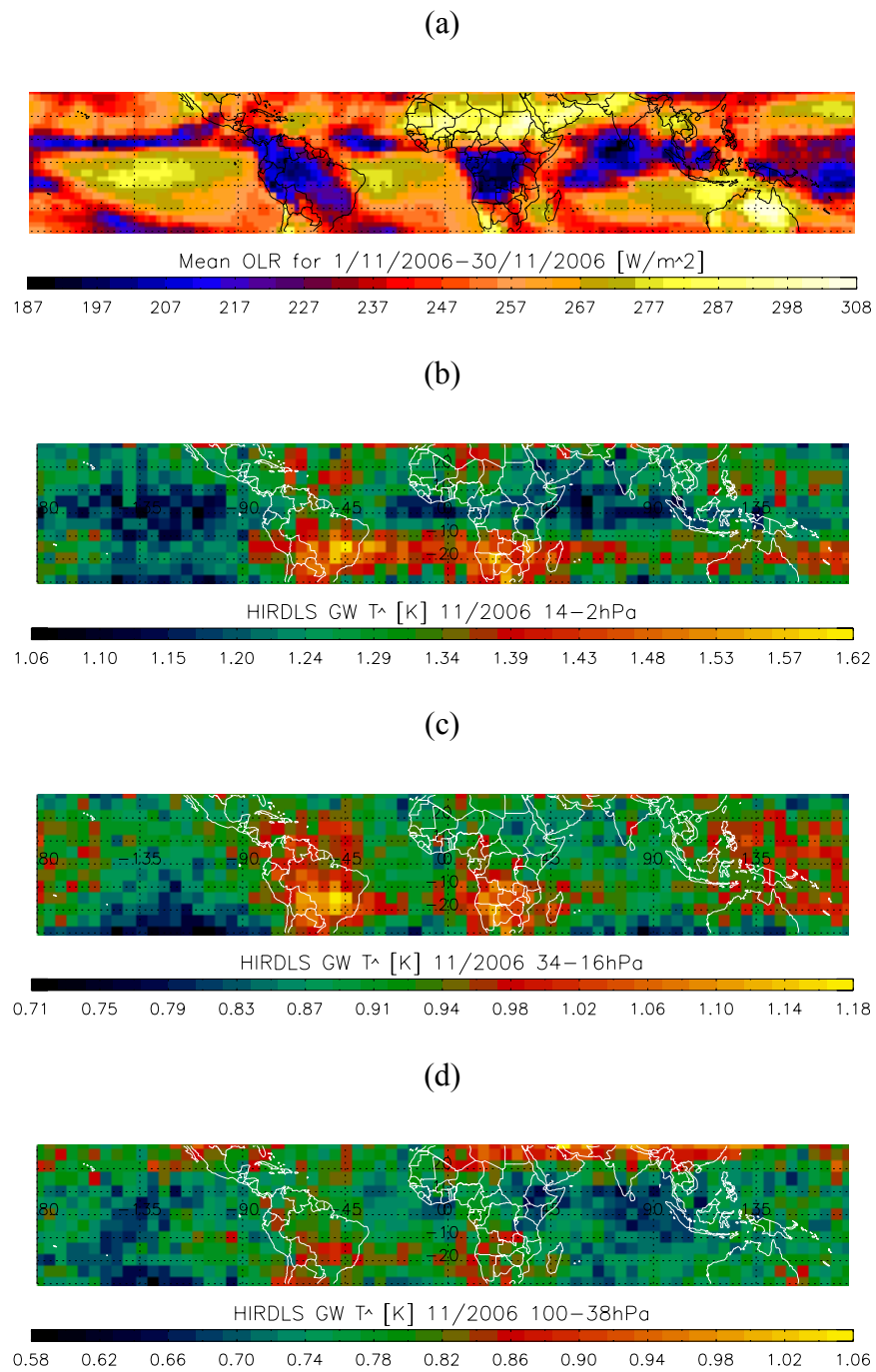


Figure 6.5 OLR from AVHRR and HIRDLS gravity wave temperature amplitudes for November 2006 over pressure ranges 14 – 2 hPa, 34 – 16 hPa and 100 – 38 hPa, respectively.

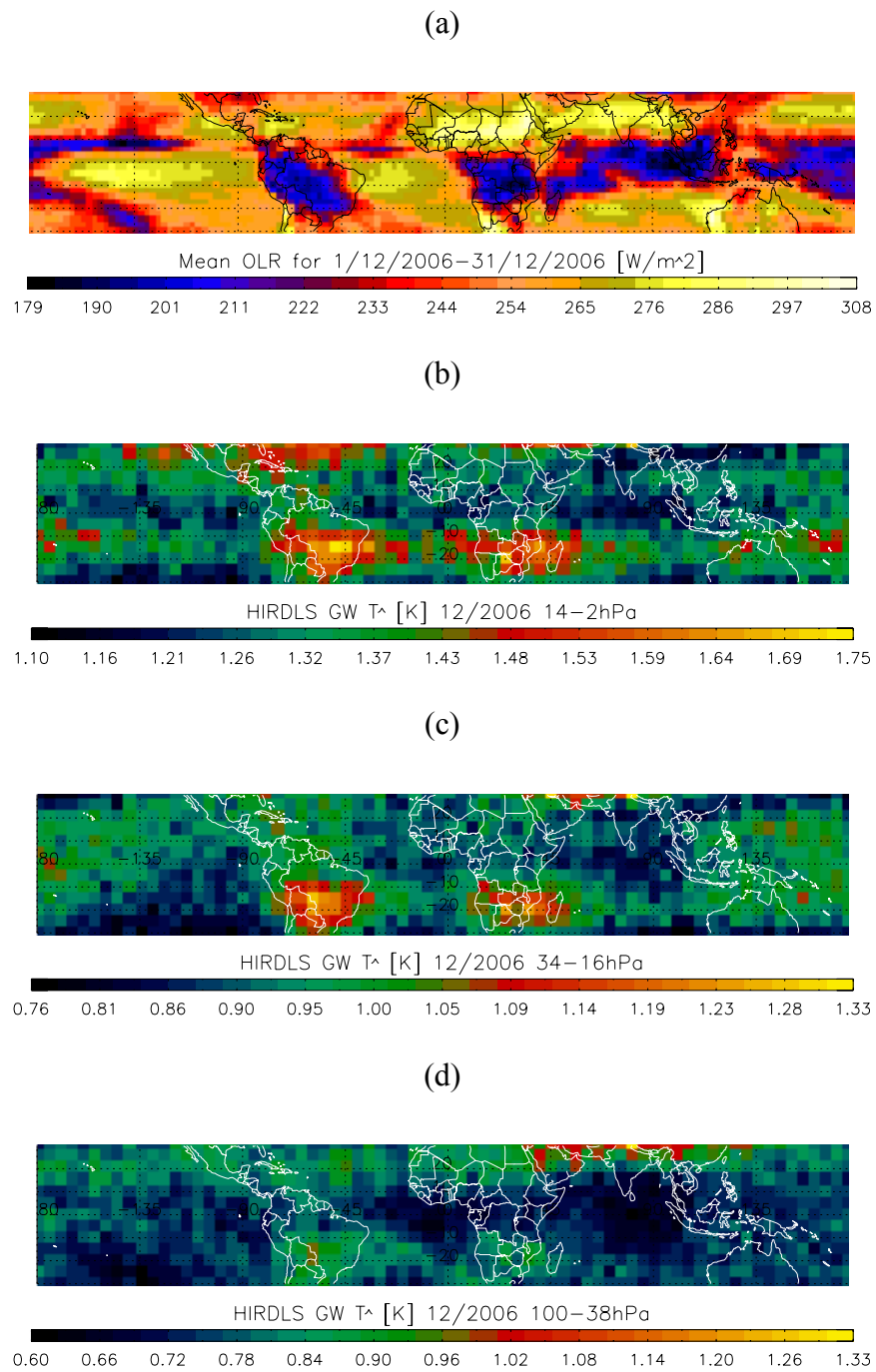


Figure 6.6 OLR from AVHRR and HIRDLS gravity wave temperature amplitudes for December 2006 over pressure ranges 14 – 2 hPa, 34 – 16 hPa and 100 – 38 hPa, respectively.

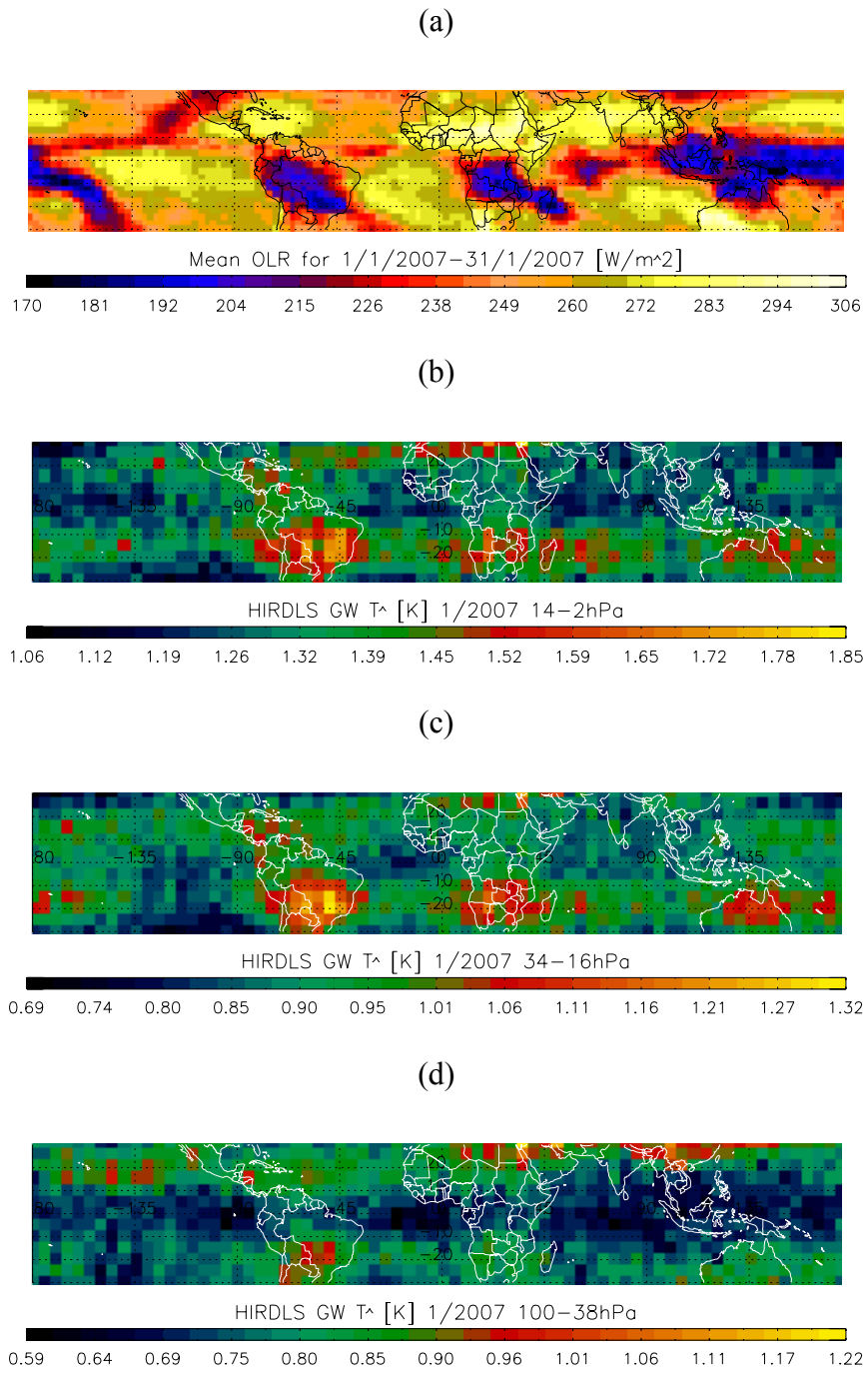


Figure 6.7 OLR from AVHRR and HIRDLS gravity wave temperature amplitudes for January 2007 over pressure ranges 14 – 2 hPa, 34 – 16 hPa and 100 – 38 hPa, respectively.

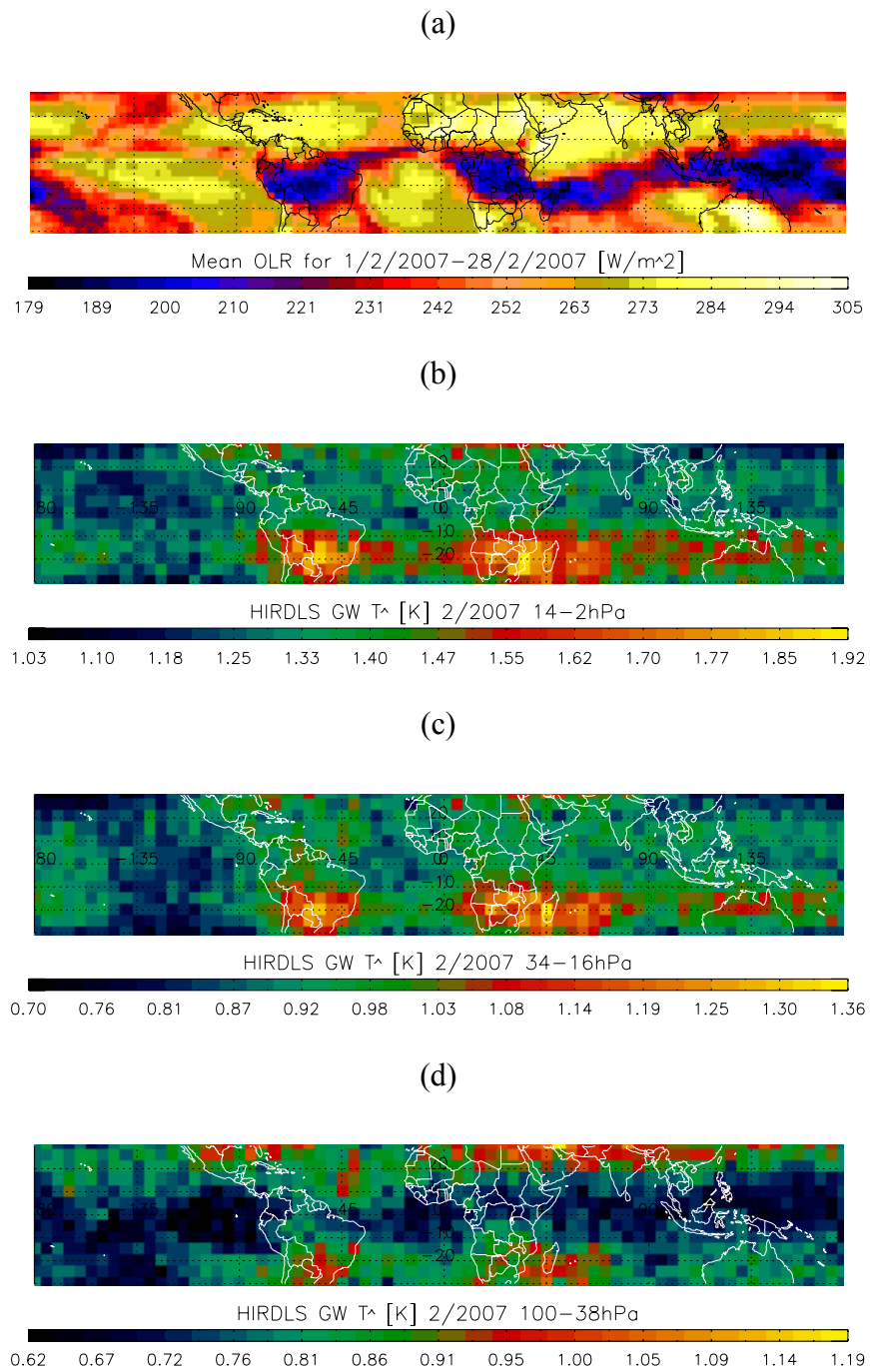


Figure 6.8 OLR from AVHRR and HIRDLS gravity wave temperature amplitudes for February 2007 over pressure ranges 14 – 2 hPa, 34 – 16 hPa and 100 – 38 hPa, respectively.

## 6.4 Gravity Waves over the Tropical South America

Figures 6.9 to 6.11 show the averaged HIRDLS gravity waves over pressure levels 100 to 16 hPa for tropical South America for DJF 2006/7, respectively. The gravity waves were compared with the AVHRR OLR and the TRMM convective rainfall at 15 km. Figure 6.10 shows that the peak gravity wave temperature amplitudes in January correspond closely to the 200-OLR and to the maximum TRMM convective rainfall. The enhanced gravity wave field agrees well with the enhanced TRMM convective rainfall. The good agreement indicates that the observed gravity waves were excited by the source of deep convection. The peak gravity wave amplitude and the minimum OLR in January geographically match each other implying an upward propagation. Following the discussion of the relationship between propagation and frequency in section 6.3, the convective gravity waves in January are very likely higher-frequency waves with larger vertical wavelength and smaller horizontal wavelength. The waves nearly equally spread around the local peaks which is clearly different from the orographic gravity waves over the southern Andes.

The HIRDLS gravity waves for Dec 2006 and Feb 2007 were compared with the AVHRR OLR and the TRMM convective rainfall in figure 6.9 and 6.11, respectively. In contrast to Jan 2007, the peak amplitudes in Dec 2006 and Feb 2007 are a few degrees in latitude poleward shifted compared with the 200-OLR. This is somewhat less than the observed 10° poleward shift by *Jiang et al.* [2004b, 2005] using MLS data. The TRMM convective rainfall does not show clearly localized enhancement making the comparison with HIRDLS gravity waves difficult, because the life cycle of deep convection is characterized with developing stage, mature stage and dissipating stage. Different classes of clouds correspond to the deep convection at each stage. The dominant clouds cumulus, cumulonimbus and anvil cloud at the three stages may not always cause convective rainfall observed by the TRMM instrument at 15 km. Thus the 15 km TRMM rainfall in these two months is likely to underrepresent deep convection.

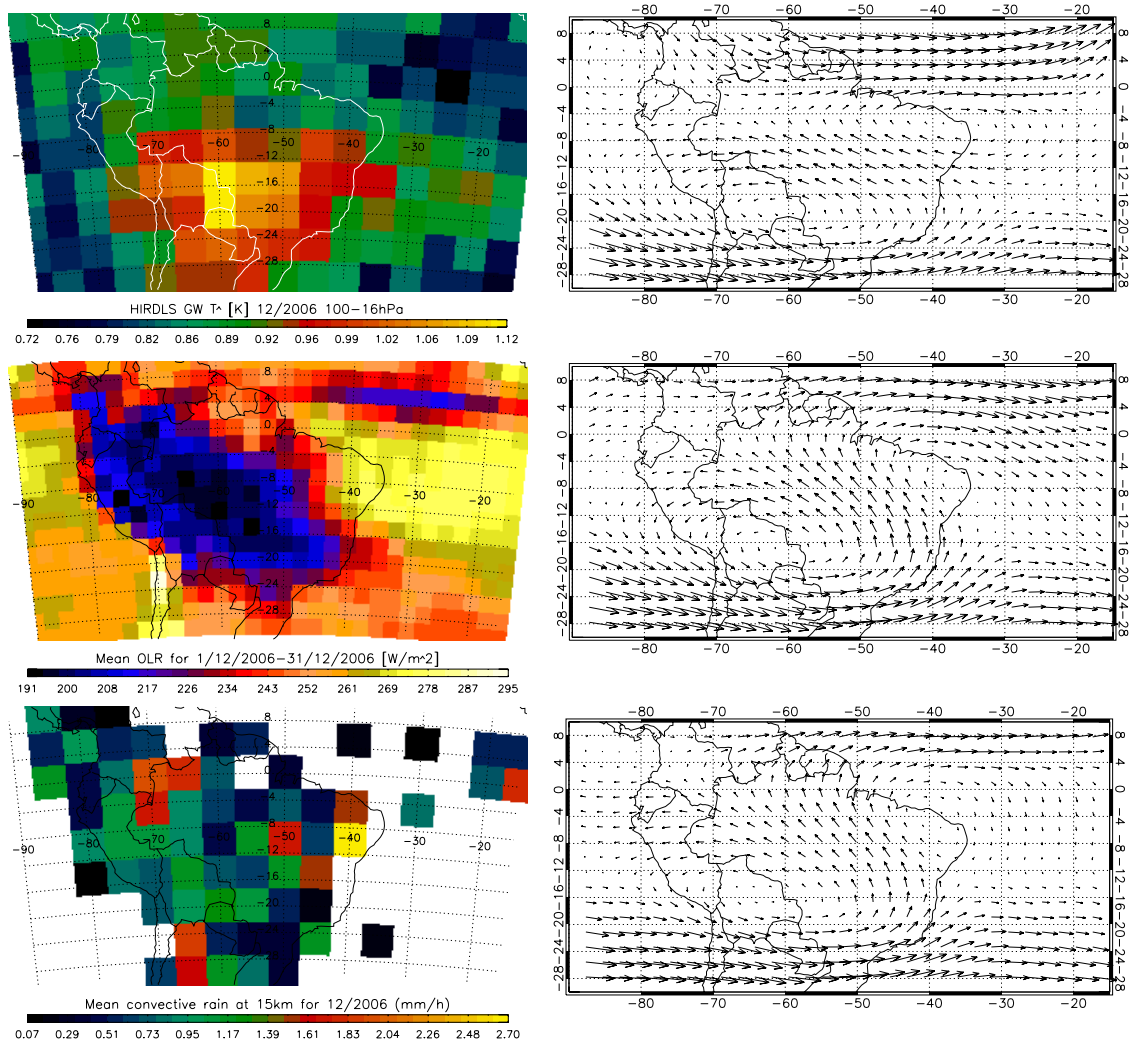


Figure 6.9 Left column: HIRDLS gravity wave temperature amplitudes (top), the AVHRR OLR (middle) and the TRMM convective rainfall at 15 km (bottom) for December 2006; and right column: monthly averaged winds at 100 hPa, 150 hPa and 250 hPa, from the top to bottom, respectively.

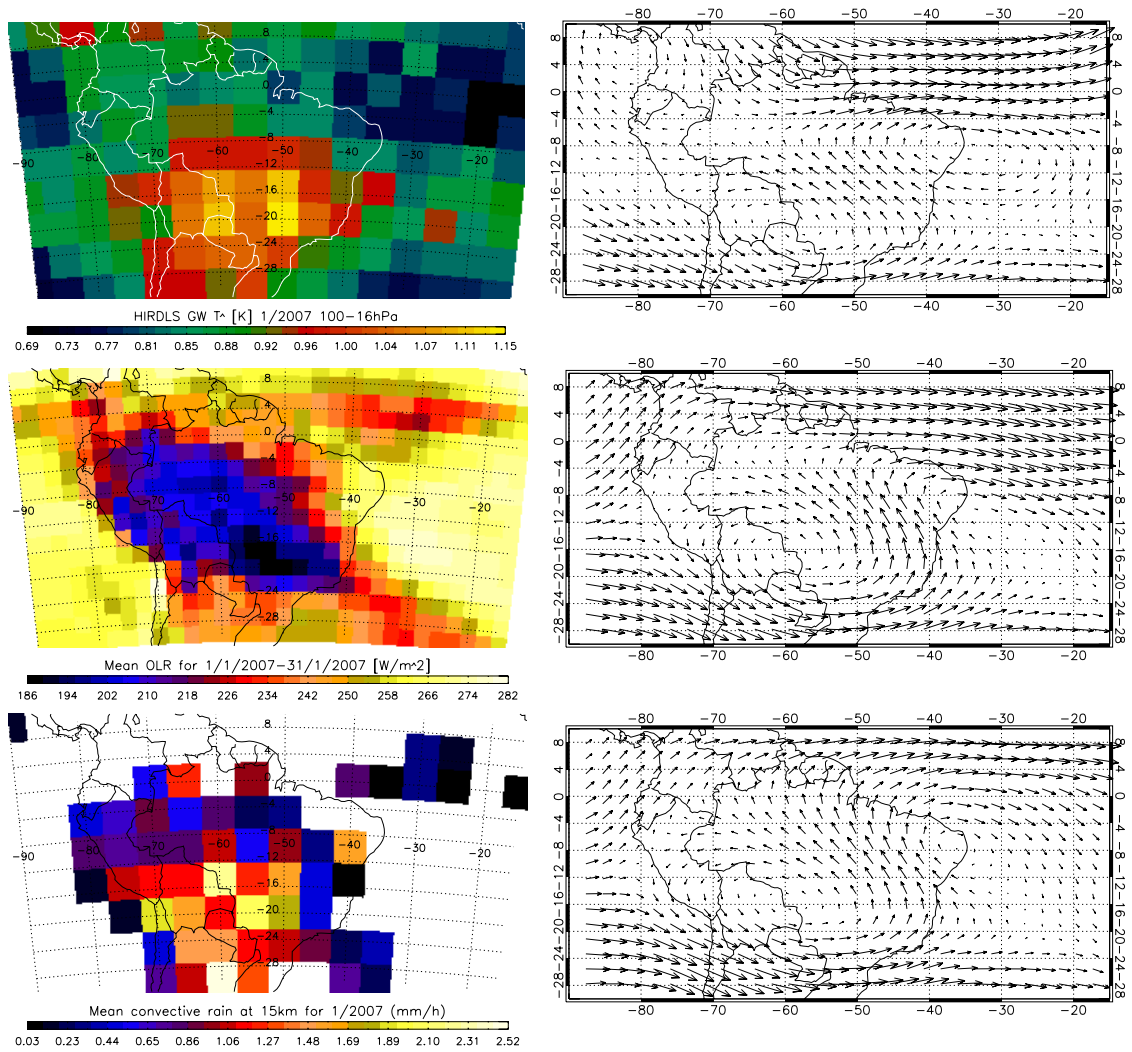


Figure 6.10 Left column: HIRDLS gravity wave temperature amplitudes (top), the AVHRR OLR (middle) and the TRMM convective rainfall at 15 km (bottom) for January 2007; and right column: monthly averaged winds at 100 hPa, 150 hPa and 250 hPa, from the top to bottom, respectively.

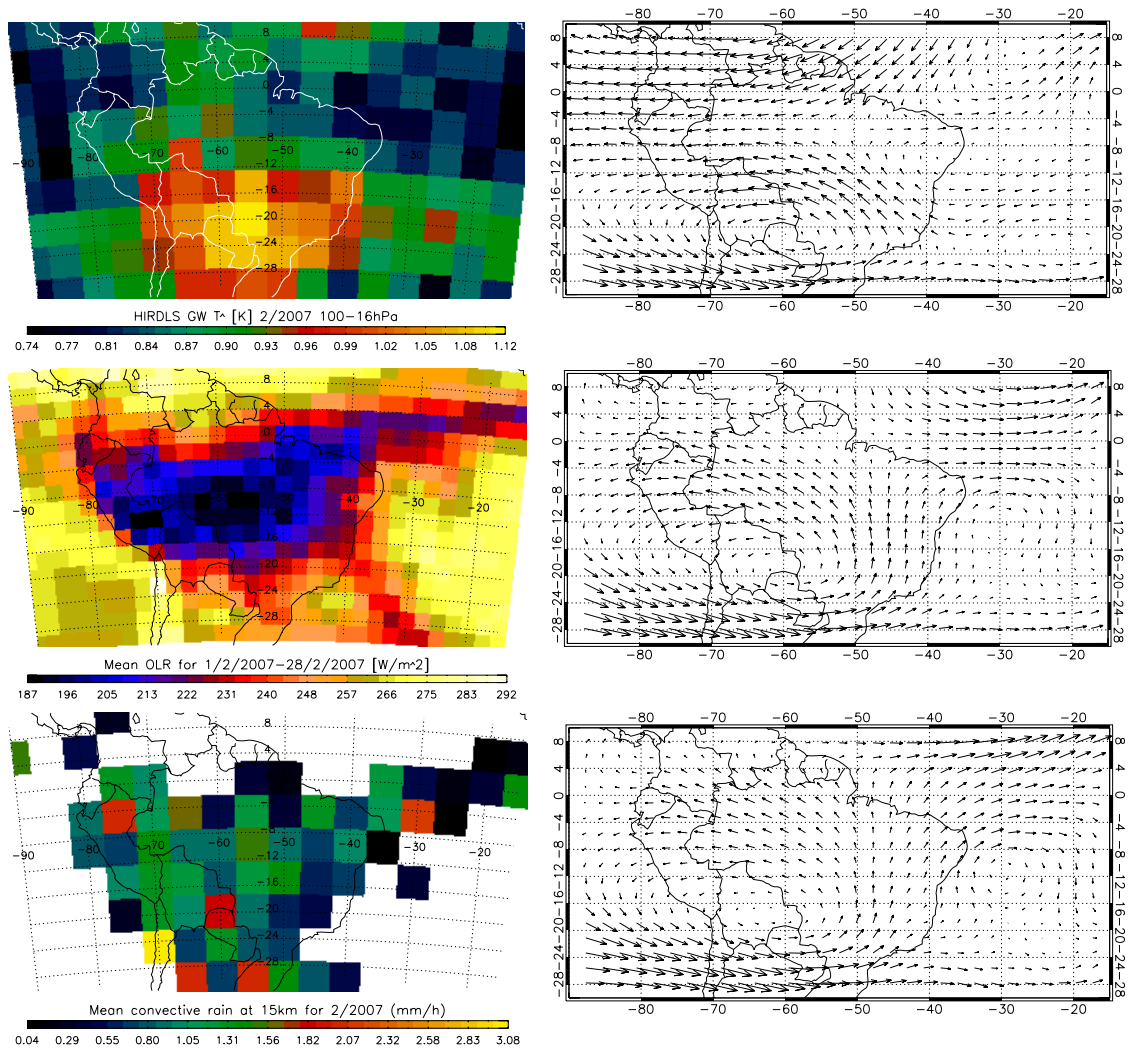


Figure 6.11 Left column: HIRDLS gravity wave temperature amplitudes (top), the AVHRR OLR (middle) and the TRMM convective rainfall at 15 km (bottom) for February 2007; and right column: monthly averaged winds at 100 hPa, 150 hPa and 250 hPa, from the top to bottom, respectively.

The wind vectors from the ECMWF operational analysis were also investigated for the gravity waves over tropical South America. The right panels of figures 6.9 to 6.11 are the monthly averaged winds at 100 hPa, 150 hPa and 250 hPa, from the top to bottom, respectively. The wind vector plots clearly show a mesoscale cyclone in each month which perfectly matches the geographic location of the enhanced gravity waves. This suggests that it might be the low OLR equatorward rather than the gravity waves poleward drifted away from the convective source supporting convectively generated gravity waves in these three months. The geographic agreement in the comparison between the gravity waves and the tropical cyclones also indicates vertical wave propagation. The same discussion that applied to Dec 2006 is suitable to Jan and Feb 2007, i.e. higher-frequency with larger vertical wavelength waves vertically propagating into the stratosphere. The monthly averaged vertical wavelengths over pressure levels 100 to 16 hPa for DJF 2006/7 are approximately 7.5 km corresponding to the enhanced temperature amplitudes.

Figures 6.12-14 show the zonally and meridionally averaged gravity waves for DJF 2006/7 compared with the ECMWF zonally and meridionally averaged vertical winds over the same region. The peak gravity wave temperature amplitudes in these three months grew with height without dissipation. By contrast, the MLS gravity waves over the tropics and subtropics by *Wu and Eckermann (2008)* show minima at  $\sim 30$  km. Comparison with both the zonally and meridionally averaged vertical winds shows that the peak gravity wave temperature amplitudes in DJF 2006/7 are clearly related to the upward air flow below 100 hPa. Above 100 hPa, the vertical winds are stable and steady. Whilst the aforementioned peak gravity waves in both Dec 2006 and Feb 2007 are slightly poleward shift compared with the 200-OLR, the good agreement between the enhanced gravity waves and the ECMWF vertical winds in geographic location indicates a deep convective source and vertical wave propagations.

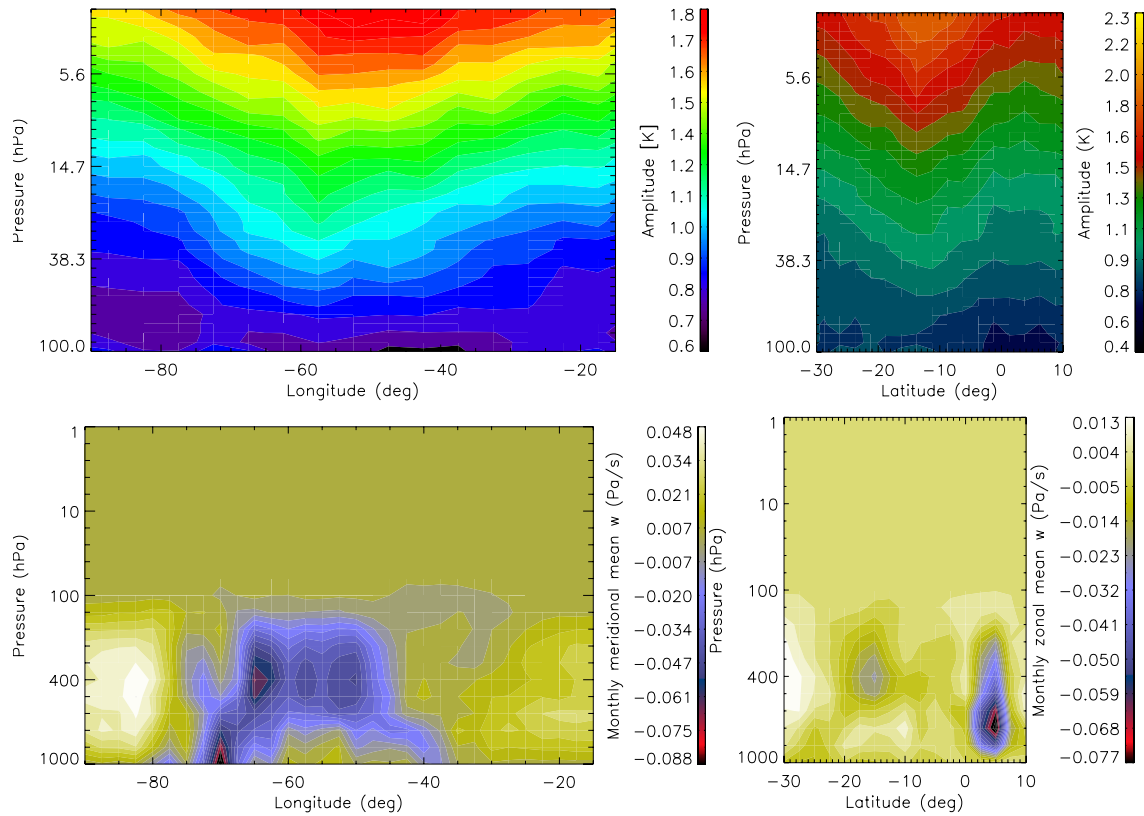


Figure 6.12 Dec 2006: meridionally and zonally averaged HIRDLS gravity wave temperature amplitudes in K (top left/right) and ECMWF vertical winds in Pa/s (bottom left/right, negative indicates ascending and positive indicates descending).

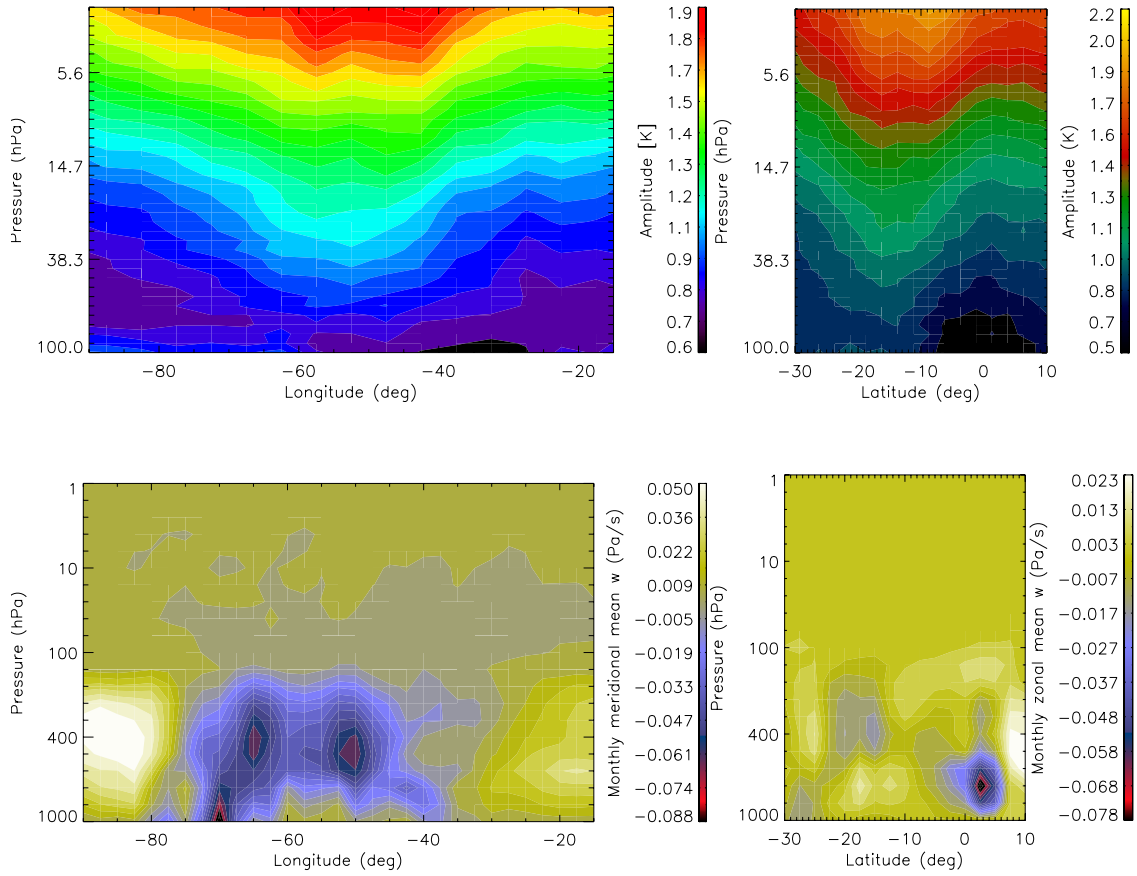


Figure 6.13 Jan 2007: meridionally and zonally averaged HIRDLS gravity wave temperature amplitudes in K (top left/right) and ECMWF vertical winds in Pa/s (bottom left/right, negative indicates ascending and positive indicates descending).

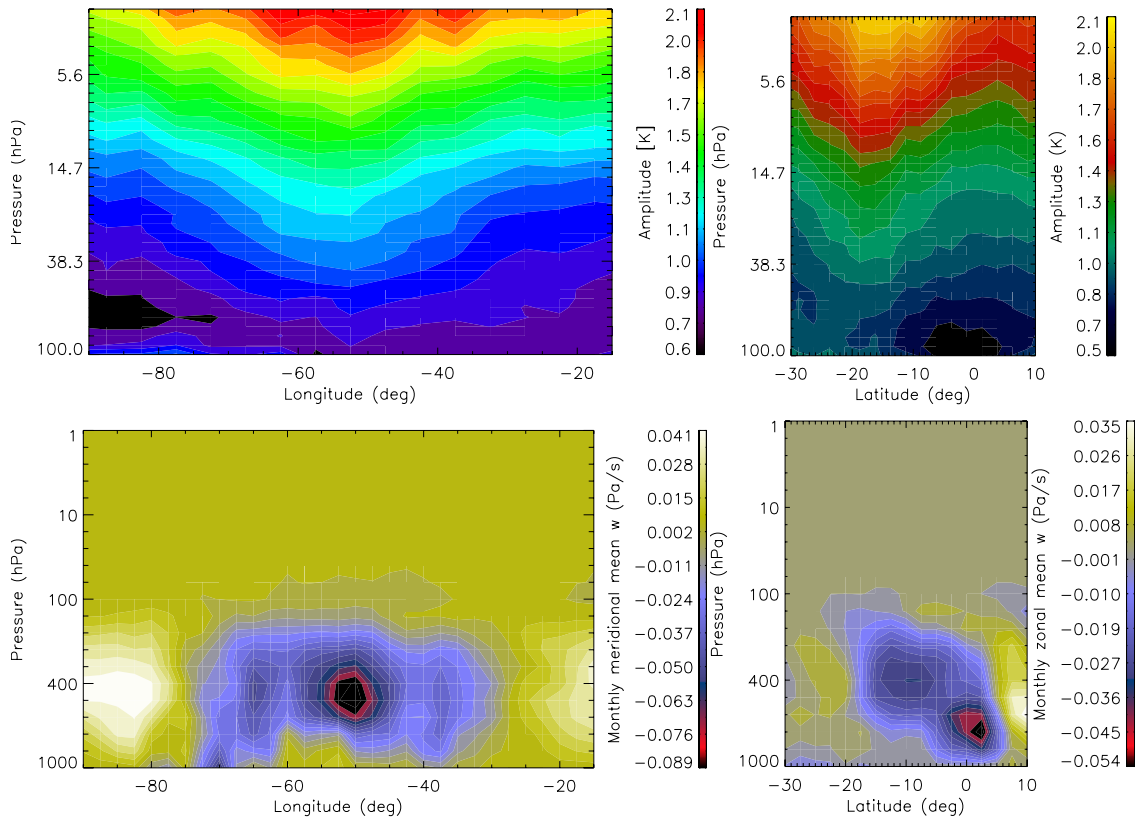


Figure 6.14 Feb 2007: meridionally and zonally averaged HIRDLS gravity wave temperature amplitudes in K (top left/right) and ECMWF vertical winds in Pa/s (bottom left/right, negative indicates ascending and positive indicates descending).

## 6.5 Summary

In this chapter, convective sources were investigated for the observed HIRDLS gravity waves over the tropics and tropical South America over the period DJF 2006/7, by comparing with the AVHRR OLR, the TRMM convective rainfall and the ECMWF winds. The peak gravity wave temperature amplitudes in Jan 2007 are in good agreement with the 200-OLR and the maximum convective rainfall at 15 km, indicating convectively radiated gravity waves observed in the stratosphere. The enhanced gravity waves match the enhanced convective rainfall in terms of geographical location implying vertical propagation. The comparison with the OLR for Dec 2006 and Feb 2007 shows a few degrees poleward drift in latitude, which is somewhat lower shifted than the observations by *Jiang et al* [2004b, 2005] using the MLS data. Moreover, the comparison with the ECMWF winds shows a good match in geographic location

between the HIRDLS observations and the mesoscale cyclones suggesting deep convective generation.

The zonally and meridionally averaged gravity waves show growing characteristics with altitude without dissipation in the stratosphere. The enhanced temperature amplitudes are present around the maximum amplitudes, indicating no significant impact from the background. Comparisons with the zonally and meridionally averaged ECMWF vertical winds show that the observed gravity waves over tropical South America are almost immediately above the updrifts below 100 hPa indicating convective excitation.

## Chapter 7

# Conclusions and Outlook

This thesis has studied stratospheric gravity waves and their global distribution, sources and propagation in the stratosphere using the satellite instrument, HIRDLS.

Gravity waves were extracted in terms of temperature perturbations from HIRDLS level 2 temperature measurements. The extraction was made by subtraction of a dynamic 31-day background field, followed by the application of a 1000 km along-track temperature filter. The dynamic 31-day background field worked as a high-pass filter to capture low frequency planetary-scale waves with periods longer than 31 days. Due to the dynamic characteristic of the background field, waves with shorter periods can also be attenuated. Subtraction of a background field of a reasonable period has been used in previous studies [e.g. *Fetzer and Gille, 1994, 1996; Eckermann and Preusse, 1999; Preusse et al., 2000, 2002; Ern et al., 2004, 2006; Alexander et al., 2008a*] to remove planetary-scale waves. After subtracting the background field, it was found in the tests that large-scale fluctuation structures can be retained by this process which are inconsistent with gravity waves and could be caused by a not completely removed background; any improvements in methodology at this stage will result in better results being obtained subsequently for the final analysed gravity wave parameters. Since the background field has blocked the planetary-scale waves with periods longer than 31 days, the retained large-scale fluctuation structures are very likely caused by higher frequency planetary-scale waves. The 1000 km along-track filter works as another high-pass filter to remove the higher frequency planetary-scale wave signal.

The combination of the background field and the 1000 km along-track filter made the extraction of gravity waves from HIRDLS temperature more complete than only subtraction of the background field and largely reduced planetary-scale wave-contamination. This made the methodology attractive. The resulting individual vertical profiles of gravity-wave temperature perturbations were then Fourier transformed (using

an FFT) to extract the gravity-wave temperature amplitudes and vertical wavelengths of  $\sim 2 - 16$  km.

A year-long record has been made for monthly mean amplitudes and vertical wavelengths. Global distribution, seasonal variation, sources and propagation of gravity waves have been investigated based on the year-long record of temperature amplitudes and wavelengths. The vertical wavelengths are, to the knowledge of the author the first observations of a year-long period of vertical wavelength, which together with the year-long record of temperature amplitudes will be a milestone in gravity wave climatologies. The findings from the investigations can be summarized as follows.

The observed wave activity is highly variable spatially with a pronounced seasonal dependence. Gravity waves are strong in the winter extratropical and high-latitude stratosphere and the summer tropical stratosphere. Some extratropical gravity wave activity is highly related to the major north-south or near north-south mountain ranges of the Earth. The investigation into gravity-wave activity in the winter extratropics indicates that orography is an important source of the waves in the extratropical stratosphere.

The peak gravity-wave wavelengths correspond closely with the peak amplitudes in terms of geographic location. In most months, the increased growth rates of amplitude with altitude in the winter extratropical stratosphere are significantly larger than those in the tropical stratosphere. Correspondingly, the wavelengths in the winter extratropical stratosphere grow faster than the wavelengths in the tropical stratosphere. These differences in the growth rates between low and high latitudes very likely reflected lower altitude sources in the extratropics and high latitudes while higher altitude sources in the tropics. The observations, over the whole year, are in good agreement with gravity wave climatologies.

The year-long record of temperature amplitudes has been either qualitatively or quantitatively compared with those available satellite observations from, for example MLS [*Wu and Eckermann, 2008*], CRISTA and SABER [*Preusse et al., 2006*] and the same satellite instrument but different method [*Alexander et al., 2008a*]. The comparisons show both differences for specific location, for example the difference with MLS observations over the tropics, and generally good agreement over most of the

globe. It should be noted that different techniques were used in the above observations. These different methods adopted in the observations can contribute to the differences between each other. Indeed, different satellite instruments with different characteristics are sensitive to different portions of the gravity wave spectrum. The contribution to the differences from this aspect is unavoidable but can be explained by the sensitivity of the instrument to different portions of the wave spectrum, which requires further work. Some differences caused by the observation techniques can be investigated based on gravity wave theories, for example the difference with MLS over the tropics was investigated by comparing with the convective activity represented by the MLS IWC (ice water content) used by *Wu and Eckermann* [2008] for seasonal variation of both gravity waves and convective activity. The results show that the HIRDLS gravity waves analysed using the method described in this thesis are better at matching the seasonal variation of convective activity than those of MLS.

The meaningful annual cycle of gravity waves presented has demonstrated the strength of the methodology described in this thesis. The systematic and regular oscillation in the HIRDLS radiometric signal that is caused by the motion of the blockage has been removed by the HIRDLS team by developing extra algorithms. The retrieved temperature has been extensively validated by the HIRDLS science team [*Gille et al.*, 2008]. The observed HIRDLS gravity waves presented in this thesis do not show any obvious signals of the oscillation.

Case studies over the southern Andes and the Cascade Range and the Rockies and the Himalayas are included for particular wave activity periods. The gravity waves over the southern Andes and the Cascade Range and the Rockies show orographic wave sources that are related to the strong westerly winds. These waves were refracted and clearly propagate downwind from the source regions. The results are clearly a challenge to the assumption of vertical propagation of orographic gravity waves in numerical models, such as *Palmer et al.*, [1986], *McFarlane*, [1987], and *Iwasaki et al.*, [1989]. The gravity waves over the Himalayas are summertime cyclone-associated waves suggesting a generation by convection sources.

Following the case studies, orographic gravity waves over the southern Andes for a three month period (JAS 2006) were thoroughly studied by comparing with model results from the UK Met Office unified model (MetUM<sup>®</sup>). The aim of the comparison

was to validate the observed gravity waves and to aid in the understanding of the application of observations in numerical models. The study was made by directly comparing the observed gravity wave temperature amplitudes with the temperature amplitudes from the orographic gravity-wave parameterization scheme in the MetUM. This avoided the calculation of momentum fluxes in which additional assumptions have to be made by using data from a single instrument. In the process of comparison, the operational parameterization scheme was modified by adjusting tunable parameters to result in three different off-line versions. Whilst the operational version of the parameterization scheme significantly under-predicts the observed wave motion in the stratosphere, much improved agreement has been obtained in the comparison with version 2 ( $F_{crit} = 4$ ,  $n_{\sigma} = 2.5$  and  $F_{sat} = 1$ ) and version 3 ( $F_{crit} = 1$ ,  $n_{\sigma} = 2$  and  $F_{sat} = 2$ ). The fact that these predictions are qualitatively similar to the observations suggests that the observed temperature fluctuations are indeed a result of mountain waves. This study demonstrates the utility of satellite measurements in constraining the tuning of mountain-wave drag parameterization schemes.

The much improved agreement with the modified versions suggests that a significant re-tuning of the operational mountain-wave drag scheme in the MetUM would be required in order to improve the representation of stratospheric orographic waves in the global forecasts. The satellite data have proved useful for the purposes of constraining the parameters which determine both the launch amplitude and the vertical structure of the wave amplitude. However, since both vertical and horizontal wave scales are required for the assessment of gravity wave effects in the stress [*Webster et al.*, 2003] in the model, further work will be necessary for obtaining reliable momentum fluxes with other instrument observations (e.g. observations from AIRS) involved for NWP or climate model performance.

Whilst reasonable agreement has been achieved, differences are found between the parameterization and observations above the southern Andes. The observations show minima in temperature amplitude just below 38 hPa that are not present in the parameterized gravity waves. The ECMWF winds suggest that the minima are very likely related to the vertical profile of winds and the background instability. Future work is needed to explore the real reasons causing the minima. Another important difference is that the observed waves show a marked downwind propagation which is

not represented by the column based parameterization. The enhanced temperature perturbations in the observations persist for a few thousand kilometres downwind of the mountains and across the Southern Ocean to the east of South America. Studies by *Preusse et al.* [2002] suggest that this downwind wave activity is likely to be associated with long horizontal wavelengths, whose vertical group velocity is sufficiently small that wave packets can be blown significant distances in the horizontal as they propagate vertically. The complete absence of these downwind waves in the OGW parameterization scheme highlights a deficiency in column based schemes [*Yan et al.*, submitted]. Further investigation will be required in order to determine the importance of this downwind propagation for NWP and climate modeling.

The convectively generated gravity waves over the tropics are very important for the equatorial QBO and SAO in the stratosphere and mesosphere. The HIRDLS gravity waves in the stratospheric tropics were investigated for convective sources over the period JJAS 2006 and NDJF 2006/7. The comparison with the AVHRR OLR shows that the enhanced temperature amplitudes are geographically above the 200-OLR region in the summer hemisphere. The comparison also shows a few-degrees poleward shift of the enhanced temperature amplitudes in both hemispheres, while there is not apparent shift in the zonal direction. The poleward shift has also been observed by *Jiang et al.* [2004b, 2005] who explained the observation as the result of the background wind filtering of the gravity wave propagating into the stratosphere and also the MLS gravity wave visibility function. *Fritts and Alexander* [2003] summarized convectively low-frequency waves in the middle atmosphere that may be away from the convective source at a large distance.

The convective gravity waves over the tropical South America are particularly interesting as a contrast to the orographic gravity waves over the southern Andes. In this study, the HIRDLS gravity waves in this area were compared with the AVHRR OLR, the TRMM convective rainfall and the ECMWF vertical winds over the period of DJF 2006/7. Although the enhanced gravity waves in Dec 2006 and Feb 2007 are slightly poleward shifted, the peak gravity wave temperature amplitudes in DJF 2006/7 are generally in good agreement with the 200-OLR. Except for Jan 2006 in which the location of the observed gravity waves matches the covered region of the TRMM maximum convective rainfall at 15 km, the comparison with Dec 2006 and Feb 2007

suggests under-represented convection in the 15 km TRMM data. Whilst poleward shift was observed for the tropics and tropical South America, the observed gravity waves perfectly match the geographical location of the mesoscale cyclones in the wind maps of DJF 2006/7. The comparison with the ECMWF vertical winds shows a good relationship between the enhanced stratospheric gravity waves and the upward air flow below 100 hPa.

The comparisons with the deep convective indicators of AVHRR OLR and TRMM convective rainfall and the ECMWF winds indicate that the observed HIRDLS gravity waves over the tropical South America are very likely generated by convective sources. The same conclusion can be drawn by the observed gravity waves over the tropics. These convective gravity waves are probably higher-frequency with larger vertical wavelength waves vertically propagating into the stratosphere. The monthly averaged vertical wavelengths over pressure levels 100 to 16 hPa for DJF 2006/7 are approximately 7.5 km corresponding to the enhanced temperature amplitudes. The vertical propagation into the stratosphere implies that the convective gravity waves were less influenced by the background winds, which makes the waves markedly different from the orographic gravity waves over the southern Andes.

Although absolute values of gravity wave momentum fluxes have been estimated using data from a single satellite instrument [e.g. *Ern et al.*, 2004], an additional assumption has to be made for horizontal wavelengths. This caused the estimated momentum fluxes suffering from large uncertainty [*Alexander et al.*, 2008a]. In the thesis, temperature amplitudes and vertical wavelengths have been derived from HIRDLS temperature data. In the future, horizontal wavelength of gravity waves should be derived using measurements from a nadir-view satellite instrument, in order to calculate momentum fluxes to be used directly in gravity wave parameterization schemes in numerical models. Ideally, both a limb and nadir-view instruments simultaneously view the same wave field for the vertical and horizontal scales.

In order to utilize observations for the constraints on gravity wave parameterizations in global models, wave generation mechanisms should be understood. This requires understanding of the sources for the observed gravity waves. The thesis discussed studies of orographic gravity waves over the southern Andes and convective gravity waves in the tropics. For a better understanding of global source distribution, in

the future, gravity waves over other major mountains and convective gravity waves at higher latitudes should be investigated and compared with the results presented in the thesis. In addition, other sources such as fronts and wind shear excited gravity waves also need to be understood. Source studies of gravity waves will also require complementary observations from other techniques such as aircrafts, radars and radiosondes. Therefore, combining satellite observations and the observations from other techniques could be future work. Models can always be a good tool to reveal the generation mechanism of observations. So comparing observations with model simulations in the future will definitely benefit gravity wave source studies.

# Appendix A

## A General Gravity-Wave Solution to Equations of Motion

Based on a simple linear theory, atmospheric gravity waves can be described as small departures from a stably stratified background state. When an air parcel is displaced away from its equilibrium position, the consequent buoyancy acts as restoring force cause gravity wave oscillations. A general gravity wave solution can then be derived from the linearized forms of the equations of motion.

The primary equations of motion in Cartesian coordinates  $(x, y, z)$  are given as follows [*Holton, 1992*]

$$\frac{du}{dt} - fv + \frac{1}{\rho} \frac{\partial p}{\partial x} = X, \quad \text{A-1}$$

$$\frac{dv}{dt} + fu + \frac{1}{\rho} \frac{\partial p}{\partial y} = Y, \quad \text{A-2}$$

$$\frac{dw}{dt} + \frac{1}{\rho} \frac{\partial p}{\partial z} + g = 0, \quad \text{A-3}$$

$$\frac{1}{\rho} \frac{d\rho}{dt} + \frac{\partial u}{\partial x} + \frac{\partial v}{\partial y} + \frac{\partial w}{\partial z} = 0, \quad \text{A-4}$$

$$\frac{d\theta}{dt} = Q, \quad \text{A-5}$$

where  $d/dt$  represents a total derivative;  $(u, v, w)$  is the fluid velocity vector; and the terms  $X, Y$  and  $Q$  represent unspecified forcings that could include wave-driven forces and diffusive missing effects accompanying wave dissipation. Equations A-1 to A-3 follow from conservation of momentum. Equations A-4 and A-5 follow from

conservation of mass and thermal energy, respectively. The remaining symbols have the same meanings given in the chapters.  $f = 2\Omega \sin \phi$  is the Coriolis parameter where  $\Omega$  is the Earth rotation rate and  $\phi$  is latitude. These five equations together with the definition of potential temperature  $\theta$  (equation 2-7) completely describe inviscid fluid motions.

By neglecting the forcings  $X, Y$  and  $Q$ , equations A-1 to A-5 and 2-7 can be linearized about a horizontally uniform hydrostatic basic state with background wind  $(\bar{u}, \bar{v}, 0)$ , potential temperature  $\bar{\theta}$ , pressure  $\bar{p}$  and density  $\bar{\rho}$  varying only in  $z$  as follows

$$\frac{Du'}{Dt} + w' \frac{\partial \bar{u}}{\partial z} - f v' + \frac{\partial}{\partial x} \left( \frac{p'}{\bar{\rho}} \right) = 0, \quad \text{A-6}$$

$$\frac{Dv'}{Dt} + w' \frac{\partial \bar{v}}{\partial z} + f u' + \frac{\partial}{\partial y} \left( \frac{p'}{\bar{\rho}} \right) = 0, \quad \text{A-7}$$

$$\frac{Dw'}{Dt} + \frac{\partial}{\partial z} \left( \frac{p'}{\bar{\rho}} \right) - \frac{1}{H} \left( \frac{p'}{\bar{\rho}} \right) + g \frac{\rho'}{\bar{\rho}} = 0, \quad \text{A-8}$$

$$\frac{D}{Dt} \left( \frac{\theta'}{\bar{\theta}} \right) + w' \frac{N^2}{g} = 0, \quad \text{A-9}$$

$$\frac{D}{Dt} \left( \frac{\rho'}{\bar{\rho}} \right) + \frac{\partial u'}{\partial x} + \frac{\partial v'}{\partial y} + \frac{\partial w'}{\partial z} - \frac{w'}{H} = 0, \quad \text{A-10}$$

$$\frac{\theta'}{\bar{\theta}} = \frac{1}{c_s^2} \left( \frac{p'}{\bar{\rho}} \right) - \frac{\rho'}{\bar{\rho}}. \quad \text{A-11}$$

Here  $D/Dt$  is the linearized form of the time derivative,

$$\frac{D}{Dt} = \frac{\partial}{\partial t} + \bar{u} \frac{\partial}{\partial x} + \bar{v} \frac{\partial}{\partial y}, \quad \text{A-12}$$

primed quantities are perturbations to the background state,  $c_s$  is the sound speed, and  $N$  is the buoyancy frequency given by 2-7.

If we assume the background flow represented by  $(\bar{u}, \bar{v})$  and  $N$  vary only slowly over a wave cycle in the vertical (the WKB approximation [e.g. Gill, 1982]) and also assume the gravity wave solutions have the form

$$\left( u', v', w', \frac{\theta'}{\bar{\theta}}, \frac{p'}{\bar{p}}, \frac{\rho'}{\bar{\rho}} \right) = (\tilde{u}, \tilde{v}, \tilde{w}, \tilde{\theta}, \tilde{p}, \tilde{\rho}) \cdot \exp \left[ i(kx + ly + mz - \omega t) + \frac{z}{2H} \right], \quad \text{A-13}$$

the linearized equations A-6 to A-11 yield a set of equations for  $(\tilde{u}, \tilde{v}, \tilde{w}, \tilde{\theta}, \tilde{p}, \tilde{\rho})$ :

$$-i\hat{\omega}\tilde{u} - \tilde{f}\tilde{v} + ik\tilde{p} = 0, \quad \text{A-14}$$

$$-i\hat{\omega}\tilde{v} + \tilde{f}\tilde{u} + il\tilde{p} = 0, \quad \text{A-15}$$

$$-i\hat{\omega}\tilde{w} + \left( im - \frac{1}{2H} \right) \tilde{p} = -g\tilde{\rho}, \quad \text{A-16}$$

$$-i\hat{\omega}\tilde{\theta} + (N^2/g)\tilde{w} = 0, \quad \text{A-17}$$

$$-i\hat{\omega}\tilde{\rho} + ik\tilde{u} + il\tilde{v} + \left( im - \frac{1}{2H} \right) \tilde{w} = 0, \quad \text{A-18}$$

$$\tilde{\theta} = \tilde{p}/c_s^2 - \tilde{\rho}, \quad \text{A-19}$$

where  $\hat{\omega} = \omega - k\bar{u} - l\bar{v}$  is the intrinsic frequency that defined as the frequency of a wave measured by an observer drifting with the fluid  $(\bar{u}, \bar{v})$ . Setting the imaginary coefficients to zero, equations A-14 to A-19 can be expressed as a single equation for the perturbation vertical velocity amplitude

$$\frac{g}{c_s^2} = \frac{1}{H} - \frac{N^2}{g}, \quad \text{A-20}$$

$$\hat{\omega}^2 \left( k^2 + l^2 + m^2 + \frac{1}{4H^2} - \frac{(\hat{\omega}^2 - f^2)}{c_s^2} \right) = N^2(k^2 + l^2) + f^2 \left( m^2 + \frac{1}{4H^2} \right). \quad \text{A-21}$$

It is noted that both gravity waves and acoustic waves exist in equation A-21. The acoustic waves can be eliminated by treating the atmosphere as a uniform and

incompressible (i.e.  $c_s \rightarrow \infty$ ) fluid in the horizontal direction, but a compressible fluid in hydrostatic equilibrium in the vertical direction. This gives the gravity wave dispersion relation,

$$m^2 = \frac{(k^2 + l^2)(N^2 - \hat{\omega}^2)}{(\hat{\omega}^2 - f^2)} - \frac{1}{4H^2}. \quad \text{A-22}$$

The dispersion reveals the relationship between the gravity-wave characteristics (wave numbers and frequency) and the background state properties ( $(\bar{u}, \bar{v})$  and  $N$ ). If gravity wave propagate vertically,  $(k, l, m)$  are real, and the intrinsic frequency is within the range  $N > \hat{\omega} > |f|$ . The wave with frequency in this spectrum can be important to middle atmospheric dynamics.

The group velocity of gravity waves that describes energy transport and wave packet propagation can be given as

$$v_{gx} = \frac{\partial \omega}{\partial k} = \bar{u} + \frac{k(N^2 - \hat{\omega}^2)}{\hat{\omega} \left( k^2 + l^2 + m^2 + \frac{1}{4H^2} \right)}, \quad \text{A-23}$$

$$v_{gy} = \frac{\partial \omega}{\partial l} = \bar{v} + \frac{l(N^2 - \hat{\omega}^2)}{\hat{\omega} \left( k^2 + l^2 + m^2 + \frac{1}{4H^2} \right)}, \quad \text{A-24}$$

$$v_{gz} = \frac{\partial \omega}{\partial m} = \frac{-m(\hat{\omega}^2 - f^2)}{\hat{\omega} \left( k^2 + l^2 + m^2 + \frac{1}{4H^2} \right)}. \quad \text{A-25}$$

The relations between perturbation amplitudes of the different variables are described by polarization relations that can be derived from equations (A-14) to (A-19).

The polarization relations between  $\tilde{u}, \tilde{v}, \tilde{w}, \tilde{p}$  and  $\tilde{\theta}$  are

$$\tilde{u} = \left( \frac{i\tilde{\omega}k - fl}{i\tilde{\omega}l + fk} \right) \tilde{v}, \quad \text{A-26}$$

$$\tilde{w} = \frac{\left(m - \frac{i}{2H}\right)\tilde{\omega}}{N^2 - \tilde{\omega}^2} \tilde{p}, \quad \text{A-27}$$

$$\tilde{p} = \begin{pmatrix} \tilde{\omega}^2 - f^2 \\ \tilde{\omega}k + ifl \end{pmatrix} \tilde{u} = \begin{pmatrix} \tilde{\omega}^2 - f^2 \\ \tilde{\omega}l - ifk \end{pmatrix} \tilde{v}, \quad \text{A-28}$$

$$\tilde{\theta} = \frac{N^2}{i\tilde{\omega}g} \tilde{w}. \quad \text{A-29}$$

## Appendix B

# The operational scheme of OGW parameterization in the MetUM

The MetUM (Met Office Unified Model®) has been described in *Davies et al.* [2005]. An orographic gravity wave-relevant summary has been given in *Yan et al.* [submitted]. For the period of interest (JAS 2006), the operational global forecasts used a grid spacing of  $0.5625^\circ \times 0.375^\circ$  in the zonal and meridional directions, respectively. This equates to a grid spacing of approximately 40 km in both directions at  $50^\circ\text{S}$ . The drag force exerted on the flow which results from gravity waves generated by the sub-grid orography cannot be resolved on the model grid and therefore must be parameterized. Note that due to the use of a long timestep in the operational MetUM (facilitated by semi-implicit time integration coupled with a semi-Lagrangian advection scheme) fewer gravity waves are in fact resolved by the model than might be expected from consideration of the grid spacing alone. Essentially, OGW (orographic gravity-wave) activity is heavily damped and this is true even of waves whose horizontal and vertical wavelengths are sufficiently long that, theoretically, they should be well resolved on the model grid. The representation of stratospheric OGWs in the operational forecast, therefore, relies almost entirely on the parameterization scheme.

The MetUM orographic scheme was described in detail by *Webster et al.* [2003] and also introduced in *Yan et al.* [submitted]. The OGW parameterization is based on the ideas of *McFarlane* [1987]. The Earth topography used in the MetUM is obtained from the 30 arcsecond resolution ‘Global Land One kilometre Base Elevation’ (GLOBE) dataset [*GLOBE task team et al.*, 1999]. The investigation by *Davis and Brown* [2001] indicated that two-grid-length features cannot be adequately resolved, whilst six-grid-length features can be adequately resolved. Therefore, a scale-selective filter is applied to the orographic fields in the MetUM to remove near-grid-scale (below six-grid-length) features.

The surface pressure drag due to the sub-grid orography is partitioned into a blocked-flow component and an OGW drag component. A proportion of the low-level flow is assumed to rise across the summits of the sub-grid mountains (OGW component), with motion in the very lowest layers forced around the mountain flanks (blocked-flow component). The depth of the summit region of the OGW component is determined by the Froude number:

$$F = \frac{U}{n_\sigma \sigma N} \quad \text{B-1}$$

where  $U$  and  $N$  are a depth averaged wind speed and Brunt-Väisälä frequency, respectively, measured from the ground up to  $n_\sigma \sigma$ , a measure of the sub-grid mountain height.  $\sigma$  is the standard deviation of the sub-grid mountains from the model grid-box mean height. The parameter  $n_\sigma$  is a tunable constant that is set to 2.5 in the operational scheme. The OGW amplitude is assumed to be proportional to the depth of the summit region.

In the MetUM, OGWs are launched for every model grid box over land at each model timestep. When  $F$  is larger than a critical value,  $F_{crit}$ , the flow is assumed to contain sufficient kinetic energy to rise entirely over the summits of the sub-grid mountains. In this situation the vertical displacements,  $\eta$ , associated with the gravity waves are equal to the sub-grid mountain height,  $n_\sigma \sigma$ . Under strongly stratified conditions, when  $F \leq F_{crit}$ , a proportion of the flow is assumed to be diverted around the mountain sides and only the flow above a dividing streamline [Snyder *et al.*, 1985] passes over the summits. In this case the effective height of the sub-grid mountains is reduced to  $\eta = n_\sigma \sigma F / F_{crit}$  and the amplitude of the parameterized gravity-wave vertical displacements are reduced in the same way. It should be noted that the amplitude of the gravity waves is proportional to  $\eta$  rather than the full depth of the sub-grid mountains. Physical understanding of stratified flows around mountains would suggest that  $F_{crit}$  should be around unity [e.g. Smith, 1980]. However, tuning considerations have led to the adoption of a value of  $F_{crit} = 4$  in the operational NWP scheme.

The gravity-wave propagation aspects of the scheme are based on the ideas of *McFarlane* [1987]. The waves are assumed to be steady and monochromatic, with a horizontal wave vector aligned with the depth averaged low-level horizontal wind vector, again averaged between the ground and the height  $n_\sigma \sigma$ . Coriolis effects are neglected and the horizontal wavelength is assumed to be sufficiently long that the wave motion is hydrostatically balanced, implying that the wave energy will radiate vertically above the sub-grid mountains and thus remain within the grid column. This approximation conveniently allows each grid column to be treated independently (since no wave energy is exchanged between adjacent columns) but clearly does not allow for the lateral propagation of wave energy. In the absence of wave breaking, the change in wave amplitude between adjacent grid levels is determined by the decay of air density with altitude (which results in a growth of wave amplitude with increasing height) and changes in both the Brunt-Väisälä frequency and the background wind. Decreases in the wind (resolved in the direction of the horizontal wave vector) will result in a growth in wave amplitude, as will decreases in the Brunt Väisälä frequency. Diagnosis of wave breaking and the deposition of wave stress follows that described by *Gregory et al.* [1998]. Wave breaking is assumed to take place when the local Froude number,  $U/(\eta N)$ , falls below a critical value,  $F_{sat}$ . When this occurs a proportion of the wave stress is exerted on the flow and the wave amplitude is reduced accordingly such that  $U/(\eta N) = F_{sat}$ . Note that the current operational implementation of the *Webster et al.* [2003] scheme (implemented operationally in August 2002) is primarily aimed at the representation of the large amplitude gravity waves generated in low Froude number cases, where wave breaking is likely to take place close to the mountain tops. This has been observed in several numerical and theoretical studies [*Smith*, 1980; *Miranda and James* 1992]. Since the waves which propagate away from low-level breaking regions are themselves likely to be close to the point of breaking, in the operational scheme it is assumed that the wave field launched by the mountains is in fact already saturated. This is equivalent to setting  $F_{sat}$  to the low-level value of  $U/(\eta N)$ . At the time of implementation, attempts to relax this assumption resulted in a significant degradation in forecast skill, particularly over most major mountain ranges such as the Himalayas. Whilst this saturation assumption might seem appropriate for the large amplitude waves (which may make the dominant contribution to the drag), for the smaller amplitude waves corresponding to larger Froude numbers, it is somewhat questionable. In

assessing the performance of the scheme against the HIRDLS observations, it will therefore be important to understand the impact of this assumption [*e.g. Yan et al.*, submitted].

## References:

Alexander, M. J. and L. Pfister (1995), Gravity wave momentum flux in the lower stratosphere over convection, *Geophys. Res. Lett.*, **22**, 2029–2032.

Alexander, M. J., J. R. Holton and D. R. Durran (1995), The gravity wave response above deep convection in a squall line simulation, *J. Atmos. Sci.*, **52**, 2212–2226.

Alexander, M. J. and K. H. Rosenlof (1996), Nonstationary gravity wave forcing of the stratospheric zonal mean wind, *J. Geophys. Res.*, **101**, 23,465–23,474.

Alexander, M. J. and J. R. Holton (1997), A model study of zonal forcing in the equatorial stratosphere by convectively induced gravity waves, *J. Atmos. Sci.*, **54**, 408–419.

Alexander, M. J. (1998), Interpretations of observed climatological patterns in stratospheric gravity wave variance, *J. Geophys. Res.*, **103**, 8627–8640.

Alexander, M. J. and T. J. Dunkerton (1999), A spectral parameterization of mean-flow forcing due to breaking gravity waves, *J. Atmos. Sci.*, **56**, 4167–4182, doi:10.1175/1520-0469(1999)056<4167:ASPOMF>2.0.CO;2.

Alexander, M. J., J. H. Beres and L. Pfister (2000), Tropical stratospheric gravity wave activity and relationships to clouds. *J. Geophys. Res.*, **105**, 22299–22309.

Alexander, M. J. and R. A. Vincent (2000), Gravity waves in the tropical lower stratosphere: A model study of seasonal and interannual variability, *J. Geophys. Res.*, **105**, 22,299–22,310.

Alexander, M. J., P. T. May and J. H. Beres (2004), Gravity waves generated by convection in the Darwin area during the Darwin Area Wave Experiment, *J. Geophys. Res.*, **109** (D20), D20S04, doi:10.1029/2004JD004729.

Alexander, M. J. and C. Barnet (2007), Using satellite observations to constrain gravity wave parameterizations for global models, *J. Atmos. Sci.*, **64**, 1652–1665.

- Alexander, M. J. and H. Teitelbaum (2007), Observation and analysis of a large amplitude mountain wave event over the Antarctic peninsula, *J. Geophys. Res.*, **112**, D21103, doi:10.1029/2006JD008368.
- Alexander, M. J., J. Gille, C. Cavanaugh, M. Coffey, C. Craig, T. Eden, G. Francis, C. Halvorson, J. Hannigan, R. Khosravi, D. Kinnison, H. Lee, S. Massie, B. Nardi, J. Barnett, C. Hepplewhite, A. Lambert and V. Dean (2008a), Global estimates of gravity wave momentum flux from High Resolution Dynamics Limb Sounder observations, *J. Geophys. Res.*, **113**, D15S18, doi:10.1029/2007JD008807.
- Alexander, S. P., T. Tsuda, Y. Shibagaki and T. Kozu (2008b), Seasonal gravity wave activity observed with the Equatorial Atmosphere Radar and its relation to rainfall information from the Tropical Rainfall Measuring Mission, *J. Geophys. Res.*, **113**, D02104, doi:10.1029/2007JD008777.
- Alexander, M. J., S. D. Eckermann, D. Broutman and J. Ma (2009), Momentum flux estimates for South Georgia Island mountain waves in the stratosphere observed via satellite, *Geophys. Res. Lett.*, **36**, L12816, doi:10.1029/2009GL038587.
- Andrews, D. G., J. R. Holton and C. B. Leovy (1987), *Middle Atmosphere Dynamics*, Academic press, London.
- Aumann, H. and R. Pagano (1994), Atmospheric infrared sounder on Earth observing system. *Opt. Eng.*, **33**, 776–784.
- ATBD-HIR-01*, Calibration and Geo-location of HIRDLS radiances, 1999.
- Bacmeister, J. T. and M. R. Schoeberl (1989), Breakdown of vertically propagating two-dimensional gravity waves forced by orography. *J. Atmos. Sci.*, **46**, 2109–2134.
- Bacmeister, J. T., M. R. Schoeberl, L. R. Lait, P. A. Newman and B. L. Gary (1990a), Small-scale waves encountered during AASE, *Geophys. Res. Lett.*, **17**, 349–352.
- Bacmeister, J. T., M. R. Schoeberl, L. R. Lait, P. A. Newman and B. L. Gary (1990b), ER-2 mountain wave encounter over Antarctica: Evidence for blocking, *Geophys. Res. Lett.*, **17**, 81–84.

## References

---

- Bacmeister, J. T. (1993), Mountain-wave drag in the stratosphere and mesosphere inferred from observed winds and a simple mountain-wave parameterization scheme, *J. Atmos. Sci.*, **50**, 377–399.
- Bacmeister, J. T., S. D. Eckermann, P. A. Newman, L. Lait, K. R. Chan, M. Loewenstein, M. H. Proffitt and B. L. Gary (1996), Stratospheric horizontal wavenumber spectra of winds, potential temperature, and atmospheric tracers observed by high-altitude aircraft, *J. Geophys. Res.*, **101**, 9441–9470.
- Barath, F. T. et al. (1993), The upper atmosphere research satellite Microwave Limb Sounder instrument, *J. Geophys. Res.*, **98**, 10751-10762, 1993.
- Blumen, W. and Hart, J. E. (1988), Airborne Doppler lidar wind field measurements of waves in the lee of Mount Shasta. *J. Atmos. Sci.* **45**: 1571-1583.
- Bowman, K. P., A. B. Phillips and G. R. North (2003), Comparison of TRMM rainfall retrievals with rain gauge data from the TAO/TRITON buoy array, *Geophys. Res. Lett.*, **30**(14), 1757, doi:10.1029/2003GL017552.
- Carslaw, K. S., T. Peter, J. T. Bacmeister and S. D. Eckermann (1999), Widespread solid particle formation by mountain waves in the Arctic stratosphere, *J. Geophys. Res.*, **104**, 1827– 1836.
- Chadwick, R. B. and E. E. Gossard (1986), Radar probing and measurement of the planetary boundary layer: Part I. Scattering from refractive index irregularities, *In Probing the Atmospheric Boundary Layer*, D. H. Lenschow, ed., pp. 163-182. Boxtton, MA: Am. Meteorological Soc.
- Chan, K. R., L. Pfister, T. P. Buil, S. W. Bowen, J. Dean-Day, B. L. Gary, D. W. Fahey, K. K. Kelly, C. R. Webster and R. D. May (1993), A case study of the mountain lee wave event of January 6, 1992, *Geophys. Res. Lett.*, **20**, 2551–2554.
- Chane-Ming, F., G. Roff, L. Robert and J. Leveau (2002), Gravity wave characteristics over Tromelin Island during the passage of cyclone Hudah, *Geophys. Res. Lett.*, **29**(6), 1094, doi:10.1029/2001GL013286.

- Charney, J. D. and J. G. Drazin (1961), Propagation of planetary-scale disturbances from the lower into the upper atmosphere, *J. Geophys. Res.*, **66**, 83-109.
- Chun, H.-Y. and Baik, J.-J. (1998), Momentum flux by thermally induced internal gravity waves and its approximation for large-scale models. *J. Atmos. Sci.* **55**: 3299-3310.
- Clark, T. L., T. Hauf and J. P. Kuettner (1986), Convectively forced internal gravity waves: Results from two-dimensional numerical experiments, *Q. J. R. Meteorol. Soc.*, **112**, 899–925.
- Collis, R. T. H. Fernald, F. G. and Alder, J. E. (1968), Lidar observations of Sierra-wave conditions. *J. Appl. Meteorol.* **7**:227-233.
- Corby, G. A. (1957), A preliminary study of atmospheric waves using radiosonde data. *Q. J. R. Meteorol. Soc.* **83**: 49-60.
- de la Torre, A., H. Teitelbaum and F. Vial (1996), Stratospheric and tropospheric wave measurements near the Andes mountains, *J. Atmos. Terres. Phys.*, **58**, 521–530.
- Dewan, E. M., R. H. Picard, R. R. O\_Neil, H. A. Gardiner, J. Gibson, J. D. Mill, E. Richards, M. Kendra and W. O. Gallery (1998), MSX satellite observations of thunderstorm-generated gravity waves in mid-wave infrared images of the upper stratosphere, *Geophys. Res. Lett.*, **25**, 939–942.
- Davies, T., M. J. P. Cullen, A. J. Malcolm, M. H. Mawson, A. Staniforth, A. A. White and N. Wood (2005), A new dynamical core for the Met Office's global and regional modelling of the atmosphere. *Q. J. R. Meteorol. Soc.*, **131**, 1759-1782.
- Davies, L. A. and A. R. Brown (2001), Assessment of which scales of orography can be credibly resolved in a numerical model. *Q. J. R. Meteorol. Soc.*, **127**, 1225–1237.
- Dörnbrack, A., M. Leutbecher, R. Kivi and E. Kyrö (1999), Mountain wave induced record low stratospheric temperatures above northern Scandinavia, *Tellus*, **51a**, 951–963.

- Dörnbrack, A., M. Leutbecher, J. Reichardt, A. Behrendt, K. P. Müller and G. Baumgarten (2001), Relevance of mountain wave cooling for the formation of polar stratospheric clouds over Scandinavia: Mesoscale dynamics and observations for January 1997, *J. Geophys. Res.*, **106**, 1569–1581.
- Dörnbrack, A. and M. Leutbecher (2001), Relevance of mountain wave cooling for the formation of polar stratospheric clouds over Scandinavia: A 20 year climatology, *J. Geophys. Res.*, **106**, 1583–1593.
- Drummond, J. R., J. T. Houghton, G. D. Peskett, C. D. Rodgers, M. J. Wale, J. G. Whitney and E. J. Williamson (1980), “The stratospheric and mesospheric sounder on Nimbus 7”, *Phil. Trans. R. Soc. London, Ser. A*, **296**, 219–241.
- Dunkerton, T. J. (1982), Theory of the mesopause semiannual oscillation, *J. Atmos. Sci.*, **39**, 2681–2690.
- Dutta, G., T. Tsuda, P. V. Kumar, M. C. A. Kumar, S. P. Alexander and T. Kozu (2008), Seasonal variation of short-period (<2 h) gravity wave activity over Gadanki, India (13.5\_N, 79.2\_E), *J. Geophys. Res.*, **113**, D14103, doi:10.1029/2007JD009178.
- Eckermann, S. D. (1995), On the observed morphology of gravitywave and equatorial-wave variance in the stratosphere, *J. Atmos. Terr. Phys.*, **57**, 105–134.
- Eckermann, S. D., I. Hirota and W. K. Hocking (1995), Gravity wave and equatorial wave morphology of the stratosphere derived from long-term rocket soundings, *Q. J. R. Meteorol. Soc.*, **121**, 149–186.
- Eckermann, S. D. and P. Preusse (1999), Global measurements of stratospheric mountain waves from space, *Science*, **286**, 1534–1537.
- Eckermann, S. D. and Wu, D. L. (2006), Imaging gravity waves in lower stratospheric AMSU-A radiances, Part 1: Simple Forward Model, *Atmos. Chem. Phys.*, **6**, 3325–3341.
- Eckermann, S. D., D. L. Wu, J. D. Doyle, J. F. Burris, T. J. McGee, C. A. Hostetler, L. Coy, B. N. Lawrence, A. Stephens, J. P. McCormack and T. F. Hogan (2006), Imaging gravity waves in lower stratospheric AMSU-A radiances, Part 2: Validation Case Study, *Atmos. Chem. Phys.*, **6**, 3343–3362.

- Ern, M., P. Preusse, M. J. Alexander and C. D. Warner (2004), Absolute values of gravity wave momentum flux derived from satellite data, *J. Geophys. Res.*, **109**, D20103, doi:10.1029/2004JD004752.
- Ern, M., P. Preusse and C. D. Warner (2006), Some experimental constraints for spectral parameters used in the Warner and McIntyre gravity wave parameterization scheme, *Atmos. Chem. Phys.*, **6**, 4361–4381.
- Fetzer, E. J. and J. C. Gille (1994), Gravity wave variance in LIMS temperatures, part I, Variability and comparison with background winds, *J. Atmos. Sci.*, **51**, 2461–2483.
- Fetzer, E. J. and J. C. Gille (1996), Gravity wave variance in LIMS temperatures, part II, Comparison with the zonal-mean momentum balance, *J. Atmos. Sci.*, **53**, 398–410.
- Fleming, E., S. Chandra, J. Barnett and M. Corney (1990), Zonal mean temperature, pressure, zonal wind and geopotential height as functions of latitude, *Adv. Space Res.*, **10**, 11–53, doi:10.1016/0273-1177(90)90386-E.
- Forbes, J. M., J. Gu and S. Miyahara (1991), On the interactions between gravity waves and the diurnal propagating tide, *Planet. Space Sci.*, **39**, 1249–1257.
- Fovell, R., D. Durran and J. R. Holton (1992), Numerical simulations of convectively generated stratospheric gravity waves, *J. Atmos. Sci.*, **49**, 1427–1442.
- Francis, G. L., D. P. Edwards, A. Lambert, C. M. Halvorson, J. M. Lee-Taylor and J. C. Gille (2006), Forward modeling and radiative transfer for the NASA EOS-Aura High Resolution Dynamics Limb Sounder (HIRDLS) instrument. *J. Geophys. Res.*, **111**, D13301, doi:10.1029/2005JD006270.
- Fritts, D. C. (1984), Gravity wave saturation in the middle atmosphere: A review of theory and observations, *Rev. Geophys.*, **22**, 275–308.
- Fritts, D. C. and T. J. Dunkerton (1985), Fluxes of heat and constituents due to convectively unstable gravity waves, *J. Atmos. Sci.*, **42**, 549–556.

## References

---

- Fritts, D. C. and R. A. Vincent (1987), Mesospheric momentum flux studies at Adelaide, Australia: Observations and a gravity wave/tidal interaction model, *J. Atmos. Sci.*, **44**, 605–619.
- Fritts, D. C., U.-P. Hoppe and B. Inhester (1990), A study of the vertical motion field near the high-latitude summer mesopause during MAC/SINE, *J. Atmos. Terr. Phys.*, **52**, 927–938, 1990.
- Fritts, D. C., L. Yuan, M. H. Hitchman, L. Coy, E. Kudeki and R. F. Woodman (1992), Dynamics of the equatorial mesosphere observed using the Jicamarca MST radar during June and August 1987, *J. Atmos. Sci.*, **49**, 2353–2371.
- Fritts, D. C. and G. D. Nastrom (1992), Sources of mesoscale variability of gravity waves, II, Frontal, convective, and jet stream excitation, *J. Atmos. Sci.*, **49**, 111–127.
- Fritts, D. C. and Isler, J. R. (1994), Mean motions and tidal and two-day structure and variability in the mesosphere and lower thermosphere over Hawaii. *J. Atmo. Sci.* **51**: 2145-2164.
- Fritts, D. C. et al. (1997), Equatorial dynamics observed by rocket, radar, and satellite during the CADRE/MALTED campaign, 2, Mean and wave structures, coherence, and variability, *J. Geophys. Res.*, **102**, 26,191–26,216.
- Fritts, D. C. and M. J. Alexander (2003), Gravity wave dynamics and effects in the middle atmosphere, *Rev. Geophys.*, **41**, doi:10.1029/2001RG000106.
- Fuller-Rowell, T. J. (1994), The impact of gravity waves on nitric oxide in the lower Thermosphere, *J. Atmos. Terr. Phys.*, **56**, 1387–1398.
- Garcia, R. R. and S. Solomon (1985), The effect of breaking gravity waves on the dynamics and chemical composition of the mesosphere and lower thermosphere, *J. Geophys. Res.*, **90**, 3850–3868.
- Garcia, R. R. and B. Boville (1994), “Downward control” of the mean meridional circulation and temperature distribution of the polar winter stratosphere, *J. Atmos. Sci.*, **51**, 2238–2245.

## References

---

- Gardner, C. S. and J. D. Shelton (1985), Density response of neutral atmospheric layers to gravity wave perturbations. *J. Geophys. Res.* **90**:1745-1754.
- Gardner, C. S. and D. G. Voelz (1987), Lidar studies of the nighttime sodium layer over Urbana, Illinois. *J. Geophys. Res.* **92**: 4673-4694.
- Garreaud, R., M. Vuille, R. Compagnucci and J. Marengo (2008), Present-day South American Climate. *PALAEO3 Special Issue (LOTRED South America)*. doi:10.1016/j.paleo.2007.10.032.
- Gary, B. L. (1989), Observational results using the microwave temperature profiler during the airborne Antarctic ozone experiment, *J. Geophys. Res.*, **94**, 11,223– 11,231.
- Gauge K. S. and B. B. Balsley (1978), Doppler radar probing of the clear atmosphere, *Bull. Am. Meteorol. Soc.* **59**:1074-1093.
- Geller, Marvin A., Hanli Liu, Jadwiga H. Richter, Dong Wu and Fuqing Zhang (2006), *Gravity Waves in Weather, Climate, and Atmospheric Chemistry: Issues and Challenges for the Community*, Inspired by the June 2006 Gravity Wave Retreat hosted by the Institute for Integrative and Multidisciplinary Earth Studies (TIIMES) at the National Center for Atmospheric Research (NCAR) in Boulder, CO, October 5.
- Gill, A. E. (1982), *Atmosphere-Ocean Dynamics*, Academic Press, New York.
- Gille, J. C. and F. B. House (1971), On the inversion of limb radiance measurements. I: Temperature and thickness. *J. Atmos. Sci.*, **28**, 1427-1442.
- Gille, J. C., P. L. Bailey, R. A. Craig, F. B. House and G. P. Anderson (1980a), “Sounding the stratosphere and mesosphere by infrared limb scanning from space”, *Science*, **208**, 397–399.
- Gille, J. C., P. L. Bailey and J. M. Russell III (1980b), “Temperature and composition measurements from the LRIR and LIMS experiments on NIMBUS 6 and NIMBUS 7”, *Phil. Trans. R. Soc. Lond. A*, **296**, 205–218.
- Gille, J. C. and J. M. Russell III (1984a), “The limb infrared monitor of the stratosphere: Experiment description, performance, and results”, *J. Geophys. Res.*, **89**, 5125–5140.

## References

---

Gille, J. C. and Russell III: Validation of temperature retrievals obtained by the Limb Infrared Monitor of the Stratosphere (LIMS) experiment on Nimbus 7. *J. Geophys. Res.*, **89**, 5125-5140, 1984b.

Gille, J. C., J. J. Barnett, J. C. Whitney, M. A. Dials, D. M. Woodard, W. Rudolf, A. Lambert and W. Mankin (2003), The High Resolution Dynamics Limb Sounder (HIRDLS) experiment on Aura, *Proc. SPIE Int. Soc. Opt. Eng.*, **5152**, 162– 171, doi:10.1117/12.507657.

Gille, J. C., T. Eden, G. Francis, A. Lambert, B. Nardi, J. Barnett, C. Cavanaugh, H. Lee, C. Craig, V. Dean, C. Halvorson, C. Krinsky, J. McInerney and B. Petersen (2005), Development of special corrective processing of HIRDLS data and early validation. *Proceedings of the SPIE*, **5883**, 92-102.

Gille, J. C. et al. (2008), High Resolution Dynamics Limb Sounder: Experiment overview, recovery, and validation of initial temperature data. *J. Geophys. Res.*, VOL. **113**, D16S43, doi:10.1029/2007JD008824.

GLOBE Task Team and others (Hastings, D.A., Dunbar, P.K., Elphingstone, G.M., Bootz, M., Murakami H., Maruyama, H., Masaharu, H., Holland, P., Payne, J., Bryant, N.A., Logan, T.L., Muller, J.-P., Schreier, G. and MacDonald, J.S.), eds. (1999), *The Global Land One-kilometer Base Elevation (GLOBE) Digital Elevation Model, Version 1.0*. National Oceanic and Atmospheric Administration, National Geophysical Data Center, 325 Broadway, Boulder, Colorado 80303, U.S.A. Digital data base on the World Wide Web (URL: <http://www.ngdc.noaa.gov/seg/topo/globe.shtml>) and CD-ROMs.

Gossard, Earl E. and William H. Hooke (1975), *Waves in the atmosphere*, Elsevier Scientific Publishing Company, Amsterdam.

Grasso, L. D. (2000), The differentiation between grid spacing and resolution and their applications to numerical modeling. *Bull. Am. Meteorol. Soc.* **81**: 579-580.

Gregory, D., G. J. Shutts and J. R. Mitchell (1998), A new gravity-wave-drag scheme incorporating anisotropic orography and low-level wave breaking: Impact upon the

- climate of the UK Meteorological Office Unified Model. *Q. J. R. Meteorol. Soc.*, **124**, 463-493.
- Gruber, A. and A. F. Krueger (1984), The status of the NOAA outgoing longwave radiation dataset, *Bull. Am. Meteorol. Soc.*, **65**(9), 958–962.
- Hamilton, K. (1991), Climatological statistics of stratospheric intertigravity waves deduced from historical rocketsonde wind and temperature data, *J. Geophys. Res.*, **96**, 20,831–20,839.
- Hawkins, G. J., R. Hunneman and C. Cole (1994), Infrared filters for space-flight focal plane array applications, *SPIE Proceedings*, **2253**, Pages 333-347.
- Haynes, P. H., C. J. Marks, M. E. McIntyre, T. G. Shephard and K. P. Shine (1991), On the “downward control” of extratropical diabatic circulations by eddy-induced mean zonal forces, *J. Atmos. Sci.*, **48**, 657–678.
- Hays, P. B., J. F. Kafkalidis, W. R. Skinner and R. G. Roble (2003), A global view of the molecular oxygen night glow, *J. Geophys. Res.-Atmosphere*, **108**, Art. No. 4646.
- Hilger, A. (1974), *Atmospheric Waves*, ADAM HILGER LTD, London.
- Hines, C. O. (1960), Internal atmospheric gravity waves at ionospheric heights, *Can. J. Phys.*, **38**, 1441–1481.
- Hines, C. O. (1967), On the nature of travelling ionospheric disturbances launched by low-altitude nuclear explosions, *J. Geophys. Res.*, **72**, 1877–1882.
- Hines, C. O. (1974), *The Upper Atmosphere in motion*, Am. Geophys. Union, Washington, DC, p. 194.
- Hines, C. O. (1997), Doppler-spread parameterization of gravity-wave momentum deposition in the middle atmosphere. Part 1: Basic formulation, *J. Atmos. Sol. Terr. Phys.*, **59**, 371 – 386, doi:10.1016/S1364-6826 (96)00079-X.
- Hirota, I. (1978), Equatorial waves in the upper stratosphere and mesosphere in relation to the semiannual oscillation of the zonal wind. *J. Atmos. Sci.* **35**, 714-722.

## References

---

- Hirota, I. (1984), Climatology of gravity waves in the middle atmosphere, *J. Atmos. Terr. Phys.*, **46**, 767–773.
- Hirota, I. and T. Niki (1985), A statistical study of inertia-gravity waves in the middle atmosphere, *J. Meteorol. Soc. Jpn.*, **63**, 1055–1066.
- Hitchman, M. H. and C. B. Leovy (1986), Evolution of the zonal mean state in the equatorial middle atmosphere during October 1978-May 1979. *J. Atmos. Sci.* **43**, 3159-3176.
- Holton, J. R. and R. S. Lindzen (1972), An updated theory for the quasi-biennial cycle of the tropical stratosphere, *J. Atmos. Sci.* **29**, 1076-1080.
- Holton, J. R. (1982), The role of gravity wave induced drag and diffusion in the momentum budget of the mesosphere, *J. Atmos. Sci.*, **39**, 791–799.
- Holton, J. R. (1983), The influence of gravity wave breaking on the general circulation of the middle atmosphere, *J. Atmos. Sci.*, **40**, 2497–2507.
- Holton, J. R. (1984), The generation of mesospheric planetary waves by zonally asymmetric gravity wave breaking, *J. Atmos. Sci.*, **41**, 3427–3430.
- Holton, J. R. (1992), *An Introduction to Dynamic Meteorology*, 507 pp., Academic, San Diego, Calif..
- Holton, J. R., M. J. Alexander and M. T. Boehm (2001), Evidence for short vertical wavelength Kelvin waves in the DOE-ARM Nauru99 radiosonde data, *J. Geophys. Res.*, **106**, 20,125–20,129.
- Houghton, J. T., F. W. Taylor and C. D. Rodgers (1984), *Remote sounding of atmosphere*, Cambridge university press, p64.
- Hunneman, R., J. J. Barnett and G. J. Hawkins (1994), High-Performance Infrared Filters for the HIRDLS 21-Channel Focal Plane Detector Array, *SPIE Proceedings*, **2210-49**, Pages 516-532.

## References

---

- Isler, J. R., M. J. Taylor and D. C. Fritts (1997), Observational evidence of wave ducting and evanescence in the mesosphere, *J. Geophys. Res.*, **102**, 26,301–26,313.
- Iwasaki, T., S. Yamada and K. Tada (1989), A parameterization scheme of orographic gravity wave drag with two different vertical partitionings, Part I: Impact on medium-range forecasts. *J. Meteor. Soc. Japan*, **67**, 11 – 27.
- Jasperson, W. H., G. D. Nastrom and D. C. Fritts (1990), Further study of terrain effects on the mesoscale spectrum of atmospheric motions, *J. Atmos. Sci.*, **47**, 979–987.
- Jiang, J. H. and D. L. Wu (2001), UARS MLS observations of gravity waves associated with the Arctic winter stratospheric vortex, *Geophys. Res. Lett.*, **28**, 527– 530.
- Jiang, J. H., D. L. Wu and S. D. Eckermann (2002), Upper Atmosphere Research Satellite (UARS) MLS observation of mountain waves over the Andes, *J. Geophys. Res.*, **107**, 10.1029/2002JD002091.
- Jiang, J. H., S. D. Eckermann, D. L. Wu and J. Ma (2004a), A search for mountain waves in MLS stratospheric limb radiances from the winter northern hemisphere: data analysis and global mountain wave modeling, *J. Geophys. Res.* **109**, No. D3, D03107, 10.1029/2003JD003974.
- Jiang, J. H., B. Wang, K. Goya, K. Hocke, S. D. Eckermann, J. Ma, D. L. Wu and W. G. Read (2004b), Geographical distribution and interseasonal variability of tropical deep convection: UARS MLS observations and analyses, *J. Geophys. Res.*, **109**, D03111, doi:10.1029/2003JD003756.
- Jiang, J. H., S. D. Eckermann, D. L. Wu, K. Hocke, B. Wang, J. Ma and Y. Zhang (2005), Seasonal variation of gravity wave sources from satellite observation, *Adv. Space Res.*, **35**, 1925-1932.
- Jones, R. M. (2005), A general dispersion relation for internal gravity waves in the atmosphere or ocean, including baroclinicity, vorticity, and rate of strain, *J. Geophys. Res.*, **110**, D22106, doi:10.1029/2004JD005654.

## References

---

- Karoly, D. J., G. L. Roff and M. J. Reeder (1996), Gravity wave activity associated with tropical convection detected in TOGA COARE sounding data, *Geophys. Res. Lett.*, **23**, 261–264.
- Kiehl, J. T., J. J. Hack, G. B. Bonan, B. A. Boville, B. P. Briegleb, D. L. Williamson and P. J. Rasch (1996), Description of the NCAR Community Climate Model (CCM3), *Tech. Note NCAR/TN-4201STR*, 152 pp., Natl. Cent. for Atmos. Res., Boulder, Colo.
- Kim, Y.-J., S. D. Eckermann and H.-Y. Chun (2003), An overview of the past, present and future of gravity-wave drag parameterization for numerical climate and weather prediction models, *Atmos. Ocean*, **41**(1), 65–98, doi:10.3137/ao.410105.
- Know, K. H. and C. S. Gardner (1990), Airborne sodium lidar measurements of gravity wave intrinsic parameters. *J. Geophys. Res.* **95**: 20, 457-20, 467.
- Kummerow, C. et al. (2000), The status of the Tropical Rainfall Measuring Mission (TRMM) after two years in orbit, *J. Appl. Meteorol.*, **39**, 1965–1982.
- Lambert, A., P. L. Bailey, D. P. Edwards, J. C. Gille, B. R. Johnson, C. M. Halvorson, S. T. Massie and K. A. Stone (1999), *HIRDLS Level-2 Algorithm Theoretical Basis Document*, British Atmospheric Data Centre (BADC).
- Lambriksen, B. H. (2003): Calibration of the AIRS microwave instruments, *IEEE Trans. Geosci. Remote Sens.*, **41**, 369–378.
- Leutbecher, M. and H. Volkert (2000), Propagation of mountain waves into the stratosphere: Quantitative evaluation of three-dimensional simulations, *J. Atmos. Sci.*, **57**, 3090–3108.
- Lilly, D. K. and P. J. Kennedy (1973), Observations of a stationary mountain wave and its associated momentum flux and energy dissipation, *J. Atmos. Sci.*, **30**, 1135–1152.
- Limpasuvan, V., D. L. Wu, M. J. Alexander, M. Xue, M. Hu, S. Pawson and J. R. Perkins (2007), Stratospheric gravity wave simulation over Greenland during 24 January 2005. *J. Geophys. Res.*, **112**, 10115.

## References

---

- Lindzen, R. S. (1967), Thermally driven diurnal tide in the atmosphere, *Q. J. R. Meteorol. Soc.*, **93**, 18-42.
- Lindzen, R. S. and J. R. Holton (1968), A theory of the quasi-biennial oscillation, *J. Atmos. Sci.*, **25**, 1095–1107.
- Lindzen, R. S. (1981), Turbulence and stress owing to gravity wave and tidal breakdown, *J. Geophys. Res.*, **86**, 9707–9714.
- Liu, H.-L., M. E. Hagan and R. G. Roble (2000), Local mean state changes due to gravity wave breaking modulated by the diurnal tide, *J. Geophys. Res.*, **105**, 12,381–12,396.
- Lu, W. and D. C. Fritts (1993), Spectral estimates of gravity wave energy and momentum fluxes, III, Gravity wave-tidal interactions, *J. Atmos. Sci.*, **50**, 3,714–3,727.
- Manson, H. A. (1990), Gravity wave horizontal and vertical wavelengths: An update of measurements in the mesosphere region (~80-100km). *J. Atmos. Sci.* **47**:2765-2773.
- Marsh, A. K. P., N. J. Mitchell and L. Thomas (1991), Lidar studies of stratospheric gravity-wave spectra, *Planet. Space Sci.*, **39**, 1541–1548.
- Massie, S. et al. (2007), High Resolution Dynamics Limb Sounder observations of polar stratospheric clouds and subvisible cirrus, *J. Geophys. Res.*, **112**, D24S31, doi:10.1029/2007JD008788.
- Mayr, H. G., J. G. Mengel, C. O. Hines, K. L. Chan, N. F. Arnold, C. A. Reddy and H. S. Porter (1997), The gravity wave Doppler spread theory applied in a numerical spectral model of the middle atmosphere. 2. Equatorial oscillations, *J. Geophys. Res.*, **102**(D22), 26093-26106, 10.1029/96JD03214.
- Mayr, H. G., J. G. Mengel, K. L. Chan and H. S. Porter (1998), Seasonal variations of the diurnal tide induced by gravity wave filtering, *Geophys. Res. Lett.*, **25**, 943–946.
- McFarlane, N. A. (1987), The effect of orographically excited gravity wave drag on the general circulation of the lower stratosphere and troposphere, *J. Atmos. Sci.*, **44**, 1775 – 1800.

- McLandress, C., M. J. Alexander and D. L. Wu (2000), Microwave Limb Sounder observations of gravity waves in the stratosphere: A climatology and interpretation, *J. Geophys. Res.*, **105**, 11,947–11,967.
- Meyer, C. K. (1999), Gravity wave interactions with the diurnal propagating tide, *J. Geophys. Res.*, **104**, 4223–4239.
- Miranda, P.M.A. and I. N. James (1992), Non-linear three-dimensional effects on gravity-wave drag: Splitting flow and breaking waves, *Q. J. R. Meteorol. Soc.*, **118**, 1057-1081.
- Mitchell, N. J., L. Thomas and A. K. P. Marsh (1991), Lidar observations of long-period gravity waves in the stratosphere, *Ann. Geophys.*, **9**, 588–596.
- Mitchell, N. J., L. Thomas and I. T. Prichard (1994), Gravity waves in the stratosphere and troposphere observed by lidar and MST radar, *J. Atmos. Terr. Phys.*, **56**, 939–947.
- Mitchell, N. J. and V. S. C. Howells (1998), Vertical velocities associated with gravity waves measured in the mesosphere and lower thermosphere with the EISCAT VHF radar, *Ann. Geophys.*, **16**, 1367–1379.
- Miyahara, S. (1985), Suppression of stationary planetary waves by internal gravity waves in the mesosphere, *J. Atmos. Sci.*, **42**, 100–107.
- Miyahara, S., Y. Hayashi and J. D. Mahlman (1986), Interactions between gravity waves and planetary-scale flow simulated by the GFDL “SKYHI” general circulation model, *J. Atmos. Sci.*, **43**, 1844–1861.
- Murayama, Y., T. Tsuda and S. Fukao (1994), Seasonal variation of gravity wave activity in the lower atmosphere observed with the MU radar, *J. Geophys. Res.*, **99**, 23,057–23,069.
- Nappo, C. J. (2002), *An Introduction to Atmospheric Gravity Waves*, Academic press, London, UK.
- Nastrom, G. D., D. C. Fritts and K. S. Gage (1987), An investigation of terrain effects on the mesoscale spectrum of atmospheric motions, *J. Atmos. Sci.*, **44**, 3087–3096.

## References

---

- Nastrom, G. D. and D. C. Fritts (1992), Sources of mesoscale variability of gravity waves, part I, Topographic excitation, *J. Atmos. Sci.*, **49**, 101–110.
- Naujokat, B. (1986), An update of the observed quasi-biennial oscillation of the stratospheric winds over the tropics. *J. Atmos. Sci.* **43**, 1873-1877.
- Newsom, R. K., R. M. Banta, J. Otten, W. L. Eberhard and J. K. Lundquist (2000), Doppler lidar observations on internal gravity waves, shear instability and turbulence during CASES-99. In *14th Symposium on Boundary Layer and Turbulence, August 7-11, 2000, Aspen, CO*, pp. 362-365. Boston, MA: Am. Meteorol. Soc.
- Ottersten, H., K. R. Hardy and C. G. Little (1973), Radar and sodar probing of waves and turbulence in statically stable clear-air layers. *Boundary-layer Meteorol.* **4**: 47-89.
- Palmer, T. N., G. J. Shutts and R. Swinbank (1986), Alleviation of a systematic westerly bias in general circulation and numerical weather prediction models through an orographic gravity wave drag parametrization. *Q. J. R. Meteorol. Soc.*, **112**, 1001-1039.
- Piani, C., D. Durran, M. J. Alexander and J. R. Holton (2000), A numerical study of three-dimensional gravity waves triggered by deep tropical convection and their role in the dynamics of the QBO, *J. Atmos. Sci.*, **57**, 3689–3702.
- Pfister, L., W. Starr, R. Craig and M. Loewenstein (1986), Small-scale motions observed by aircraft in the tropical lower stratosphere: Evidence for mixing and its relationship to largescale flows, *J. Atmos. Sci.*, **43**, 3210–3225.
- Pfister, L., S. Scott and M. Loewenstein (1993a), Mesoscale disturbances in the tropical stratosphere excited by convection: observations and effects on the stratospheric momentum budget, *J. Atmos. Sci.*, **50**, 1058–1075.
- Pfister, L., K. R. Chan, T. B. Bui, B. Bowen, M. Legg, B. Gary, K. Kelly, M. Proffitt and W. Starr (1993b), Gravity waves generated by a tropical cyclone during STEP tropical field program: A case study, *J. Geophys. Res.*, **98**, 8611 –8638.
- Pielke, R. A. (1984), *Mesoscale Meteorological Modeling*, San Diego: Academic Press.

- Plumb, R. A. (1977), The interaction of two internal waves with the mean flow: implications for the theory of the quasi-biennial oscillation. *J. Atmos. Sci.* **34**, 1847-1858.
- Plumb, R. A. and A. D. McEwan (1978), The instability of a forced standing wave in a viscous stratified fluid: a laboratory analogue of the quasi-biennial oscillation. *J. Atmos. Sci.* **35**, 1827-1839.
- Preusse, P., S. D. Eckermann and D. Offermann (2000), Comparison of global distributions of zonal-mean gravity wave variance inferred from different satellite measurements. *Geophys. Res. Lett.*, **27**, 3877–3880.
- Preusse, P., A. Dörnbrack, S. D. Eckermann, M. Riese, B. Schaeler, J. T. Bacmeister, D. Broutman and K. U. Grossmann (2002), Space-based measurements of stratospheric mountain waves by CRISTA, 1. Sensitivity, analysis method, and a case study, *J. Geophys. Res.*, **107**(D23), 8178, doi:10.1029/2001JD000699.
- Preusse, P., M. Ern, S. D. Eckermann, C. D. Warner, R. H. Picard, P. Knieling, M. Krebsbach, J. M. Russell III, M. G. Mlynczak, C. J. Mertens and M. Riese (2006), Tropopause to mesopause gravity waves in August: Measurement and modeling, *J. Atmos. Solar-Terr. Phys.*, **68**, 1730–1751.
- Preusse, P., S. D. Eckermann, M. Ern, J. Oberheide, R. H. Picard, R. G. Roble, M. Riese, J. M. Russell III and M. G. Mlynczak (2009), Global ray tracing simulations of the SABER gravity wave climatology, *J. Geophys. Res.*, **114**, D08126, doi:10.1029/2008JD011214.
- Ralph, F. M., P. J. Neiman, T. L. Keller, D. Levinson and L. Fedor (1997), Observations, simulations, and analysis of nonstationary trapped lee waves. *J. Atmos. Sci.* **54**:1308-1333.
- Ratnam, M. V., G. Tetzlaff and C. Jacobi (2004), Global and seasonal variations of stratospheric gravity wave activity deduced from the CHAMP/GPS satellite, *J. Atmos. Sci.*, **61**, 1610-1620.

- Ray, E. A., M. J. Alexander and J. R. Holton (1998), An analysis of the structure and forcing of the equatorial semiannual oscillation in zonal wind, *J. Geophys. Res.*, **103**, 1759–1774.
- Reed, R. J. (1965), The quasi-biennial oscillation of the atmosphere between 30 and 50 km over Ascension Island. *J. Atmos. Sci.* **22**, 331-333.
- Roche, A. E., J. B. Kumer, J. L. Mergenthaler, G. A. Ely, W. G. Uplinger, J. F. Potter, T. C. James and L. W. Serritt (1993), “The cryogenic limb array etalon spectrometer (CLAES) on UARS: Experiment description and performance”, *J. Geophys. Res.*, **96**, 10,763–10,775.
- Rodgers, C. D. and A. J. Prata (1981), Evidence for a travelling two-day wave in the middle atmosphere, *J. Geophys. Res.*, **86**, 9661-9664.
- Rodgers, C. D. (2000), *Inverse methods for atmospheric sounding: theory and practice*, World Scientific press, London.
- Rosenlof, K. H. (1996), Summer hemisphere differences in temperature and transport in the lower stratosphere, *J. Geophys. Res.*, Vol. **101**, No. D14, 19,129-19,136.
- Salby, M. L. and R. R. Garcia (1987), Transient response to localized episodic heating in the tropics, part I, Excitation and shorttime near-field behaviour, *J. Atmos. Sci.*, **44**, 458–498.
- Sassi, F. and R. R. Garcia (1994), A one-dimensional model of the semiannual oscillation driven by convectively forced gravity waves, *J. Atmos. Sci.*, **51**, 3167–3182.
- Sato, K. (1992), Vertical wind disturbances in the afternoon of midsummer revealed by the MU radar, *Geophys. Res. Lett.*, **19**, 1943–1946.
- Sato, K. (1993), Small-scale wind disturbances observed by the MU radar during the passage of typhoon Kelly, *J. Atmos. Sci.*, **50**, 518–537.
- Sato, K. (1994), A statistical study of the structure, saturation and sources of inertio-gravity waves in the lower stratosphere observed with the MU radar, *J. Atmos. Terr. Phys.*, **56**, 755–774.

## References

---

- Sato, K., F. Hasegawa and I. Hirota (1994), Short-period disturbances in the equatorial lower stratosphere, *J. Meteorol. Soc., Japan*, **72**, 859-872.
- Sato, K., H. Hashiguchi and S. Fukao (1995), Gravity waves and turbulence associated with cumulus convection observed with the UHF/VHF clear-air Doppler radars, *J. Geophys. Res.*, **100**, 7111–7120.
- Sato, K. and T. J. Dunkerton (1997), Estimates of momentum flux associated with equatorial Kelvin and gravity waves, *J. Geophys. Res.*, **102**, 26,247–26,261.
- Satomura, T and K. Sato (1999), Secondary Generation of Gravity Waves Associated with the Breaking of Mountain Waves, *J. Atmos.Sci.*, **56**, 3847-3858.
- Sawyer, J. S. (1959), The introduction of the effects of topography into methods of numerical forecasting. *Q. J. R. Meteorol. Soc.* **85**:31-43.
- Schwiesow, R. L. (1986), Lidar measurements of boundary-layer variables. *In Probing the Atmospheric Boundary Layer*, D. H. Lenschow, ed., pp. 139-162. Boxton, MA: Am. Meteorological Soc.
- Shimizu, A. and T. Tsuda (1997), Characteristics of Kelvin waves and gravity waves observed with radiosondes over Indonesia, *J. Geophys. Res.*, **102**, 26,159–26,171.
- Shutts, G. J., M. Kitchen and P. H. Hoare (1988), A large amplitude gravity wave in the lower stratosphere detected by radiosonde, *Q. J. R. Meteorol. Soc.*, **114**: 580.
- Shutts, G. J. (1998). Stationary gravity wave structure in flows with directional wind shear, *Q. J. R. Meteorol. Soc.*, **124**, 1421-1442.
- Smith, R. B. (1980), Linear theory of stratified hydrostatic flow past an isolated mountain. *Tellus*, **32**, 349-364.
- Snyder, W. H., R. S. Thomson, R. E. Eskridge, R. E. Lawson, I. P. Castro, S. T. Lee, J. C. R. Hunt and J. Ogawa, (1985), The structure of strongly stratified flows over hills: Dividing streamline concept. *J. Fluid Mech.*, **152**, 249-288.

Strobel, D. F., M. E. Summers, R. M. Bevilacqua, M. T. DeLand and M. Allen (1987), Vertical constituent transport in the mesosphere, *J. Geophys. Res.*, **92**, 6691–6698.

Swenson, G. R., M. J. Alexander and R. Haque (2000), Dispersion imposed limits on atmospheric gravity waves in the mesosphere: Observations from OH airglow, *Geophys. Res. Lett.*, **27**, 875–878.

Taylor, F. W., C. D. Rodgers, J. G. Whitney, S. T. Werrett, J. J. Barnett, G. D. Peskett, P. Venters, J. Ballard, C. W. P. Palmer, R. J. Knight, P. Morris, T. Nightingale and A. Dudhia (1993), “Remote Sensing of atmospheric structure and composition by pressure modulator radiometry from space: The ISAMS experiment on UARS”, *J. Geophys. Res.*, **98**, 10,799–10,814.

Taylor, M. J., Y. Y. Gu, X. Tao, C. S. Gardner and M. B. Bishop (1995), An investigation of intrinsic gravity wave signatures using coordinated lidar and nightglow image measurements, *Geophys. Res. Lett.*, **22**, 2853–2856.

Taylor, M. J., W. R. Pendleton Jr., S. Clark, H. Takahashi, D. Gobbi and R. A. Goldberg (1997), Image measurements of short period gravity waves at equatorial latitudes, *J. Geophys. Res.*, **102**, 26,283–26,299.

Tsuda, T., S. Kato, T. Yokoi, T. Inoue, M. Yamamoto, T. E. VanZandt, S. Fukao and T. Sato (1990a), Gravity waves in the mesosphere observed with the middle and upper atmosphere radar, *Radio Sci.*, **25**, 1005–1018.

Tsuda, T., Y. Murayama, M. Yamamoto, S. Kato and S. Fukao (1990b), Seasonal variation of momentum flux in the mesosphere observed with the MU radar, *Geophys. Res. Lett.*, **17**, 725–728.

Tsuda, T., Y. Murayama, H. Wiryosumarto, S. W. B. Harijono and S. Kato (1994a), Radiosonde observations of equatorial atmosphere dynamics over Indonesia, 2, characteristics of gravity waves, *J. Geophys. Res.*, **99**, 10,507–10,516.

Tsuda, T., Y. Murayama, T. Nakamura, R. A. Vincent, A. H. Manson, C. E. Meek and R. L. Wilson (1994b), Variations of the gravity wave characteristics with height, season, and latitude revealed by comparative observations, *J. Atmos. Terr. Phys.*, **56**, 555–568.

## References

---

- Tsuda, T., M. Nishida, C. Rocken and R. H. Ware (2000), A global morphology of gravity wave activity in the stratosphere revealed by the GPS occultation data (GPS/MET), *J. Geophys. Res.*, **105**, 7257–7274.
- Tsuda, T., M. V. Ratnam, P. T. May, M. J. Alexander, R. A. Vincent and A. MacKinnon (2004), Characteristics of gravity waves with short vertical wavelengths observed with radiosonde and GPS occultation during DAWEX (Darwin Area Wave Experiment), *J. Geophys. Res.*, **109**, D20S03, doi:10.1029/2004JD004946.
- “U.S Standard Atmosphere” (1976), U.S. Gov. Print. Off., Washington, D.C.
- V004 data quality document*, (2008).
- Vincent, R. A. and I. M. Reid (1983), HF Doppler measurements of mesospheric momentum fluxes, *J. Atmos. Sci.*, **40**, 1321– 1333.
- Vincent, R. A., S. J. Allen and S. D. Eckermann (1997), Gravity-wave parameters in the lower stratosphere, in *Gravity Wave Pro-Processes: Their Parameterization in Global Climate Models*, NATO ASI Ser., Ser. I, vol. **50**, edited by K. Hamilton, pp. 7–25, Springer-Verlag, New York.
- Vincent, R. A. and M. J. Alexander (2000), Gravity waves in the tropical lower stratosphere: An observational study of seasonal and interannual variability, *J. Geophys. Res.*, **105**, 17,971–17,982.
- Wada, K., T. Nitta and K. Sato (1999), Equatorial inertia-gravity waves in the lower stratosphere revealed by TOGACOARE IOP data, *J. Meteorol. Soc. Jpn.*, **77**, 721–736.
- Wallace, J. M. and J. R. Holton (1968), A diagnostic numerical model of the quasi-biennial oscillation. *J. Atmos. Sci.* **25**, 280-292.
- Wallace, J. M., S. Tibaldi and A. Simmons (1983), Reduction of systematic forecast errors in the ECMWF model through the introduction of an envelope orography, *Q. J. R. Meteorol. Soc.*, **109**, 683-717.

- Walterscheid, R. L. (1981), Inertio-gravity wave induced accelerations of mean flow having an imposed periodic component: Implications for tidal observations in the meteor region, *J. Geophys. Res.*, **86**, 9698–9706.
- Walterscheid, R. L., J. H. Hecht, R. A. Vincent, I. M. Reid, J. Woithe and M. J. Hickey (1999), Analysis and interpretation of airglow and radar observations of quasi-monochromatic gravity waves in the upper mesosphere and lower thermosphere over Adelaide, Australia (35°S, 138°E), *J. Atmos. Sol. Terr. Phys.*, **61**, 461–478.
- Warner, C. D. and M. E. McIntyre (2001), An ultrasimple spectral parameterization for nonorographic gravity waves, *J. Atmos. Sci.*, **58**, 1837–1857, doi:10.1175/1520-0469(2001)058<1837:AUSPFN>2.0.CO;2.
- Webster, S., A. R. Brown, D. R. Cameron and C. P. Jones (2003), Improvements to the representation of orography in the Met Office Unified Model, *Q. J. R. Meteorol. Soc.*, **129**, pp. 1989-2010.
- Wheeler, M. and G. N. Kiladis (1999), Convectively coupled equatorial waves: Analysis of clouds and temperature in the wavenumber-frequency domain, *J. Atmos. Sci.*, **56**, 374–399.
- Whiteway, J. A. and A. I. Carswell (1995), Lidar observations of gravity wave activity in the upper stratosphere over Toronto, *J. Geophys. Res.*, **100**, 14,113–14,124.
- Wilson, R., M.-L. Chanin and A. Hauchecorne (1991), Gravity waves in the middle atmosphere observed by Rayleigh lidar, part 2, Climatology, *J. Geophys. Res.*, **96**, 5169–5183.
- Wolff, D. B., D. A. Marks, E. Amitai, D. S. Silberstein, B. L. Fisher, A. Tokay, J. Wang and J. L. Pippitt (2005), Ground validation for the Tropical Rainfall Measuring Mission (TRMM), *J. Atmos. Oceanic Technol.*, **22**, 365–380.
- Wu, D. L. and J. W. Waters (1996a), Gravity-wave-scale temperature fluctuations seen by the UARS MLS, *Geophys. Res. Lett.*, **23**, 3289–3292.
- Wu, D. L. and J. W. Waters (1996b), Satellite observations of atmospheric variances: A possible indication of gravity waves, *Geophys. Res. Lett.*, **23**, 3631–3634.

- Wu, D. L. and J. W. Waters (1997), Observations of gravity waves with the UARS Microwave Limb Sounder, in *Gravity Wave Processes and Their Parameterization in Global Climate Models*, edited by K. Hamilton, Springer-Verlag, New York.
- Wu, D. L. and J. H. Jiang (2002), MLS observations of atmospheric gravity waves over Antarctica, *J. Geophys. Res.*, **107**(D24), 4773, doi:10.1029/2002JD002390.
- Wu, D. L., J. H. Jiang and C. Davis (2006), EOS MLS cloud ice measurements and radiative transfer model, *IEEE Trans. Geosci. Remote Sens.*, **44**, 1156-1165.
- Wu, D. L. and S. D. Eckermann (2008), Global Gravity Wave Variances from Aura MLS: Characteristics and Interpretation, *J. Atmos.Sci.* DOI: 10.1175/2008JAS2489.1
- Yan, X, S. Vosper, N. Arnold and H. Wells (2009), Gravity waves over the southern Andes: a comparison of HIRDLS satellite observations with predictions from an orographic gravity-wave parameterization scheme, *submitted*.
- Zink, F. and R. A. Vincent (2001), Wavelet analysis of stratospheric gravity wave packets over Macquarie Island, 1, Wave parameters, *J. Geophys. Res.*, **106**, 10,275–10,288, 2001.